Transient Behaviour of Lock Exchange Gravity Currents Encountering Current Scale Roughness Fields

Alex Meredith

Supervisors: Prof. Roger Nokes

Dr. Craig McConnochie

Dr. Claudia Cenedese

Department of Civil and Natural Resources Engineering

University of Canterbury

Christchurch, New Zealand

A thesis submitted in partial fulfilment of the requirements for the degree of

Doctor of Philosophy in Civil Engineering

20 January 2021

Acknowledgements

Firstly I would like to thank my supervisor, Roger Nokes. Roger, it was your brilliant, passionate teaching that first got me excited about fluid mechanics when I was an undergraduate student, without which I would likely have never pursued a PhD in the field. Under your supervision I felt a little spoilt by how much time and effort you found to ensure my success. Every page of writing you returned to me practically dripping in (digital) highlighter had a massive impact on not only the quality of this thesis but of my own skills and abilities.

I would also like to thank my associate supervisors Craig McConnochie and Claudia Cenedese for their feedback and contributions to this thesis. Craig; in addition to your supervision I must thank you for expanding my horizons beyond the scope of this thesis. Whether through organising meetings to learn about the fluid mechanics of COVID-19 during lock-down or lunchtime conversations about obscure phenomenon in fluid mechanics I really appreciate your passion and have come out the other side better because of it.

The experiments presented in this thesis could not have been carried out without the technical assistance of Patrick Branje, Kevin Wines, Ian Sheppard and Phillippe Bruneau. From building my experimental setup to being good spirited about my (accidental) attempts to flood the lab I am very grateful for all of your contributions.

I am grateful for the community of postgraduate students in our department. Our regular coffee time, lunchtime chats and BYOs have really helped to keep me sane throughout the whole process. In particular, I would like to acknowledge my office mates and fellow fluid mechanics students Lizzy, Jane and Rondo. While I may well have finished much sooner without the spontaneous office chats or the (sometimes less than) gentle ribbing I would not have had nearly as much fun without you.

To Akira; you came into my life in the final year of my PhD, just as I was starting to become busy writing my thesis but somehow I never managed to scare you away. Thank you for putting up with the breakdowns and the long nights of being neglected as my thesis kept sucking up my

attention. I am so grateful to have had you in my life for this past year and I look forward to all of the adventures yet to come.

To Blaze; while you will never be able to read this and probably don't even know what a thesis is, I must thank you for your wagging tail and loving stare that always brightened my mood whenever I doubted myself. My spirits could never get too low when I knew your boundless energy and excitement would be there to greet me when I got home.

Finally, and perhaps most importantly, to Mum, Dad and Katie; you are some of very few people in my life who I know will be there for me no matter what. You deserve my gratitude more than anybody else for your endless support, advice and kindness. I feel eternally grateful to have been born into a family with whom I feel truly at home and I would not be here today without you.

UNIVERSITY OF CANTERBURY
Te Whare Wānanga o Waitaha
CHRISTCHURCH NEW ZEALAND

Deputy Vice-Chancellor's Office
Postgraduate Office

Co-Authorship Form

This form is to accompany the submission of any thesis that contains research reported in co-authored work that has been published, accepted for publication, or submitted for publication. A copy of this form should be included for each co-authored work that is included in the thesis. Completed forms should be included at the front (after the thesis abstract) of each copy of the thesis submitted for examination and library deposit.

Please indicate the chapter/section/pages of this thesis that are extracted from co-authored work and provide details of the publication or submission from the extract comes:

Chapter 8 consists of a paper accepted for publication in the Journal of Fluid Mechanics. The thesis author is the second author on this paper. The reference for this paper is as follows:

Köllner, T., Meredith, A., Nokes, R., and Meiburg, E. (In Press). Gravity currents over fixed beds of monodisperse spheres. J.Fluid Mech.

Please detail the nature and extent (%) of contribution by the candidate:

The experiments outlined in Section 8.2.1 were conducted by the thesis author and the results presented from these experiments are presented in Section 8.3.

The numerical modelling described in Sections 8.2.2 and 8.2.3 was not conducted by the thesis author. The majority of the analysis in Section 8.4 was based on the numerical modelling and was not carried out by the thesis author.

The manuscript was written collaboratively by the thesis author and the primary author who was responsible for the numerical modelling.

Certification by Co-authors:

If there is more than one co-author then a single co-author can sign on behalf of all

The undersigned certifys that:

- The above statement correctly reflects the nature and extent of the PhD candidate's contribution to this co-authored work
- In cases where the candidate was the lead author of the co-authored work he or she wrote the text

Name: Professor *Roger Nokes* Signature:  Date: *27 August 2020*

Abstract

Gravity currents are predominantly horizontal flows generated by density differences between two or more fluids. They exist throughout the natural and engineered environment. Understanding the impact of roughness on gravity currents is important because of the prevalence of rough boundaries in the environment – for example aquatic vegetation or cities.

This thesis describes a series of experiments conducted to explore the impact of rough boundaries on gravity currents. The experiments were carried out in a long rectangular channel and the currents were generated using a lock exchange technique. Light attenuation and particle tracking velocimetry were used to generate density and velocity fields respectively. Roughness consisting of vertical circular cylinders and closely packed spheres were attached to the base of the channel. The height of the roughness was of a similar order of magnitude to the current. The experiments with closely packed spheres are compared with direct numerical simulations carried out at the University of California, Santa Barbara.

In experiments utilising vertical circular cylinders the distribution of the cylinders was varied, along with the relative roughness height – defined as the height of the cylinders relative to the total depth of fluid. As a current interacts with the roughness its Froude number decreases and the fluid near the front dilutes. When the roughness is sparsely distributed, or the relative roughness height is small, a current propagates between rows of roughness and is hence referred to as through-flowing. While a smooth bed current has a distinctive head and tail structure, a through-flowing current takes on a wedge-like structure. The through-flowing current is driven by a balance between the pressure gradient in its tail and the drag force imposed on the current by the cylinders. In the through-flowing regime, the Froude number and the pressure gradient in the tail of the current are independent of the relative roughness height when the spatial co-ordinates are non-dimensionalised by the total fluid depth. A simple mathematical model suggests that a current in the through-flow regime is driven by a balance between the pressure gradient in the tail and the drag force imposed on the current by the roughness. However, as the relative roughness height decreases the head becomes more prominent and the current transitions from being a

wedge-driven flow to resembling a smooth bed current. Additionally, the rate of entrainment of ambient fluid into a through-flowing current is similar to that of a smooth bed current.

When the roughness is densely distributed, or the relative roughness height is small, a current travels atop the roughness with a head and tail structure similar to a smooth bed current and hence is termed to be in an over-flowing regime. However, unlike a smooth bed current, the bed contains unstable light fluid beneath the dense current and hence a convective exchange of fluid exists between the current and the bed. This exchange of fluid dilutes and slows the current as it travels. However, the fluid contained within the roughness may not all mix with the current and some of it may penetrate the full depth of the current and be mixed with the ambient fluid. Over time an over-flowing current approaches a steady state as the loss of dense fluid in the head of the current becomes in balance with the dense fluid entering the head from the tail.

When the roughness is densely distributed across the channel but sparsely distributed along the channel, and the relative roughness height is sufficiently small, a current is deflected over each row of roughness individually and plunges downwards between rows of cylinders. Hence this current is termed to be in a plunging regime. When the spacing across the channel is sufficiently sparse a small through-flowing front will initially propagate through the roughness before the remainder of the current fluid plunges over the top of the roughness. As the relative roughness height increases the current becomes completely through-flowing and individual bores reflect from each row of roughness.

Experiments with closely packed solid spheres show that as this roughness is densely distributed a current travels in an over-flowing regime. However, unlike a current interacting with densely distributed cylinders, the structured matrix of the bed means that the convective exchange of fluid between the current and the bed occurs slowly. This exchange consists of two separate processes and these occur over different timescales. The first process is the exchange between the current and the exposed pore spaces. This process occurs rapidly and is similar to the exchange seen in an over-flowing cylinder experiment. The second process is the penetration of dense fluid into the bed. This process takes longer to develop and is more significant in currents with large relative roughness heights.

Table of contents

List of figures

List of tables

Nomenclature

A	Combined velocity multiplier
B	Channel width
C	An empirical coefficient for modelling Froude number
D	Depth of dense fluid in a submerged lock exchange experiment
E	An empirical coefficient for modelling Froude number
F_D	Drag force
Fr	Froude Number
Fr_H	Froude number based on total fluid depth
Fr_h	Froude number based on current height
H	Total depth of fluid
I	Light intensity
$I(c)$	Light intensity when dye is present with a concentration c
I_0	Light intensity when no dye is present
N	Number of cylinders within a control volume
N_l	Numbers of sphere layers
P	Pressure
Re	Reynolds Number
Re_c	Cylinder Reynolds number

S_x	Cylinder spacing in the x direction
S_z	Cylinder spacing in the z direction
Sc	Schmidt number
U	Gravity current front speed
V	Control volume
$\Delta\rho$	Difference in density between ambient and source fluid
α	Velocity multiplier
η_c	Cylinder roughness height
κ	Molecular diffusivity
μ	Dynamic viscosity
μ_x	Average array density in x direction
μ_z	Average array density in z direction
ν	Kinematic viscosity
ϕ	Ratio of gravity current depth to total fluid depth
ϕ_c	Horizontally averaged array density
ρ	Density
ρ_1	Density of ambient fluid
ρ_2	Density of source fluid
ρ_t	Density of PTV tracer particles
τ_s	Response time of PTV tracer particles to fluid movements
$\tilde{H}$	Unobstructed fluid depth
ζ	Attenuation coefficient
*	Represents dimensionality

a	Current height multiplier
c	Dye concentration
c_D	Drag coefficient
d	Optical thickness
d_c	Cylinder diameter
d_p	Sphere diameter
d_t	Diameter of PTV tracer particles
e^g	Unit vector in the direction of gravity
$f(c)$	Absorbency
$f(d)$	Inverse absorbency function
g	Gravitational acceleration
g'	Reduced gravity
h	Gravity current height
h_B	Buoyant height
h_c	Current envelope
p	Pressure
q_A	Two-dimensional ambient volume flux
q_C	Two-dimensional current volume flux
q_T	Two-dimensional total volume flux
s	Distance along a light path
$sigma$	Relative Roughness Height
u	Velocity vector
u_B	Buoyant velocity

u_F Front speed

x Spatial co-ordinates

x_1 Length of a control volume

x_F Front location

x_c Length of a control volume

Chapter 1: Introduction

1.1 General Introduction

Gravity currents, sometimes known as density currents or buoyancy currents, are fluid flows induced by differences in density between two or more horizontally aligned fluids or by horizontal density gradients within fluids. These density differences are commonly generated by variations in salinity, temperature, turbidity or other fluid properties. They are ubiquitous in a range of natural environments but can also be caused by human influences and are easily generated in a laboratory setting. For these reasons investigations into the mechanics of gravity currents and their many applications has been of an interdisciplinary nature. An in-depth discussion of gravity currents and their many applications can be found in Simpson (1997).

1.2 Motivation

In the atmosphere, cold air at the centre of thunderstorms can produce dense gravity currents. These can travel large distances damaging city infrastructure and interfering with aircraft. Furthermore, when travelling through arid regions these currents can entrain significant quantities of sediment, causing the currents to develop into large dust storms known as Haboobs. A photograph of one such haboob, captured in Arizona by Lehtonen (2018), is shown in Figure 1.1. From this photograph the potential scale of these currents can be appreciated. The properties of such gravity currents are of interest to not only climate scientists but also engineers developing city infrastructure in at-risk regions, aircraft mechanics and operators, and civil-defence personnel. Other atmospheric examples of gravity currents include sea-breeze fronts, the spread of dense gasses such as leaked liquefied petroleum gas (LPG) or avalanches driven by entrained snow or sediment. Gravity currents also occur within water bodies, for example due to salinity in fjords and estuaries, or due to entrainment of sea-floor sediment after landslide events.

Due to the far-reaching implications for gravity current dynamics, both experimental and numerical studies have investigated how they travel over smooth boundaries. How gravity currents travel over smooth beds is now relatively well understood. However, where gravity

currents commonly occur boundaries are rarely smooth and how gravity currents travel over rough beds is less understood. Therefore, the interactions between gravity currents and bottom roughness has recently been identified as an important area of research (Cenedese et al., 2016; Özgökmen et al., 2004; Tokyay et al., 2012; Zhou et al., 2017). It should be noted that in this thesis the word roughness is used broadly to include any field of obstacles, of any scale interfering with the current development. A literature review showing the present state of knowledge is presented in Chapter 2. This chapter includes a detailed description of gravity currents as they travel over smooth beds, followed by a description of studies to date attempting to explain the impact of rough boundaries on these currents. A number of research questions are developed based on gaps in our present state of knowledge.

1.3 Problem Overview and Structure

The present study involved carrying out laboratory experiments to build on research investigating how gravity currents, generated in a long channel, are impacted by bottom roughness. A detailed description of the methods used to carry out these experiments can be found in Chapter 3. Based on the literature review two sets of experiments were conducted.

Fig. 1.1 Photograph of a haboob reproduced from Lehtonen (2018)

The first set of experiments was carried out to identify how developed, smooth bed currents react when suddenly encountering a field of vertical circular cylinders. While gravity currents interacting with circular cylinders have been studied (Cenedese et al., 2016; Zhou et al., 2017), this thesis adresses two novel apsects of these flows – the transition between smooth and rough beds and the transient nature of gravity currents interacting with fields of vertical circular cylinders. The arrangements of the cylinders was varied along with the depth of the water. Initial results from these experiments are presented in Chapter 4 with more detailed analyses presented in Chapters 5, 6 and 7.

The final set of experiments consisted of covering the base of a channel with a field of closely-packed solid spheres. The depth of the fluid was varied as well as the number sphere layers. A number of numerical simulations were carried out in parallel with this project at University of California, Santa Barbara. This work has been accepted for publication (Köllner et al., 2020) and Chapter 8 consists of a reformatted version of this article. The thesis author was the second author of this paper and conducted the experiments presented Sections 8.2 and 8.3 as well as co-writing and co-editing the manuscript.

Final conclusions from this thesis are then presented in Chapter 9.

Chapter 2: Literature Review

2.1 Introduction

This chapter presents a review of literature that is relevant to the following study in order to provide the reader with an understanding of the current state of knowledge. Section 2.2 outlines the basic properties of gravity currents and explores some of the earlier attempts to understand them. Section 2.3 outlines several important non-dimensional quantities used in understanding gravity currents. Sections 2.4, 2.5.1 and 2.5.2 then discuss techniques used to study gravity currents in the laboratory, analytically and numerically, respectively, along with an exploration of studies conducted using these methods. Section 2.6 describes the mixing processes between gravity currents and the ambient fluid that they displace. Section 2.7 describes investigations into how gravity currents travel on sloping boundaries. Section 2.8 describes studies conducted to investigate how gravity currents interact with obstacles and rough boundaries. Section 2.8, in particular, is used to identify research gaps in order to guide the present study. Section 2.9 describes gravity currents in the environment and presents results from a number of field studies before a summary and implications for the present study are described in Section 2.10.

2.2 Basic Properties of Gravity Currents

Some of the earliest recorded experiments investigating gravity currents were carried out by Schmidt (1911). In these experiments a series of gravity currents were generated with increasing density differentials (due to temperature differences) and were captured as *shadowgraphs*. Shadowgraphs are optical images captured by shining light through the flow and observing flow dynamics due to the impact of the density variation on the refractive index. The images can be seen in Figure 2.1a to f, where the density difference increases. This figure illustrates some important physical properties of gravity currents. Firstly, a clear discontinuity can be seen between the two fluids (lighter fluid in white above the dense fluid in black). It should, however, be noted that significant mixing occurs between the two layers (which increases from Figure 2.1a to f).

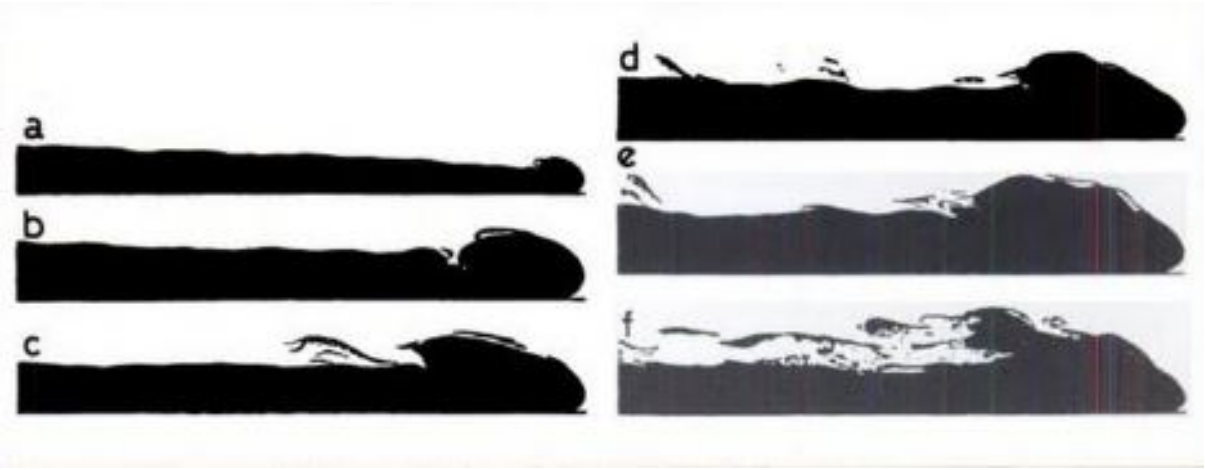

Fig. 2.1 An early shadowgraph of a gravity current created by Schmidt (1911).Subfigures a to f show an increasing temperature difference between two fluids from very little to 35 degrees Celsius. Figure is reproduced from Simpson (1997).

The front of the current consists of a deep flow termed the *head*. The majority of mixing between the two fluids takes place within and just behind this head (Simpson, 1997). The flow behind the head is often termed the *tail* and is slightly shallower. This structure is visible in Figure 2.1. Also visible is a characteristic *nose* raised above the boundary at the leading edge of the head. The nose occurs in currents propagating along solid boundaries because of the no-slip condition. In essence, because the fluid at the bottom boundary must be stationary, the leading edge must be raised slightly above the boundary in order to propagate forwards.

Intrusive gravity currents can also exist where fluid propagates between two stably stratified fluid layers. An example of an intrusive gravity current, produced by Britter and Simpson (1981), is shown in Figure 2.2. An intrusive current can be thought of as two boundary currents symmetrically travelling along the original interface. They have a similar structure to boundary currents, including deep heads trailed by shallower tails; however because the centre line does not experience a no-slip boundary condition the noses are not raised above the boundary.

2.3 Important Non-Dimensional Quantities

The Froude number, defined as a ratio of the flow inertia to gravitational effects is often used as a non-dimensional measure of a fluid velocity. It is given by

$$Fr = \frac{U}{\sqrt{gH}} \tag{2.1}$$

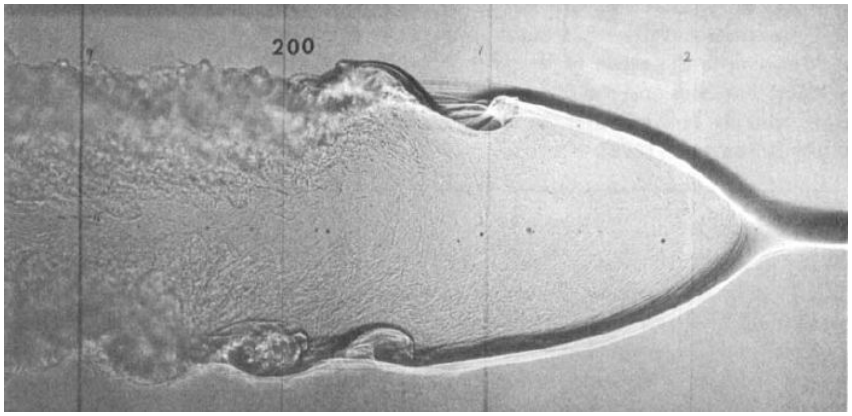

Fig. 2.2 A shadowgraph of an intrusive gravity current produced by Britter and Simpson (1981).

where U is a representative velocity scale, g is gravitational acceleration and H is a representative length scale usually taken as the total fluid depth. The Froude number is commonly used as a non-dimensionalised form of the front speed of gravity currents. However, the gravity term in the Froude number definition must be altered for these currents to account for the driving force being buoyancy, rather than gravity alone, and thus dependent on the fluid density. Therefore, for gravity currents, the reduced gravity, g', replaces g in Equation 2.1. It is given by

$$g' = \frac{g\Delta\rho}{\rho_2} = \frac{g(\rho_2 - \rho_1)}{\rho_2} \tag{2.2}$$

where ρ_1 and ρ_2 are the densities of the light and dense fluids respectively. In Equation 2.1 $\sqrt{g'H}$ is a velocity scale representative of the buoyancy of the prior to the formation of the current.

In most environments where gravity currents are found the density difference between the fluids is very small. As an example, for a haboob caused by a front of cold air, as shown in Chapter 1, the difference in density will usually be less than 5 percent (Simpson, 1997). Therefore, it is considered reasonable to assume that the densities of the two fluids are equivalent when computing the inertia of the current and that their differences only need to be considered when computing the buoyancy force. This is known as the *Boussinesq approximation*. As the density difference is assumed to be small the denominator in Equation 2.2 can be taken as the density of either fluid.

It can also be concluded from Figure 2.1 that altering the density difference (and hence the reduced gravity) will affect the structure of the flow as the shadowgraphs vary dramatically from Figure 2.1a to f. This trend occurs because the reduced gravity increases, causing the driving force to increase. Observations show that the Froude number tends to be constant leading to the front speed increasing like $\sqrt{g'H}$. As the current speed increases the ratio of inertia to viscous forces, known as the Reynolds number, also increases. This number is defined as

$$Re = \frac{UH}{\nu} \tag{2.3}$$

where ν is the kinematic viscosity.

As the reduced gravity and hence Reynolds number increases from Figure 2.1a to f, the current is dependent on the Reynolds number. When the Reynolds number reaches a large enough value the flow can be considered to be *fully turbulent* and hence the properties of the flow become independent of the Reynolds number. This value was experimentally determined and stated by Simpson and Britter (1979) to be approximately 1000. Most environmental flows have very large Reynolds numbers so can be considered to be fully turbulent. Therefore, environmental flows can be approximated in a laboratory setting provided care is taken to ensure such flows have Reynolds numbers above 1000. The shadowgraph in Figure 2.1 f has a Reynolds number of around 1000 and is considered fully turbulent.

2.4 Laboratory Experiments

2.4.1 Lock Exchange Gravity Currents

Gravity currents have been studied extensively in the laboratory. Due to its simplicity one of the most popular methods for generating them in the laboratory is via *lock exchange*. This method (also known as *constant mass*) involves placing a separator (gate) in a channel between two fluids of different densities and removing it to generate a current. The section of the channel containing the dense fluid is termed the *lock*. This method is used to generate gravity currents in the present study. There have been many studies investigating the dynamics of lock exchange gravity currents and Rottman and Simpson (1983) produced Figure 2.3 as a summary of much of the early work.

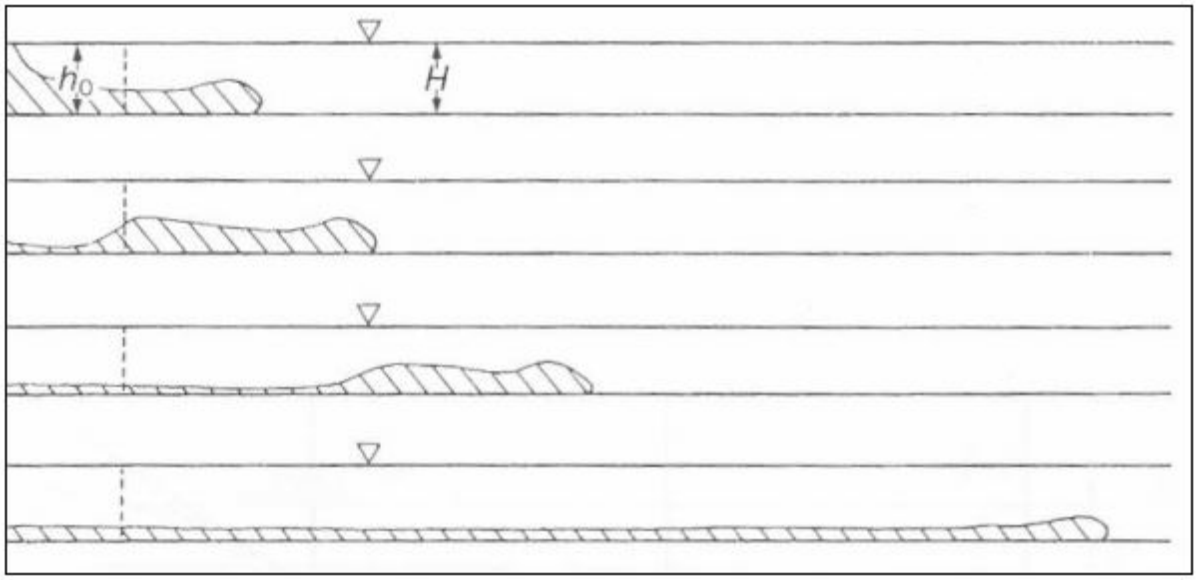

Fig. 2.3 Representation of a lock exchange gravity current reproduced from Rottman and Simpson (1983). The dashed line shows the original location of the lock gate, H is the total depth of ambient fluid and h_0 is the total depth of dense lock fluid before the gate was removed.

A lock exchange gravity current undergoes several regimes over time as it travels. In Figure 2.3 the multiple regimes of lock exchange gravity currents are visible. When the gate is removed a pair of currents travelling in opposite directions are generated. A surface current of light fluid propagates into the lock, while a dense, bottom current propagates away from it. Initially, the dense current travels at a constant speed, while there is still sufficient fluid in the lock region to drive it forward. This first regime (seen in the top image in Figure 2.3) was initially observed by Barr (1967). It is known as the *constant speed* (or *slumping*) phase.

Later phases of lock exchange gravity currents were then considered by Huppert and Simpson (1980) and later Rottman and Simpson (1983). They considered lock exchange gravity currents in more detail and observed two additional regimes after the slumping phase. The first of these regimes takes place once the lock runs out of fluid to drive the dense current. At this time a bore propagates along the interface between the two fluids, eventually reaching the head of the current as seen in the final three images of Figure 2.3. The time taken by the bore to reach the front has been shown to be approximately the time taken for the current to travel 10 times the length of the lock (Rottman and Simpson, 1983). Once the bore reaches the head the current begins to lose speed and collapse in size. At this point the current is said to be in the *self-similar* (or *inertia-buoyancy*) regime. In this regime the flow is governed solely by buoyancy and inertia

providing the Reynolds number is large enough that viscosity can be considered unimportant (due to the flow being fully turbulent).

In the self-similar regime the current depth is observed to be approximately constant along the channel and this can be approximated by the collapse of a series of rectangles over time. This is termed the box model. Rottman and Simpson (1983) tracked the distance travelled by currents with time as they transitioned between the multiple regimes to understand how the speed of the currents changed. The distance travelled with time for these currents are shown on a log-scale in Figure 2.4. The slopes of these lines relate to the speed of the currents. This figure confirms that the current speeds were roughly constant in the slumping regime. Subsequently, in the self-similar regime, the velocity of the currents decreased with a time dependence of $t^{-\frac{1}{3}}$. When the speed and depth of the current decreased significantly it entered a viscous regime, where the Reynolds number had reduced sufficiently that instead of being governed by inertia and buoyancy it was governed by viscosity and buoyancy. In this regime the speed began to decrease more rapidly with a time dependence of $t^{-\frac{4}{5}}$.Lowe et al. (2002) produced intrusive gravity currents through lock exchange mechanisms. They found the same regimes to exist for these currents.

2.4.2 Constant Flux Gravity Currents

While the lock exchange configuration has the advantage that it is relatively simple, it is not always the best representation of naturally occurring gravity currents. Rather than a constant mass of fluid being released it is often more realistic to assume that a gravity current is generated by a constant flux of dense (or light) fluid. Therefore, in recent years some methods have been designed to study gravity currents generated by a constant flux of fluid.

Sher and Woods (2017) created an apparatus where a constant flux of salt water was introduced at the base of a channel as shown in Figure 2.5. Flow straighteners were employed along the inlet to ensure that fluid entered the channel evenly and straight throughout the width. Hogg et al. (2005) created an apparatus that generated a constant flux gravity current by introducing dense fluid near the surface of the lighter fluid in the centre of the channel. The introduction of dense fluid at the surface created a plume, pre-mixing the currents before they reached the floor. Additionally they used a recirculating pump to create a flow in the channel prior to the introduction of the currents. A schematic for this experiment is seen in Figure 2.6. Due to

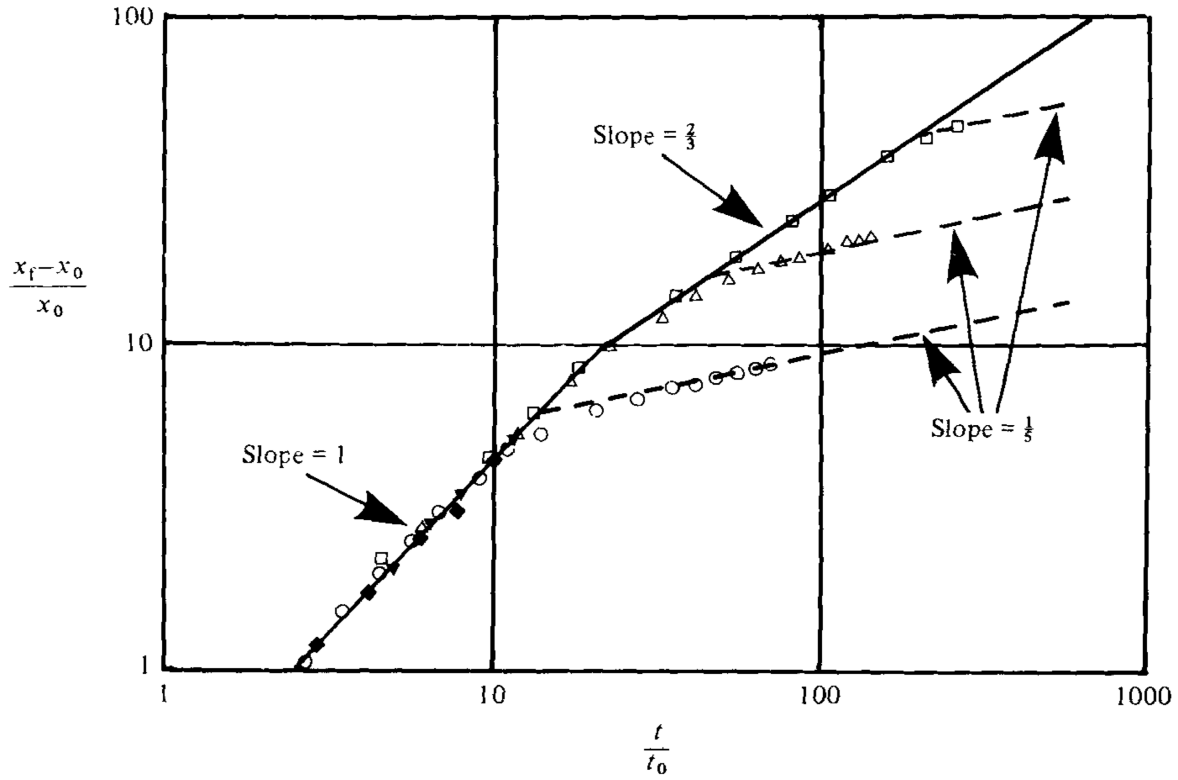

Fig. 2.4 Front location of lock-exchange gravity currents undergoing multiple regimes with time. x_0 represents the length of the lock and $t_0 = \frac{x_0}{\sqrt{g'H}}$, reproduced from Rottman and Simpson (1983)

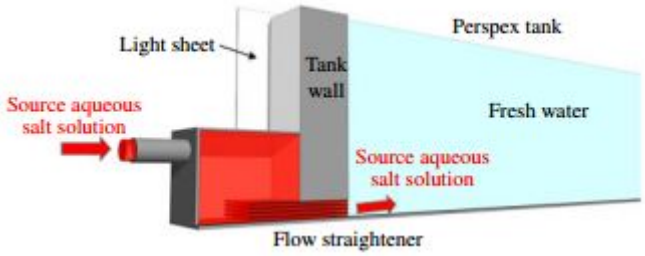

Fig. 2.5 Apparatus used by Sher and Woods (2017) to generate constant flux gravity currents.

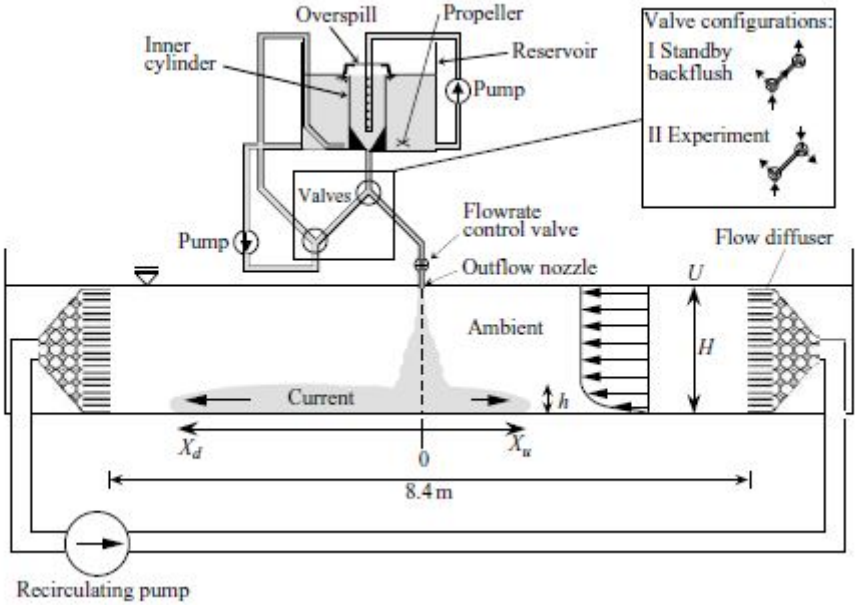

Fig. 2.6 Apparatus used by Hogg et al. (2005) to generate constant flux gravity current.

the constant flux of fluid entering the channel these currents had constant speeds for all time without entering the self-similar regime. Lock exchange gravity currents have also been used to approximate constant flux currents when the lock is long enough that the current stays in the slumping regime for a sufficient period of time (Shin et al., 2004).

2.5 Mathematical Gravity Current Models

2.5.1 Idealised Mathematical Models

Many idealised, two dimensional models have been developed to predict the front speed of gravity currents. The earliest of these came from von Karman (1940) and Benjamin (1968). von Karman (1940) modelled the idealisation of a gravity current shown in Figure 2.7. He considered the gravity current to be at rest within an infinite depth of fluid. Assuming the flow

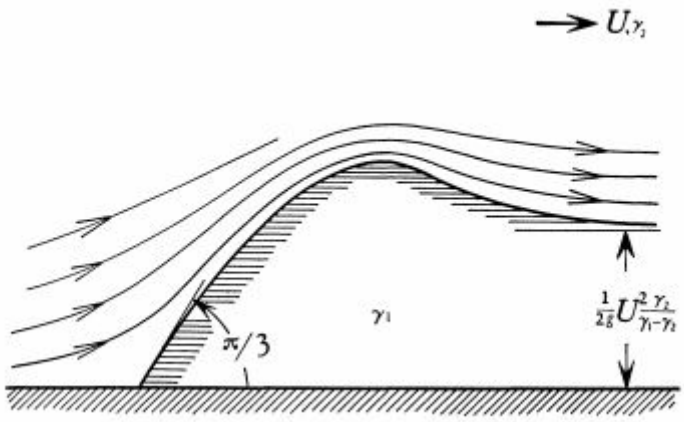

Fig. 2.7 Simplified gravity current analysed by von Karman (1940). Stationary current with ambient fluid flowing over it with average velocity of U above the tail.

was inviscid and irrotational he applied conservation of energy along the interface between the two fluids and along the floor in front of the current. He found the Froude number (based on the current tail height and the front speed) to be $\frac{1}{\sqrt{2}}$ as long as the density difference was small (so the Boussinesq approximation could be applied).

Benjamin (1968) argued that energy would not be conserved along the interface. Instead he modelled a gravity current as flow past a stationary air cavity at the top of a finite-depth channel. He argued that the pressure far in front of and behind the current would be hydrostatic so he applied conservation of mass and momentum in a control volume that included fluid far upstream and downstream of the head. Like Von Karmen he considered the flow to be inviscid and irrotational. In doing this he calculated the Froude number for a Boussinesq current based on the height of the channel and of the current to be

$$Fr_H = \sqrt{\frac{\phi(1-\phi)(2-\phi)}{1+\phi}} \tag{2.4}$$

$$Fr_h = \frac{F_H}{\sqrt{\phi}} \tag{2.5}$$

where Fr_H and Fr_h are the Froude numbers based on the channel depth (H) and current depth(h) and ϕ is the ratio $\frac{h}{H}$.

Benjamin considered conservation of energy along the bottom surface of the cavity (the top surface of a gravity current) and was surprised to find that the only energy conserving flow was one where $\phi = \frac{1}{2}$. Thus, the Froude number, based on the current height, was in fact $\frac{1}{\sqrt{2}}$ as discovered by Karman.

Since Benjamin (1968), many simple mathematical models have been created. Shin et al. (2004) built on Benjamin's model, considering a current generated from a dense, finite volume of fluid initially completely submerged in a lighter fluid (of the same density as the ambient). Like Benjamin, they assumed that the flow was inviscid, irrotational and hydrostatic upstream and downstream of the front. Carrying out a similar analysis to Benjamin they found that the only way for energy to be conserved was for the ratio of the current height to the channel height to be half of the initial ratio of fluid height to the channel height. Assuming a Boussinesq flow, the Froude number based on the initial depth of dense fluid was found to be

$$Fr_H = \frac{1}{2}\sqrt{\frac{D}{H}(2-\frac{D}{H})} \tag{2.6}$$

where D is the initial depth of the dense fluid (or light fluid for the case of an air cavity). If the dense fluid was full-depth (D=H) the result was the same as from Benjamin's analysis.

Marino et al. (2005) investigated many of these models and concluded that none have a sound theoretical basis because real currents exhibit energy losses behind the head. They created a model for the Froude number based on an "equivalent depth" and found that once a current enters the inertia-buoyancy regime its initial height becomes unimportant. Nokes et al. (2008) developed a model for the Froude number by arguing that the front velocity of a gravity current is governed by the head, where energy is assumed to be conserved, without making any assumptions about energy loss in the tail. They also assumed that the flow was inviscid-irrotational and that it was horizontal above the current. This model had to be solved numerically but the Froude number based on the depth of the current head was approximated to be

$$Fr_h = 0.91 - 0.80\phi^2 \tag{2.7}$$

Comparing this model with Benjamin's model is problematic because the current height (h) in Benjamin's model was based on the current downstream of the head and for this model it was based on the head of current. However, for $\phi = 0.5$, as Benjamin's model predicts for energy conserving currents, this Froude number matches Benjamin's model. Furthermore, when mixing has taken place across the interface between the current and ambient, the interface is smeared such that the there is no longer a clear distinction between current fluid and ambient fluid. Thus, calculation of the local height of the current head can be challenging. Anjum et al. (2013) proposed a number of ways in which the current height and head location could be represented in order to use such models more effectively. They proposed to calculate the Froude number using local reduced gravity and height and showed using numerical simulations that this Froude number is constant with time in both the constant speed and inertia-buoyancy regimes. The value of this Froude number was found to closely match the model of Nokes et al. (2008).

Studies highlighting newly developed mathematical models often feature experiments run using a lock exchange configuration to assess the accuracy of the model. Shin et al. (2004) ran a series of lock exchange experiments to compare with their mathematical model and with Benjamin's model. To accurately make this comparison they also generated lock exchange gravity currents where the dense side of the lock was stratified with light fluid (the same fluid as on the ambient side) above it. Nokes et al. (2008) ran a series of intrusive lock exchange gravity current experiments to compare with their model. Intrusive currents were selected because their model did not include the features of a raised nose along the boundary so it was better at predicting the behaviour of intrusive currents than of boundary currents. They also compared their experimental results with those of Lowe et al. (2002). In all cases the analytical models slightly over-predict the Froude number because none of these models account for boundary effects or mixing between current and ambient fluid. However, the predicted Froude numbers are very close to those measured in laboratory studies.

2.5.2 Numerical Models

In early gravity current research, most studies consisted of laboratory and simple mathematical modelling. As computational capacity has increased, high resolution numerical models have been developed. Meiburg et al. (2015) provide a comprehensive review of the many numerical simulations that have been used to model gravity currents.

Most models of gravity currents consist of solving the Navier-Stokes equations. These are commonly expressed in non-dimensional form using the Boussinesq approximation and can be written in Einstein's index notation as

$$\frac{\partial u_j}{\partial x_j} = 0 \tag{2.8}$$

$$\frac{\partial u_i}{\partial t} + \frac{\partial (u_i u_j)}{\partial x_j} = -\frac{\partial p}{\partial x_i} + \frac{1}{Re}\frac{\partial^2 u_i}{\partial x_j \partial x_j} + \rho e_i^g \tag{2.9}$$

$$\frac{\partial \rho}{\partial t} + \frac{\partial (\rho u_j)}{\partial x_j} = \frac{1}{ReSc}\frac{\partial^2 \rho}{\partial x_j \partial x_j} \tag{2.10}$$

where $\mathbf{u}$ is the velocity vector, $\mathbf{x}$ is the spatial co-ordinates, p is a modified pressure, ρ is density, $\mathbf{e}^g$ is a unit vector pointing downwards (in the direction of gravity) and Sc is the Schmidt number, which is given by

$$Sc = \frac{\nu}{\kappa} \tag{2.11}$$

where κ is the molecular diffusivity of the stratifying component.

These have been non-dimensionalised by

$$\mathbf{u} = \frac{\mathbf{u}^*}{u_B} \tag{2.12}$$

$$\mathbf{x} = \frac{\mathbf{x}^*}{H} \tag{2.13}$$

$$\rho = \frac{\rho^* - \rho_1}{\rho_2 - \rho_1} \tag{2.14}$$

$$t = \frac{t^* H}{u_B} \tag{2.15}$$

$$p = \frac{p^*}{\rho_1 u_b^2} \tag{2.16}$$

where variables with superscript * have not been non-dimensionalised and u_B is the *buoyant velocity* given by

$$u_B = \sqrt{g'H}$$

Where velocity appears in the Reynolds Number this velocity is also the buoyant velocity. These non-dimensionalisations are also commonly used in analysing laboratory results.

These equations are valid for salinity or temperature- driven currents. To model turbidity currents these equations are adjusted by incorporating a settling velocity term in the concentration equation (Equation 2.10).

When modelling gravity currents these equations must be solved numerically. However, resolving these equations numerically is challenging because to apply them accurately the full range of turbulent scales must be resolved from the large scales, dictated by the boundary conditions in the flow, to the smaller scales of turbulence dictated by viscous dissipation. To resolve the smallest scales very fine grids are required and these involve large computational demands (even for small domains). Therefore, several different approaches are used, often making simplifying assumptions about the nature of turbulence in order to minimise the required computational demand.

The most exact approach is to use the direct numerical simulation (DNS) technique. This approach directly resolves the equations without making simplifying assumptions about the nature of turbulence. Therefore, all scales are resolved directly.

Härtel et al. (2000a) developed one of the earliest successful DNS models for simulating gravity currents and this model has been utilised to model gravity currents under a variety of different circumstances (Härtel et al., 2000b; Nasr-Azadani et al., 2016; Ouillon et al., 2019). It has also been used as a comparison for simple mathematical models (Borden and Meiburg, 2013). Klemp et al. (1994) used DNS as a comparison with both shallow water models and Benjamin's original

model and found that they both slightly over-estimate the front speed of gravity currents. Other significant uses for DNS have included investigations into non-Boussinesq currents (Birman et al., 2005), cylindrical gravity currents (Cantero et al., 2007) and particle-laden (turbidity) currents (Necker et al., 2002).

Due to the considerable difference in scale between small and large scale turbulence, computational demand scales with Re^3 (Meiburg et al., 2015). Therefore, DNS can only be used for laboratory-scale modelling with relatively small Reynolds numbers. Laboratory scale DNS simulations have been conducted with Reynolds numbers as high as 15,000 (Cantero et al., 2008). The Schmidt number places an additional constraint on numerical capacity due to the smallest scales for the diffusion of stratifying components (e.g. salt, sediment or heat) usually being significantly smaller than the smallest scales of turbulence. The Schmidt number of salt in water is approximately 700 and for entrained sediment it can be even larger as for sediment the Schmidt number scales with the diameter of the entrained sediment cubed (Meiburg et al., 2015). However, simulating a gravity current with a Schmidt number of 700 would require an unreasonably fine grid. Thus, to reduce computational demands the Schmidt number is commonly approximated to be 1 when using DNS (Meiburg et al., 2015). Birman et al. (2005) investigated the affect of the Schmidt number in the range of $Sc \sim 0.2 - 5$ and found that providing the Reynolds number was large enough the effect was minimal. It is, therefore, commonly assumed that, providing the Reynolds number is sufficiently large, a Schmidt number of 1 will suffice. Large Schmidt numbers in the range of 700 have not been investigated, thus the impact of assuming Schmidt numbers of 1 is still an open question.

Large eddy simulation (LES) models are also popular for simulating gravity currents. LES numerically resolves the energy containing large scales of motion as these tend to control the mean behaviour of the flow. However this method filters and approximates (usually with an eddy-viscosity model) the smaller scales of turbulence. This method improves the computational demand when compared to DNS models because the grid spacing of the simulations can be much larger. Constantinescu (2014) provides a review of LES used to simulate gravity currents. LES has been used for a variety of purposes, including to investigate gravity currents propagating over roughness elements (Gonzalez-Juez et al., 2009; Tokyay et al., 2012), the evolution of gravity currents (Ooi et al., 2009) and to compare simulations of high and low release volumes of dense fluid (Ooi et al., 2007a,b). As the smallest scales of turbulence and diffusion are not resolved

using LES and instead modelled, currents with Schmidt number of 700 can be generated without needing to have very fine grids (Constantinescu, 2014).

A less computationally demanding approach is to average the Navier-Stokes equations such that turbulence is modelled entirely. This process results in the Reynolds Averaged Navier Stokes (RANS) equations, which can only simulate mean quantities of the flow. This approach has been used for several different purposes including sediment transport, turbidity currents and gravity current flow down slopes (Choi and García, 2002; Sequeiros et al., 2009). However, Choi and García (2002) showed that models of this type need to be adjusted for individual, local flow conditions. Therefore, it is challenging to develop these into universally applicable models. Thus, they are infrequently used to model gravity currents.

2.6 Dynamics and Mixing of Gravity Currents

How gravity currents mix as they travel is of particular interest when considering environmental flows. Thus, many studies have investigated these dynamics. The following discussion considers some of the key results from these studies. It primarily considers fully turbulent flows because these occur more commonly in the environment.

The majority of mixing in a gravity current occurs in and just behind the head. There are two primary methods by which this mixing occurs and these are shown in Figure 2.8. The first is Kelvin-Helmholtz (K-H) instabilities. These occur commonly throughout oceanographic and atmospheric flows where two fluid layers, separated by a smooth interface, travel at different velocities (Smyth and Moum, 2012). When a perturbation occurs in the interface it grows unstably to form the billows seen in Figure 2.8a. Eventually these billows cannot continue to grow and they break down into turbulence causing the two fluids to mix. The development of these billows is a predominantly two-dimensional process but the breakdown and subsequent mixing is three-dimensional.

The second major method of gravity current mixing occur through a structure of lobes and clefts as seen in Figure 2.8b. The theory for why these occur was initially proposed by Allen (1971). Due to the no-slip boundary condition, the nose of the dense current is lifted slightly above the base of the channel. The lifted nose causes a pool of lighter fluid to become trapped below the dense current fluid. This stratification is unstable so the lighter fluid percolates upwards through

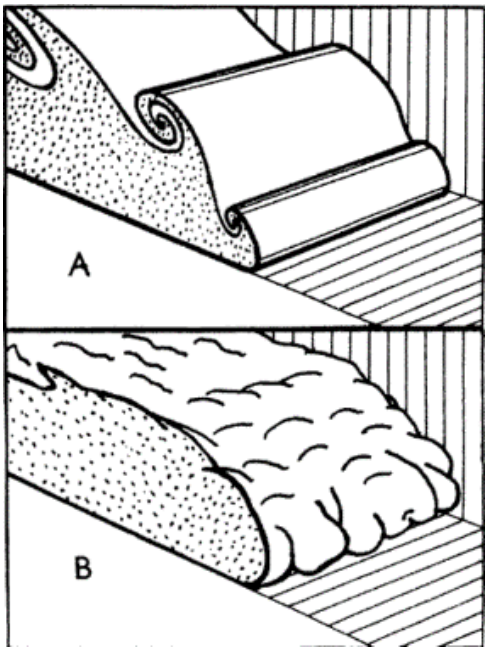

Fig. 2.8 A representation of mixing processes in gravity currents. A shows Kelvin-Helmholtz instabilities and B shows a structure of lobes and clefts. Reproduced from Simpson (1997).

the head as the current travels over it. As it percolates upwards it causes the complicated pattern of lobes and clefts seen in Figure 2.8b and in doing so the fluids mix. This process is three dimensional.

When comparing Figure 2.1 to Figure 2.2 it can be seen that in the intrusive current the lobes and clefts are not present while the K-H instabilities are visible and two dimensional. However, in the boundary current the structure is much more complex because the raised nose is present so both forms of instability are visible. Britter and Simpson (1978) confirmed this experimentally by generating a gravity current over a floor moving at the same speed as the current. Under these conditions the nose dropped to the floor, the lobe and cleft structure disappeared and a boundary current was created with only K-H instabilities visible. This is shown in Figure 2.9.

Following this study, Simpson and Britter (1979) created a two-dimensional model of gravity currents in a frame of reference such that the current is considered stationary. This model is shown in Figure 2.10. In this model $U(h)$ and $C(h)$ show the non-dimensional velocity and concentration profiles behind the head, where they used h to represent the height above the u=0 contour. $U(h)$ is non-dimensionalised by the front speed and $C(h)$ is non-dimensionalised such that undiluted lock fluid has a concentration of 1 and ambient fluid has a concentration of 0. A key feature of this model is that near the bed in and behind the head of the current

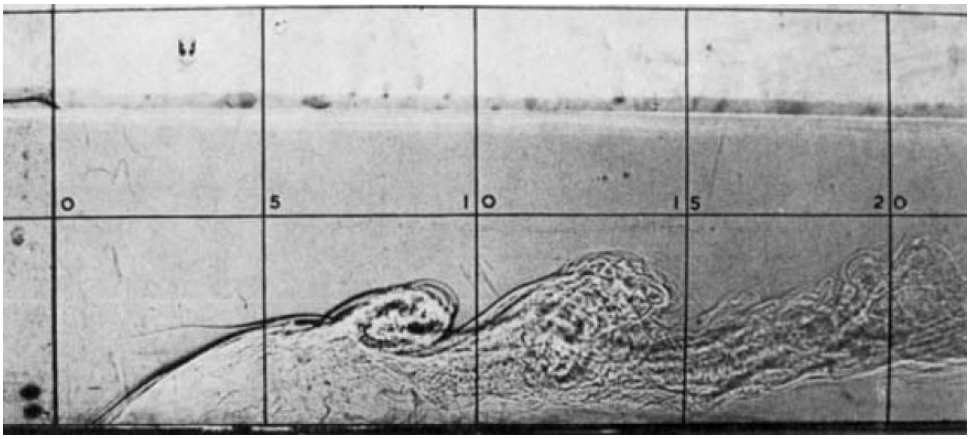

Fig. 2.9 Boundary current propagating over moving floor. Reproduced from Britter and Simpson (1978).

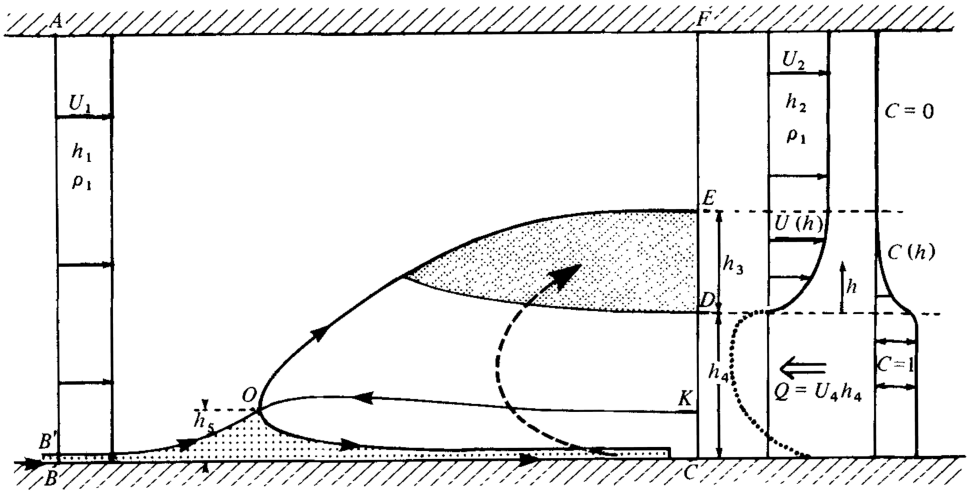

Fig. 2.10 Two-dimensional model for gravity currents reproduced from Simpson and Britter (1979).

there is a mostly undiluted zone where the velocity is faster than the current itself (or above 0 in the stationary frame of reference) and the current has a concentration of 1. Above this zone is a mixing zone where the velocity transitions towards the velocity of the ambient fluid and the concentration transitions towards 0. Finally above this there is an ambient zone where the velocity is roughly uniform and the concentration is 0. The mixing zone contains the fluid that has mixed due to both the lobes and clefts and the K-H instabilities.

In analysing the success of numerical models it has been seen that because the K-H instabilities alone are primarily two-dimensional, these can be accurately reproduced by both two- and three-dimensional simulations (Härtel et al., 2000b). However, because the lobes and clefts and breakdown of the K-H instabilities are three-dimensional processes these are not observed in

two-dimensional simulations. Thus, two-dimensional simulations under-represent the amount of ambient fluid entrained into the current, leading to unrealistic results.

Recently, Sher and Woods (2015) and Sher and Woods (2017) investigated the mixing of gravity currents in more detail using low- volume lock exchange and constant flux experimentation respectively. These built on Simpson and Britter (1979) by carrying out experiments where slugs of dye were injected into the current at different times. Their results are illustrated in Figures 2.11 and 2.12. They found, similarly to Simpson and Britter (1979), that the fluid at the bottom boundary behind the head was denser than the mixed fluid above it. They additionally found that this was denser than the fluid within the head, causing it to travel more quickly than the fluid in the head. It, therefore, catches up with the head and replaces the head fluid, which is pushed upwards and backwards towards the tail. The fluid pushed upwards then begins mixing with the ambient fluid (by the processes laid out by Britter and Simpson (1978)). When the fluid is in the lock-exchange slumping regime or driven by a constant flux of fluid this process keeps the current head in a quasi-steady state - in the frame of reference where the current head is stationary. This model is seen in Figure 2.12. As the current moves into the self-similar regime there is no longer dense fluid being driven in from the tail so the fluid begins circulating, where the dense fluid near the bed becomes less and less dense and the current head decreases in size and speed (Figure 2.11).

2.7 Gravity Currents on Sloping Boundaries

Another area of interest is how gravity currents propagate along sloping boundaries due to many naturally occurring gravity currents existing under these conditions. A major example of this is deep-ocean currents where the sea-bed is rarely horizontal. Many laboratory studies of these currents have taken place. Britter and Linden (1980) ran a series of constant flux experiments where gravity currents were generated on a sloping boundary of varying angle of incline. Figure 2.13 shows shadow-graphs for three of their experiments. They found for an incline of between five and ninety degrees from the horizontal the speed of the current was not impacted by the slope but increasing the slope caused an increase in mixing and head height.

Beghin et al. (1981) formulated a model for lock exchange gravity currents propagating down slopes. This study has formed the basis for much of the work in this area. A schematic for it is

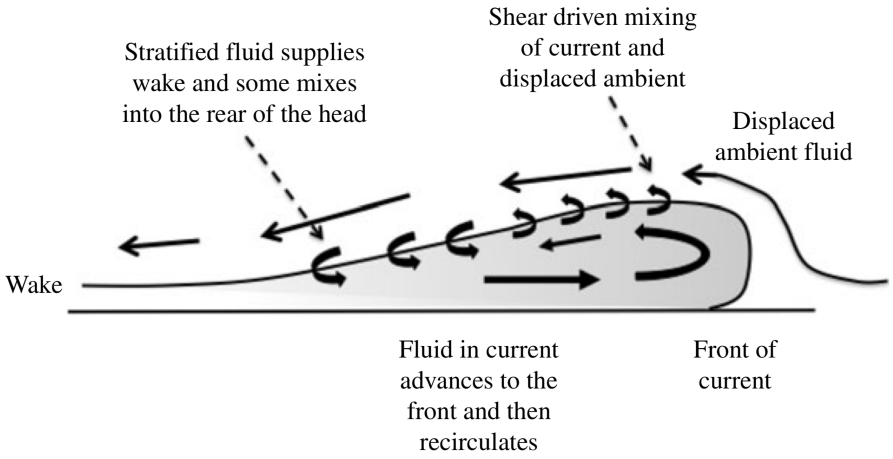

Fig. 2.11 Model of mixing in gravity currents in transition to self-similar phase by Sher and Woods (2015).

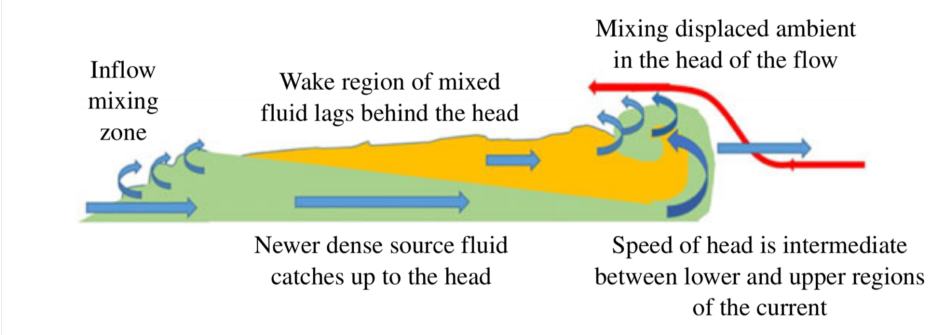

Fig. 2.12 Model of mixing in Constant-flux gravity currents or lock exchange gravity currents with long locks by Sher and Woods (2017).

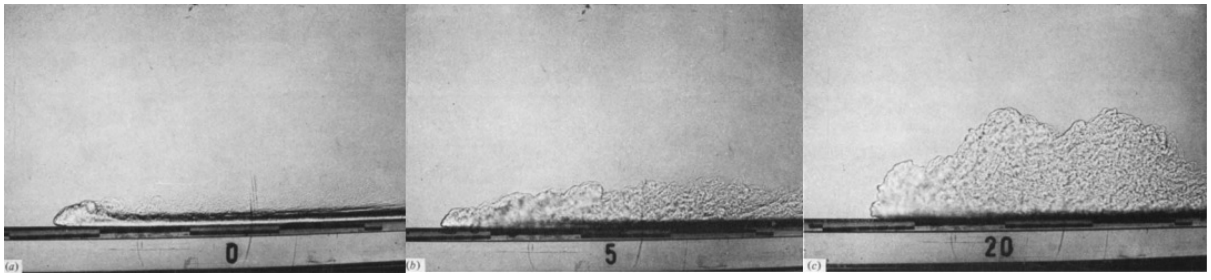

Fig. 2.13 Shadowgraphs produced by (Britter and Linden, 1980) showing how boundary gravity currents change with changing slopes (of 0, 5 and 20 degrees).

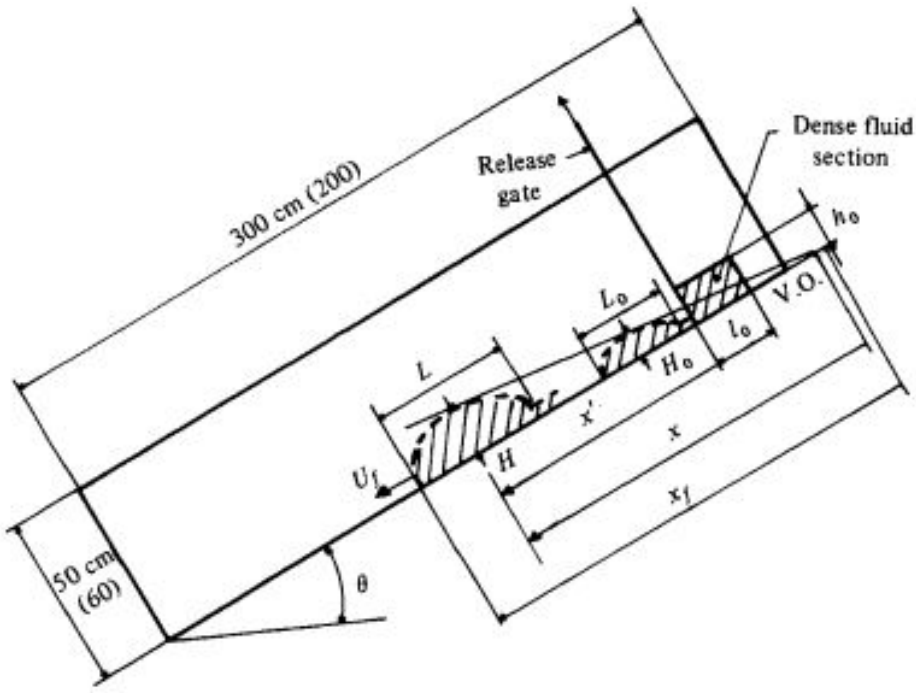

Fig. 2.14 Experimental setup/ idealised model used by Beghin et al. (1981)

shown in Figure 2.14. They approximated the current head as it propagated along the slope as a half ellipse that increased in size as it travelled. A virtual origin (where the ellipse had a height of zero) was assumed behind the lock region. They also assumed that the boundary itself caused a negligible effect on the current and that buoyancy was constant with distance. Their model used thermal theory and showed that the current, initially at rest, accelerated according to

$$U = \sqrt{\frac{2C}{x_0}}\frac{x_0}{x}\sqrt{\frac{x}{x_0} - 1} \tag{2.17}$$

where C depends on the angle of the slope, geometry of the ellipse and density of the fluid, x is the distance down the slope from the virtual origin and x_0 is the distance from the virtual origin to the gate.

This acceleration phase was seen to continue until $\frac{x}{x_0} = 4^{1/3}$ after which the current started to decrease in speed with $x^{-1/2}$. They also carried out a set of experiments that provided moderate support for the model when the slope angle was greater than five degrees. As the slope angle became small they found that the results started to diverge from the model.

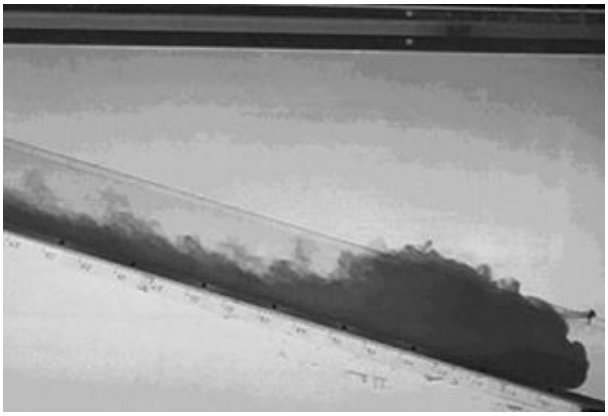

Fig. 2.15 Shadow plot by Maxworthy and Nokes (2007) illustrating elliptical shape of current head.

More recently, Maxworthy and Nokes (2007) studied sloping bed gravity currents as they exited a lock and found that in the acceleration phase the head was being fed by the following fluid, which caused the buoyancy within the head to increase. They therefore adapted the model of Beghin et al. (1981) to account for the dependency of buoyancy on distance down the slope. From this model they were able to accurately predict the Froude number of these currents with distance during the initial acceleration phase. A shadowgraph from their study is shown in Figure 2.15. This figure illustrates the elliptical shape of the current head. This study was followed by a second paper (Maxworthy, 2010), which used a longer channel to observe the current slowing and continuously entraining fluid from the ambient, leading the average density of the current to decrease with time after it passed its maximum velocity. During this stage he noticed the current losing buoyancy via entrainment of ambient fluid and losing dense fluid from its rear but noted that the model by Beghin et al. (1981) was able to accurately describe the evolution of the current, despite assuming constant buoyancy.

Cenedese et al. (2004) used a constant flux apparatus to study gravity currents propagating down slopes in the presence of rotation, that is, systems where the Coriolis force may be relevant. The rotation rate, slope angle, flow rate and density difference were varied. They found three regimes present in such a flow: a laminar regime, a regime where disturbances with wavelike characteristics occur at the interface between the fluids and a regime where cyclonic eddies appear in the overlying fluid.

2.8 Gravity Currents Interacting with Roughness and Obstacles

Most of the research mentioned to this point has investigated how gravity currents propagate along smooth boundaries. However, in the natural environment boundaries are likely to have some form of roughness. Examples include atmospheric currents interacting with cities or aquatic vegetation influencing deep ocean currents. Motivated by these scenarios, recent studies have investigated the impact of rough boundaries on gravity currents.

A LES model was used by Tokyay et al. (2011, 2014) to simulate the propagation of gravity currents over arrays of dunes and square ribs. They considered roughness with a depth of between 15 and 30 percent of the total fluid depth. They showed that the roughness decreased the current velocity in the slumping regime, as well as decreasing the time before the onset of the viscous regime. They also found that the current speed decayed with time more quickly when the height of the roughness was larger, as the larger roughness imposed a greater drag force.

A recent study utilising LES by Bhaganagar and Pillalamarri (2017) investigated lock-exchange gravity currents over fields of square and triangular roughness elements of a scale much smaller than the current. They found that the enhanced mixing induced by the roughness was related to the strength of the shear layer formed between dense over-flowing fluid and lighter fluid contained in the roughness. Ozan et al. (2015) highlighted the role of dilution in gravity currents propagating through arrays of cylinders with horizontal axes and showed a significant change in shape for such currents as the domain was more densely populated by cylinders.

A recent laboratory study by Cenedese et al. (2016) used lock exchange to investigate the influence of rough beds, consisting of staggered arrays of vertical circular cylinders, on gravity currents. They ran experiments with both dense and sparse arrays of cylinders, corresponding to approximately 35 % and 9 % of the bottom boundary being covered by the cylinders, respectively. They measured density fields for each scenario. They found that for the sparse configuration the current would flow between the cylinders whereas for the dense array the current would mostly ride over the top. This is illustrated in Figure 2.16, which displays density fields from one each of their dense and sparse configurations.

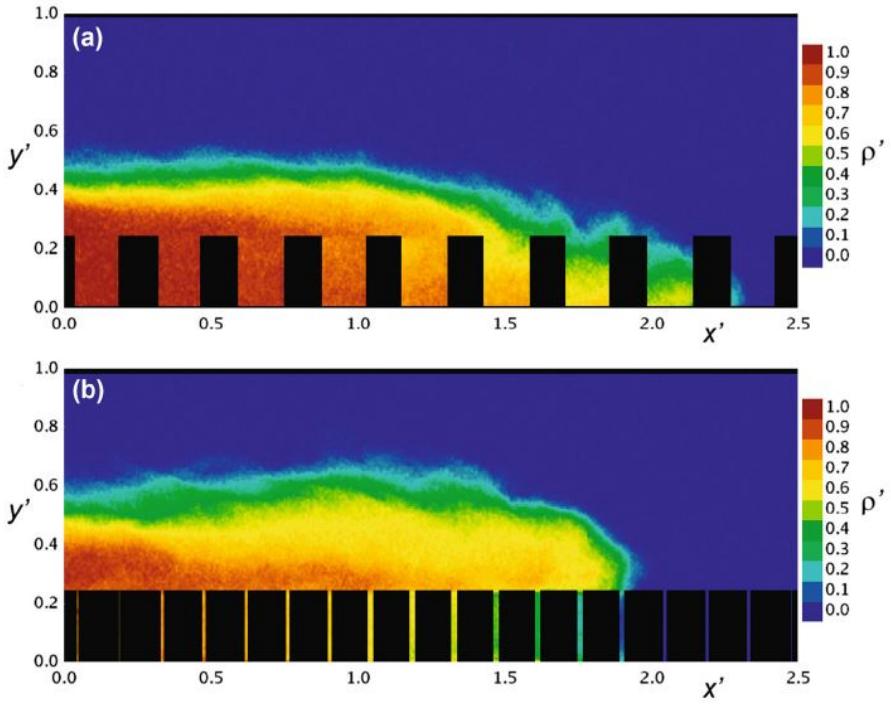

Fig. 2.16 Density fields generated by (Cenedese et al., 2016). Top image is of a gravity current propagating over a sparse array of cylinders and the bottom is over a dense array.

In the case of the dense configuration, because the dense current rode over the top of the roughness, the fluid between the cylinders was unstably stratified relative to the fluid in the current. This instability caused convective motion to occur between the fluid within the roughness elements and the fluid within the current. The convective instabilities led to a large quantity of fluid from within the roughness being entrained into the current. The dense configuration was also found to have a smaller Froude number than the sparse configuration (which in turn had a smaller Froude number than a smooth bed). For each regime they varied the cylinder height from 3 to 50 percent of the total fluid depth. The Froude number decreased as the relative height of the roughness elements increased.

Zhou et al. (2017) extended this work by considering arrays of cylinders that were either in-line or staggered and considered cases where spacing was different across and along the channel. They used LES to model these flows. They held the cylinder height constant at approximately 19 % of the total fluid depth but varied the horizontally averaged array density, ϕ_c and decomposed this into stream-wise and span-wise components respectively as

$$\mu_x = \frac{S_x}{d_c} \tag{2.18}$$

$$\mu_z = \frac{S_z}{d_c} \tag{2.19}$$

where S_x and S_z are the centre-centre spacings between cylinders and d_c is the cylinder diameter. They assumed that the currents were in a quasi-steady state. Thus, they calculated Froude numbers at times of between 2 and 21, assuming the Froude numbers were constant. The outcomes of their study is plotted in Figure 2.17. This Figure shows the Froude number relative to that of a smooth bed current in $\mu_x - \mu_y$ space with contours being lines of equal ϕ_c and arrows showing transitions between regimes. Additionally to the over flow and through flow regimes identified by Cenedese et al. (2016), they discovered a plunging flow regime that occurred when there was large spacing in the direction of flow but dense across the flow and a channelised skimming flow regime where the current travelled through the channels formed by in-line arrays when the cross channel spacing was large. Density contours for currents in these regimes are shown in Figure 2.18. In this figure, a shows a current propagating over a smooth bed where N denotes the current nose, b shows a current travelling through a sparsely distributed set of roughness where the current travels through them and TN denotes the nose propagating through, c shows a current propagating over a dense bed where there is not only a nose propagating through the roughness but also a nose propagating over (ON) and a vertical convective exchange of fluid because of this (VC), d shows a current propagating over a bed where the roughness is dense enough for there not to be a visible nose propagating through, e shows a current propagating over a bed which is dense across the channel and sparse along it such that the current plunged over successive rows, and f shows a current travelling through a bed which is sparse across the channel and dense along it such that the current propagates through longitudinal channels.

Additionally, Negretti et al. (2008) used a similar geometry, employing a sparse and dense array of rigid cylinders (but with very small diameters and packed much more densely for the dense case) on a sloped sill for gravity currents to propagate over. They found that while mixing and entrainment was greater in the dense case than a smooth bed, the sparse case in fact generated less mixing than over the smooth bed when employed on a slope.

This work is closely related to the field of flow through submerged canopies. A review of some of this work is outlined in Nepf (2012). A paper particularly related to the present study is Zhang

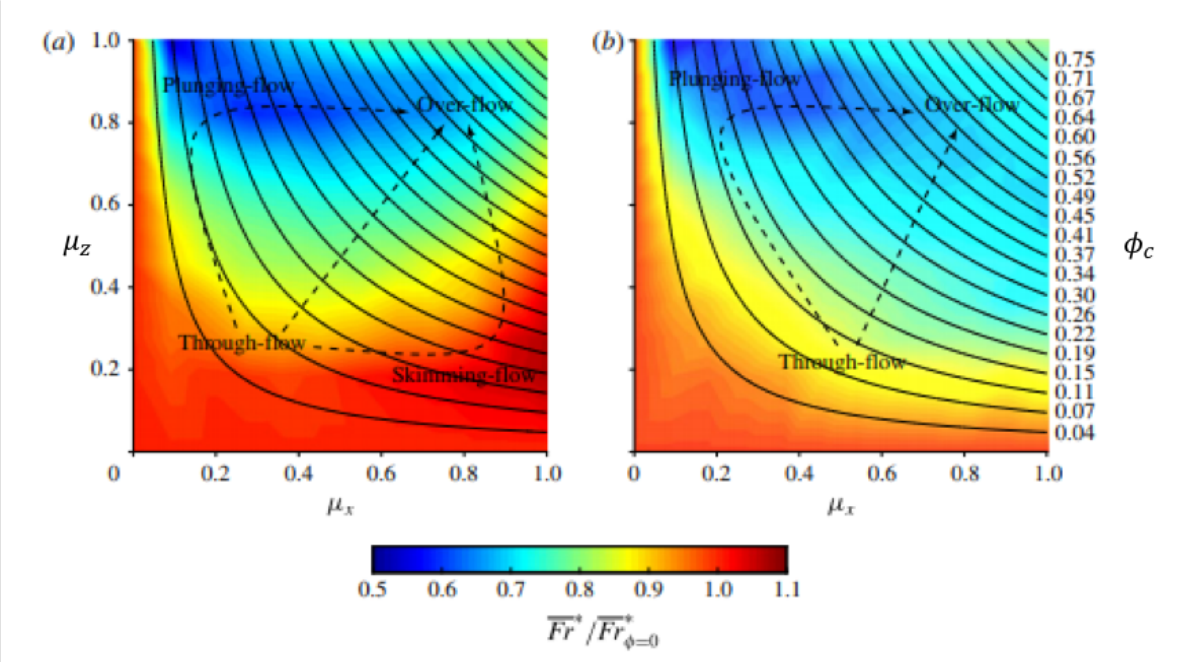

Fig. 2.17 Variation in the time averaged Froude number relative to that of a smooth bed current in the $\mu_x - \mu_z$ space. Panel a is for staggered arrays of cylinders and panel b is for in-line arrays of cylinders.

Adapted from Zhou et al. (2017). Arrows show transitions between different regimes.

and Nepf (2011), which considered surface gravity currents interacting with the roots of floating vegetation. These roots were idealised by arrays of circular cylinders extending through the top surface. They noticed similarly to Cenedese et al. (2016) that when the cylinders were dense enough the current would travel primarily beneath the cylinders rather than travelling through them.

There have also been efforts to study the influence of less idealised bottom roughness on gravity currents. Keramaris and Prinos (2016) studied gravity currents propagating through a trapezoidal channel where the bottom was covered in flexible grass vegetation to simulate a gravity current in a valley. They noted that the shape of the channel affected the current more than the vegetation itself; however they did note that the current speed was reduced by the vegetation. Nogueira et al. (2013) studied gravity currents propagating over a bed of graded pebbles of different sizes. They noted that the roughness caused the phases of a lock exchange gravity current to develop at different speeds and found that while the buoyancy within the current head decreased with time, this was balanced by a decrease in velocity (or inertia).

Little work has been done identifying how gravity currents transition from a smooth boundary to a rough boundary; however several papers have looked at how smooth bed gravity currents

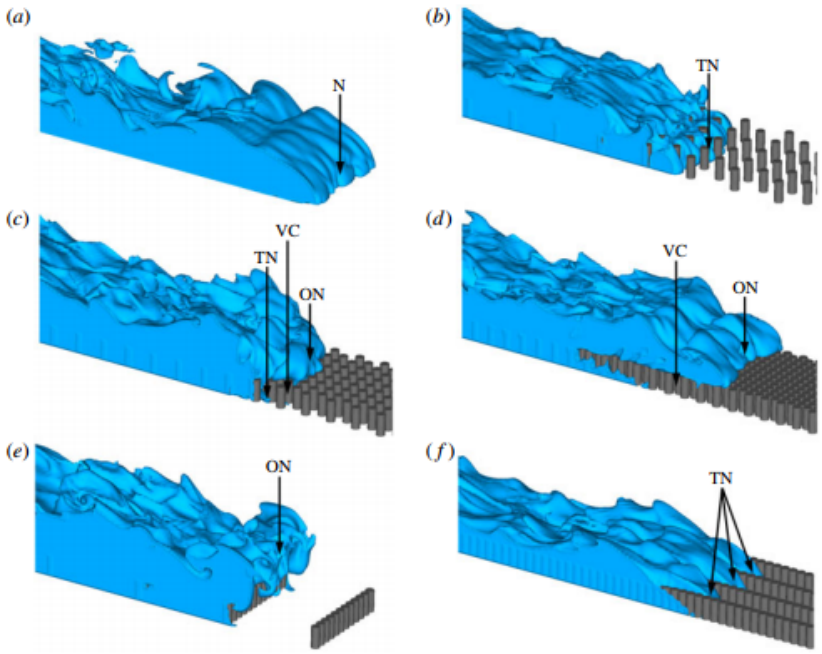

Fig. 2.18 Density contours showing regimes as gravity currents propagate over roughness elements of varying densities. Reproduced from Zhou et al. (2017). a) shows a smooth bed current where N denotes the nose. b) shows a through-flowing current where TN denotes the through-flowing nose. c) shows a transitioning case where both a through-flowing and over-flowing (ON) nose is visible as well and fluid in the bed due to vertical convection (VC). d) shows a fully over-flowing nose where the fluid in the bed is entirely cause by vertical convection. e) shows the plunging configuration where the over-flowing nose plunges over individual rows of roughness. f) shows the skimming flow regime where the through-flowing nose propagates through longitudinal channels.

interact with individual objects. Rottman et al. (1985) carried out a large set of experiments to observe how gravity currents propagate through and over individual porous and solid objects. They observed that upon interacting with objects a portion of the fluid would be reflected backwards while the rest would be transmitted forward. This was also observed by Wilson et al. (2018) who investigated the effect of a single object on turbidity currents and observed this flow propagating backwards off the obstacle as well as noting that while the current was slowed by the obstacle it had little effect on the velocity structure. Nasr-Azadani et al. (2016) and Tokyay et al. (2012) used DNS and LES respectively to investigate developed currents interacting with single roughness elements. They saw that these elements alter the speed and shape of the currents and that turbidity currents deposit large amounts of sediment around the obstacles. They also observed three-dimensional vortical structures as the currents propagated over and around the elements.

Another area related to gravity current roughness is how gravity currents propagate over porous boundaries. Thomas et al. (1998) used a lock exchange mechanism to investigate how a gravity current propagated over a porous boundary approximated by a metal grid. They found that the current mass exponentially decayed and they generated a simple model to capture this. Ungarish and Huppert (2000) built on this by generating a shallow water model of gravity currents propagating over porous boundaries. They formulated a parameter that represented the boundary by the ratio of drainage speed to the horizontal propagation speed. This was found to be consistent with the results of Thomas et al. (1998).

The studies mentioned in this section highlight several key impacts of roughness on gravity currents. In almost all studies mentioned the roughness caused the currents to travel more slowly than smooth bed currents and induced dilution of their heads. In most cases the speed and dilution was impacted more strongly by roughness with larger sizes relative to the currents and when the roughness was more densely packed. Furthermore, while mixing between the current and ambient fluid for a smooth-bed current is predominantly caused by the shear layer above the current, when roughness is small compared to the current or densely packed an additional, large shear layer can form beneath the current and this can cause significant mixing.

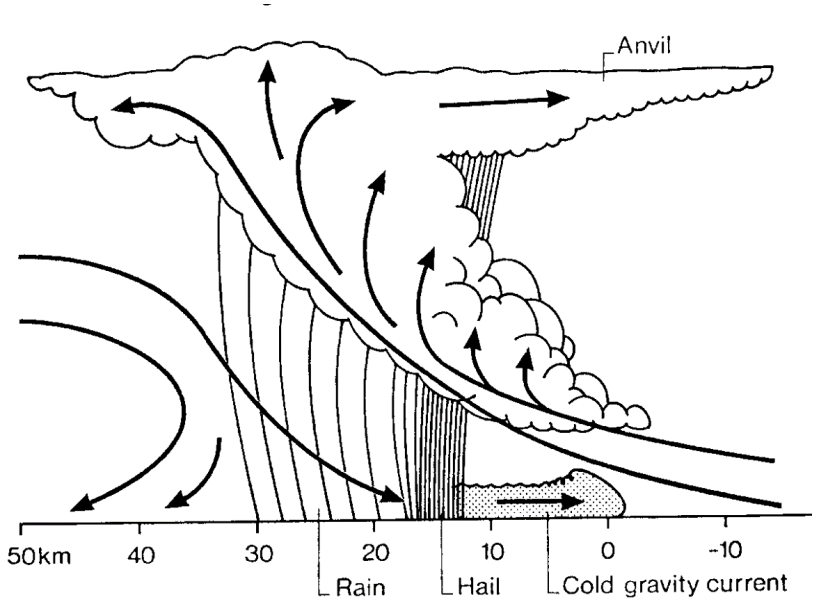

Fig. 2.19 A schematic of a thunderstorm outflow reproduced from Simpson (1997).

2.9 Applied studies of Gravity Currents

2.9.1 Gravity Currents in the Atmosphere

Gravity currents occur, and have been studied, in a variety of different environmental and man-made scenarios. A thunderstorm is a common example of a gravity current, where warm air is unstable and rises upwards until it reaches a stable layer known as the tropopause, along which it travels as a gravity current. At the same time in the centre of the thunderstorm where rain and hail occurs, air will cool and drop to the ground where it will also travel as a gravity current. These cold, boundary currents can move at very high speeds and be damaging for aircraft. A schematic summarising the generation process is provided in Figure 2.19.

Charba (1974) carried out one of the first studies to investigate thunderstorm outflows as gravity currents. They used wind and temperature measurements to construct features of an outflow in Oklahoma and found the outflow to be geometrically similar to laboratory generated gravity currents as well as finding a good fit with the Froude number. This was then supported by several following studies (Mitchell and Hovermale, 1977; Mueller and Carbone, 1987), which observed the head-tail structure with a raised nose as well as the K-H billows. They also observed mixing behind the head of the outflows.

Analysis of thunderstorm outflows in non-coastal areas has been ongoing because they form the predominant horizontal loading on man-made structures in many of these areas (Twisdale and Vickery, 1992). In recent times, much of this research focused on using aviation to get above-ground velocities (Brandes et al., 1995) and Doppler radars to generate near-ground velocities (Gunter and Schroeder, 2015) as well as the effect of surface roughness and other obstacles on the currents (Gunter and Schroeder, 2015; Mason et al., 2009). These continue to be compared with laboratory and numerical models of gravity currents in order to properly understand their dynamics.

Another example of commonly occurring gravity currents is in sea-breeze fronts. These occur because of differential warming of air over the land and sea causing an unstable air interface. The difference in density between the cold air over the sea and the relatively warmer air over the land causes a gravity current to propagate onto the land. Research into sea-breezes dates back as far as 2500 years and a review of much of this research was carried out by Miller et al. (2003).

As with thunderstorm outflows, sea-breeze fronts have been shown to possess a similar structure to gravity currents in the laboratory (Reible et al., 1993; Sha et al., 1991). These include K-H billows and the head-tail structure. The Froude numbers of thunderstorm outflows and sea-breeze fronts have also been shown to be similar to laboratory generated currents (Sha et al., 1991). In many coastal areas these form the predominant winds, hence the horizontal loading in the design of man-made structures in many regions is based on sea-breeze fronts (Miller et al., 2003). Recent studies into sea-breeze fronts have focused on Doppler and aircraft measurements as well as comparisons with numerical and laboratory experiments (Chen et al., 2019; Wood et al., 1999). The interactions with urban structures is also an area of present research (Emmanuel and Johansson, 2006; Thompson et al., 2007).

As was alluded to in Chapter 1, when thunderstorm outflows or sea-breeze fronts travel through arid areas these can entrain large quantities of dry soil, forming large dust storms. These dust storms are known as *haboobs* and can have large impacts on public safety in areas where they occur (Idso et al., 1972). Field studies have been carried out around the world. Their impact on man made structures and similarity to laboratory generated currents have been the focus of much of this work (Crouvi et al., 2017; Idso et al., 1972; Karami et al., 2017; Pantillon et al., 2016).

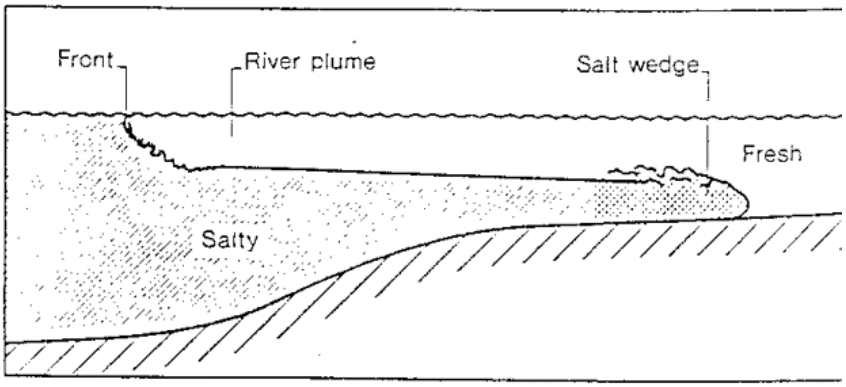

Fig. 2.20 A possible configuration for a gravity current in an estuary reproduced from Simpson (1997).

A man-made example of an atmospheric gravity current is the release of toxic gasses (such as LPG), which can spread along the ground as a gravity current causing a hazard to human health. One of the worst examples of this occurred in Bhopal, India in 1984 when 40 tonnes of methyl-isocyanate was released from a storage tank killing about 2500 people. This event has been studied and modelled to understand how it occurred and how it could be prevented in the future (Singh and Ghosh, 1987).

2.9.2 Gravity Currents in Water Bodies

Gravity currents occur in a wide range of water bodies. They are common in fjords and estuaries where dense seawater meets light freshwater fed from rivers. These currents can travel significant distances inland. A possible configuration for these is shown in Figure 2.20. Field measurements have confirmed the presence of gravity currents in estuaries (Geyer and Cannon, 1982). They also occur within lakes and reservoirs due to inflows and outflows as well as being due to differential rates of heating and cooling (Roget and Colomer, 1996).

Gravity currents can be found in the ocean generated by differences in temperature or salinity. Additionally, turbidity currents are common where material on an unstable slope may form a submarine landslide that travels along the ocean floor as a gravity current. A recent example of these is a large turbidity current that formed after the 2016 Kaikoura earthquake (Barnes et al., 2017). The speeds of these currents can cause them to pick up additional material from the bed of the ocean causing them to grow further and scour sediment from the ocean floor. These are termed *self-stoking* and can be highly damaging to human infrastructure such as underwater cables (Krause et al., 1970).

2.9.3 Avalanches

One final example of a gravity current is an avalanche. It has been shown that while dense, packed-snow avalanches can be approximated using open-channel flow theory, lighter, powder-snow avalanches have properties similar to turbidity currents (Hopfinger, 1983). In these cases the snow is separate and light enough that it can be considered as particles entrained in the air, similar to sediment entrained in oceanic turbidity currents. As with many oceanic and atmospheric gravity currents, the interactions between avalanches and obstacles or roughness is important. Feistl et al. (2015) investigated the interactions between powder-snow avalanches and forests, finding the sizes of powder-snow avalanches to be important because, while they are often slow-moving, if they are sufficiently large they can generate significant moments on trees that cause overturning. Studies have also looked at defence structures and identified the abilities of different structures to deflect avalanches under different conditions (Kumar, 2014; Naaim-Bouvet et al., 2002).

2.10 Summary and Implications for Current Study

This chapter has discussed the significant body of work that has gone into understanding the dynamics of gravity currents. For propagation over smooth, flat boundaries, these dynamics have been studied extensively and this has led to a good understanding of naturally occurring gravity currents, provided their boundaries are relatively smooth. In many natural occurrences, however, gravity currents must negotiate a variety of obstacles and terrain and knowledge of this interaction is required to understand the dynamics of these currents. Therefore, while some recent studies have focused on how gravity currents interact with rough boundaries this is still not well understood.

Section 2.8 provided an outline of the work that has been conducted into the interaction between gravity currents and rough beds. It was seen that the density of the roughness can have a strong impact on the behaviour of a current. When the roughness is sparsely packed a current may propagate through the roughness, whereas when the roughness is densely distributed a current is more likely to propagate atop it. When the current propagates atop the roughness convective instabilities can occur between the dense current fluid and the light fluid contained in the bed. Additionally, roughness causes increased mixing of currents with their ambient as well

as slowing of the currents. Roughness with large vertical extents relative to the current appear to have a larger impact on the Froude number and dilution of the current.

Most of the studies investigating the impact of roughness on gravity currents have consisted of roughness present from the onset of the current in space. Where currents were allowed to develop before encountering roughness most studies focused on the impact of single objects rather than fields of roughness. Therefore, one focus of this study is the impact of a field of roughness on a developed gravity current. Furthermore, the transient nature of the interaction with the roughness is examined where most previous studies assumed the currents to be in a steady regime.

Recent experiments have investigated the impact on gravity currents of open fields of roughness or porous boundaries where convective exchange can occur relatively unimpeded. Very little quantitative research has investigated the impact of closely packed roughness where vertical convective exchange between the current and fluid within the roughness is impeded (though still allowed to occur). Therefore, this is the other focus of this thesis.

Chapter 3: Experimental System and Design

3.1 Introduction

The previous chapter highlighted research gaps relating to how gravity currents interact with rough boundaries. To address these gaps a series of experiments were carried out. These experiments used flow visualisation techniques to measure important parameters. This chapter will outline the experimental system used along with these visualisation techniques.

Section 3.2 provides a detailed description of the experimental system including the channel and optical equipment employed. Due to the importance of mixing, shape and physical extent of gravity currents a measure of the density is provided by employing a *light attenuation* (LA) technique. An outline of this technique, along with a description of its present use and limitations, is provided in Section 3.3.

To understand the physical processes involved in gravity current propagation and mixing, knowledge of velocity fields is also necessary. These were measured using a *Particle Tracking Velocimetry* (PTV) technique. This technique is discussed in Section 3.4. Final sections outlining the experiments carried out in this study are presented in Section 3.5 and a brief description of the analysis used in Section 3.6. Finally, a summary is provided in Section 3.7.

3.2 Experimental System

The experiments were conducted in the fluid mechanics laboratory in the Department of Civil and Natural Resources Engineering at the University of Canterbury in Christchurch, New Zealand. The experiments were conducted in a rectangular channel and data were captured with a set of high definition cameras. The channel was located in a dark room to ensure minimal ambient light entered the cameras.

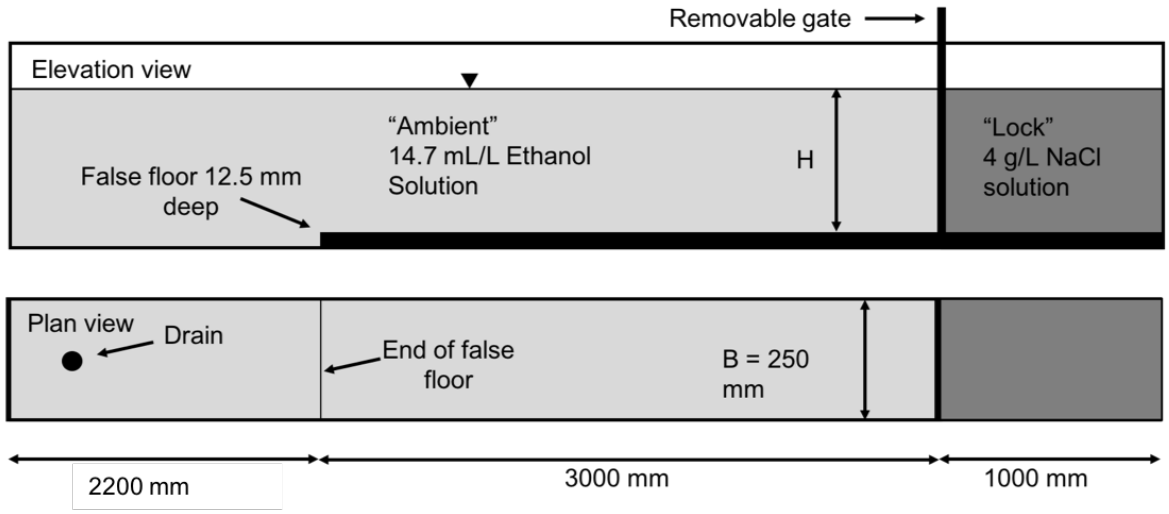

Fig. 3.1 Schematic of the channel used in experimental study. Not to scale

A schematic of the channel used for all experiments is shown in Figure 3.1. The channel utilised the *lock exchange* technique outlined in Chapter 2. This 6.2 m long channel contained a 1 m long *lock* separated from a 5.2 m *ambient* section by a stainless steel gate. This gate was sealed by plastic foam to ensure leakage did not occur. The channel walls were constructed from 18 mm thick perspex to allow for flow visualisation. The perspex wall sheets were joined by bolts every 2.5 meters. Flow visualisation was hindered at these joins and therefore images of the flow could not be captured at these locations.

The lock was filled with a 4 g/L *NaCl* solution and the ambient was filled with a 14.7 mL/L colourless *denatured alcohol* solution. This created a density difference, $\Delta\rho$, of approximately 0.5 %, while ensuring that the fluids had matching refractive indices of 1.3336 (Haynes, 2014). Ensuring that the refractive indices of the two fluids matched was important for flow visualisation and the density difference was selected such that the *Boussinesq approximation* could be made. Both sides of the gate were filled simultaneously to minimise the pressure differential across the gate. To begin the experiments the gate was removed to allow the fluids to interact.

The denatured alcohol and NaCl solutions were mixed in 450 L tanks with submersible pumps. The same pumps were used to transfer the solutions to the channel. Water was treated with activated carbon filters then allowed to stand for 24 hours before use. The standing time allowed time for dissolved gasses to come out of solution. After mixing, both solutions were allowed to stand for a further one hour in a room of constant temperature to ensure there were not significant

temperature differentials between the solutions and to allow for any gasses dissolved during mixing to come out of solution.

While care was taken to ensure that concentrations were as close as possible to those stated, some variation occurred. Therefore, samples of fluid were collected on either side of the gate before the gate was removed and the densities of these were measured with an *Anton Parr DMA5000* density meter. This was accurate to 5×10^{-2} kg/m^3.

Regularly spaced steel ties connected the walls at the top of the channel to resist lateral loading when the channel was filled with water. These prevented significant lateral deflection of the channel walls. Steel ties were also employed at the top of the channel on either side of the gate. These ensured that the gate could be removed vertically with little lateral movement. The channel was mounted atop a steel truss, allowing the channel to be lifted above the floor and levelled.

A 12.5 mm deep false floor was placed in the lock region and the first 3 m of the ambient region. The floor contained threaded bolt holes to allow roughness elements to be screwed to the floor. The nature and configuration of the roughness utilised is discussed in Section 3.5. Whenever roughness was not present these holes were taped to ensure the holes did not interfere with the dynamics of the current. A drain was present on the base of the channel downstream of the false floor to remove water between experiments.

Flow data was captured by a set of *JAI GO-5101C-PGE* cameras mounted on tripods. The locations of these cameras, relative to the channel, are shown in Figure 3.2. Cameras were labelled C0, C1, C2 and C3 and were placed five meters from the front face of the channel. Maximising this distance between the cameras and the channel minimised parallax errors. The cameras were set up orthogonal to the front face of the channel.

Zoom lenses were employed to minimise the length of viewing windows and hence reduced parallax errors. A gap of 150 mm was present between the viewing windows 1 and 2 because a connection between sheets of perspex was present at this location. All other viewing windows had small overlaps to ensure contiguous measurements. Camera 0 was not employed for a number of experiments and was added later once it became clear that additional information would be valuable. The cameras had frame rates of 22.701Hz and captured 8-bit colour images

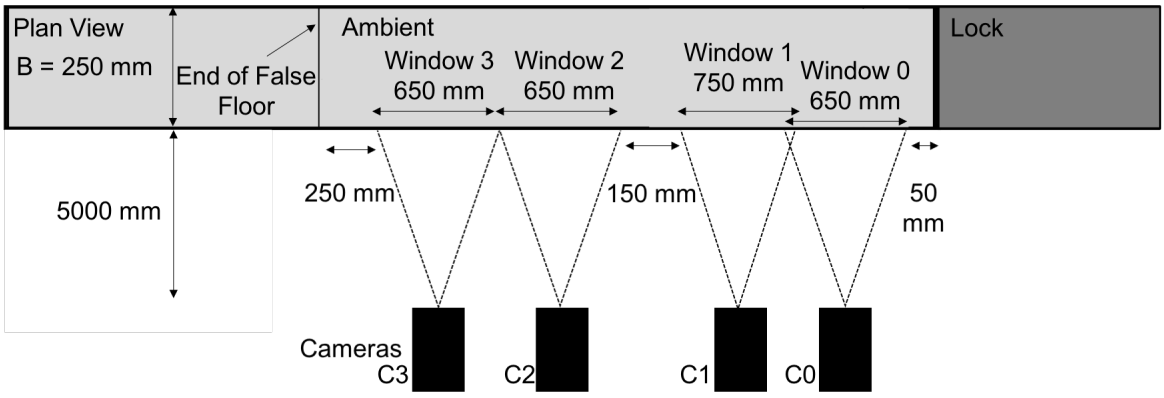

Fig. 3.2 Schematic showing locations of cameras relative to the front face of experimental channel. Any dimensions not shown can be found in Figure 3.1.

with resolutions of 2,464 x 2,056 pixels. The images were transferred directly to a fast hard drive on a PC during image capture.

In order to stitch images associated with the four cameras together, rulers were laid along the centre of the channel with images taken of these with each camera. These were used to find accurate locations of each viewing window. The rulers began at the location of the gate to allow the camera locations to be found to the nearest millimetre relative to the gate location. Due to the inaccuracy in placing cameras at exact locations the measured locations varied somewhat from those shown in Figure 3.2. The rulers were also used convert from camera pixels to physical co-ordinates.

3.3 Density Measurement Using Light Attenuation

3.3.1 Introduction

Due to the lock exchange gravity currents being generated by density differences between two fluids, density field measurements were deemed important to understand the driving forces and mixing behaviour. In order to measure the density fields the *Light Attenuation* (LA) technique was employed. This technique allowed for full spatial and temporal resolution of width-averaged densities to be measured within the analysed domain.

3.3.2 Theory of Light Attenuation

LA allows a density field to be determined by measuring the degree to which light is *attenuated* (reduced in intensity) as it passes through a fluid to which dye has been added. Based on the degree to which the light is attenuated, the dye concentrations can be calibrated with the density of the fluid to generate a density field.

In order to use this technique a uniform white light is directed through the fluid. This light attenuates as it travels through different media. This attenuation is due to two main mechanisms. The first is absorption where, in the case of a fluid dynamics experiment, light is absorbed by the water, dye, perspex and air as it travels through them. The amount that is absorbed increases with distance. The second mechanism is reflection off the interfaces (e.g. between water and perspex or between perspex and air). If the locations and properties of the lights, cameras capturing the data and experimental apparatus do not change then differences in light attenuation should be solely due to the absorption of light by the dye. Hence, this attenuation can be related to the concentration of dye.

Calibrations between the absorption of light and the density of fluid are based on the *Beer-Lambert law* which states that *intensity*, I, of light as it attenuates through a material is governed by

$$\frac{\partial I}{\partial s} = -\zeta I \tag{3.1}$$

where s is the distance along the light path and ζ is a property of the material attenuating the light.

Cenedese and Dalziel (1998) integrated this equation along the light path and assumed that dye concentration was approximately constant along it. A rearranged version of the resulting equation is

$$Bf(c) = -ln\left(\frac{I_0}{I(c)}\right) \tag{3.2}$$

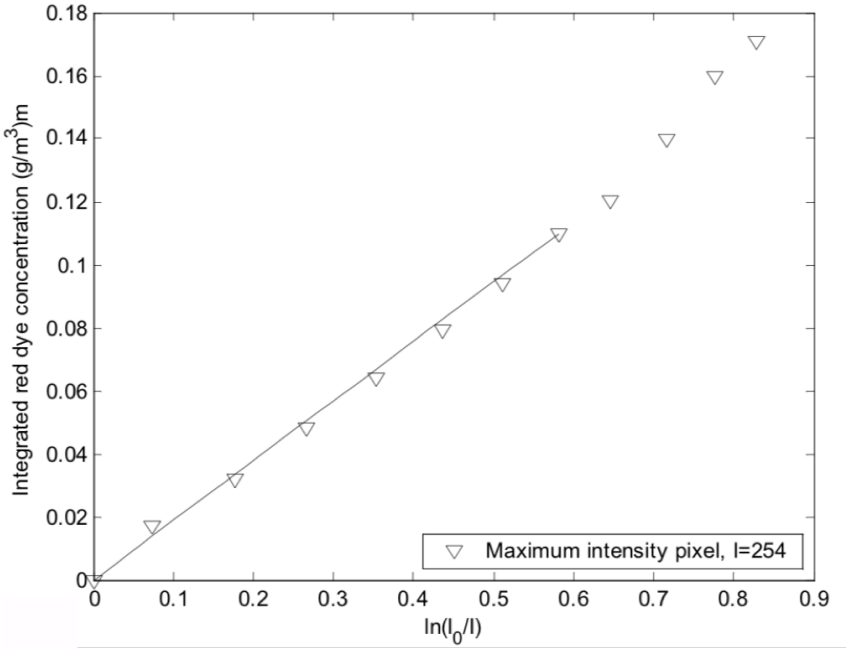

Fig. 3.3 Carmoisine concentration attenuation calibration by McBryde (2008).

where c is the concentration of dye, f(c) is a function of the concentration of dye known as the *absorbency*, B is the distance travelled through the dye by the light (the width of a tank), I_0 is the intensity of light if no dye is present and $I(c)$ is the intensity as a function of dye concentration, c. As B is generally a constant it can be incorporated into the absorbency.

The crux of this technique is being able to accurately calculate the absorbency function. Cenedese and Dalziel (1998) tested four different dyes and showed that, when the concentration of dye was low, absorbency could be considered linearly proportional to dye concentration. McBryde (2008) tested a red food dye known as *carmoisine powder*, the same dye used for the present study. He carried out calibrations using absorption of only the green light intensities and this calibration for a single pixel is shown in Figure 3.3. This figure shows absorbency to be linear until a width integrated dye concentration of 0.12 g/m^{3}m.The units g/m^{3}m refer to the concentration of the dye divided by the length of the light path through the dye. Based on this finding he deemed it suitable to carry out two-point pixel by pixel calibrations assuming a linear fit between the two points. Cenedese et al. (2016) used the same dye but carried out a calibration using 8 different concentrations of dye. The multiple point calibration allowed them to assume a higher order absorbency function to reduce errors. This approach was used in the present study.

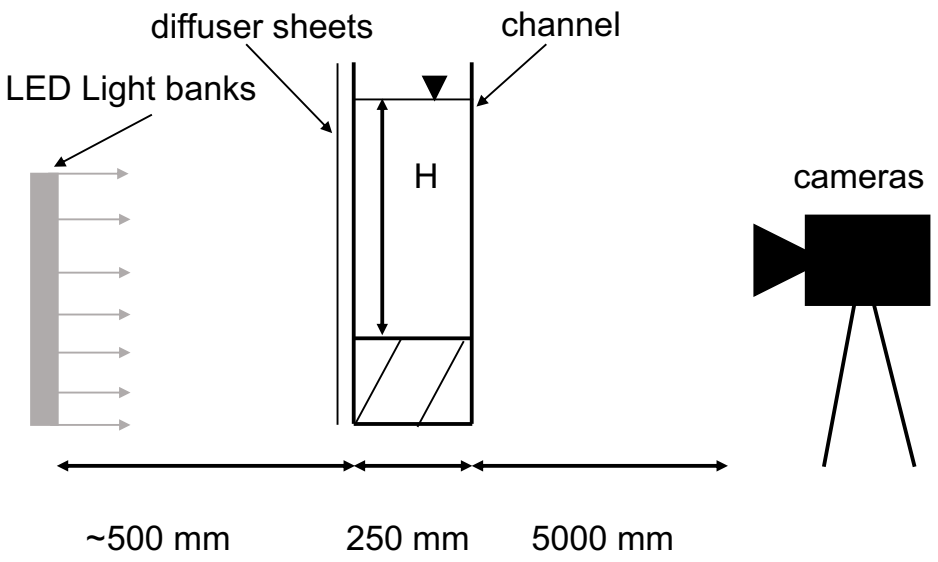

Fig. 3.4 Schematic for optical setup in LA experiments. Not to scale

3.3.3 Light Attenuation Setup

Figure 3.4 shows a schematic for the light attenuation setup employed in this study. Light banks were placed approximately 0.5 m behind the channel with a light diffuser attached to the channel wall between the lights and the channel. Each bank of lights contained six 1.2 m long horizontal bulbs emitting light via light emitting diodes (LEDs). The bulbs were equally spaced vertically. Three of these light banks were employed alongside one another to ensure light coverage over all 4 camera viewing windows. The light diffuser was made from 2 mm thick translucent perspex. The diffuser removed the strong light signatures of the individual lights, thus ensuring the light intensity was more uniform in nature.

In order for the experiments to be conducted confidently the accuracy and consistency of the lighting system was investigated. If the intensity of light varied significantly with time or if the intensity measured was different when carrying out a calibration and when conducting experiments the lighting system would be unsuitable. To carry out this investigation, all light was eliminated from the room with the lights off and undyed water in the channel. One camera was set to record an image every 30 seconds for 8 hours and green intensities were plotted with time. Shortly after setting the camera to record the light bank was switched on and the time when they were switched on was defined to be a time of 0. The first three hours of these results are plotted in Figure 3.5. For less than 10 minutes the lights decreased in intensity before then

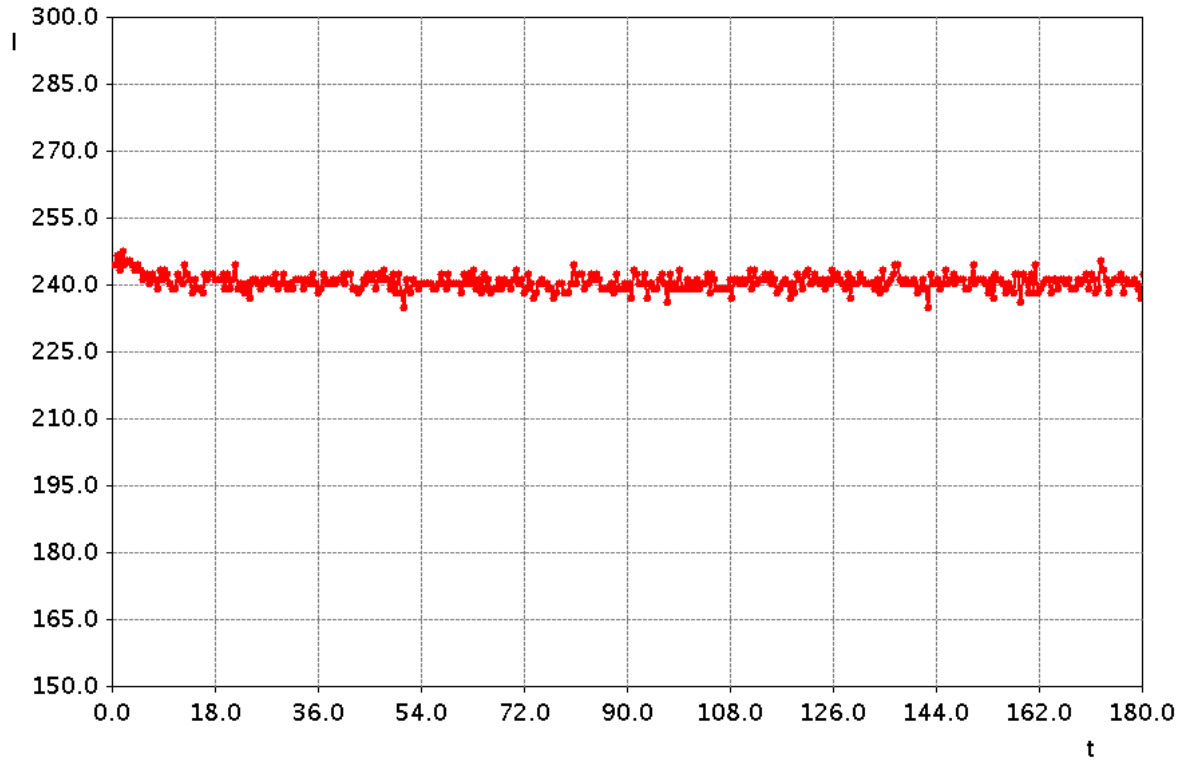

Fig. 3.5 Green intensities with time in minutes at a single pixel for LED lights. A time of 0 corresponds to the time when the lights were switched on.

reaching a steady state. Once the lights reached a steady state the intensities fluctuated, with these fluctuations reaching a maximum intensity variation of less than 3% of the mean intensity and a root mean squared error of 0.3%. Similar results were found for the red and blue intensities. The investigation was conducted again 24 hours later, with a negligible difference found between the mean intensities at the two times. Based on this investigation, lights were always switched on an hour before an experiment was begun. Exposure and gains on the cameras were adjusted to ensure that maximum green intensities were as large as possible but never saturated.

Red carmoisine power was used to trace the concentration of salt. This dye has been shown not to react with NaCl (salt) and ageing effects have been shown to be minimal (McBryde, 2008). Dye was added to the salt solution in the lock so that it could be used as a surrogate for the salt concentration and hence density. To use dye as a surrogate for salt, a solution, referred to as the *master solution*, with salt and dye concentrations ten times larger than the lock was created. This solution was mixed into both the full channel for calibration and the lock region for the experiments to ensure that the ratio of salt to dye was always fixed. As water in Christchurch was chlorinated at the time of the experiments and chlorine reacts with carmoisine dye, all

water used in these experiments was pre-filtered using activated carbon filters and measurements indicated that chlorine was undetectable in the filtered water.

The maximum width integrated concentrations were kept below 0.11g/m^{3}m, in keeping with the recommendations of McBryde (2008). The channel width was held constant at 0.25 m and hence a concentration of 0.44 g/m^3 of dye was used. The calibration using Equation 3.2 links the intensity of light measured by the cameras with the concentration of dye (and hence salt). The presence of red carmoisine power caused a significant reduction in the intensity of green light measured by the cameras but only caused a small reduction in the red intensity. Thus, the light intensity in Equation 3.2 could have been taken to be only the green intensity, assuming that the red intensity was not affected by the dye. However, the ratio of green and red intensities was used to ensure any small variations in the red intensity were included as this has been shown to lead to a more linear absorbency function McBryde (2008).Therefore, $I(c)$ in Equation 3.2 was taken to be the intensity of green light measured at each pixel divided by the intensity of red light measured at each pixel.

3.3.4 Experimental Process

With the setup complete the following procedure was carried out for a typical LA experiment.

1. Water was filtered and left to sit in the tanks for at least 24 hours in order to ensure that it had achieved room temperature and excess dissolved gases had escaped.

2. The master solution was mixed in a 450 L tank with 40 g/L of NaCl and 4.4 g/m^3 of dye. A submersible pump was used to mix this and it was left to sit for 24 hours before use.

3. The lock fluid was mixed in a separate 450 L tank containing 1 part master solution to 9 parts filtered water.

4. Rulers were laid along the centre of the channel and images were taken from each camera to allow images to be stitched together and spatial co-ordinates to be calibrated with the camera pixel densities.

5. The LED light bank was switched on at least 1 hour before capturing any images.

6. Calibration images were then captured by the following process

(a) The channel was filled to above the depth of the subsequent experimental runs with filtered, undyed water without NaCl or denatured alcohol and 250 images were captured with each camera. A sample of fluid was collected and the density was recorded with the Anton Parr density meter.

(b) The volume of master solution required to achieve a salt and dye concentration in the channel of 1.2 times the lock fluid was calculated. This was divided evenly by 6 to calculate the volume of master solution to be added to the channel for each calibration image.

(c) This known volume of master solution was then added to the channel, hand mixed and left to rest for at least 10 minutes.

(d) 250 images were captured and a sample of fluid was collected. The density of this sample was measured with the Anton Parr density meter.

(e) This process was repeated until 7 sets of images had been captured by each camera and 7 densities had been measured. The final image had a dye concentration of approximately 1.2 times the lock solution.

7. In a separate 450 L tank denatured alcohol was diluted in filtered water at a concentration of 14.7 mL/L. This was mixed for an hour with a submersible pump then left for an hour to settle.

8. An experimental run proceeded as follows

(a) Using submersible pumps the previously prepared denatured alcohol solution was transferred to the ambient section of the channel and the NaCl solution to the lock. Fluid was transferred slowly, ensuring water levels on either side of the gate stayed approximately equal to avoid large pressure differences across it.

(b) Samples of fluid on either side of the gate were collected and the densities were measured with the Anton Parr density meter.

(c) A ruler was used to measure the fluid depth.

(d) The fluid was left to sit for at least 10 minutes in order for any background motion to decay.

(e) With all light eliminated except the LED light banks, 250 images were captured with each camera. These were used as background images.

(f) The cameras were then set to begin capturing 3000 images. The ceiling lights in the dark room were switched on before capturing these images and switched off immediately after the cameras began recording. The frame when the lights were switched off was used to synchronise the starting time of the cameras.

(g) Immediately after the lights were switched off the gate was removed vertically to enable the experiment to begin.

9. At the conclusion of the experiment the fluid in the channel was drained and the channel was rinsed with filtered water to remove any remaining NaCl, denatured alcohol and dye.

10. Images were transferred to hard drives and were processed using the in-house software *Streams* (Nokes, 2017).

11. Up to four experiments were carried out after a single calibration. These were followed by a second calibration. The two calibrations were compared to ensure consistency.

3.3.5 Calibration and Processing

Before any experiments were undertaken a calibration was performed. Once calibration images had been captured by the process outlined in Section 3.3.4 each set of 250 images captured were averaged to remove any fluctuations in light intensity. The optical thickness, d, was calculated at each pixel as

$$d = ln\left(\frac{I_0(x,y)}{I(x,y)}\right) \tag{3.3}$$

with intensities based on the ratio of green to red guns. For clarity, the optical thickness is a surrogate for the concentration of dye (causing a reduced light intensity) and the absorbency mentioned earlier is the function relating the optical thickness with the density (or concentration) of salt. As the channel width was kept constant and the density was directly related to the salt concentration, the inverse of the absorbency in Equation 3.2 could be used to determine the density as

$$\rho = f(d) \tag{3.4}$$

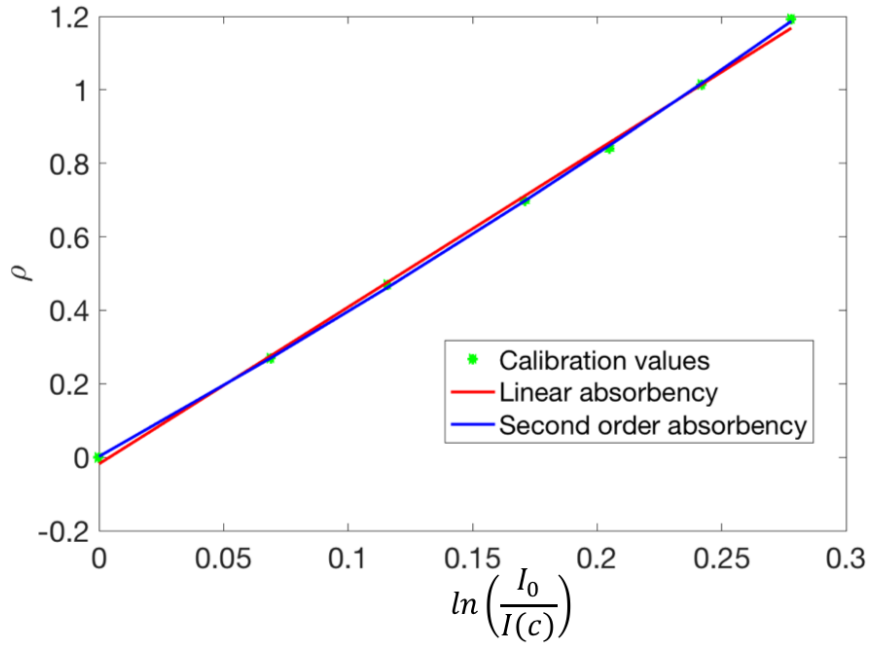

Fig. 3.6 Typical calibration curve with linear and second order absorbency functions.

where $f(d)$ is referred to as the *inverse absorbency function*. In order to determine the inverse absorbency function the optical thickness was plotted pixel by pixel with the measured densities to generate calibration curves. For these curves, densities were non-dimensionalised such that lock fluid had a density of 1 and fluid without dye had a density of 0.

A typical curve from this analysis is shown in Figure 3.6. Both linear and quadratic fits were considered for the inverse absorbency function. The slight non-linearity of the calibration curve suggested a quadratic fit was justified.

When experiments were conducted the background images were averaged and their green/red ratios were taken as I_0. The inverse absorbency function was known from the calibration images via a second order approximation so the experimental optical thickness could be converted pixel by pixel into density values. The measured densities were then projected onto an evenly spaced grid to give full width-averaged density fields. This had a grid spacing of 4 mm in the x direction and 2 mm in the y direction.

The images contained regions outside the flow domain such as the bottom of the channel or above the water level. These were trimmed before analysis. Any obstructions such as structural elements were also removed. All frames before switching off the ceiling lights were removed to synchronise camera times. Additionally any frames before the current reached the first viewing

window were removed. Figure 3.7 shows an instantaneous image from the C1 camera for a single experiment and the resulting field. The density fields measured using the four cameras were stitched together as the images with rulers captured earlier allowed accurate locations of each viewing window relative to the gate location to be known. Wherever viewing windows overlapped the fields were averaged.

3.3.6 Errors and Limitations in Light Attenuation Experiments

There were a number of errors present in the light attenuation experiments. What follows is an analysis of these errors and a discussion of how they were minimised.

Time

There were multiple errors and limitations associated with timescales in the analysis.

- Cameras were synchronised by switching off ceiling lights and the time when this occurred was found to an accuracy of one frame. This introduced error of ± 0.022s in the synchronisation.
- The time associated with t=0 was generally selected arbitrarily based on when the currents became visible in the first viewing window. There was therefore no accurate representation of time since the opening of the gate.

Parallax

There were parallax errors associated with the experimental setup. Parallax errors occur because a camera views different locations of a channel at different angles as shown in Figure 3.8 and this distorts the image. At the centre of the image the light path travelling from the light sheet to the camera through the channel (e-d-c) is orthogonal to the channel. However, at the edge of the image the light path through the channel (a-b-c) is viewed at an angle. Minimising the length of a viewing window and maximising the distance between the camera and the channel reduces the overall impact of parallax. Therefore, cameras were placed at least five meters from the channel. The cameras were also positioned at heights such that the aspects of the flow deemed most important were in the vertical centre of the viewing windows. When the channel contained

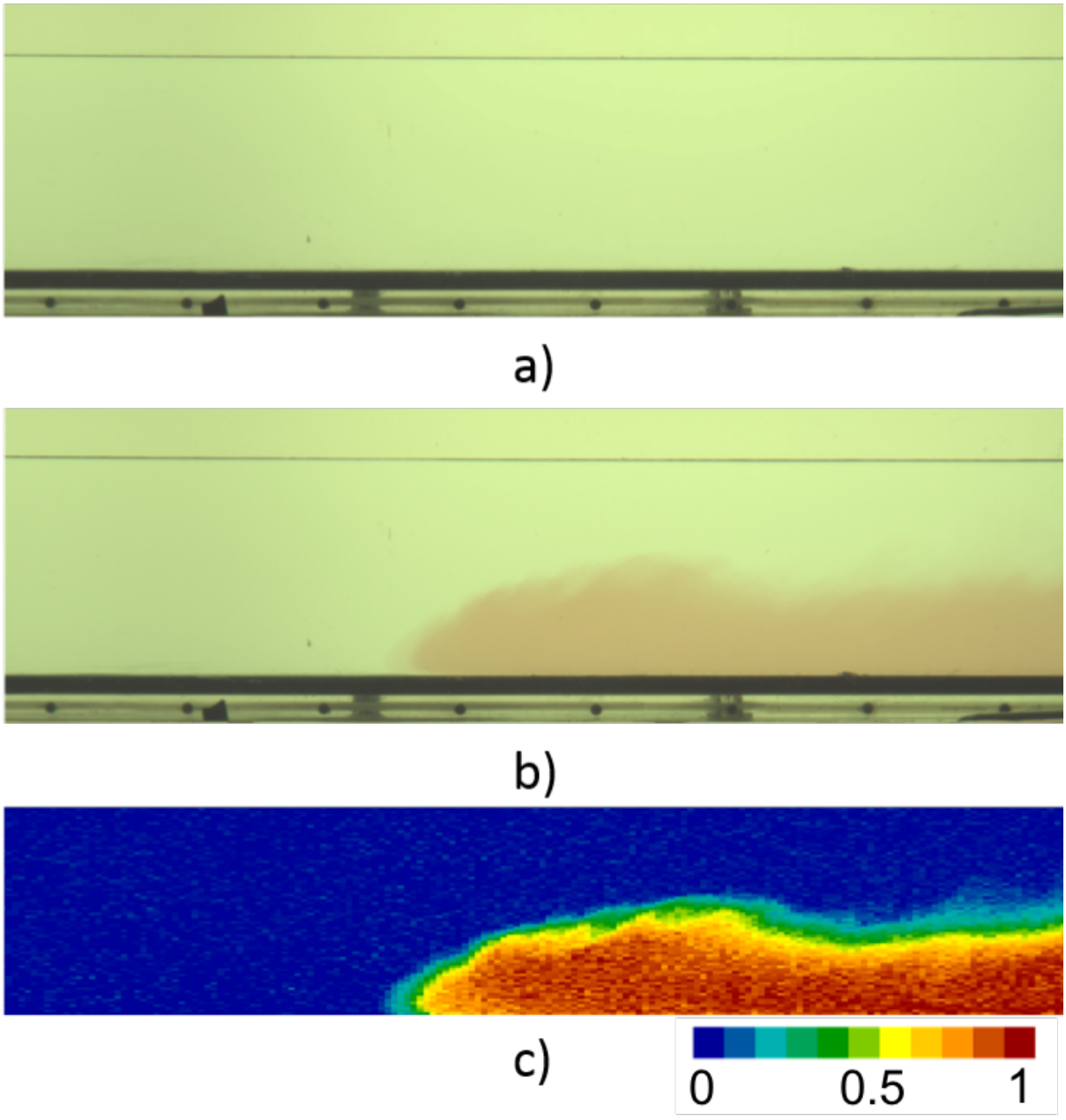

Fig. 3.7 a) A background image from a smooth-bed gravity current experiment, b) An instantaneous image once the current was in view, and c) The processed field from b) displaying a false colour image of density on an evenly spaced grid. Images were captured with the C1 camera.

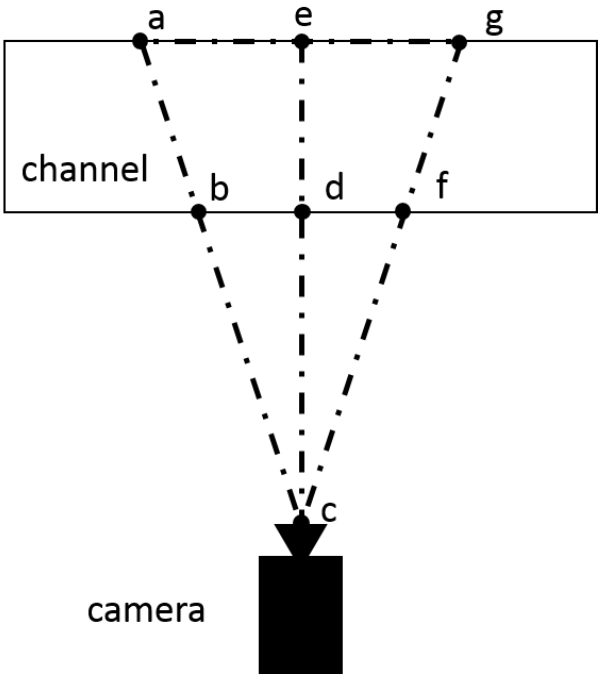

Fig. 3.8 Schematic illustrating error associated with light path parallax issues.

roughness the cameras were orientated such that the top of the roughness was in the centre of the viewing window.

One effect of parallax was an error in length scale at the edge of the viewing windows. This effect occurred due to the camera being slightly further away from the edges of the viewing windows than the centre of the viewing windows. Thus, the conversion from pixels to spatial co-ordinates was impacted. The camera was at worst only 1.004 times further away at the edges of the viewing windows than the centre so this error was minimal. The parallax error in the length scale also had an impact vertically but the small height of the viewing windows meant that this was negligible.

The larger error associated with parallax was the difference in light path through the channel. At the centre of the channel the light path was orthogonal to the flow direction. However, at the edges the light path was at an angle through the channel. Light travelling along the path e-d-c in Figure 3.8 propagated directly across the channel so the measurements were directly width averaged. Light travelling along the path a-b-c or g-f-c travelled across the channel at an angle, meaning rather than the density being width-averaged it was averaged along this path. This was most extreme at the edges of the viewing windows and had largest implications at the front of the current where a sharp interface between ambient and current fluid occurred.

When measuring the front speed of the current this introduced errors of up to 2 %. However, the calibration allows for different light path lengths so parallax did not introduce errors to the calibration.

Length Scales

There were errors associated with using rulers to generate length scales and determine viewing window locations. Measurements used to relate pixel locations to distances from the gate involved reading rulers to the nearest millimetre. This introduced errors of $\pm 0.5mm$ in spatial co-ordinates. Fluid depth was also determined using rulers, which were read to the nearest millimetre. Therefore, fluid depths had an accuracy of $\pm 0.5mm$.

Lighting system

The intensity of light measured by the cameras temporally fluctuated as shown in Figure 3.5. The fluctuations were caused by a combination of variability in the lights and camera noise and were found to have a root mean square error of 0.3 %. The variations were random so, where appropriate, time averaging was used to minimise these effects. Any spatial variability in the lighting system was removed by the calibration process.

Density Samples

Densities of fluid samples were measured with an Anton Parr density meter. This was accurate to $\pm 5 \times 10^{-2}$ kg/m^3. Furthermore, densities were measured based on individual samples collected and there may have been slight heterogeneities in the fluid domain being sampled. As solutions were well mixed prior to being added to the channel the samples were assumed to be representative.

3.4 Particle Tracking Velocimetry

3.4.1 Introduction

To understand the mechanics of gravity currents, knowing the fluid velocities within the current and ambient fluid was important. Therefore, the *particle tracking velocimetry* (PTV) technique was employed to measure velocity fields along the centreline of the channel. This technique

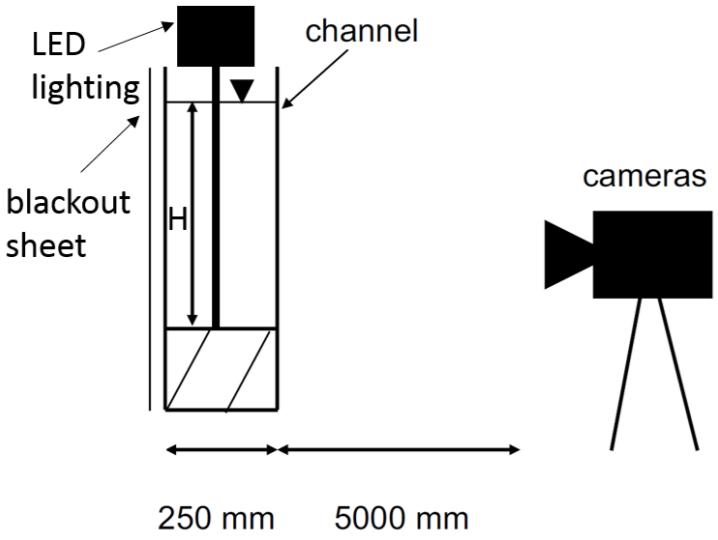

Fig. 3.9 Schematic for PTV experiments. Not to scale.

allowed for measurement of temporally and spatially resolved two-dimensional centreline velocity measurements within a vertical plane.

Similar to LA, PTV is a non-intrusive method of measuring fluid properties. The theory behind PTV is that by seeding the fluid with small particles that stay suspended in, and move with, the fluid, velocities can be measured by tracking the paths of these particles. Particles are tracked frame by frame and velocities are calculated from particle displacements with known time steps.

3.4.2 Experimental Setup

The PTV experiments were conducted in the channel described in Sections 3.2 and 3.3. The cameras were arranged as described in Section 3.2 with rulers being employed to generate length scales and accurate camera locations. Viewing windows were present in the same locations as the LA experiments and the distance between the cameras and the channel was similarly maximised. Instead of lighting from behind the channel this method employed lighting from above, illuminating a 10 mm slot along the centre as illustrated in Figure 3.9.

The lighting comprised a linear array of individual *light emitting diode* (LED) lights that were each mounted in their own reflective lens. This ensured that the light was focused into beams with small divergence angles. These beams were then guided by a pair of parallel plates (painted matt black and 5 mm apart) to produce a relatively parallel sheet of light of approximate uniform intensity along its length. Three such light boxes were used along the length of the channel. The

first of these was 1.5 m long and contained white LED lights. The other two were 800 mm long and contained green LED lights. As the lights were used to indicate the presence of, and track locations of, the particles but not to understand the properties of the particles the colour of the lights was unimportant. The back of the channel was blackened to provide a dark background for the particles.

The particles used to seed the flow were *pliolite resin*. Pliolite resin is a white material used in rubber manufacturing (McBryde, 2008; Nokes, 2017; Thomas et al., 2003) and has a density approximately 3% greater than fresh water. It can be ground into particles with diameters ranging from a few microns to thousands of microns.

In order to be used as tracers the particles had to be small enough to rapidly respond to fluid movement but large enough that they could be easily identified by their reflected light. Raffel et al. (1998) determined a crude approximation for the time to respond to flow movements given by

$$\tau_s = \frac{d_t^2 \rho_t}{18\mu} \tag{3.5}$$

where τ_s is the response time of tracer particles to fluid movements, d_t and ρ_t are the diameter and density of tracer particles and μ is the fluid dynamic viscosity.

In order to accurately measure flow velocities the response time has to be significantly smaller than the shortest time scale of the flow features of interest. Therefore, the response time puts a limit on the smallest eddies that can be captured as smaller eddies are associated with shorter timescales. In reality, the frame-rate of the camera already provides a constraint on the shortest timescales that can be captured and hence if particles are selected such that their response times are shorter than the frame-rate of the camera the response time is unimportant. Crushed pliolite particles were sieved and those of diameter $180 - 250$ μm were used for the present study. These were large enough to be easily visualised and by Equation 3.5 they had response times smaller than the frame rate of the cameras (of the order of 10^{-3} s).

The other issue that must be considered for particles is their fall velocity. Large fall velocities not only cause the resulting velocity fields to falsely indicate the presence of negative vertical

velocities but also cause a loss of particle coverage at the top of the domain. Settling of spherical particles in stationary fluid is often approximated by *Stokes law* and this is given by

$$v_s = \frac{g\left(\rho_t - \rho_1\right){d_t}^2}{18\mu} \tag{3.6}$$

where v_s is the fall velocity of the particle. For pliolite particles of diameter $180-250$ μm Equation 3.6 gives fall velocities of between 0.5 and 1 mm/s. This velocity would be inappropriate for typical experiments because experiments with fluid depths of 100 mm can last for up to 1 minute and these velocities imply that more than half of the particles would have fallen to the bottom of the channel in this time. However, by seeding stationary fluid with particles and observing them falling for large times their actual fall velocities were seen to be much smaller than that found from Equation 3.6. The discrepancy between Stokes law and reality may indicate the presence of trapped air bubbles on the surface of particles and these may have caused the particles to stay suspended longer than expected. Particles were observed over a period of greater than one hour and in this time settled by less than ten millimetres. Therefore, settling speeds were assumed to be negligible.

Due to surface tension effects, small particles can be difficult to mix into large bodies of water without them clumping together. To circumvent this problem the particles were added to a small quantity of water mixed with surfactant. They were then mixed until all particles appeared to be fully wetted before the solution was transferred to the channel.

3.4.3 Particle Tracking Velocimetry Experimental Process

The following procedure was followed for a typical experiment.

1. Water was filtered and left to sit in tanks for at least 24 hours to de-aerate and ensure it was at the room temperature.

2. A 4 g/L NaCl solution was mixed with filtered, de-aerated water in a 450 L tank using a submersible pump for an hour then left to sit for at least another hour before beginning experiments.

3. In a separate 450 L tank denatured alcohol was mixed with filtered water at a concentration of 14.7 mL/L and this was mixed for an hour with a submersible pump then left for an hour to settle.

4. A small drop of surfactant was added to a 100 mL sample of filtered water. Particles, as outlined in the previous section, were added to this sample. The total number of particles was chosen such that 1,000 to 2,000 were visible in each viewing window. These were mixed until the particles were evenly distributed throughout the sample.

5. The lights atop the channel were switched on.

6. Rulers were laid along the centre of the channel and images were taken from each camera so that viewing windows could be stitched together and spatial co-ordinates could be calibrated with the camera pixel densities.

7. Using submersible pumps the previously prepared denatured alcohol solution was transferred to the ambient section of the channel and the NaCl solution was transferred to the lock section. Fluid was added slowly, ensuring that fluid levels remained approximately equal on either side of the gate.

8. 80 mL of the particle solution was evenly mixed through the ambient fluid and the remaining solution was mixed through the lock fluid.

9. Samples of fluid on either side of the gate were collected and the densities of these were measured with the Anton Parr density meter.

10. A ruler was used to measure the fluid depth.

11. The fluid was left to sit for at least 10 minutes to allow for any background motion to reduce to an acceptable level.

12. The cameras were set to begin capturing 3000 images. The ceiling lights in the dark room were switched on before capturing these images and they were switched off immediately after setting the cameras to record. The frame when the lights were switched off was used to synchronise the starting time of the cameras.

13. Once the ceiling lights were switched off the gate was removed vertically to enable the experiment to begin.

14. At the conclusion of the experiment the fluid in the channel was drained and the channel was rinsed to remove any remaining NaCl, denatured alcohol and pliolite particles.

15. All images were transferred to hard drives and were processed using the in-house software *Streams* (Nokes, 2017).

3.4.4 Processing

Once an experiment was complete, the captured images were processed to produce velocity fields. This process involved three steps - *particle identification*,*particle tracking* and *velocity field generation*.

Particles were identified for each frame by using an algorithm that searched images for pixels with intensities greater than a specified threshold. Green light intensity was used to test for exceedance of a specified threshold. Using green light intensity was particularly appropriate for the green light sheets but worked equally well for the white light sheet. Thresholds were selected individually for each camera by visual inspection. These thresholds were selected to ensure 1000-2000 particles were identified in each frame. Light reflections were present at the free surface and base of the channel and particles were removed in these regions. Once particles had been identified for each frame *particles records* were generated. These particle records consisted of lists of particles present in each frame.

Once a particle record had been generated the next step was to undertake particle tracking. The purpose of particle tracking was to match particles in one frame to those in the next. In order to match particle between frames a cost was assigned for each match between a particle in one frame and a particle in the following frame. The algorithm for determining particle matches searched for the lowest total matching cost. A number of different strategies are available within the software Streams and these strategies are outlined in Nokes (2017). The strategy used in the present study is outlined in Appendix A.

With particle tracking complete, velocity fields were generated. To generate these, first velocities were calculated for each particle with matches in the previous and following frames. Velocities were calculated using a second order finite difference approximation where time steps were considered small enough that velocities could be assumed linear with displacement. This generated velocities at individual particles distributed throughout the domain. These particle-

based velocities were interpolated onto a uniform, rectangular grid with a spacing of 4 mm in the x direction and 2 mm in the y direction. An interpolation technique based on *Delaunay triangulation* was used. See Nokes (2017) for further details.

3.4.5 Errors and Limitations

As with LA there were a number of errors inherent in the PTV analysis. What follows in an analysis of these errors and their impact on the results.

Errors Shared with LA

As both LA and PTV experiments used the same channel and camera set up several errors were common to both. The errors that are common to both techniques are summarised here while a full discussion can be found in Section 3.3.6.

- Times of different cameras were synchronised via a single frame inducing timing errors of ± 0.022s.
- The parallax errors present in the LA experiments were also present in the PTV experiments.
- There were errors associated with using rulers to generate length scales and determine viewing window locations.
- Samples of density were measured to an accuracy of 5×10^{-2} kg/m^3.

Particle Size and Properties

As discussed in Section 3.4.2 the pliolite particles had densities slightly larger than that of water and hence, some settling occurred. Over a period of an hour this settling was seen to be less than 10 mm. Therefore, all experiments were conducted within 30 minutes of seeding the fluid to ensure significant settling did not occur prior to their start.

As previously discussed the particles seeded in the flow had response times, τ_s, which represented the time for the particles to respond to fluid motion. These were found to be up to 10^{-3} s. As the response time was small compared to the frame rate of the camera errors were considered to be unimportant.

Particle Identification and Processing

Particle locations are typically accurate to 0.25 of a pixel. Typically length scales were calculated as being 0.33mm/pix, therefore particle locations were accurate to ± 0.08 mm. This introduced small errors in velocity gradients. In addition, if intensity thresholds were set too high an insufficient quantity of particles would be identified, leading to a reduced coverage of particles. Resolution of flow gradients is dependent on the number of particles utilised to generate velocity fields. Intensity thresholds were carefully adjusted and particle records were identified to ensure enough particles were present for good coverage. However, particle coverage could not be large enough to resolve flow gradients of small scale behaviour. Thus, the velocity fields were predominantly used to understand bulk fluid motion.

Errors would also be introduced by faulty matching in the particle tracking stage. These were reduced through careful visual inspection and by thoughtfully considering the costing strategies used.

Ambient Motion

Ambient motion was generated in the channel during filling and was also present during the experiments. For this motion to decay the fluid was left undisturbed for 10 minutes before the gate was removed. Despite leaving the ambient motion to decay some motion was still present and this motion impacted the velocities. The maximum velocities of the ambient motion were at worst 4 % of the current speed.

3.5 Experimental Programme

3.5.1 Overview

Two sets of experiments were carried out based on the research gaps identified in Chapter 2. The first involved exploring the impact of roughness on developed, smooth bed gravity currents and how currents which had encountered roughness re-emerged to travel over smooth beds. These experiments employed roughness consisting of arrays of vertical circular cylinders similar to those used by Cenedese et al. (2016). These experiments were followed by an investigation into the interaction between gravity currents and beds of closely-packed solid spheres.

Except where mentioned, all of the experiments were conducted twice using both PTV and LA techniques. The nominal density difference between the lock and ambient fluid, $\Delta\rho$, was held constant throughout the experiments. In all sets of experiments the total depth of fluid was varied along with properties of the roughness.

3.5.2 Smooth-bed Gravity Currents Encountering Vertical Cylinders

The first set of experiments involved investigating the impact of rough boundaries on developed, smooth bed gravity currents. The first 1200 mm of the false floor was left without roughness and the bolt holes in the false floor were taped to ensure they did not interfere with the current dynamics. The following 1200 mm contained roughness consisting of plastic cylinders screwed into the base of the channel. The final 600 mm was without roughness. The cylinder height, η_c, was held constant at 50 mm and the cylinder diameter, d_c, was held constant at 20 mm.

To better identify how the currents emerged from the roughness, and to provide a better comparison with the experiments of Cenedese et al. (2016), additional experiments were conducted with the roughness beginning at the location of the lock gate and with the same roughness properties. As multiple cameras were used to capture the currents over a larger area these experiments were able to capture the transient interactions between the currents and the roughness where the experiments of Cenedese et al. (2016) were not. The roughness in these experiments was present for 1200 mm before the remainder of the false floor was without roughness. These experiments were conducted only once, using the LA technique.

The cylinders were arranged in 3 different configurations as displayed in Figure 3.10. The first of these, as seen in the right hand panel, was termed the *sparse configuration*. This configuration consisted of staggered arrays of cylinders with centre-centre distances of 64 mm. The second was termed the *dense configuration*. For this configuration the roughness elements were arranged in an identical way to the sparse case but with centre-centre spacings reduced to 32 mm. These can be seen in the centre panel of Figure 3.10. The sparse and dense configurations are similar to those utilised by Cenedese et al. (2016). Finally, the experiments termed plunging featured in-line cylinders with 32 mm spacing across the channel and 128 mm centre-centre spacing in the direction of flow. These can be seen in the left-most panel in Figure 3.10 and are similar to those in the *plunging regime* seen by Zhou et al. (2017). The total depth of fluid for all cylinder arrangements was varied from 100 mm, 150 mm, 200 mm to 270 mm. These

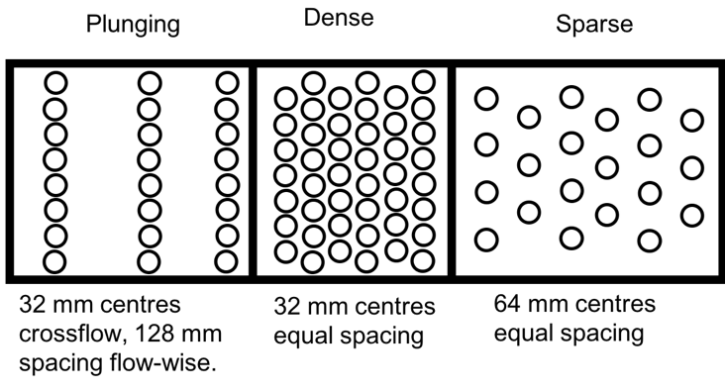

Fig. 3.10 Panels showing from left to right: Plunging, Dense and Sparse cylinder arrangements. Not to scale.

experiments were labelled XYHxx where X represents cylinder regime - S for sparse, D for dense and P for plunging, Y represents cylinder height in cm (for all experiments this was 5) and xx represents water depth in cm. For example, a experiment with a sparse array of 50 mm high cylinders and 150 mm total water depth would be named S5H15. The experiments with the roughness beginning at the location of the lock gate were only carried out with the dense and sparse configuration roughness. To differentiate these experiments from those with the roughness beginning downstream of the gate a G was appended to the names of those experiments beginning at the gate. Initial, quantitative results from these experiments can be found in Chapter 4 before detailed results for the three roughness configurations can be found in Chapters 5, 6 and 7.

3.5.3 Interactions with Beds of Solid Spheres

For the second set of experiments the false floor in the ambient section was covered by a closely packed bed of mono-disperse solid spheres. The glass spheres were of diameter, $d_p = 10$ mm and were set in a *hexagonal close pack* (HCP) arrangement, allowing the spheres to be packed as densely as possible. For two layers of spheres this arrangement is shown in Figure 3.11. The spheres had a very different refractive index to water so flow properties could not be visualised within the bed. All analysis was, therefore, carried out on the current above the spheres.

The spheres were pressed against the gate with a strip of double sided tape on the base of the channel utilised to ensure they did not break structure when the gate opened. At the downstream end a block of perspex with the same width as the channel and a depth slightly larger than the

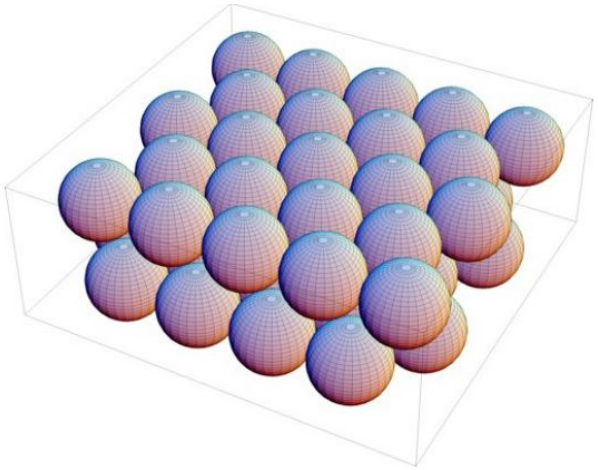

Fig. 3.11 Representation of hexagonal closed packing, reproduced from Jacobson (2007).

false floor was placed to stop the spheres breaking structure and rolling off the end of the false floor.

The total depth (including the roughness) was varied between 100 mm, 150 mm, 200 mm and 270 mm. The number of sphere layers, N_l, was varied between 1, 2 and 3. The total height of the roughness with 1, 2 and 3 rows of spheres was 10 mm, 18 mm and 26 mm respectively. The experiments were labelled LXHYY where X is the number of sphere layers (1, 2 or 3) and YY is total depth in cm. Thus, 100mm deep experiment with 2 layers of spheres would be labelled L2H10. If experiments were repeated then a numerical subscript was used to distinguish between experiments. The results of this investigation can be found in Chapter 8.

3.6 Experimental Analysis

All experimental results were non-dimensionalised, as introduced in Equations 2.12, 2.13, 2.14 and 2.15. While a number of different methods could have been used to non-dimensionalise the data, this method was chosen because it aligns with most recent studies. Additionally, this method ensures that current properties are related to the fluid depth which has been shown to be important in understanding current behaviour (see Chapter 2).

A small region of data was frequently trimmed at the top and bottom of the domain due to obstructions to visualisation and light reflections off both the boundary and the free surface. Therefore, the velocity and density fields were extrapolated to fill these gaps. It is known from the no-slip condition that velocity fields should be zero at the bottom boundary so a second order

polynomial was used to interpolate between this and the known velocities above the boundary. At the top boundary, it is known from Britter and Simpson (1978) that bottom gravity currents have a relatively uniform velocity near the free surface so it was assumed that the velocity was constant between the measured velocities and the surface.

For the density measurements, it was known that at the top boundary, well above the current, the density was zero. Thus, any missing data at the top of the domain was assigned a density of zero. At the bottom of the domain the density was not known; however both upstream and downstream of the nose the density should be constant close to the boundary according to the model of Britter and Simpson (1978). Therefore, the density at the boundary was assumed to be constant between the boundary and measured densities. The extrapolation caused slight errors at, and around, the current nose where the density was not constant near the bed due to the over-running of light fluid; however there was never more than a very small region involved so the impact of this process would be minimal.

In the following chapters the density and height of the current will commonly be analysed using the buoyant height defined as

$$h_B(x,t) = \int_0^1 \rho dy \tag{3.7}$$

This was introduced by Shin et al. (2004) and is commonly used in the analysis of gravity currents. This height is indicative of the buoyant driving force within the current, depending on both the density within the current and the vertical extent of the current. The vertical extent alone will be isolated by the current envelope, h_c, calculated as the maximum height where the density is larger than 0.05, or

$$h_c(x,t) = max\{y : \rho > 0.05\} \tag{3.8}$$

The main parameter used to distinguish between different experiments with the same roughness configuration is the *relative roughness height*. This parameter is calculated as the ratio of the height of the roughness to the total fluid depth, defined as

$$\sigma = \frac{\eta}{H} \tag{3.9}$$

3.7 Summary

This chapter described the experimental programme carried out to explore how gravity currents interact with rough boundaries. Section 3.2 introduced the channel and set up used for the experimentation. It described the lock exchange system used for generating the currents and the cameras used for capturing data. Sections 3.3 and 3.4 outlined the LA and PTV techniques employed to measure density and velocity fields respectively. They included a detailed description of experimental procedures as well as a discussion of the limitations of these techniques. Finally, Sections 3.5 and 3.6 outlined the experimental programme and some of the experimental processing. The following chapters will explore results from these experiments.

Chapter 4: Qualitative Observations of Transitions from Smooth to Rough Boundaries

4.1 Introduction

This chapter provides initial results from the investigation into developed, smooth-bed gravity currents suddenly encountering fields of roughness consisting of vertical circular cylinders. A qualitative overview of the results is presented, discussing how the currents travelled through the roughness and how the roughness impacted their shape and structure. Additionally, this chapter explores the development of currents as they emerged from fields of roughness. The following chapters will then provide more in-depth and quantitative results. Tables 4.1 and 4.2, respectively, show the full list of experiments where the roughness was placed downstream of the gate carried out using the LA and PTV techniques respectively. Table 4.3 provides the full list of LA experiments carried out with the roughness beginning at the location of the lock gate. The experiments described in Table 4.3 were only carried out using LA and not PTV.

4.2 Experimental Analysis

For the experiments with the roughness downstream of the lock gate the origin of space was redefined such that an x location of 0 corresponds to the front face of the first row of roughness. Subsequently the origin of time was redefined such that it corresponds to the first time where the buoyant height at x=0 had a value of greater than or equal to 0.02. For the experiments where the roughness began at the lock gate the origin corresponds to the location of the gate and t=0 corresponds to the time at which the gate was opened.

Table 4.1 Transition experiments carried out using light attenuation.

Name	Configuration	η_c (m)	H (m)	$\Delta\rho$ (kg/m^3)	g' (m/s^2)	u_B (m/s)	Re_B	σ
S5H10	Sparse	0.05	0.104	5.61	0.0549	0.08	7859	0.481
S5H15	Sparse	0.05	0.154	5.62	0.0550	0.09	14173	0.325
S5H20	Sparse	0.05	0.202	5.59	0.0548	0.11	21251	0.248
S5H27	Sparse	0.05	0.278	5.59	0.0548	0.12	34302	0.180
D5H10	Dense	0.05	0.104	4.93	0.0483	0.07	7373	0.481
D5H15	Dense	0.05	0.15	5.16	0.0505	0.09	13061	0.333
D5H20	Dense	0.05	0.2	5.31	0.0519	0.10	20398	0.25
D5H27	Dense	0.05	0.27	5.62	0.0551	0.12	32924	0.158
P5H10	Plunging	0.05	0.1	4.80	0.0470	0.07	6857	0.5
P5H15	Plunging	0.05	0.154	5.76	0.0564	0.09	14355	0.325
P5H20	Plunging	0.05	0.204	5.59	0.0548	0.11	21561	0.245
P5H27	Plunging	0.05	0.274	5.73	0.0561	0.12	33980	0.182

Table 4.2 Transition experiments carried out using particle tracking velocimetry.

Name	Configuration	η_c (m)	H (m)	$\Delta\rho$ (kg/m^3)	g' (m/s^2)	u_B (m/s)	Re_B	σ
S5H10	Sparse	0.05	0.1	5.52	0.0541	0.07	7353	0.500
S5H15	Sparse	0.05	0.15	5.30	0.0519	0.09	13237	0.333
S5H20	Sparse	0.05	0.2	5.40	0.0529	0.10	20571	0.250
S5H27	Sparse	0.05	0.274	5.36	0.0525	0.12	32865	0.182
D5H10	Dense	0.05	0.102	5.37	0.0526	0.07	7471	0.490
D5H15	Dense	0.05	0.152	5.49	0.0538	0.09	13743	0.329
D5H20	Dense	0.05	0.202	5.35	0.0524	0.10	20784	0.248
D5H27	Dense	0.05	0.274	5.42	0.0531	0.12	33048	182
P5H10	Plunging	0.05	0.1	5.43	0.0532	0.07	7293	0.500
P5H15	Plunging	0.05	0.154	5.54	0.0543	0.09	14078	0.325
P5H20	Plunging	0.05	0.204	5.30	0.0519	0.10	20993	0.245
P5H27	Plunging	0.05	0.27	5.51	0.0540	0.12	32593	0.185

Table 4.3 Transition experiments with roughness beginning at the gate carried out using light attenuation.

Name	Configuration	η_c (m)	H (m)	$\Delta\rho$ kg/m^3	g' (m/s^2)	u_B (m/s)	Re_B	σ
S5H10G	Sparse	0.05	0.102	5.03	0.049	0.071	7234	0.490
S5H15G	Sparse	0.05	0.15	5.08	0.050	0.086	12974	0.333
S5H20G	Sparse	0.05	0.201	4.60	0.045	0.095	19139	0.249
S5H27G	Sparse	0.05	0.27	5.08	0.050	0.116	31332	0.185
D5H10G	Dense	0.05	0.106	4.14	0.041	0.066	6954	0.472
D5H15G	Dense	0.05	0.152	4.13	0.040	0.078	11921	0.329
D5H20G	Dense	0.05	0.206	4.19	0.041	0.092	18963	0.243
D5H27G	Dense	0.05	0.27	4.21	0.041	0.106	28529	0.185

4.3 Sparse Configuration

Figure 4.1 shows an instantaneous density field for the experiment S5H20 at 5 different times. In this figure, the series of small, black rectangles along the channel floor correspond to the locations of roughness where flow could not be visualised and the long black rectangle at an approximate location of x = -2 corresponds to the structural element in the channel where flow visualisation was unavailable.

Figure 4.1a shows the current before it had reached the roughness (at a time of t = -2). At this time the current was observed to have fully developed and was in the slumping phase as outlined in Chapter 2. Kelvin-Helmholtz billows were observed in the shear layer between the fluids and these can be seen in the shape of the buoyant height and current envelope. At the front of the current the head was observed to be deeper than the tail behind it and the raised nose was observed at the leading edge. In and just behind the head the density was observed to be slightly lower than in the tail. These were in line with previous observations such as those by Britter and Simpson (1978).

When the current first interacted with the roughness, fluid was deflected upwards and the depth of fluid above the first row of cylinders increased. Alongside this a bore was reflected and propagated backwards from the front face of the roughness. This deepening is seen in Figure 4.1b. The small bore reflected off the roughness is seen travelling towards the lock in Figure 4.1c before the bore reflected off the lock wall encountered it in the following images. The bore that reflected off the roughness will henceforth be referred to as the *roughness bore* to distinguish it from the *lock bore* associated with the lock as it runs out of fluid.

In Figure 4.1b, the current is seen to have entered the roughness and its shape has begun to change. As the current travelled forward through the roughness it gradually transitioned from having a typical smooth bed gravity current structure to a wedge-like shape. This shape lost its well defined head and the location of maximum height (both h_c and h_B) occurred at the upstream end of the roughness. This is visible in the current shape in Figures 4.1b, c and d..

The wedge shape is similar to that observed by Tanino et al. (2005) in flows with full-depth roughness. They saw currents taking on more of a wedge shape as they transitioned from inertia-dominated to drag-dominated regimes, causing the front of the current to decrease in

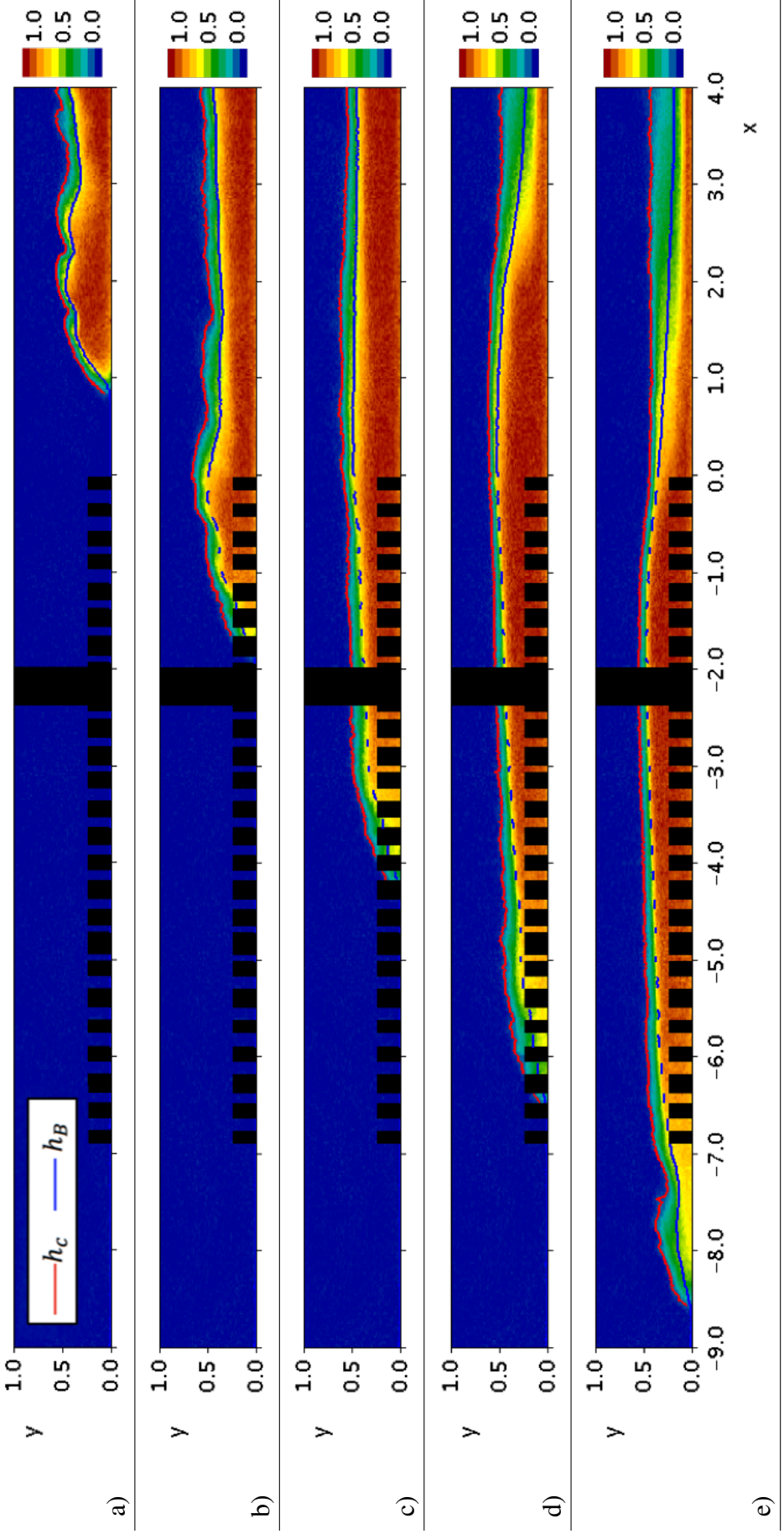

Fig. 4.1 Density field for experiment S5H20 at times of -2, 4, 10, 16 and 22. The red line shows h_c and blue line shows h_B.

height. The final wedge shape of this current as the nose reached the final row of cylinders is similar to that seen by Cenedese et al. (2016).

As the current travelled it was diluted by the ambient fluid. For the purpose of this thesis dilution is defined as any process where ambient fluid mixes with current fluid causing its density to decrease. The dilution can be observed by the false-colour near the front of the current between Figures 4.1b, c and d changing from an orange to yellow to green colour. The dilution, height and shape of the currents are explored further in Chapter 5.

In Figure 4.1e, the current is seen to have exited the roughness and re-established as a smooth-bed current with a typical head-tail structure. However, the length of measurements over which the current re-emerged from the roughness was insufficient to determine how, if at all, it developed with time. Therefore, Figure 4.2 shows an instantaneous density field for the experiment S5H20G at 4 different times. This figure not only allows for qualitative analysis of how the current re-established after emerging from the roughness, it also allows for a qualitative comparison between this experiment and the S5H20 experiment at the end of the roughness.

Figure 4.1d and 4.2a appear qualitatively similar, indicating that by the time the current reached the end of the roughness the structure of the current on entry to the roughness was unimportant. This finding is further examined in Chapter 5. Figures 4.2b, c and d show that as the current re-emerged from the roughness and the typical head and tail structure re-developed, the head grew in vertical extent and the density of fluid in the head increased. The growth of the head upon re-establishment was likely driven by the dense fluid behind the head travelling faster than the front of the current. The model by Sher and Woods (2017) showed that a smooth-bed gravity current reaches steady state because the dilution in the head of the current is balanced by the replenishment of fluid into the head by faster moving dense fluid from within the tail. When the current was travelling through the roughness the head fluid diluted faster than it could be replenished by the fluid in the tail due to either increased dilution in the head or a reduction in the speed of the tail fluid (or both). However, once the current exited the roughness, the replenishment of fluid from the tail was greater than the head dilution. The re-establishment of sparse configuration currents is further examined in Chapter 5.

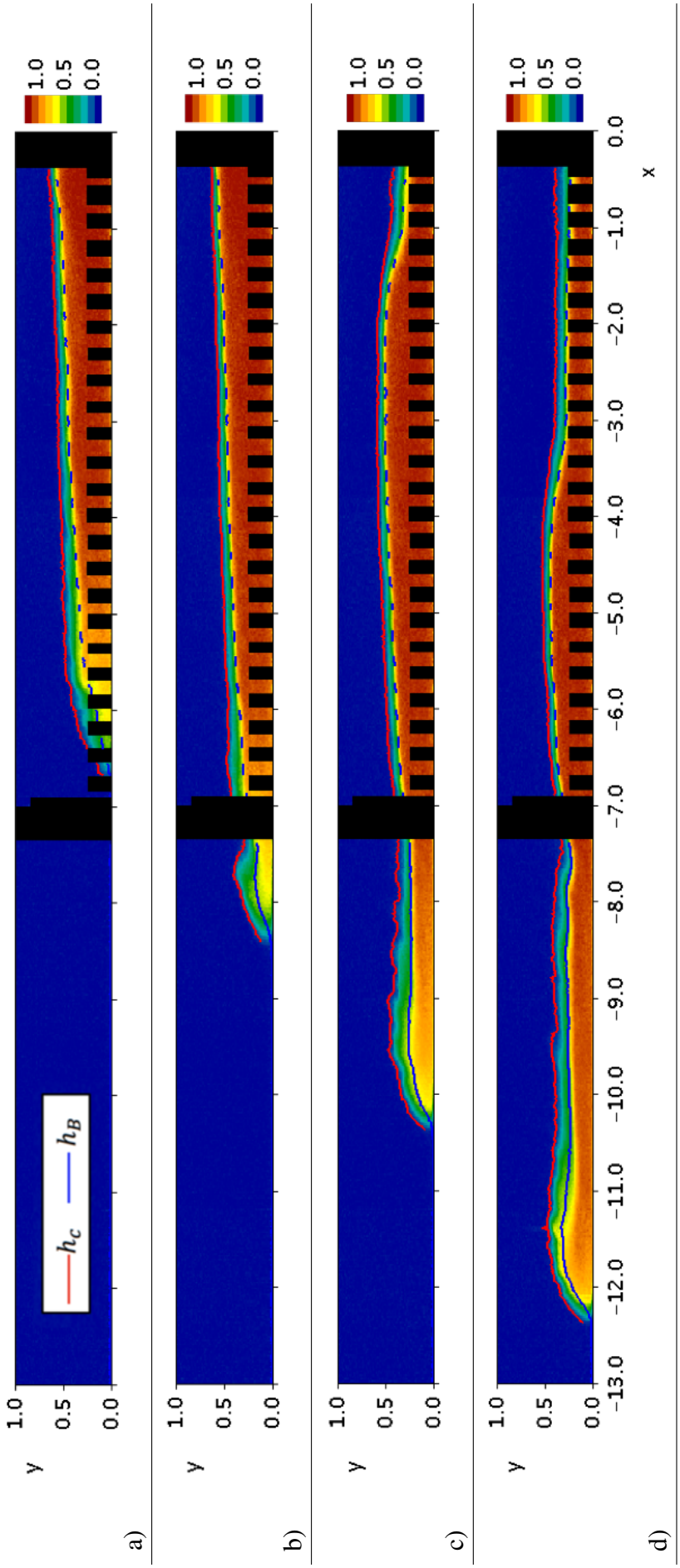

Fig. 4.2 Instantaneous density field for S5H20 experiment at times of 16, 21, 26 and 31. The red line shows h_c and blue line shows h_B.

Figure 4.3 shows density fields for the sparse experiments S5H10, S5H15, S5H20 and S5H27 as the currents reached the final row of cylinders. This figure shows the interface transitioning from an almost linear wedge shape towards a more typical smooth-bed gravity current shape as the relative roughness height decreased. This trend implies that as the relative roughness height decreased the currents transitioned from a drag-dominated regime, which Tanino et al. (2005) predicted to have a linear interface, towards an inertia-dominated regime. However, only in the S5H27 experiment was a clear head and tail structure still apparent when the current reached the end of the roughness. Therefore, for all other experiments the drag forces appeared to be dominant.

Figure 4.3 also displays a transition from emergent to submerged roughness elements. When the water depth was low (particularly in the S5H10 experiment) the roughness was completely emergent and the current was comparable to those analysed by Tanino et al. (2005). As the relative roughness height decreased the roughness became submerged across a longer length with only the current fluid near the nose being shallower than the roughness.

4.4 Dense Configuration

Figure 4.4 shows an instantaneous density field for the experiment D5H20 at 4 different times. These are in time increments of 10 starting in Figure 4.4a at a time of 2 seconds. In the dense configuration, because gaps between cylinders were smaller than in the sparse configuration, less visualisation was possible. At the edges of the viewing windows parallax effects meant that no flow could be visualised between the cylinders. Thus, long regions without data are visible in Figure 4.4, for example at x=-6.

In Figure 4.4 it can be seen that, similar to the sparse configuration experiments, when the current reached the front face of the roughness a roughness bore was produced. The vertical extent of the bore is seen to be larger for the dense case in Figure 4.4 than the bore generated by the current encountering the sparse configuration roughness. The greater deflection, causing a larger roughness bore, is due to the greater impedance to the flow caused by the increased obstruction. The roughness bore is seen propagating backwards in Figure 4.4b until the lock bore was seen to have encountered it in Figures 4.4c and d.

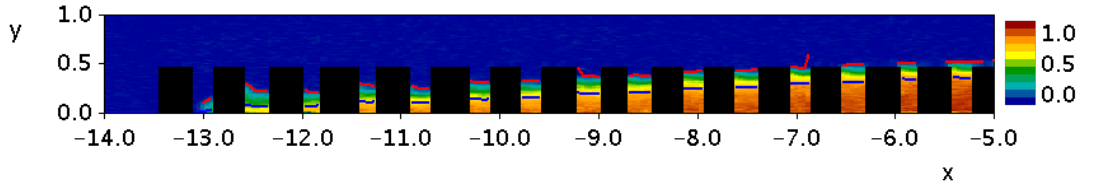

a)

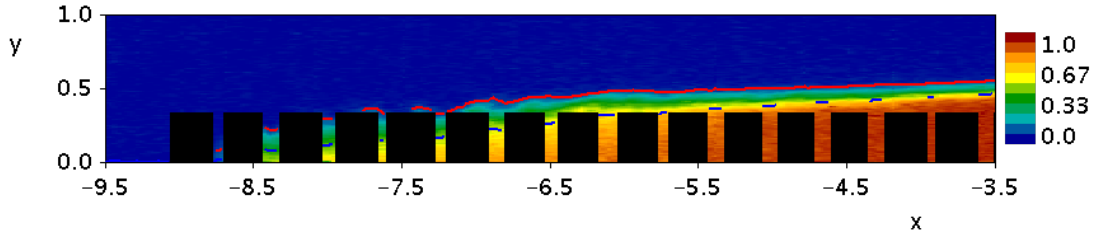

b)

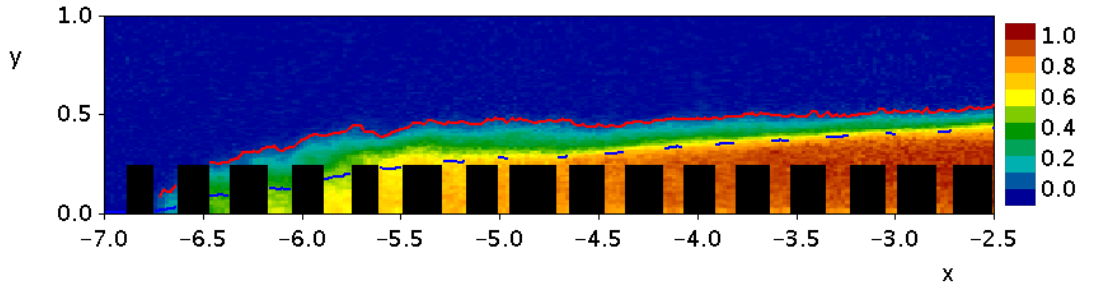

c)

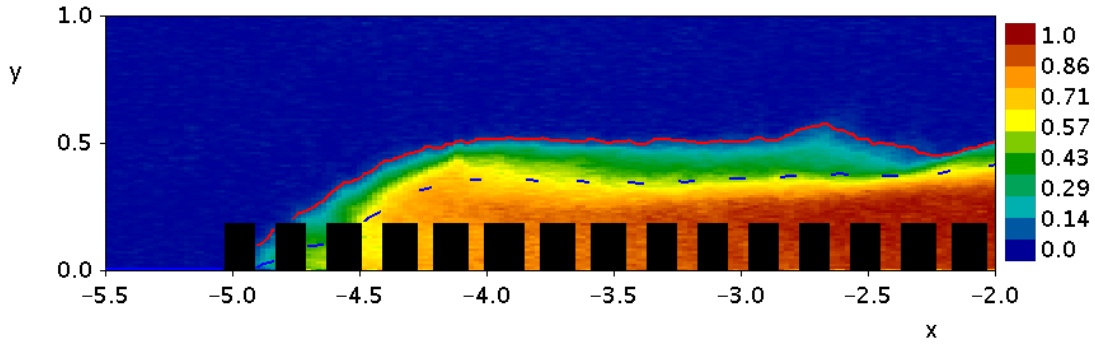

d)

Fig. 4.3 Density fields for experiments a) S5H10, b) S5H15, c) S5H20 and d) S5H27 as currents reached the final row of roughness elements. Red line shows h_c and blue line shows h_B.

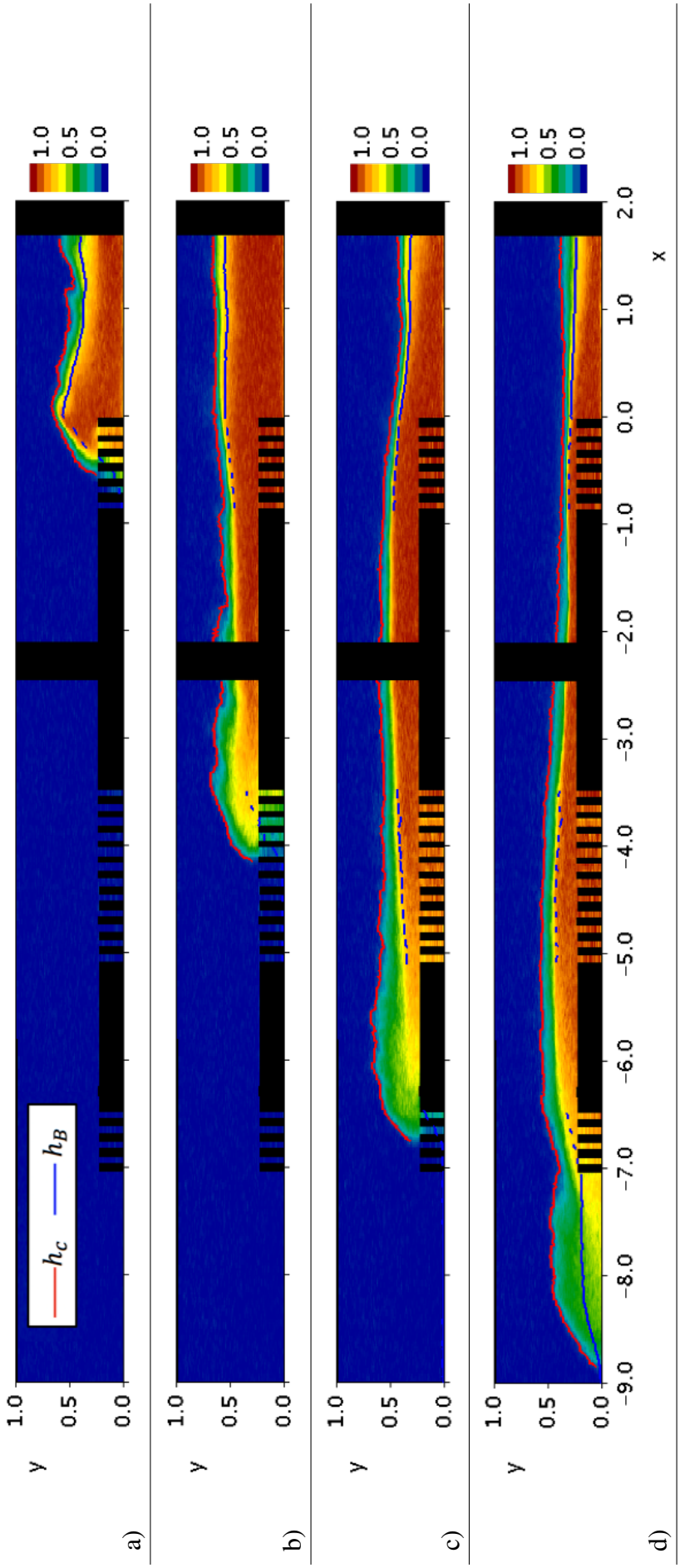

Fig. 4.4 Density field for experiment D5H20 at times of 2, 12, 22 and 32. Red line shows h_c and blue line shows h_B.

When the current initially encountered the roughness field it had two alternative ways to negotiate it. The first was to propagate through the roughness, as the sparse configuration currents did. However, because of the dense nature of the roughness this caused significant losses in energy and momentum due to the form drag on the cylinders. The second option was to be deflected over top of the cylinders. The portion travelling over the cylinders is referred to as *over-flow* and the fluid travelling through the cylinders is referred to as *through-flow*. These terms are used for similar regimes by Cenedese et al. (2016) and Zhou et al. (2017).

Initially the through-flow portion of the current dominated with the leading edge travelling through the roughness because it took time for the over-flowing currents to be deflected upwards and establish atop the cylinders. However, this was quickly retarded by the large form drag imposed by the cylinders and in subsequent images it can be seen that the overflow front rapidly overtook it. Hence, the current transitioned to being in the overflow regime defined by Cenedese et al. (2016). In this regime the main flow was entirely above the cylinders and very little through-flow occurred. The density inversion led to an instability where the current over-ran a reservoir of lighter fluid contained within the bed of cylinders and this caused a convective exchange of fluid between the current and the bed. The instability resulted in dilution in the head of the current in Figure 4.4b and c relative to a smooth-bed current (e.g. Figure 4.1a). Cenedese et al. (2016) assumed the flow was in steady state so did not observe the current diluting as it travelled. The dilution will be discussed further in Chapter 6.

As with the sparse configuration, once the current exited the roughness it re-established as a smooth-bed current and began to grow in size, density and speed. It is observed that the currents in the dense regime were more diluted upon exit of the roughness than in the sparse experiments because of the additional dilution caused by the convective instability. Additionally, when the dense current in the overflow regime exited the roughness the current had to return from propagating above the cylinders to the smooth floor. To re-establish it plunged downwards and in doing so further entrained fluid, as shown in Figure 4.5 where red arrows represent velocity vectors from the PTV experiments. The lack of velocity vectors around x = -8 is because at this location there was a gap in lighting, meaning particles could not be identified.

Similar to Figure 4.1, measurements over which the D5H20 current re-emerged from the roughness were insufficient to determine how, if at all, it developed with time. Therefore, Figure 4.7 shows an instantaneous density field for the experiment D5H20G at 4 different times. This

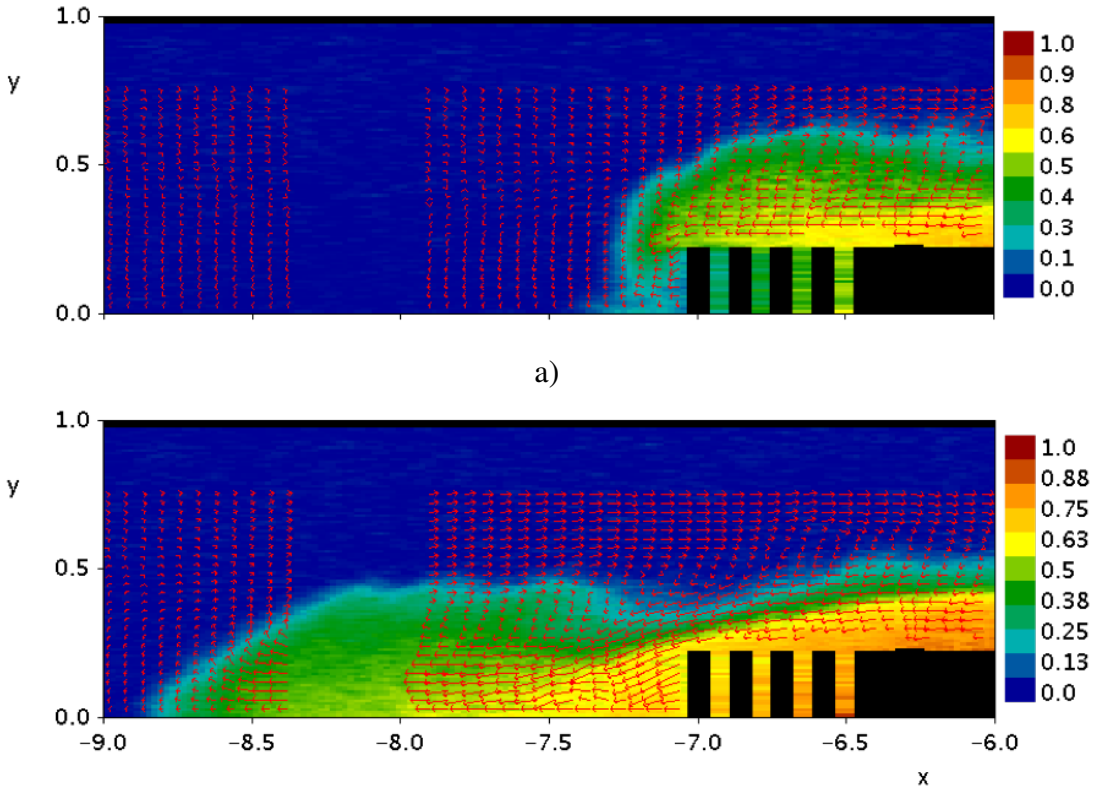

Fig. 4.5 Density field with overlaid velocity vector for D5H20 experiment as a) the current plunges from the overflow regime towards the smooth bed and b) the smooth-bed current re-establishes.

figure not only allows for qualitative analysis of how the current re-established after emerging from the roughness, it also allows for a qualitative comparison between the current that was allowed to develop before encountering the roughness and one where the roughness was present at the lock gate.

Figures 4.4c and 4.7a appear qualitatively similar, indicating that once the current reached the end of the roughness the structure of the current on entry to the roughness was unimportant. This finding is similar to the sparse configuration experiments and is further examined in Chapter 6. Figures 4.7b, c and d show that as the current re-emerged from the roughness the head and tail structure developed above the floor and the density within the head of the current increased. The mechanism by which dense fluid re-entered the head of the current is similar to the S5H20G experiment shown in Figure 4.2. However, the over-flowing current maintained a large head so there was no need to re-establish a head structure after the current moved beyond the roughness field. The re-establishment of dense configuration currents is further examined in Chapter 6.

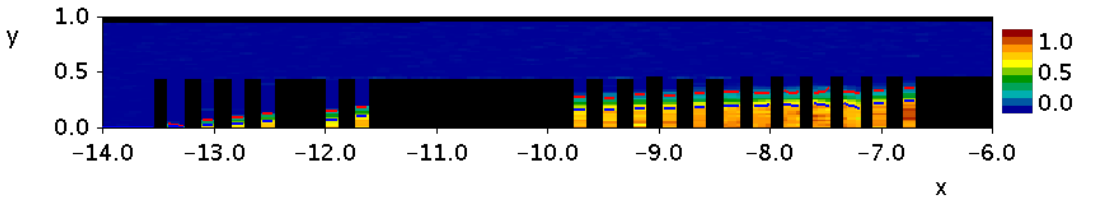

a)

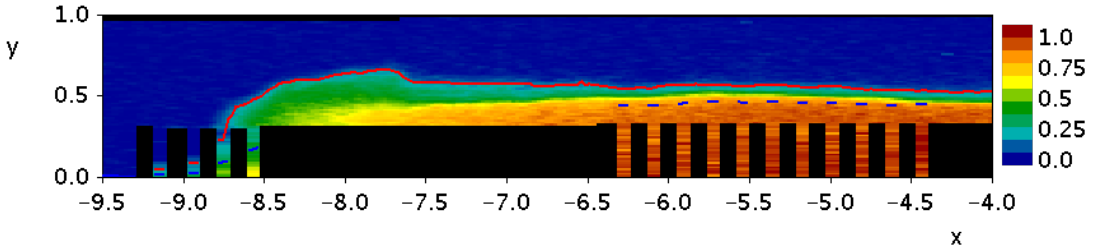

b)

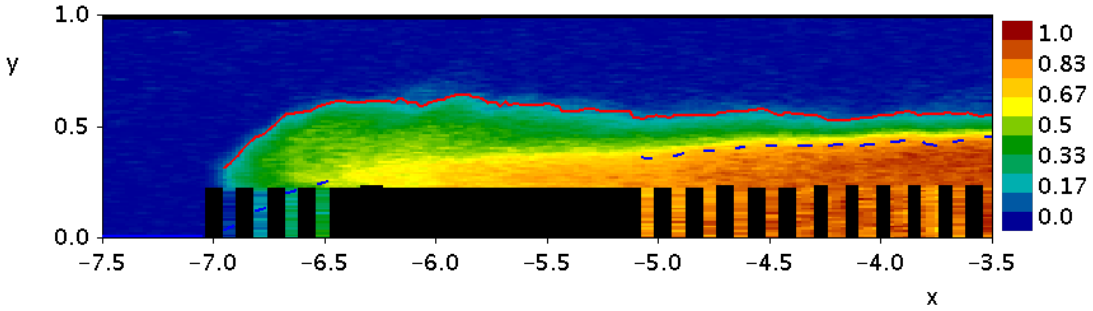

c)

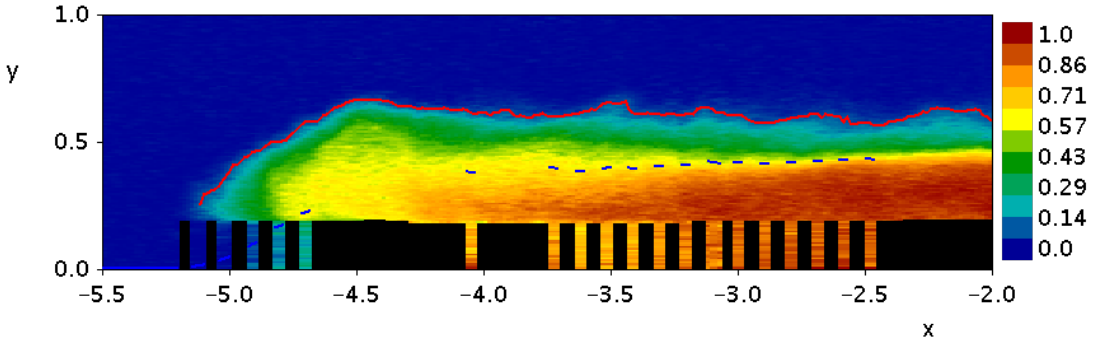

d)

Fig. 4.6 Density fields for experiments a) D5H10, b) D5H15, c) D5H20 and d) D5H27 as currents reached the final roughness element. Red line shows h_c and blue line shows h_B.

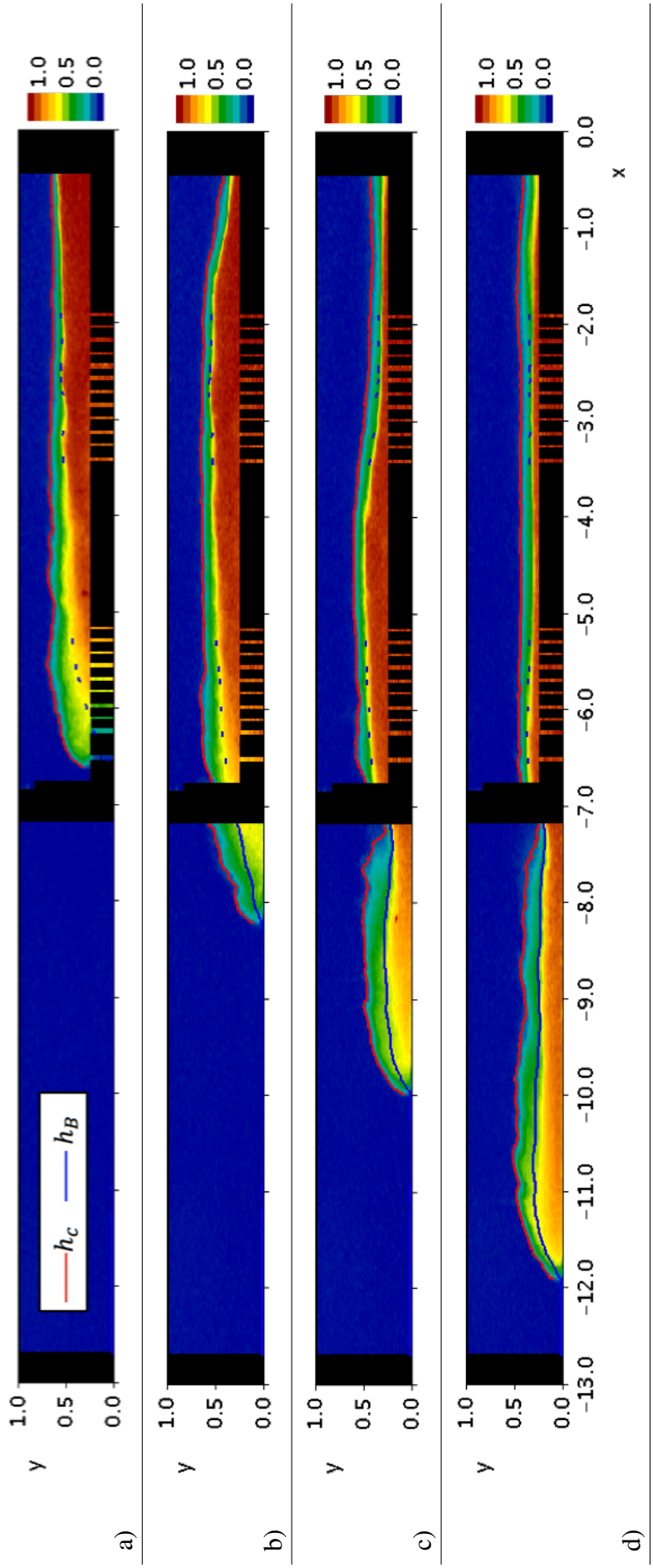

Fig. 4.7 Density field for experiment D5H20G at times of 22, 27, 32 and 37. Red line shows h_c and blue line shows h_B.

Figure 4.6 shows density fields for all of the dense configuration experiments as the currents reached the final row of cylinders. In Figure 4.6, by the time the D5H10 current reached the final row of cylinders the dense current was travelling entirely through the roughness, forming a shape similar to that seen in the S5H10 experiment. As this current was small compared to the size of the roughness it did not have sufficient energy to propagate atop the roughness.

As the fluid depth increased the regime transitioned from a through-flow to over-flow regime. It can be seen in Figure 4.6b that the D5H15 experiment represents a transition between the two regimes. In this experiment the leading nose of the current travelled through the roughness but slightly behind it there was also a head travelling above the roughness in the overflow regime. Figure 4.6 shows the D5H20 and D5H27 experiments being entirely in an overview regime.

4.5 Plunging Configuration

Figure 4.8 shows an instantaneous density field for the experiment P5H20 at 5 different times. These are in time increments of 6 starting in Figure 4.8a at a time of 1. In this configuration, while the overall density of roughness was very close to that for the sparse configuration the distance between rows of cylinders was much larger.

In Figure 4.8a it can be seen that, similar to the D5H20 experiment, the current initially took two separate routes to overcome the obstacles. Some of the fluid travelled through the gaps between the cylinders and some was deflected upwards and over them. Similar to the dense regime, initially the path to travel over the cylinders was longer than the through-flowing path. This meant that the leading edge of the current was the through-flowing fluid with the overflowing fluid travelling behind it. However, unlike in the dense regime, the gaps between cylinders were large enough that instead of the over-flowing fluid staying in an overflowing regime it plunged downwards between the cylinders before being deflected upwards again by the next row. This is equivalent to the plunging regime outlined by Zhou et al. (2017). As with all experiments the current also experienced a deepening atop the first row of cylinders and a bore was reflected backwards from them. The roughness bore can be seen prominently in Figure 4.8b before being interrupted by the lock bore in the following images.

As the fluid plunged over the cylinders a small pocket of lighter fluid just downstream of the cylinders was trapped within the dense fluid. This unstable, trapped fluid had to percolate

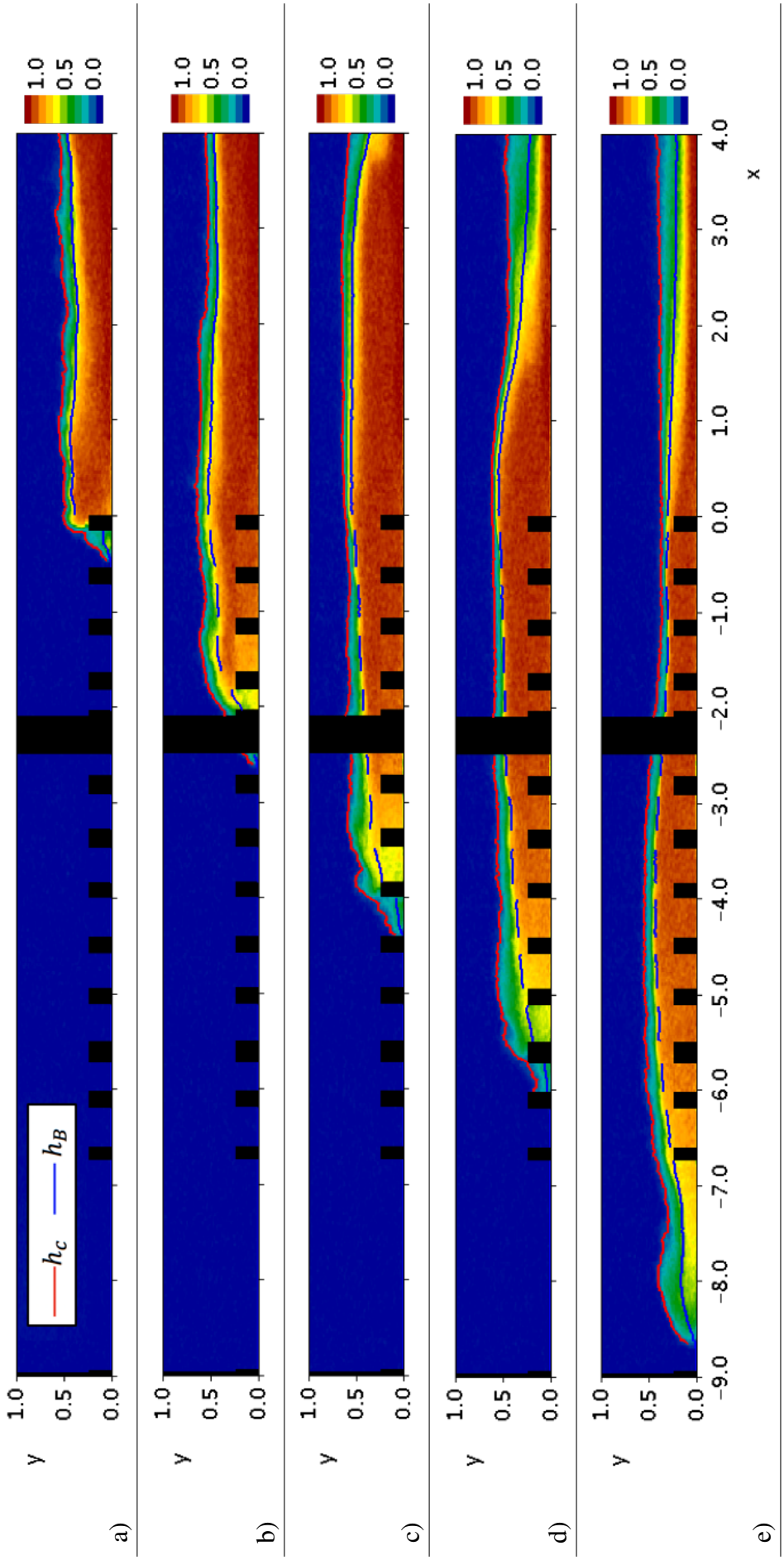

Fig. 4.8 Density field for experiment P5H20 at times of 1, 7, 13, 19 and 25. Red line shows h_c and blue line shows h_B.

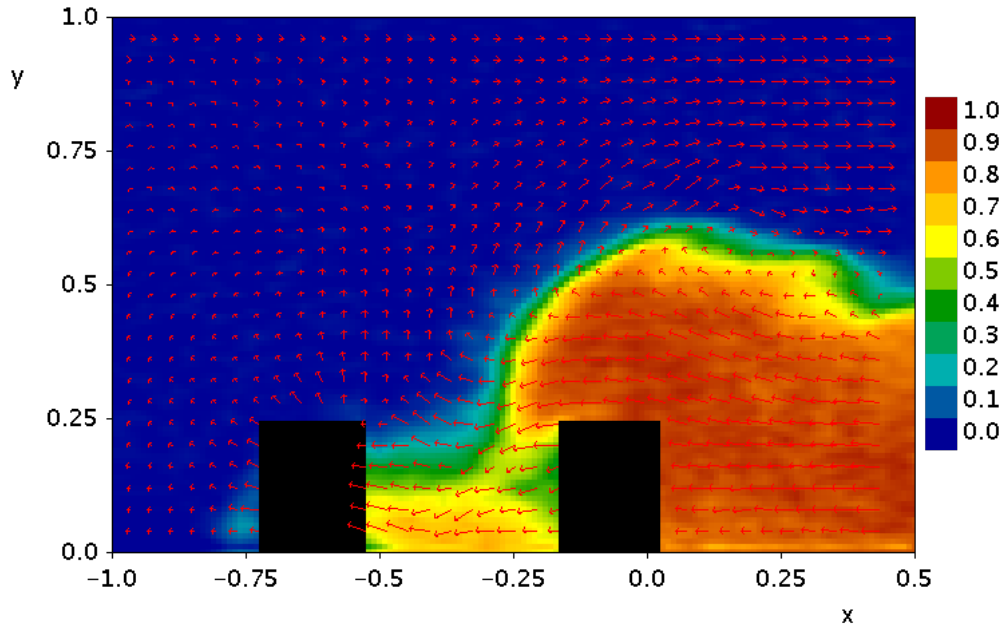

Fig. 4.9 Experiment P5H20 as the current nose reached the second row of roughness where false colour shows fluid density and arrows show velocity vectors. Current fluid is seen plunging over the first row of roughness

upwards through the current causing additional mixing. This trapped fluid is visible in Figure 4.9. This figure displays a false-colour image representing the density of the P5H20 experiment plunging over the first row of cylinders with red arrows showing velocity vectors measured at the centreline. The unstable, trapped fluid is seen as the region of green fluid between the downwards plunging fluid and the right hand row of cylinders. It should be noted that the velocity data was from a separate experiment from the density data and was measured along the centre-line whereas the density field was width averaged. Therefore, rising motion is not seen and only mild plunging characteristics are visible in the velocity field.

In Figures 4.8b, c and d it can be seen that as the current travelled the head fluid continually diluted. The dilution is similar to that seen in the dense and sparse configurations. Additionally, in Figures 4.8c and d it can be seen that the current began to take on a wedge shape similar to the sparse experiment in Figure 4.1 with the angle that the wedge formed with the horizontal similarly decreasing with time. Therefore, it could be postulated that the forces driving the flow were similar between the sparse and plunging configuration experiments. In Figure 4.8e it can be seen that, similar to the dense regime, the fluid plunged over the final obstacle before re-establishing on the smooth bed. The head of this current also increased in density as it travelled after exiting the roughness.

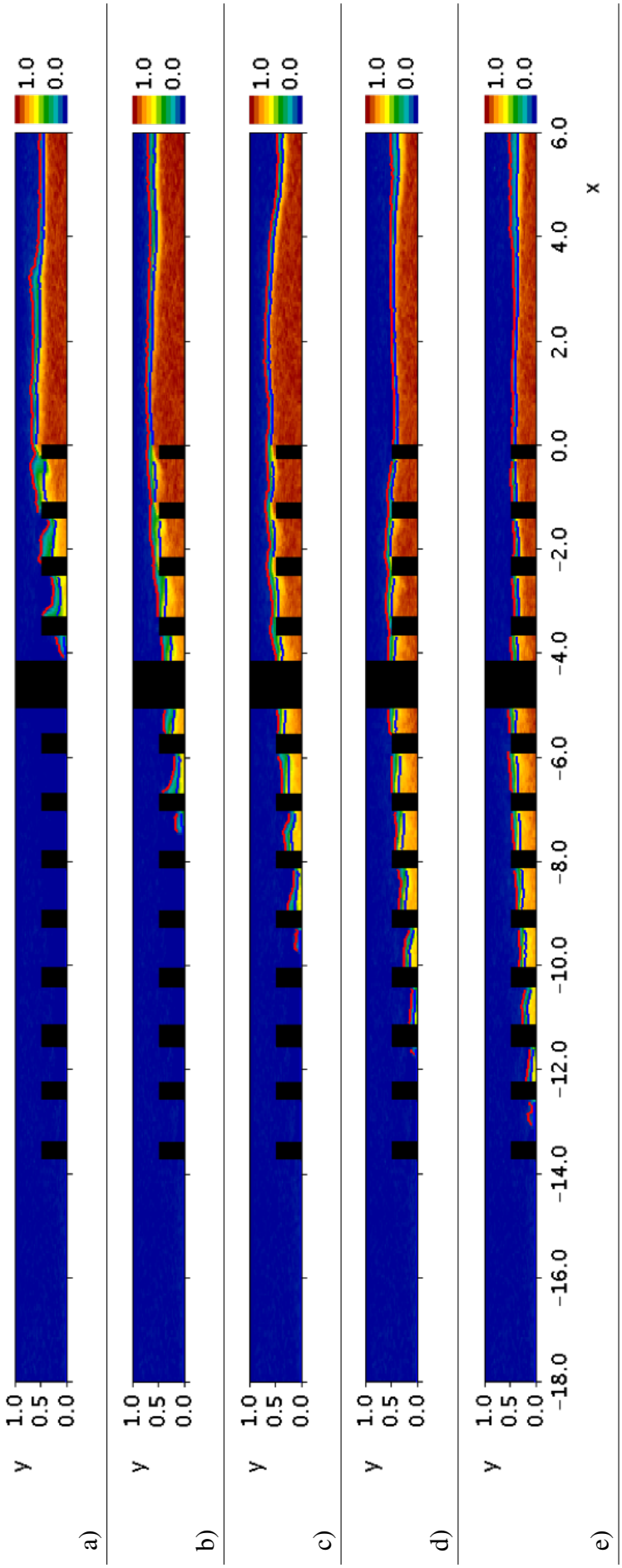

Fig. 4.10 Density field for experiment P5H10 at times of 10, 20, 30, 40 and 50.. Red line shows h_c and blue line shows h_B.

Figure 4.10 shows an instantaneous density field for the experiment P5H10 at 5 different times. These are in increments of 10 starting in Figure 4.10a at a time of 10. As this experiment had a large relative roughness height the fluid did not plunge over the roughness elements, instead it only travelled through them. Similar to the P5H20 experiments the fluid reached individual roughness elements and some fluid propagated through the roughness while other fluid was deflected upwards. However, the fluid deflected upwards did not plunge over the roughness. This meant that for all time the roughness was effectively emergent.

With time the P5H10 current took on a wedge shape where the flow was clearly drag dominated, as seen for D5H10 and S5H10 experiments. However, between individual rows of cylinders the depth often decreased in the upstream direction because of the individual bores. It can be seen that the current continued to dilute and decrease in size until the front was barely visible. The angle of the overall wedge was also seen to decrease as with the shallow dense and sparse experiments.

The bores reflected from individual rows of cylinders can be seen more explicitly in Figure 4.11. This figure shows false-colour instantaneous density fields for the P5H10 experiment with overlaid velocity vectors at six different times between the third and fourth rows of cylinders. These show some of the fluid propagating through the cylinders and the rest being deflected upwards. Due to the large relative roughness height, fluid deflected upwards could not reach a height larger than the cylinders. Therefore, the fluid deflected upwards was reflected back upstream as individual bores, while the rest of the fluid propagated between the cylinders.

Figure 4.12 shows density fields for the experiments in the plunging configuration as the currents reached the final row of roughness. In Figure 4.12a the P5H10 current propagated through the cylinders with bores being reflected off individual rows of roughness as in Figure 4.11. In Figure 4.12b the P5H15 experiment is seen to have been in a transitional regime where the portion of the flow that was deflected upwards by the cylinders both plunged over the cylinders and was reflected backwards from them. In Figures 4.12c and d as the relative roughness height becomes small the reflected bores are not visible.

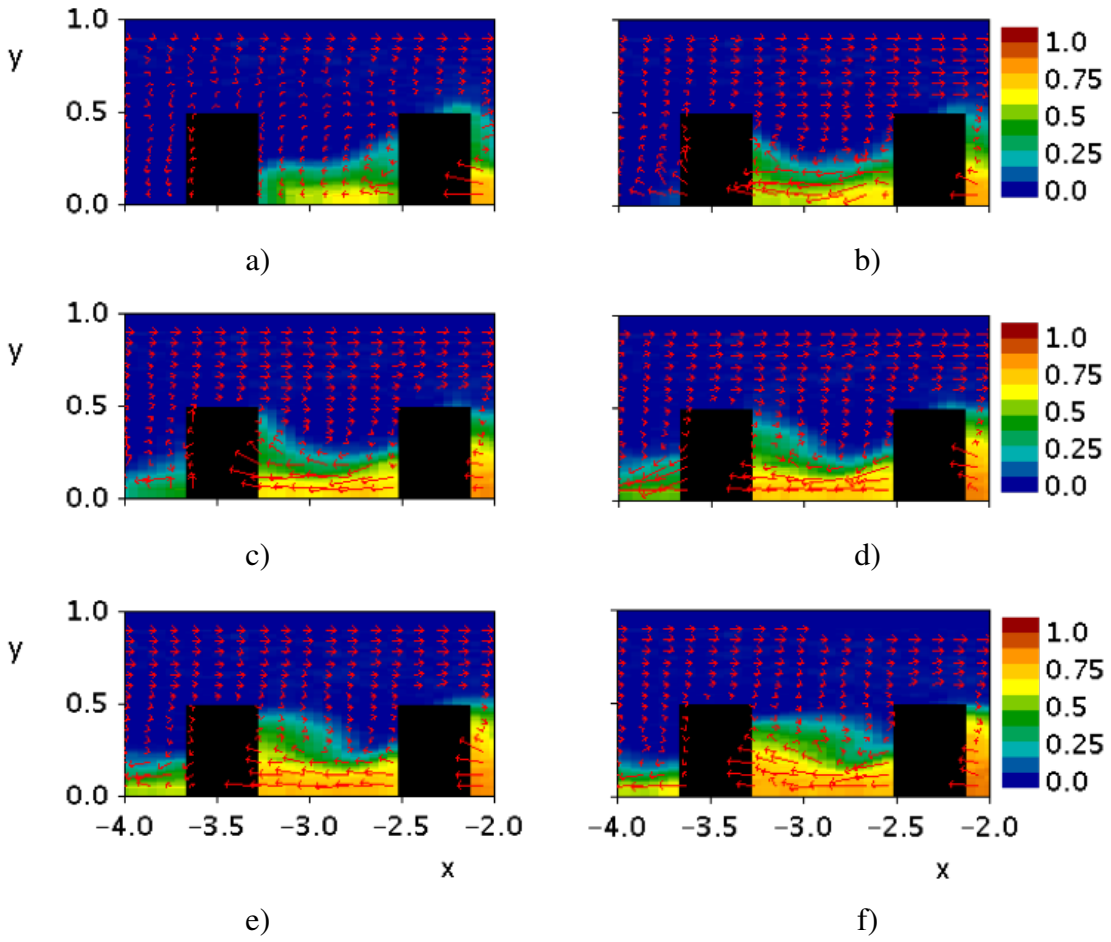

Fig. 4.11 Density fields and velocity vectors between the third and fourth cylinders for P5H10 experiment at times of 8, 9, 10, 11, 12 and 13. False colour shows density and red arrows show velocity vectors.

4.6 Summary

This chapter provided a qualitative overview of the development of the gravity currents as they transitioned from smooth boundaries to fields of vertical circular cylinders. For all experiments before the currents reached the roughness they took on the characteristics of smooth bed currents similar to those studied by Britter and Simpson (1978). When the currents encountered the roughness elements they were seen to increase in depth above the first row of roughness and a bore was seen to propagate upstream. In the following chapters this bore is referred to as the *roughness bore*. The bore was seen to be larger if the relative roughness height was larger or the front face of the roughness field was more densely populated.

Fluid near the front of the current was seen to dilute for all experiments as they travelled. However, the dilution of the currents by the time they reached the end of the roughness depended

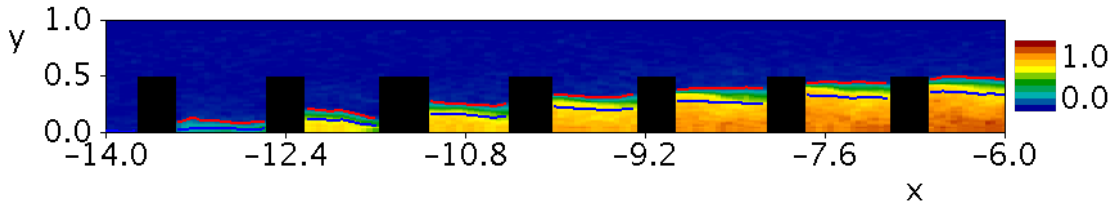

a)

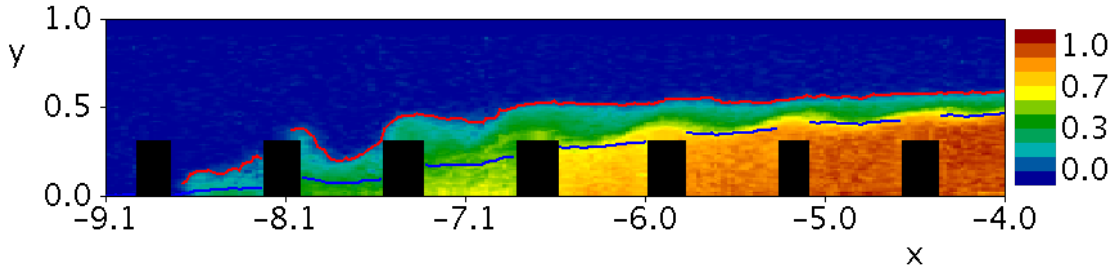

b)

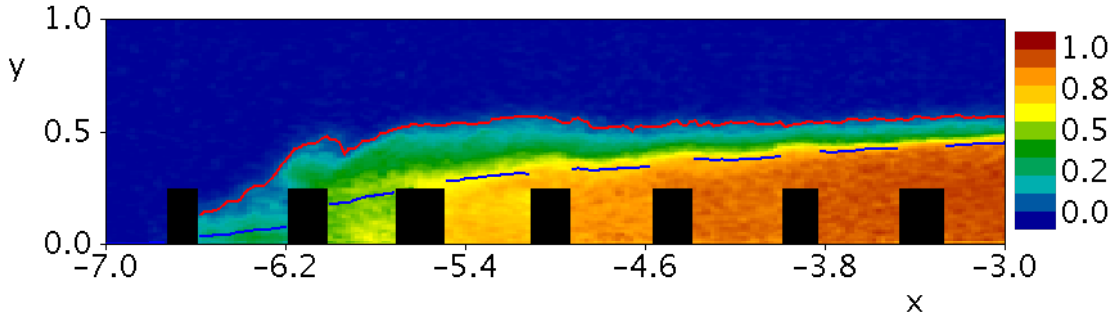

c)

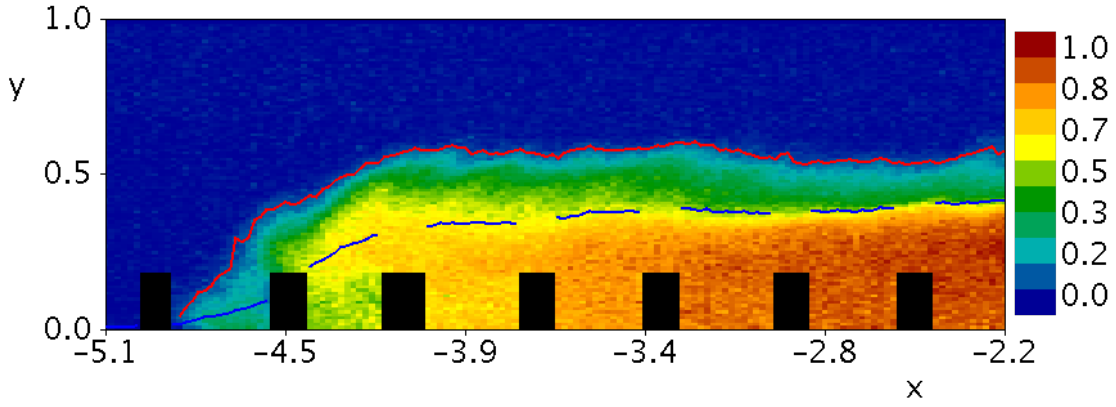

d)

Fig. 4.12 Density fields for experiments a) P5H10, b) P5H15, c) P5H20 and d) P5H27 as currents reached the final roughness element. Red line shows h_c and blue line shows h_B.

on the roughness configuration and the relative roughness height. When the relative roughness height was small and the roughness was densely distributed the dilution was predominantly due to a convective instability between the current travelling atop the cylinders and the lighter fluid contained between them. However, when the relative roughness height was large or the roughness was sparsely distributed the current predominantly propagated between rows of roughness. When the cylinders were densely distributed across the channel but sparsely distributed in the direction of flow the current plunged over the roughness and this provided additional mixing at the front of the currents.

Regardless of the distribution of roughness, when the relative roughness height was large the currents propagated entirely through the roughness field. For these experiments the roughness field could be treated as though it was fully emergent. The main sources of mixing for these currents were from the shear layer between the light and dense fluid and from the wakes behind the cylinders. When the roughness was sparsely distributed in the direction of flow bores were seen to reflect from individual cylinders.

For all of the experiments, when the currents exited the roughness they re-established to resemble smooth bed currents, albeit with diluted heads. For the over-flowing currents the head had to plunge downwards to re-establish atop the smooth bed but the through-flowing currents grew and re-established from wedge-like structures. As the currents travelled the dilute fluid within the current heads was replaced by denser, faster moving fluid from within the tail.

The following chapters will further explore the ideas presented in this section. In particular, quantitative measures of the speed, shape and dilution of the currents will be presented.

Chapter 5: Results From Sparse Configuration Experiments

5.1 Introduction

The previous chapter provided preliminary, qualitative results from the investigation into the interaction between "developed", smooth bed gravity currents and the sudden onset of roughness. In this thesis the word *developed* is taken to mean currents that have formed and are in the slumping regime prior to encountering roughness. The full list of experimental runs discussed can be found in Chapter 4. It was qualitatively seen that as a current interacts with sparsely distributed roughness it transitions from a head and tail structure into a wedge-like structure. As a current travels through the roughness it dilutes and the angle the wedge forms with the horizontal decreases. Meanwhile, a bore, termed the roughness bore, is reflected off the front face of the roughness in order to provide sufficient energy for the current to propagate forwards. Additionally, when a current emerges from the roughness it re-establishes to resemble a smooth bed current. This chapter builds on these results by exploring more derived, quantitative measures. In particular, for a current encountering sparsely distributed roughness several questions are addressed

- How does the current dilute with time and relative roughness height?
- How is the structure of the current impacted by the relative roughness height and time?
- How does its Froude number develop with time and how is this impacted by the relative roughness height?
- Does the current reach a quasi-steady state, wherein it propagates forward with a constant Froude number and a constant head structure with time?
- How does the structure and speed of the current develop as it emerges from the roughness?

- How does the velocity structure of the current vary with time and relative roughness height?
- How is the entrainment of ambient fluid into the current affected by the roughness?

Section 5.2 explores the results from the density fields generated using the LA technique. Within this Section, 5.2.1 provides an overview of the results by examining the buoyant height of a single experiment. It is seen that the buoyancy and speed of this current decreased with time as it travelled through the roughness. Section 5.2.2 then builds on these findings by comparing how the front speed and Froude number of all of the experiments varied with time. Regardless of the relative roughness height all of the currents decelerated at the same rate and their speeds never approached constant values within the length of roughness employed in these experiments. To understand why this occurred, and to address how the current density and structure varied with time, Section 5.2.3 compares the buoyant height and current envelope of all of the experiments with time. It is seen that the currents lost their head and tail structures and took on wedge-like characteristics as they travelled. The angle that the wedge formed with the horizontal decreased with time. At the same time the currents were strongly diluted in the head region.

By comparing the currents with different relative roughness heights in Section 5.2.3 it is seen that at a given time the extent to which the heads had been replaced by wedge-like structures depended on the relative roughness height. Therefore, the currents with smaller relative roughness heights had larger vertical extents and were less diluted near the front of the currents. However, behind the head region all of the experiments displayed wedge-like characteristics with similar vertical extents and dilutions. Behind the head region the buoyancy was larger than that in the head region. The larger buoyancy in the tail suggests that the reason for the similarity in Froude numbers is because the currents were driven by a balance between the pressure gradient and drag force due to the cylinders in the tail region. In Section 5.3 a simple model based on a balance between the drag force per unit volume and the pressure gradient in the tail is formulated. This model is used to show that the Froude number is independent of the relative roughness height when a current is non-dimensionalised by the total fluid depth but it does depend on the ratio between the cylinder height and spacing.

Section 5.4 explores the results from the velocity fields generated using the PTV technique. Within this, Section 5.4.2 provides velocity profiles to confirm that the currents could all be

classified as through-flowing. Furthermore, this section shows that the amount of fluid through and above the roughness near the front depends on the relative roughness height. Finally, Section 5.4.3 provides volume fluxes to show that the rate of ambient fluid entrained into the current is not impacted by the roughness. However, it is argued that the roughness does cause the ambient fluid entrained into the current to remain in, and dilute, the current head.

5.2 Density Fields

5.2.1 Overview

This section explores results from the density fields generated from the light attenuation experiments. This analysis makes use of the buoyant heights of experiments; analysing how they varied with time, space and between experiments. The buoyant height contains information about both the average current density and vertical extent. Therefore, to understand which of these was responsible for buoyant height variations the current envelope is also analysed.

To provide an overview of the main features of these currents Figure 5.1 shows the buoyant height in false colour for the S5H20 experiment as a function of x and t. This experiment is chosen because the main features seen in Figure 5.1 are representative of all of the experiments presented in this section. The thin vertical black lines represent the locations of the roughness. The buoyant height is an integral over the full depth of fluid and in locations of roughness visualisation was not possible over the full depth. Therefore, the buoyant height could not be calculated at these locations. Similarly the wider black rectangle at x = -2.2 represents the structural element in the channel where visualisation was also not possible.

The red line in Figure 5.1 represents the frontal location of the current calculated as the minimum value of x at each time where the buoyant height was less than or equal to 0.02. At locations to the left of this line the buoyant height was close to 0 because there was no, or very little, dense fluid present. This line had a reasonably constant slope before the current reached the roughness (up to a time of 0), indicating that before the current reached the roughness the current was travelling at a constant speed. This is consistent with various experimental studies into smooth-bed gravity currents in the slumping regime (Britter and Simpson, 1978; Cenedese et al., 2016; Huppert and Simpson, 1980; Rottman and Simpson, 1983). Once the current encountered the roughness the slope of this line is seen to diverge from the original path indicating that the

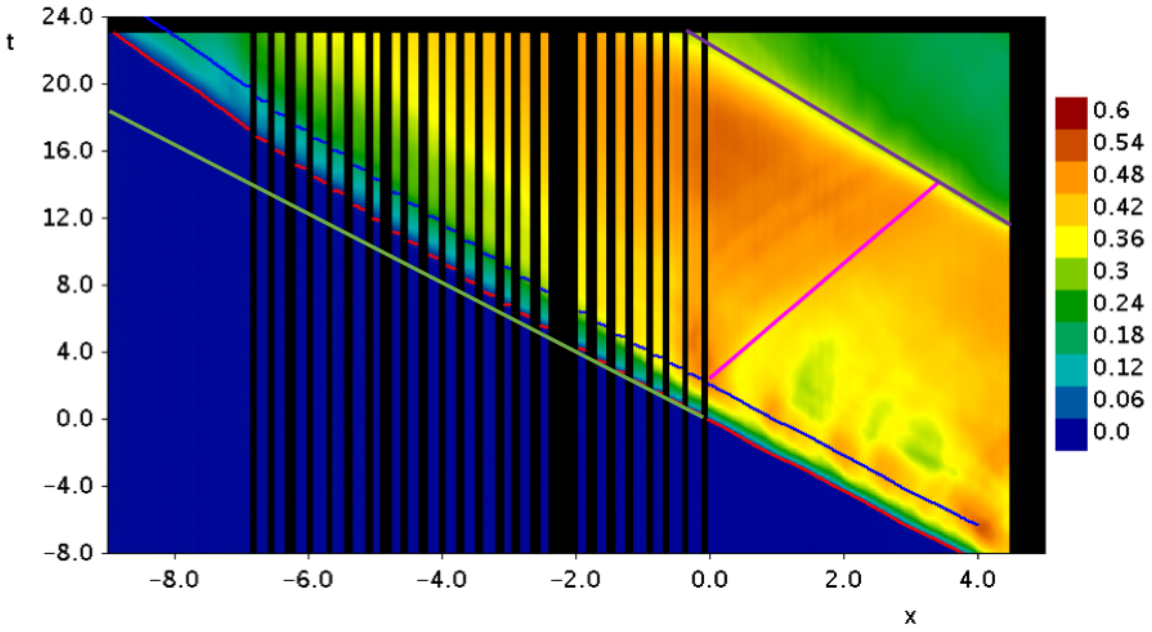

Fig. 5.1 S5H20 h_B displayed as false-colour with x and t. The red line shows the front location of the current, the green line is an extrapolation of the front location of a smooth bed current, the blue line represents the standard head location, the pink line shows the path of the roughness bore and the purple line shows the path of the lock bore. The black regions represent locations where visualisation was insufficient to calculate the buoyant height.

current speed decreased as it travelled. The current began accelerating again after exiting the roughness. This is explored further in Section 5.2.2.

In smooth bed currents the location of the current head can often be defined as the location with the maximum buoyant height. However, because the buoyant heights of the currents discussed in this chapter did not display clear local maxima at their heads, this location is defined to be a distance of 1 behind the front location. This location is selected because it is the approximate location of the maximum buoyant height for a smooth bed current and is termed the *standard head location*. The standard head location is shown by the blue line in Figure 5.1. Before the current reached the roughness it can be seen that the average buoyant height along this line is reasonably constant apart from fluctuations associated with K-H instabilities. However, once the current entered the roughness the buoyant height decreased as it penetrated the roughness field (visible by the changing false-colour alongside this line). Similar trends are found behind the head and this is explored further in Section 5.2.3.

Both the lock bore and the roughness bore are also visible in Figure 5.1. Their paths are approximately represented by the purple and pink lines respectively. It can be seen by observing

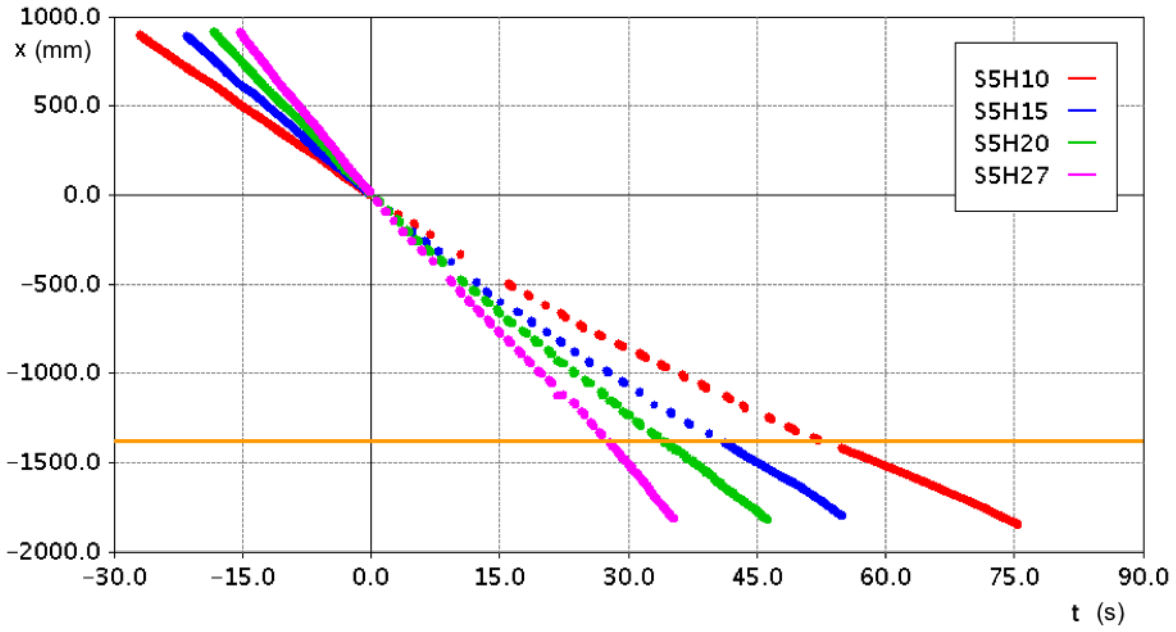

Fig. 5.2 Dimensional front location with time for the sparse experiments S5H10, S5H15, S5H20 and S5H27. The currents entered the roughness at a time and location of 0 and the orange line shows the location where the currents exited the roughness.

either side of the pink line that the buoyant heights increased at locations where the roughness bore had passed. This corresponds to an increase in height associated with the roughness bore. Conversely, the arrival of the lock bore was associated with a decrease in the buoyant height as the lock ran out of fluid to continue driving the current forward.

5.2.2 Front Location and Speed

Figure 5.1 showed that as the S5H20 experiment travelled through the roughness its front speed decreased. However, it was not clear from this figure whether the speed continuously decreased with time or whether it eventually asymptoted towards a constant value. This section explores this by observing how the current path and speed varied with time and relative roughness height.

Figure 5.2 shows the dimensional front location for the four sparse experiments with time. This figure shows a clear trend where currents with deeper fluid depths moved at faster speeds. Larger fluid depths correspond to larger driving forces allowing the currents to propagate at larger speeds. This trend is observed before, during and after the currents travelled through the roughness.

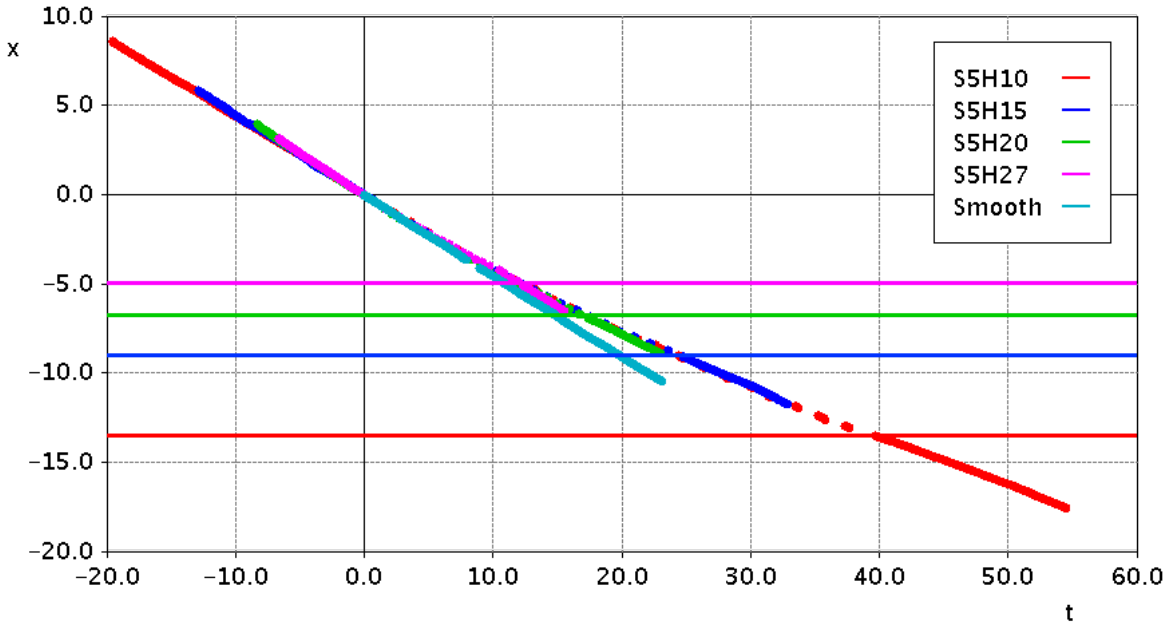

Fig. 5.3 Front location with time for the sparse experiment data from Figure 5.2 non-dimensionalised based on the framework introduced in Chapter 3. The currents entered the roughness at a time and location of 0 and the horizontal lines show the locations where the currents exited the roughness. The smooth bed current is an extrapolation of behaviour prior to the roughness field.

While Figure 5.2 is useful to compare the absolute paths of the experiments with differing relative roughness heights, the non-dimensionalisation introduced in Chapter 2 is applied to better compare the different experiments. The non-dimensionalised front locations with time are shown in Figure 5.3. The slopes of the curves in Figure 5.3 are the Froude numbers of the currents. Before the currents entered the roughness they all had constant and similar Froude numbers.

Once the currents entered the roughness they began to decelerate and this continued as they travelled. Their paths diverged from those followed by smooth bed currents travelling at constant speeds. It could be expected that the slowing of these currents would depend on the relative depth of fluid because the drag force imposed on the currents by the roughness would be greater with larger relative roughness heights. However, the front locations of all of the sparse experiments, regardless of their relative roughness heights, were similar with time.

While it is clear from Figure 5.3 that the currents slowed as they travelled through the roughness, it is not clear how this varied with time and whether the currents approached a constant speed. To address the variation with time the front location was differentiated with time to identify the

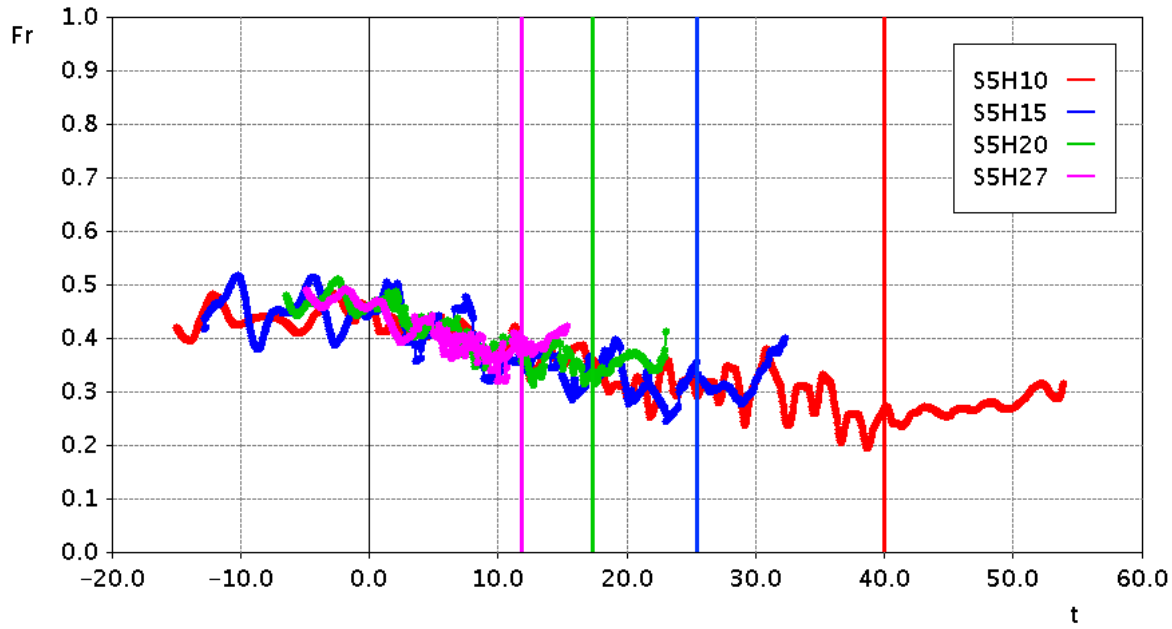

Fig. 5.4 Froude Number with time for the sparse experiments - S5H10, S5H15, S5H20 and S5H27. The currents entered the roughness at a time of 0 and the vertical lines show the times when the currents exited the roughness.

Froude number of the currents. The Froude numbers with time for the four sparse experiments are shown in Figure 5.4. This figure shows a constant Froude number of approximately 0.46 for all of the experiments before the currents entered the roughness, closely matching results from previously studies (Britter and Simpson, 1978; Cenedese et al., 2016; Shin et al., 2004). Oscillations are visible due to the presence of seiche waves generated by the opening of the gate. As such point measurements from these experiments would not be meaningful. These seiche waves are discussed in detail in Chapter 8. After the currents encountered the roughness a reduction in the Froude Number with time occurred and, as seen in Figure 5.3, the rate of this reduction was similar for all of the experiments.

The similarity in the slowing of the currents with differing relative roughness heights could be explained by the currents with larger relative roughness heights passing fewer rows of roughness after travelling the same non-dimensional distance. Therefore, while the individual rows of roughness may have had more impact on the currents with larger relative roughness heights, the overall effect of the roughness after travelling the same non-dimensional distance was similar in all experiments. These ideas are quantified in an analytical model presented in Section 5.3.

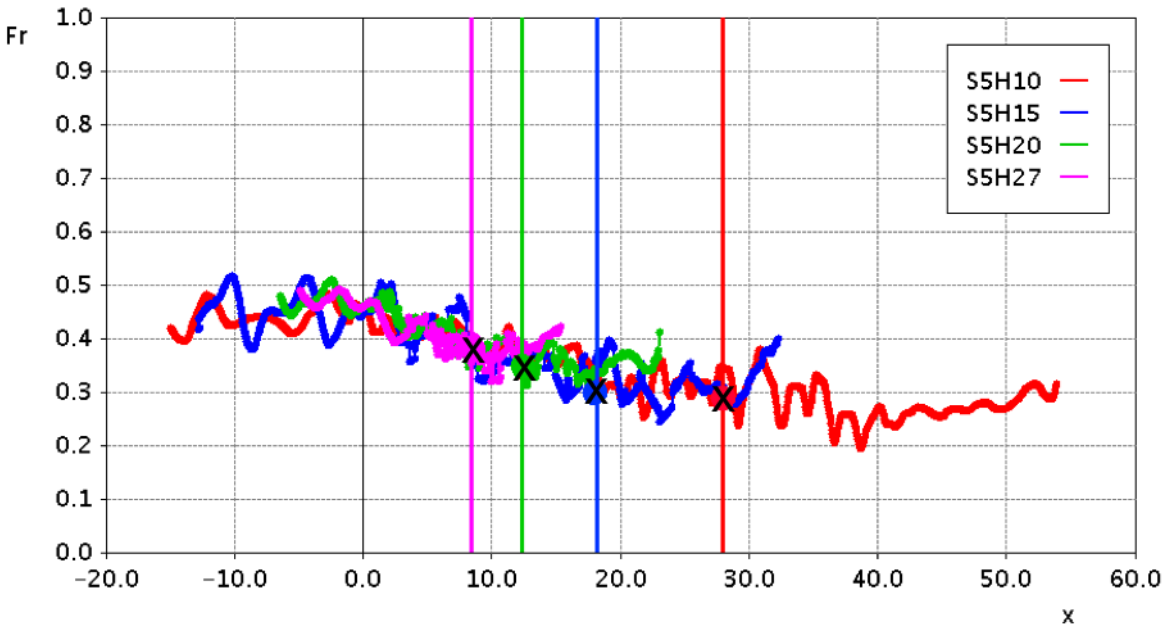

Fig. 5.5 Froude Numbers with time for S5H10, S5H15, S5H20 and S5H27. The currents entered the roughness at a time of 0 and the vertical lines show the times when the currents had travelled a distance of 1000 mm, the location of measurements in the experiments of Cenedese et al. (2016). The black crosses show the Froude numbers from experiments by Cenedese et al. (2016).

It was explained in Chapter 2 that Cenedese et al. (2016) carried out experiments similar to the present experiments in the sparse configuration but with the roughness beginning at the lock gate. They measured density fields in a 650 mm long window centred at a distance of 1000 mm downstream of the gate (the beginning of the roughness) and assumed that the currents were in a quasi-steady state with constant Froude numbers. These Froude numbers were measured to be 0.29, 0.31, 0.35 and 0.38 for the equivalents of the S5H10, S5H15, S5H20 and S5H27 experiments respectively. The roughness in the present study spanned approximately 1400 mm, so to compare the results better Figure 5.5 shows Figure 5.4 but with vertical lines at times when the currents had travelled 1000 mm from the start of the roughness and black crosses at these times representing the Froude numbers of Cenedese et al. (2016). The Froude numbers measured by Cenedese et al. (2016) are seen to be consistent with those measured in the current experiments. However, while Cenedese et al. (2016) deduced that the currents were at steady state at these locations the Froude numbers in the present study continued to decrease.

Figure 5.5 indicates that whether or not a current is allowed to develop before encountering roughness does not significantly impact its Froude number within the roughness region. To investigate this further, Figure 5.6 compares the Froude numbers of two of the sparse config-

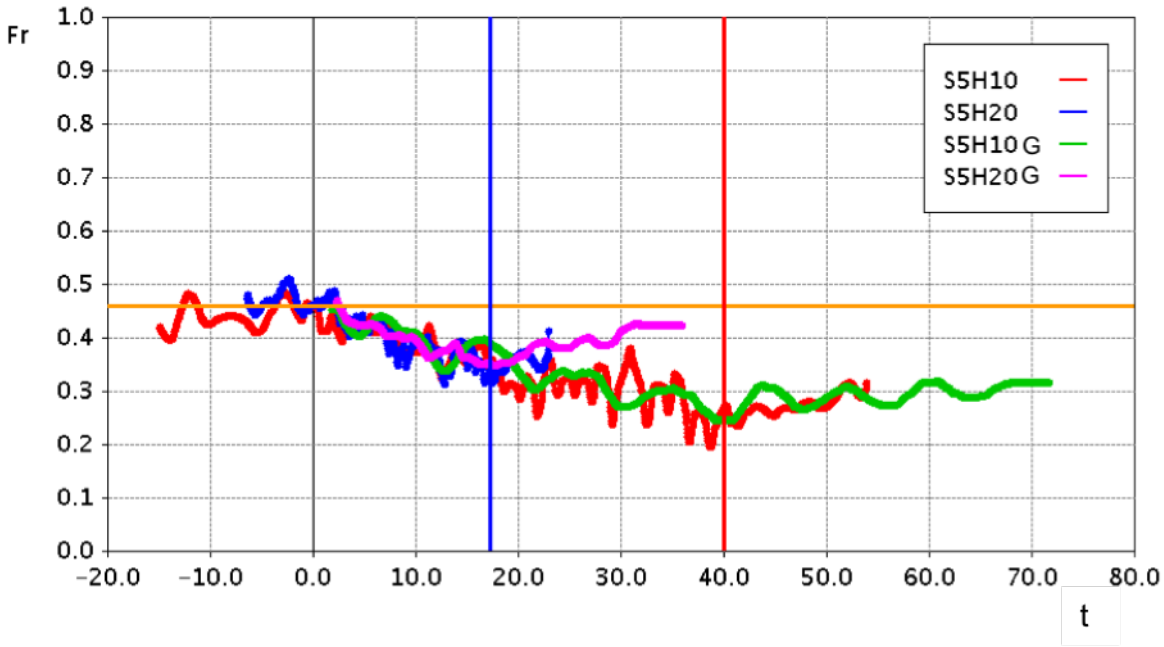

Fig. 5.6 Froude number with time for the S5H10, S5H20, S5H10G and S5H20G experiments. Currents entered the roughness at a time of 0 and the vertical lines show the times when the currents exited the roughness. The orange line is an extrapolation of the Froude number of a smooth bed current.

uration experiments with the roughness beginning downstream of the lock gate (S5H10 and S5H20) with two of the sparse configuration experiments with roughness beginning at the lock gate (S5H10G and S5H20G). The differences in fluctuation sizes between the two data sets in this figure are due to different amounts of smoothing of the data rather than differences in physical behaviour. This figure, confirms that the location of the front face of the roughness has a minimal impact on the Froude number. Additionally, because the S5H10G and S5H20G experiments are very similar to the experiments of Cenedese et al. (2016), Figure 5.5 indicates that the Froude numbers of their currents likely decreased further after their measurements.

The vertical lines in Figures 5.4 and 5.6 represent the locations where the currents exited the roughness. At these locations the Froude numbers began increasing. To further understand how the currents emerged from the roughness, the sparse experiments with the roughness beginning at the gate were investigated. Due to there being no distance between the gate and the roughness these experiments allowed for the currents to be measured over a significantly longer distance after exiting the roughness. Figure 5.7 shows the Froude numbers for these experiments after they exited the roughness. In this figure the origin of time is redefined such that it represents the time when the currents exited the roughness.

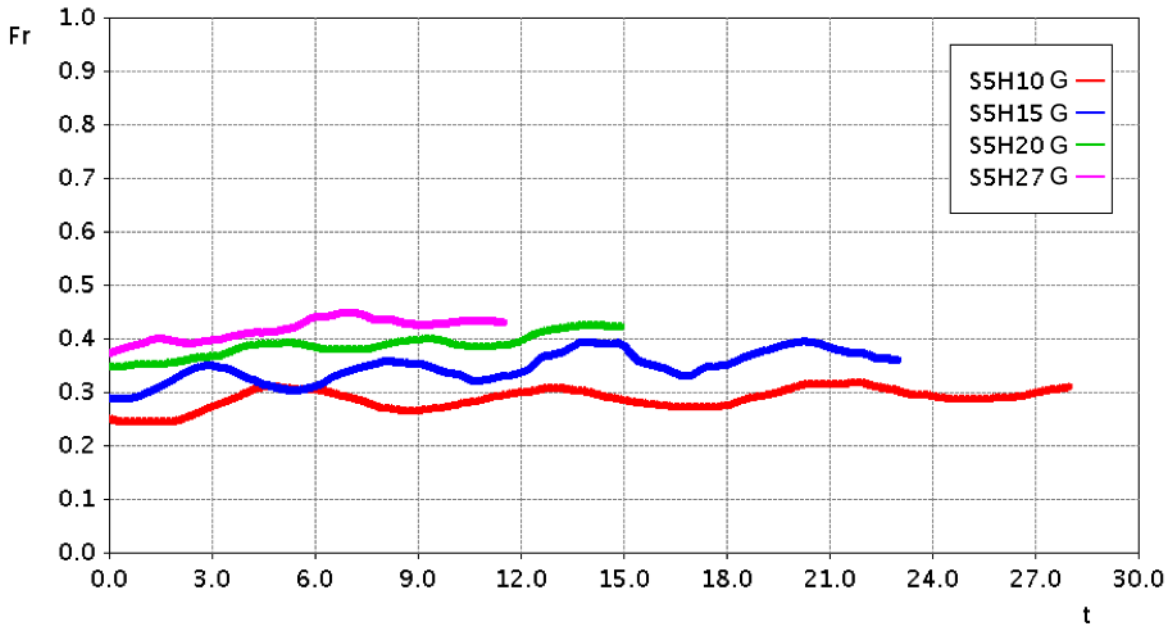

Fig. 5.7 Froude number with time for the S5H10G, S5H15G, S5H20G and S5H27G experiments after the currents re-emerged from the roughness. The origin of time is redefined such that it corresponds to the time when the currents exited the roughness.

It is clear from Figure 5.7 that when the currents exited the roughness their Froude numbers depended on the relative roughness height. While the Froude numbers of all currents decreased at the same rate within the roughness the currents with larger relative roughness heights travelled larger non-dimensional distances allowing more time for the Froude number to decrease before re-emerging from the roughness. The increase in speed as the currents travelled beyond the roughness is, in part, because once the currents exited the roughness the drag force from the cylinders was removed. With the drag force on the cylinders removed, dense fluid within the tail was allowed to re-enter the head region, allowing the buoyancy of the heads to increase and for the currents to be driven forward at larger speeds. The growth and increased buoyancy of the heads was observed in Chapter 4 and is illustrated further in Section 5.2.3.

After travelling a sufficient distance after emerging from the roughness these currents appear to have approached steady states. The steady states of these currents appear to be a function of the relative roughness height, or the distance travelled through the roughness before the currents emerged, with the S5H27G experiment reaching a steady state of approximately 0.42, slightly less than that of a smooth bed current, and the S5H10G experiment reaching a steady state significantly lower than that of a smooth bed current, of approximately 0.31. The reason for the Froude numbers not completely recovering is likely to be because the dilution of the currents as

they travelled through the roughness may have limited the maximum driving force available for these currents. The reason for the trend in the initial Froude numbers is due to these currents all travelling different dimensionless distances through the roughness, though the differing relative roughness heights may have also played a role.

5.2.3 Current Height and Density

Overview

In the previous section it was seen that regardless of the relative roughness height all experiments in the sparse configuration displayed the same reduction in Froude number with time. Furthermore, a buoyant height reduction with time was seen in Section 5.2.1 for the S5H20 experiment and in Chapter 4 it was seen that the currents transitioned from traditional head and tail structures to wedge-like structures as they travelled. This section builds on these results while attempting to answer the question of what impact the roughness had on the height and density of the currents and how this varied with time and relative roughness height. In particular, attempts are made to find mechanisms for why the Froude number was seen to not depend on the relative roughness height.

Variation of Height and Density with x

To understand the development of these currents as they travelled the buoyant height of the S5H20 experiment is displayed in Figure 5.8 as a function of x at 5 different times. Many of the characteristics of Figure 5.8 are typical of all of the sparse configuration experiments. This figure shows the buoyant height changing from a head and tail structure, where the largest driving force is associated with the head, to a wedge, where the driving force is associated with a pressure gradient along the entire roughness domain.

At a time of 0 the current displays the head and tail structure commonly observed in smooth-bed gravity currents (Britter and Simpson, 1978). At a time of 4 the current has travelled a distance of 2 into the roughness. At this time the current still resembles the shape of a smooth bed current with a distinct head and a shallower tail. This head, located near the front face of the roughness, has a larger buoyant height than the smooth bed current because of the increase in the current depth due to the bore reflected from the start of the roughness. At a time of 8 the current has

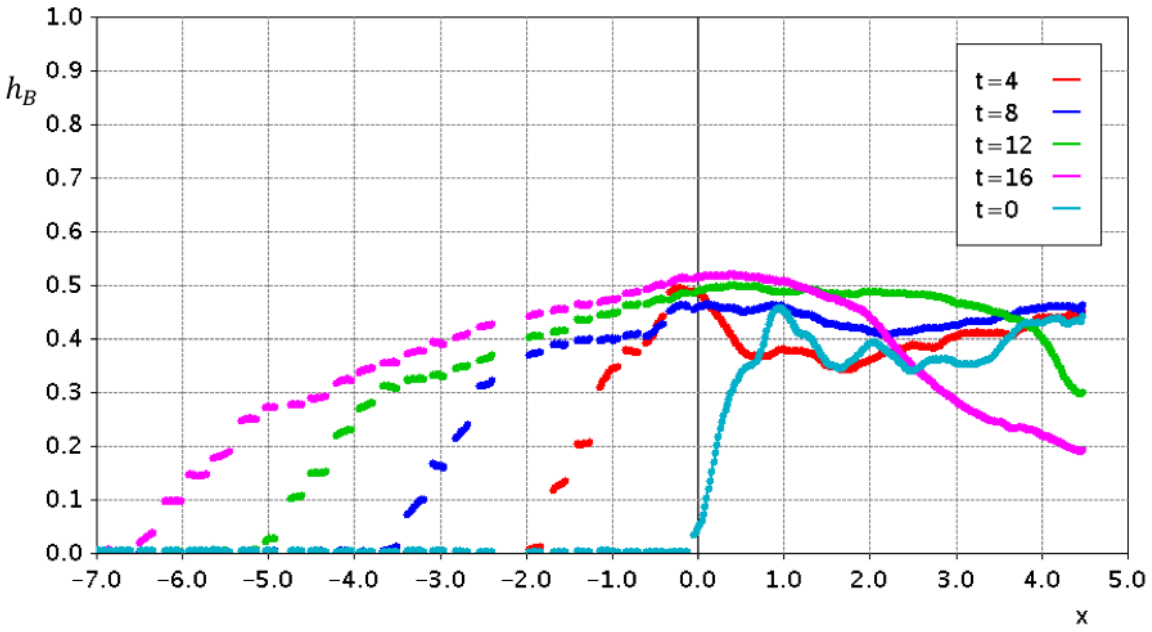

Fig. 5.8 h_B for the S5H20 experiment with x at times of 4,8,12 and 16 when the current was travelling through the roughness and a time of 0 when the current was about to enter the roughness. The front face of the roughness is at a location of x=0.

started transitioning into a wedge and the roughness bore has begun propagating backwards with its nose at a location of 2. At this time the maximum buoyant height (at x = 0, the front face of the roughness) decreased as the fluid being deflected upwards was transferred to the transmission of the roughness bore. In subsequent times the current continues to transition to a wedge-like structure as it travels and the buoyant height at the front face of the roughness begins to increase again. At the final two times the lock bore has encountered the roughness bore, causing a large drop in the buoyant height upstream of the roughness.

In order to better determine how the buoyant height within the roughness changed as the current travelled Figure 5.9 displays the data from Figure 5.8 with the current front location translated such that at all times it lies at x=0. Vertical lines show the relative locations of the front face of the roughness for different times. Over the timescale analysed the current never reached a quasi-steady state. Instead, as the current travelled the angle of the wedge decreased. The reducing gradient of the buoyant height with time is consistent with the reducing Froude number in Section 5.2.2.

The reduction in the buoyant height could be due to either a decrease in the average density of the current or a reduction in its vertical extent. In order to determine which of these contributed

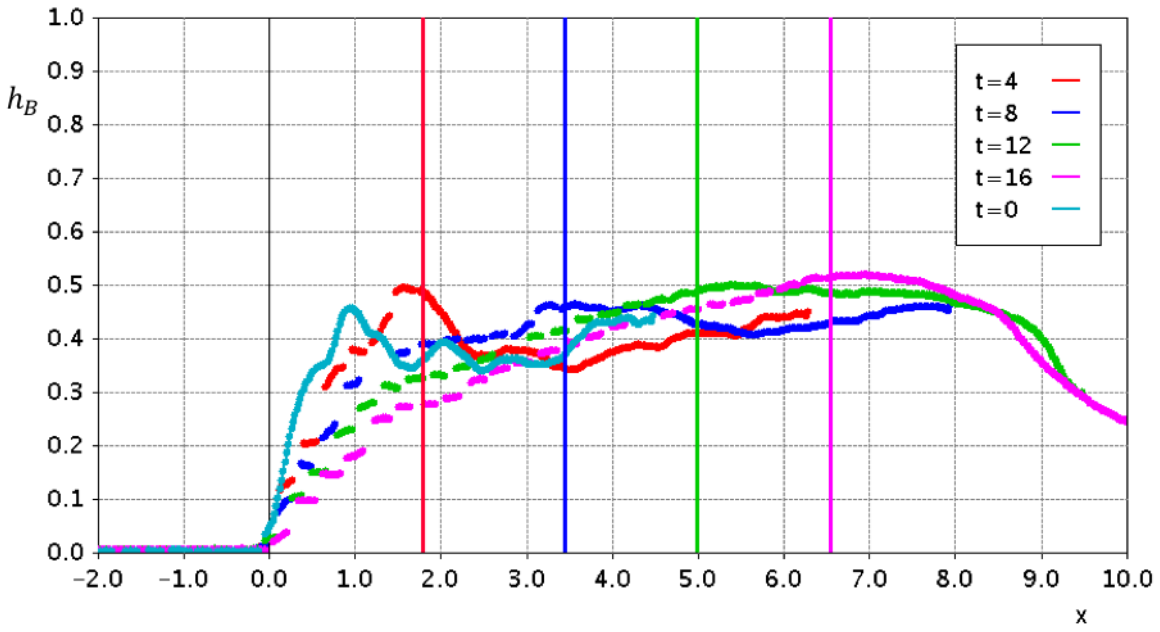

Fig. 5.9 h_B for the S5H20 experiment with x at times of 4,8,12 and 16 when the current was travelling through the roughness and a time of 0 when the current was about to enter the roughness. The nose is translated backwards such that at all times the current front (considered to be where h_B=0.02) corresponds to x=0. Vertical lines represent the front face of the roughness for the times of corresponding colours. Gaps in lines are due to locations of the roughness where measurements were unavailable.

to changes in the buoyant height Figure 5.10 shows the current envelope for the same times as Figure 5.8. The current envelope also shows the current taking on a wedge-like structure as it travelled.

Like the buoyant height, the current envelope was seen to initially increase at the front face of the roughness (x=0). However, unlike the buoyant height the current envelope at this location quickly became constant. Thus the increase in buoyant height with time was due to an increase in salt concentration rather than an increase in the vertical extent. When the current initially hit the front face of the roughness a considerable amount of mixing occurred and the fluid forced backwards in the bore and forwards in the current was diluted. However, over time this fluid became replaced by dense, unmixed fluid from within the lock. Therefore, while the vertical extent of the current at this location became constant after the initial spike, the buoyant height increased as the dilute fluid was replaced by dense, relatively unmixed tail fluid.

From Figure 5.10 it is difficult to see how the vertical extent varied in the frontal region as the current travelled. Therefore, Figure 5.11 shows the data from Figure 5.10 translated such

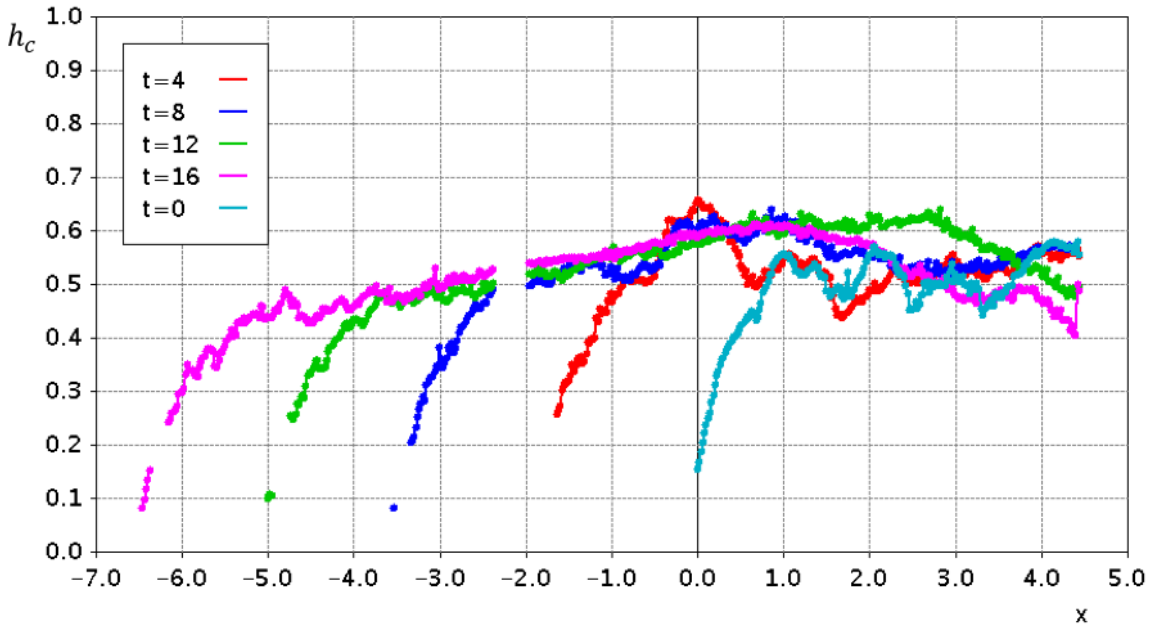

Fig. 5.10 h_c for the S5H20 experiment with x at times of 4,8,12 and 16 when the current was travelling through the roughness and a time of 0 when the current was about to enter the roughness. The front face of the roughness is at x=0.

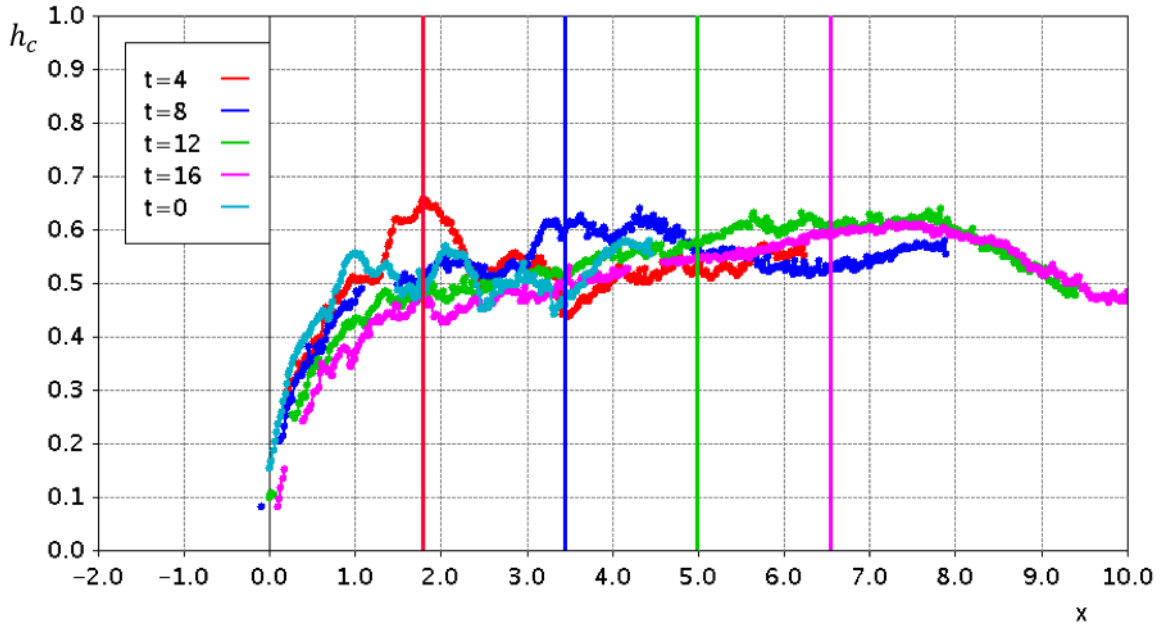

Fig. 5.11 h_c for the S5H20 experiment with x at times of 4,8,12 and 16 when the current was travelling through the roughness and a time of 0 when the current was about to enter the roughness. The nose is translated backwards such that at all times the current front corresponds to x=0. Vertical lines represent the front face of the roughness for the times of corresponding colours.

that at all times the front location is at x=0. This figure shows the current transitioning from having a head and tail structure to a wedge shape and the wedge angle decreasing with time. However, it can be seen that as the current travelled the vertical extent changed less drastically than the buoyant height. Thus, both dilution and vertical extent played a role in the decrease in the buoyant height with time.

Thus far this section has only considered how the properties of an experimental current with a fixed relative roughness height varied as it travelled. While many of the features are applicable to currents with different relative roughness heights there are differences between these experiments. Figure 5.12 shows the buoyant height of the four sparse experiments (S5H10, S5H15, S5H20 and S5H27) at a time of 11. This corresponds to the largest time when all experiments could be compared, i.e the time when the S5H27 experiment had reached the final row of roughness. While the S5H27 experiment had reached the final (24th) row of roughness at this time the S5H10 experiment had only reached the eighth row of roughness. However, as was observed in Section 5.2.2, the currents had all travelled the same non-dimensional distance. In this figure the front location of all of the currents are translated such that they lie at a location of x = 0. The orange line represents the location of the front face of the roughness, which was the same for all currents.

The S5H27 experiment, with the smallest relative roughness height, had a slightly pronounced head. To a lesser extent this is also true of the S5H20 experiment but not of the currents with larger relative roughness heights. However, upstream of the head the buoyant height still formed a wedge and this had a buoyant height significantly larger than in the head region. The wedge behind the head was seen in all experiments but as the relative roughness height decreased the head became more pronounced.

Section 5.2.2 showed that all of the currents travelled at the same non-dimensional speed. Therefore, it was postulated that the total drag force imposed on a current by the roughness must be independent of relative roughness height. A current with a large relative roughness height would encounter fewer rows of roughness than one with a smaller relative roughness height after travelling one distance unit. Thus, the greater impact of the roughness on a current with a small relative roughness height would be offset by the current passing fewer rows of roughness. Clearly, from Figure 5.12, the gradient in the wedge behind the heads of all currents were similar. Thus, the pressure gradients behind the head were likely to be similar. As these

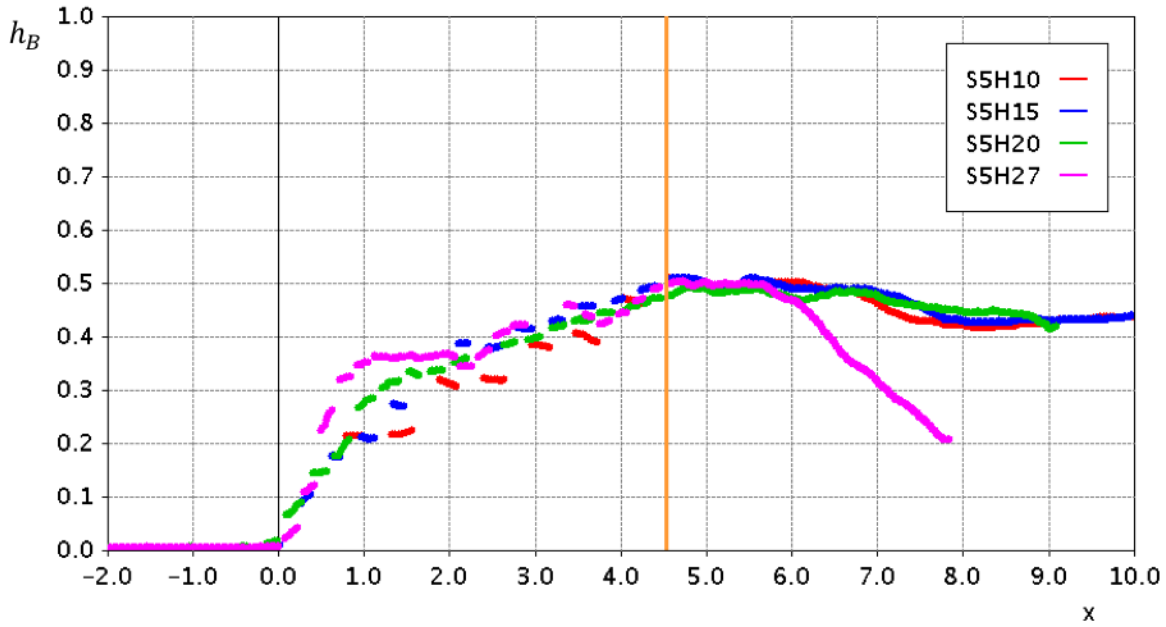

Fig. 5.12 h_B with x for sparse experiments - S5H10, S5H15, S5H20 and S5H27 at a time of 11 corresponding to when the deepest experiment (S5H27) reached the final row of roughness. Experiments are translated such that the noses of the currents lie at x=0. The orange line represents the average location of the front face of the roughness.

currents all had similar Froude numbers it would not be unreasonable to consider these currents to be driven predominantly by the pressure gradient behind the head of the currents rather than by the buoyancy of the heads themselves. In Section 5.3 a simple model is developed to test this hypothesis.

Immediately upstream of the front face of the roughness (the orange line in Figure 5.12) the buoyant heights of all experiments became independent of x once the roughness bore had passed, indicating that the buoyant height at the front face of the roughness was determined solely by the roughness configuration. Further upstream at this time it can be seen that for all experiments, except for the S5H27 experiment, the roughness bores had not yet encountered the lock bore. The noses of the roughness bores at this time were located between x=7 and x=8. These are visible by a drop in the buoyant height between x=6 and x=9. For the S5H27 experiment the roughness bore and lock bore had met. The lock bore caused the much larger drop in buoyant height seen upstream of the roughness in this experiment.

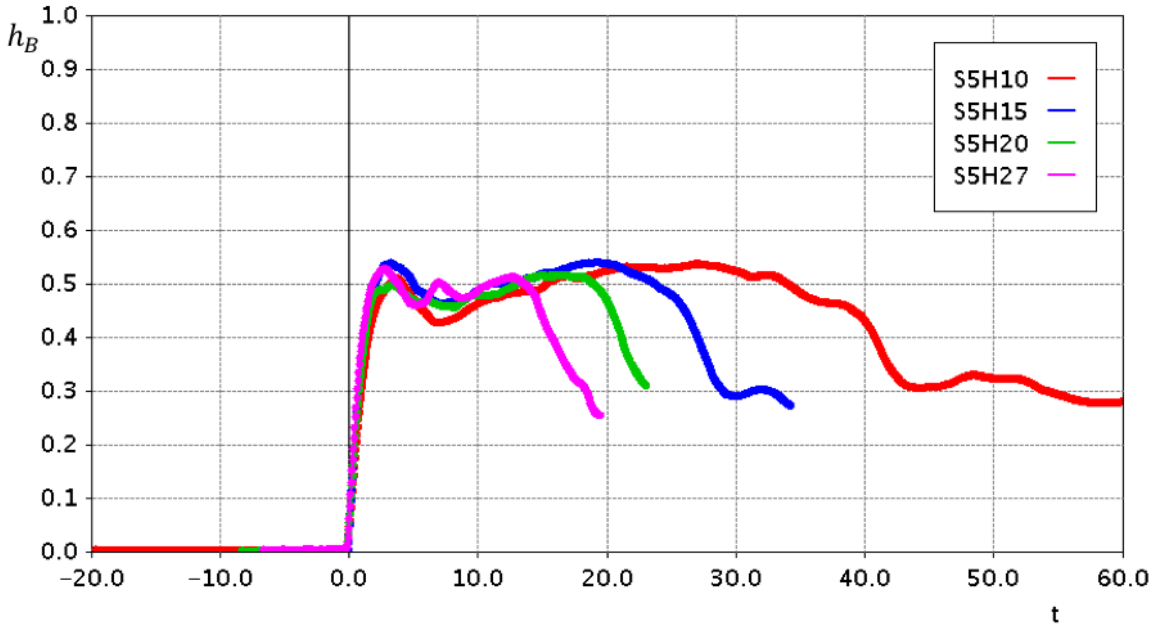

Fig. 5.13 h_B at the front face of the roughness with time for thesparse experiments S5H10, S5H15, S5H20 and S5H27.

Variation of Height and Density at the Front Face of the Roughness with time

With the pressure gradient behind the heads being thought to drive the flow, how the buoyant height of fluid at the front face of the roughness varied with time is likely to be important. Figure 5.13 shows the buoyant height at this location (x = 0) with time. As was seen in Figure 5.8, there was an initial increase in buoyant height at a time of approximately 3 before it sharply reduced. The fluid hitting the front face of the roughness was initially deflected upwards before the roughness bore began propagating backwards. After this drop the buoyant height began to increase again and continued to increase until the lock bore arrived. This behaviour can be seen for all of the experiments with the increase and decrease of the buoyant heights all occurring on roughly the same timescale. The arrival of the lock bores for all experiments can be seen by the large drop in buoyant height with time, for example at a time of 13 for the S5H27 experiment.

Figure 5.14 shows the current envelope with time at x=0 for the sparse experiments. Like Figure 5.13, all experiments show similar behaviour. The initial peak which was seen in the buoyant height is also seen in the current envelope. However, unlike the buoyant height, after the current envelope decreased from the initial peak it showed little variation with time. Thus the increase in the buoyant height with time was due to more dilute fluid being swept downstream at the front face of the roughness and being replaced by denser fluid.

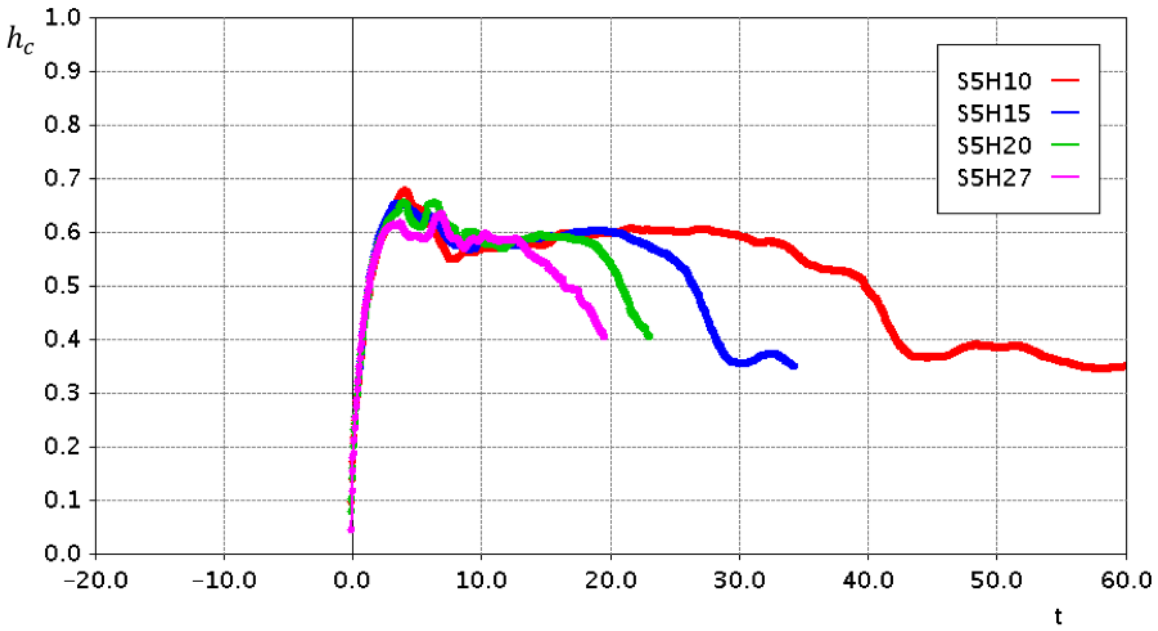

Fig. 5.14 h_c at the front face of the roughness with time for all sparse experiments - S5H10, S5H15, S5H20 and S5H27.

Variation of Height and Density with Time

Figure 5.12 only showed a comparison between the currents of varying relative roughness height at a single time. Therefore, while the behaviour seen in this figure provides insights into how the experiments varied with relative roughness height one could not be certain that this behaviour would be consistent for all times. Furthermore, the blue line in Figure 5.1 indicated that for the S5H20 experiment the buoyant height in the head region decreased with time and this was reinforced by Figure 5.9. The reduction in the buoyant height in the head region was caused by both a reduction in the size of the current at the head and by dilution of fluid near the front. This section will consider how the buoyant height and current envelope of the experiments varied with time.

Figure 5.15 shows the buoyant height of the four sparse experiments with time at the standard head location. While the currents were still travelling over smooth beds (where t<0) they had reasonably constant buoyant heights of approximately 0.44. The buoyant height fluctuated around this value due to instabilities predominantly associated with K-H billows. Beyond this time the buoyant heights of all of the currents rapidly decreased.

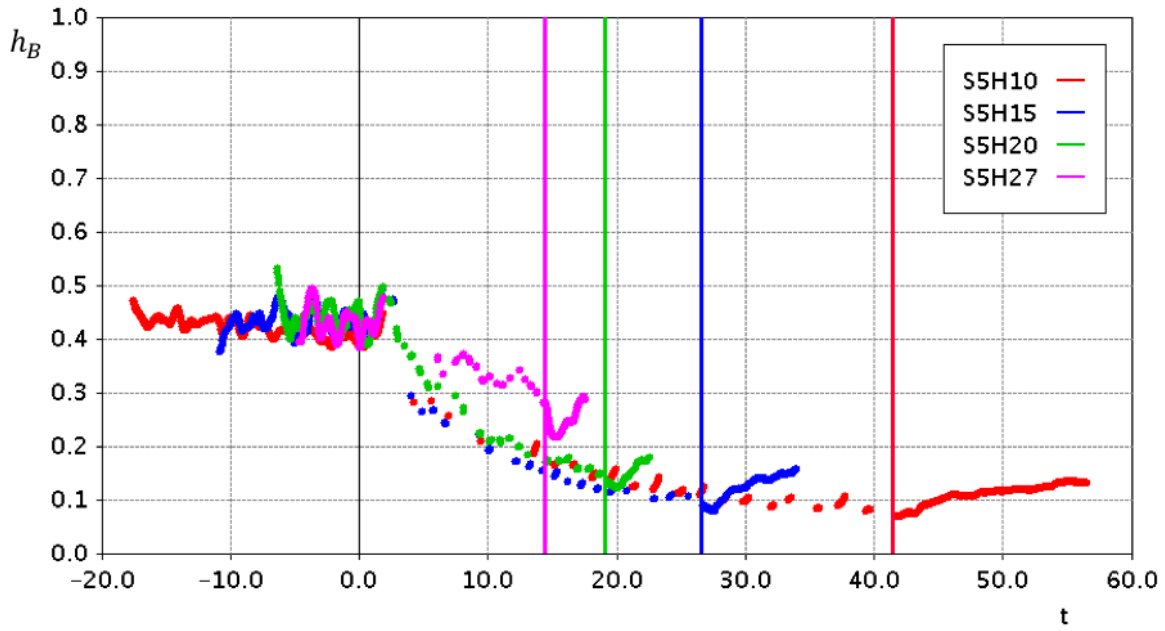

Fig. 5.15 h_B at the standard head location with time for the sparse experiments S5H10, S5H15, S5H20 and S5H27. Vertical lines correspond to locations where the currents exited the roughness. A time of 0 corresponds to the time when the currents encountered the front face of the roughness.

At an early time the rate of buoyant height decrease was dependent on the relative roughness height. This trend was caused by the currents with smaller relative roughness heights having more pronounced heads, as was seen in Figure 5.12. However, as time increased the buoyant heights became similar with only the S5H27 experiment not matching the other experiments before reaching the end of the roughness. As Figure 5.12 indicated that at earlier times the currents all had similar buoyant heights in the tail, the implication of Figure 5.15 is that once the currents became similar in the frontal region, with the exception of the S5H27 experiment, they all took on matching wedge-like characteristics. The S5H27 experiment did not match the others at the end of the roughness because, as was seen in Figure 5.12, it still maintained a pronounced head at this time. However, this figure does suggest that further behind the front all experiments would exhibit similar variations in the buoyant height. Therefore, it would be expected that at a distance further behind the front all of the experiments would exhibit similar temporal development. The similarity further upstream from the standard head location is tested in Figure 5.16, which shows the buoyant height a distance of 4 behind the front. It is seen that the currents were similar for all times at this location, indicating that the only variation between currents with time was in the frontal region.

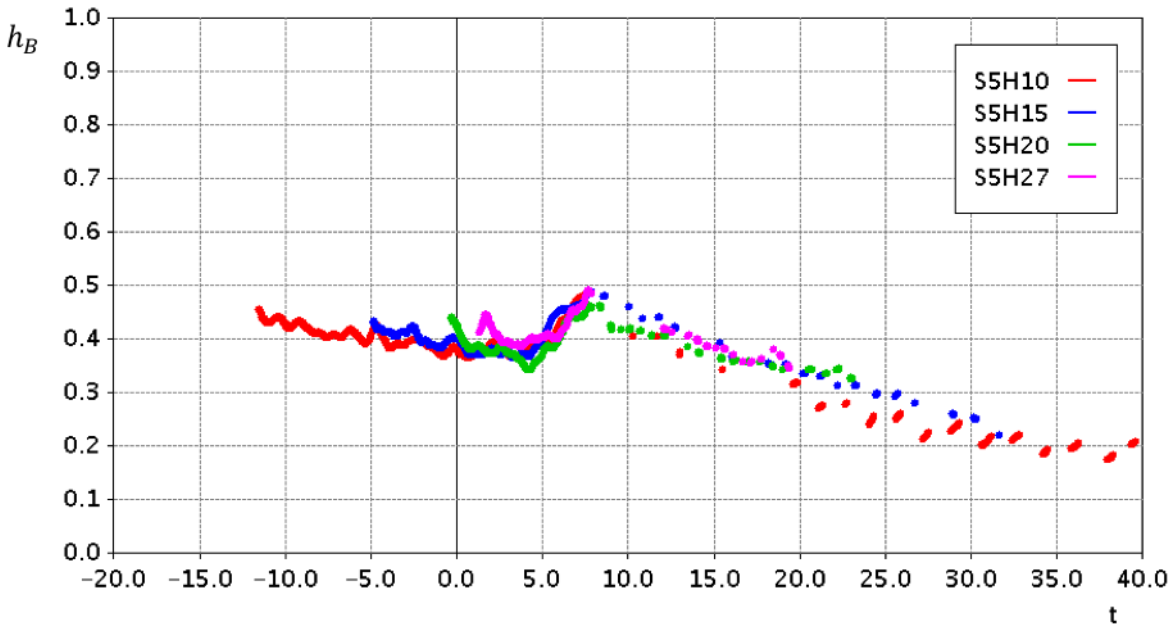

Fig. 5.16 h_B a distance of 4 behind the front location with time for all of the sparse experiments S5H10, S5H15, S5H20 and S5H27.

The vertical lines in Figure 5.15 indicate times when the currents exited the roughness. When the currents exited the roughness and re-established as smooth bed currents their buoyant heights continued to decrease for a short distance, likely as the currents still acted as if they were travelling through the roughness. After a short distance the buoyant heights began to increase again as the currents grew to resemble smooth bed currents. This increase is consistent with the increase in Fr with time seen in Section 5.2.2 and is thought to be caused by both the growth of the currents, due to a transition from a wedge-like structure back to a head and tail structure as they travelled, and by dense fluid in the tail, no longer hindered by the roughness, being able to re-enter the head.

Figure 5.17 shows the current envelope of the same four sparse experiments at the standard head location with time. This figure shows that the vertical extent of the currents varied similarly to the buoyant height with all experiments except for the S5H27 experiment reducing at different rates at early times and collapsing as time increased. Therefore, the vertical extent was a major driver of the buoyant height reduction with time.

The current envelope of the S5H27 experiment did not significantly decrease with time because the current still maintained a head-like, deep portion of flow. This experiment likely represents a transition between a wedge-like regime and a head and tail regime where currents with smaller

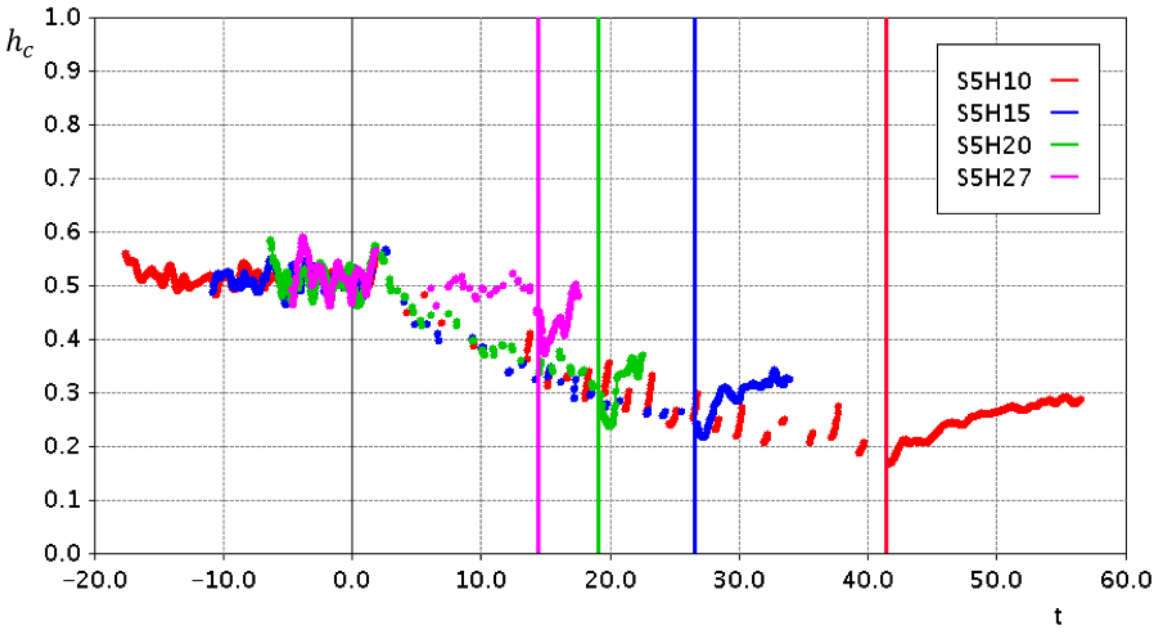

Fig. 5.17 h_c at the standard head location with time for the sparse experiments S5H10, S5H15, S5H20 and S5H27. Vertical lines correspond to locations where the currents exited the roughness and t=0 corresponds to the time when the current front encountered the front face of the roughness.

relative roughness heights would begin to take on characteristics similar to smooth bed currents. It can logically be expected that as the relative roughness height decreases a current should become similar to a smooth bed current. Therefore, it is not unexpected that the experiment with the smallest relative roughness height would be the most similar to a smooth bed current. Once the currents re-emerged the envelopes were all seen to begin increasing again, indicating that the increase in the buoyant height was not only due to denser fluid re-entering the head but also due to an increase in the vertical extent after the currents exited the roughness.

Figure 5.18 shows the average non-dimensional density (computed as $\frac{h_B}{h_c}$) within the four sparse experiments at the standard head location. As the currents travelled through the roughness a similar trend to that seen is Figure 5.15 is visible. This similarity indicates that the decrease in buoyant height was due to both a decrease in vertical extent and the density of fluid in the head.

Experiments with roughness beginning at the lock gate

Section 5.2.2 showed that there was a negligible difference in the Froude number when currents were allowed to develop before encountering the roughness rather than the roughness beginning at the lock gate. Therefore, it could be reasonably expected that there would also be a negligible

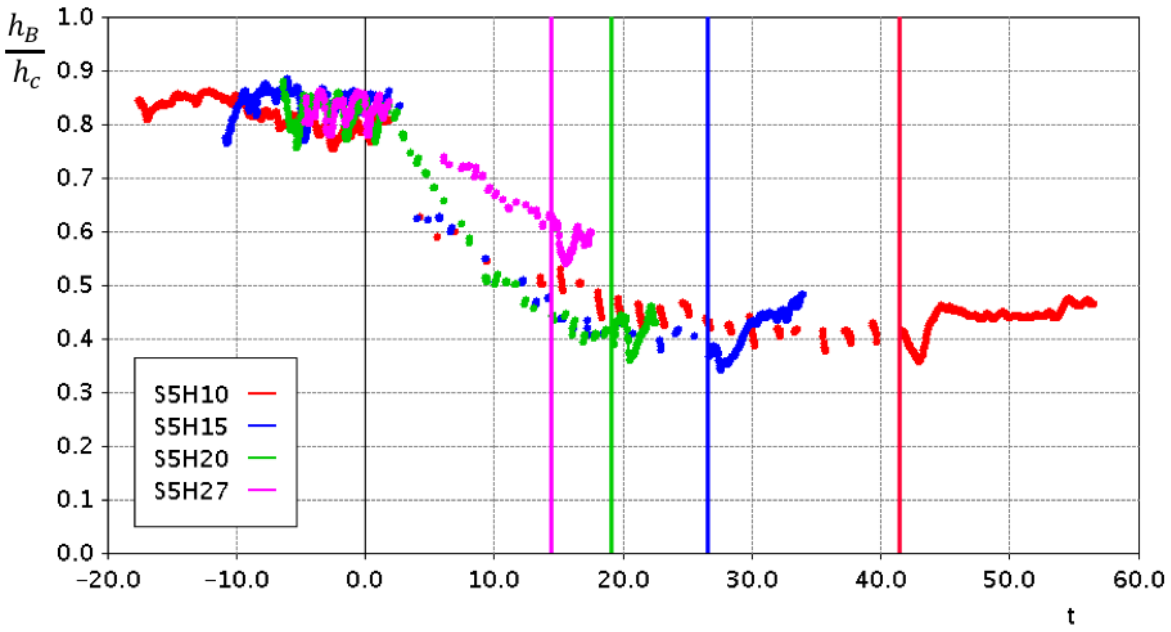

Fig. 5.18 h_B/h_c at the standard head location with time for sparse experiments S5H10, S5H15, S5H20 and S5H27. Vertical lines correspond to locations where the currents exited the roughness.

impact on the buoyant height. To investigate this finding Figure 5.19 compares the buoyant height at the standard head location for the S5H10 and S5H20 experiments with the S5H10G and S5H20G experiments. This figure shows that the impact of allowing a current to establish before interacting with roughness is minimal. However, at early times the experiments with the roughness beginning at the lock gate had slightly higher buoyant heights than the experiments where the currents were allowed to establish first. This difference is not unsurprising as the head of the currents which had been allowed to establish before reaching the roughness would have been slightly diluted when the currents reached the roughness. When the currents had travelled for a short time into the roughness and as they emerged from the roughness the buoyant heights were very similar.

Section 5.2.2 also showed that as the currents re-established after exiting the roughness their Froude numbers increased. The previous section indicated that this increase was due to a transition from a wedge-like structure back to a head and tail structure as they travelled, and by faster moving dense fluid in the tail, no longer hindered by the roughness, being able to enter the head. However, the experiments with the roughness located downstream of the gate only allowed for measurements of the currents over a short distance after they exited the roughness. Therefore, to further investigate how the currents developed with time as they exited the roughness Figure

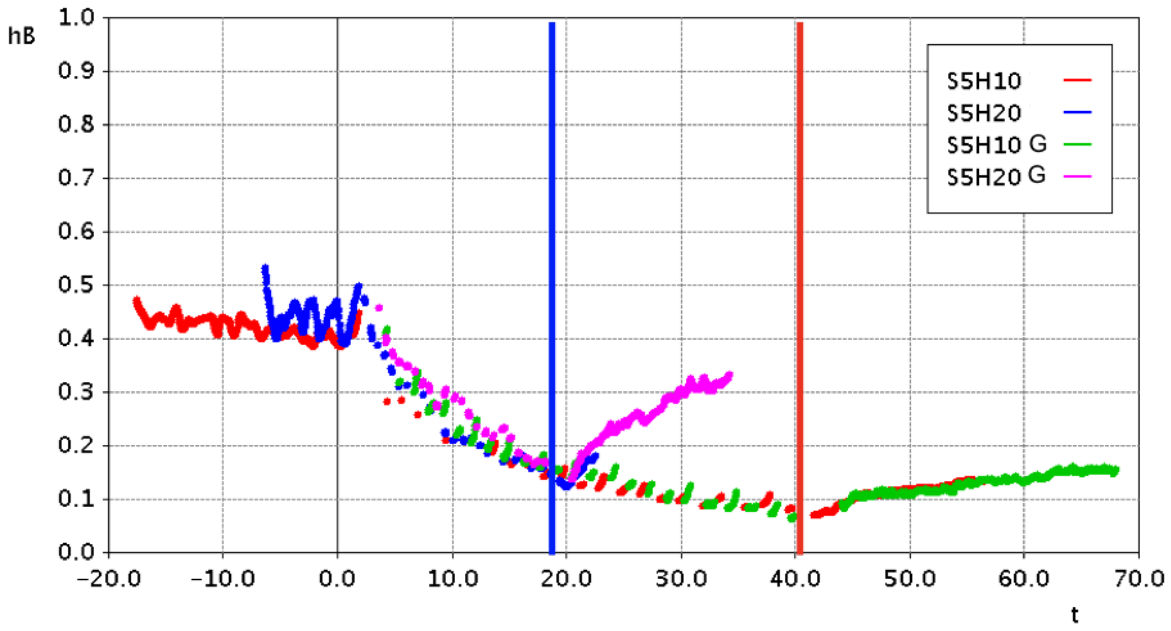

Fig. 5.19 h_B at the standard head location for the S5H10, S5H10, S5H10G and S5H20G experiments. A time of 0 corresponds to when the currents first encountered the roughness and the vertical lines show locations when the currents exited the roughness.

5.20 shows the buoyant height at the standard head location with time for the S5H10G, S5H15G, S5H20G and S5H27G experiments as the currents exited the roughness. In this figure a time of 0 corresponds to the time when the currents exited the roughness.

Similar to the Froude number discussed in Section 5.2.2 the buoyant height when the currents exited the roughness can be seen to depend on the relative roughness height. This trend is due to the experiments with larger relative roughness heights travelling larger non-dimensional distances through the roughness before exiting. The rate of buoyant height increase and the distances the currents travelled before their heights became constant also depends on the relative roughness height. The S5H27 experiment reached a steady state after a time of approximately 3 where even after a time of 20 the S5H10G and S5H15G experiments had not yet reached steady states. This trend could be explained by the experiments with smaller relative roughness heights having structures closer to the head and tail structures of smooth bed currents when they reached the end of the roughness. Therefore, it was easier for these currents to re-establish as smooth bed currents.

Figure 5.21 shows the equivalent of Figure 5.20 but for the current envelope. The trend in the current envelope with time and relative roughness height is very similar to the trend in the

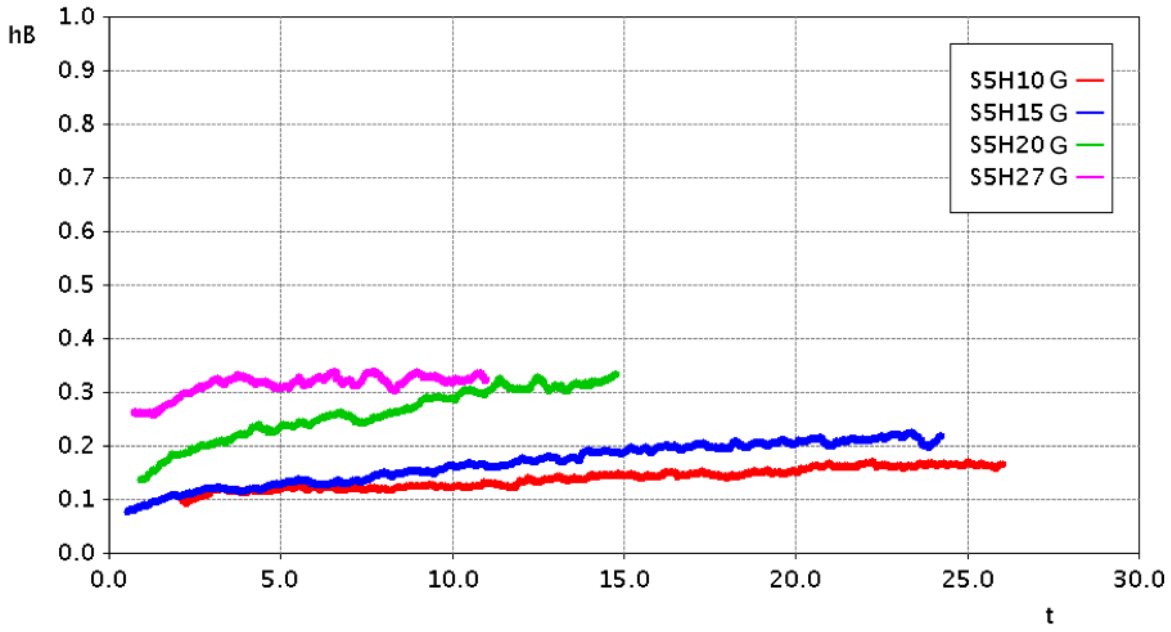

Fig. 5.20 h_B at the standard head location for the S5H10G, S5H15G, S5H20G and S5H27G experiments. A time of 0 corresponds to the time when the currents exited the roughness.

buoyant height. However, the current envelope reached steady states slightly earlier. Therefore, it can be concluded that dense fluid continued to enter the current heads from the tail after the currents had re-established as smooth bed currents.

5.3 Mathematical Model

It was seen in Section 5.2 that when the currents encountered roughness in the sparse configuration they took on wedge-like characteristics. While some currents still displayed the raised head characteristic of smooth bed experiments they were all shown to display wedge-like characteristics with increasing buoyant heights behind the heads. It was postulated that the wedge-like structure caused the currents to become driven predominantly by a balance between the pressure gradients in the wedge and the drag forces imposed on the currents by the roughness. The buoyant heights behind the head were seen to be similar for all experiments, regardless of the relative roughness height, as were the Froude numbers of the currents. This section develops a simple mathematical model assuming a balance between the drag force imposed on the currents per unit volume by the cylinders and the driving pressure gradient in an attempt to explain some of this behaviour.

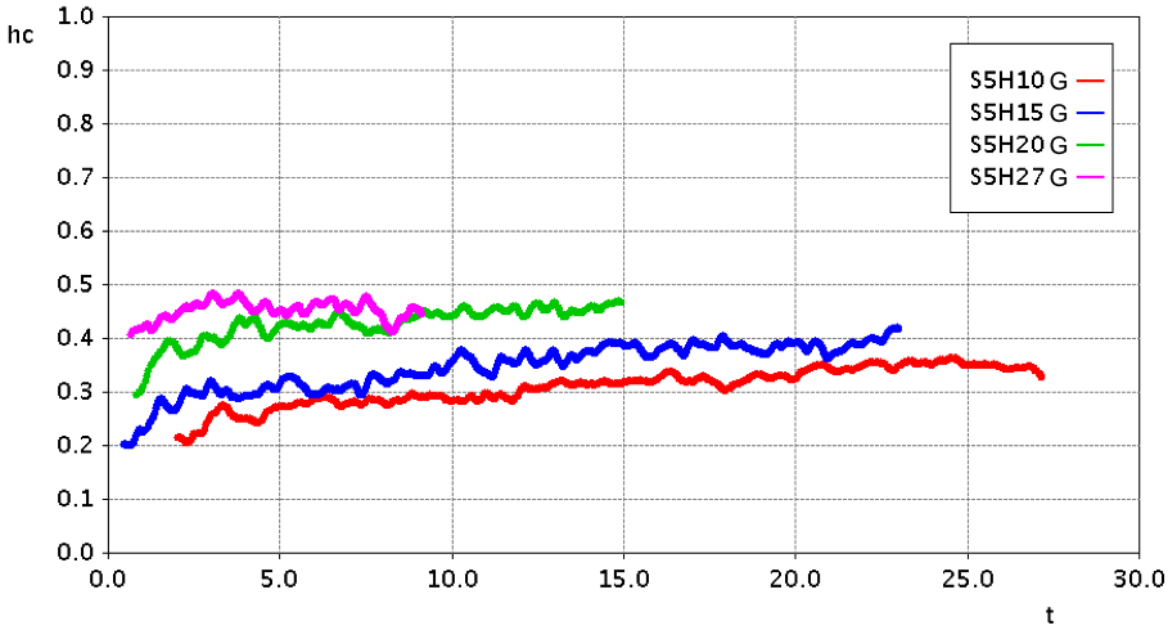

Fig. 5.21 h_c at the standard head location for the S5H10G, S5H15G, S5H20G and S5H27G experiments. A time of 0 corresponds to the time when the currents exited the roughness.

Figure 5.22 shows a schematic for this model. Despite it being seen in Section 5.2 that significant mixing occurred as the currents travelled it is assumed that the currents in the wedge region can be represented by unmixed linear wedges with the current having a density of ρ_2 and the ambient fluid having a density of ρ_1. In this region the roughness is assumed to be completely submerged within the current with a height and diameter η_c and d_c and spacings in the x and z directions of S_x and S_z. It was seen in Section 5.2 that the buoyant height at the front face of the roughness increased slightly with time, however this occurred over a much longer timescale so the height at this location is assumed to be constant and proportional to the total fluid depth. This height is referred to as aH where a is a constant. The height of the wedge downstream of the front face of the roughness but upstream of the head region, h, is allowed to vary with time. Assuming the current formed a wedge-like structure with its angle decreasing in time, the downstream height is given by

$$h = \frac{x_F^* - x^*}{x_F^*} aH \tag{5.1}$$

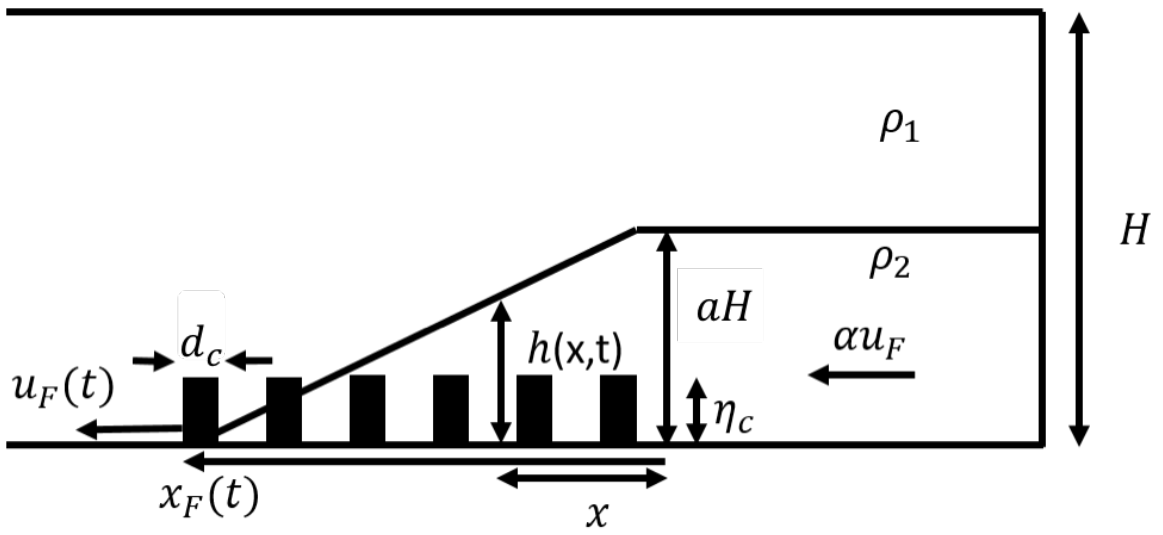

Fig. 5.22 Schematic showing a simplified geometry to generate balance between pressure gradient and drag.

where x is defined such that x=0 corresponds to the front face of the roughness. Assuming the pressure is hydrostatic throughout the current, the pressure at the base of the channel at a given time (constant x_F) is given by

$$P(x^*)^* = \rho_1 g(H-h) + \rho_2 gh \tag{5.2}$$

Substituting 5.1 into 5.2 and differentiating it with respect to x gives

$$\frac{dP^*}{dx^*} = \frac{(\rho_2 - \rho_1)gaH}{x_F^*} \tag{5.3}$$

It is assumed that the drag force imposed by each individual cylinder is equal and cumulative and that this can be represented by a quadratic drag law. The drag force is calculated within a control volume of length x_1 rather than over the whole length of the current as the head dynamics are neglected. As the wedge is considered to be linear, x_1 could be any length providing it only covers an area where the height of the current is larger than the roughness. Within this control volume the fluid velocity is considered to be proportional to the front speed so is termed αu_F^* where α is a constant of proportionality. Therefore, the drag force per unit volume is given by

$$\frac{F_D}{V} = \frac{c_D \rho_2 (\alpha u_F^*)^2 N d_c \eta_c}{2Bx_1 H} \tag{5.4}$$

where c_D is the drag coefficient and N is the number of cylinders within the control volume. Balancing the pressure gradient with the drag force per unit volume gives

$$\frac{c_D \rho_2 (\alpha u_F^*)^2 N d_c \eta_c}{2Bx_1 H} \sim \frac{(\rho_2 - \rho_1) g c H}{x_F^*} \tag{5.5}$$

As a reminder, B is the width of the channel. This equation is rearranged for the dimensional front speed to give

$$u_F^* = \sqrt{\frac{Ag' S_x S_z H^2}{d_c \eta_c x_F^*}} \tag{5.6}$$

where A combines the constants c_D and α as $A = 2c_D\alpha^2$ as well as incorporating the proportionality in Equation 5.5, and $S_x S_z = \frac{N}{Bx_1}$. Equation 5.6 is then divided by $\sqrt{g'H}$ to obtain the Froude number in terms of the non-dimensional front location (where $x_F^* = x_F H$). The roughness properties are left in dimensional form. This gives

$$Fr = \sqrt{\frac{AS_x S_z}{d_c \eta_c x_F}} \tag{5.7}$$

Equation 5.7 leads to several interesting results. Firstly, it provides insight as to why the Froude number was seen in Section 5.2.2 to be independent of the relative roughness height. The relative roughness height is not present in 5.7 and instead, two non-dimensional parameters, $\frac{\eta_c}{S_x}$ and $\frac{d_c}{S_z}$are present. These parameters could alternatively be thought of as $\frac{\eta_c}{S_z}$ and $\frac{d_c}{S_x}$. The independence of the relative roughness height arises due to the currents with smaller H being more strongly impacted by each row of cylinders than currents with larger H but these currents passing fewer rows of cylinders after travelling the same non-dimensional distance. Thus, the overall impact of the roughness was unaffected by the relative roughness height if $\frac{\eta_c}{S_x}$ and $\frac{d_c}{S_z}$ are held constant. As the height, spacing and diameter of the roughness is not varied for currents in this chapter, $\frac{\eta_c}{S_x}$ and $\frac{d_c}{S_z}$ are the same for all of the currents. Moreover, this equation shows that Fr varies with x as $Fr \sim \frac{1}{\sqrt{x_F}}$. To compare this to Figure 5.4 equation 5.7 is expressed in terms of time. The full derivation for this can be found in Appendix B. The result is

$$Fr = \left(Ct \frac{d_c \eta_c}{S_x S_z} + E \right)^{-\frac{1}{3}} \tag{5.8}$$

where $C = \sqrt{\frac{3}{2A}}$ and E is a constant of integration. The constant E is determined by the initial conditions (where t=0, Fr = 0.46) to be approximately 10.3 and should not depend on the

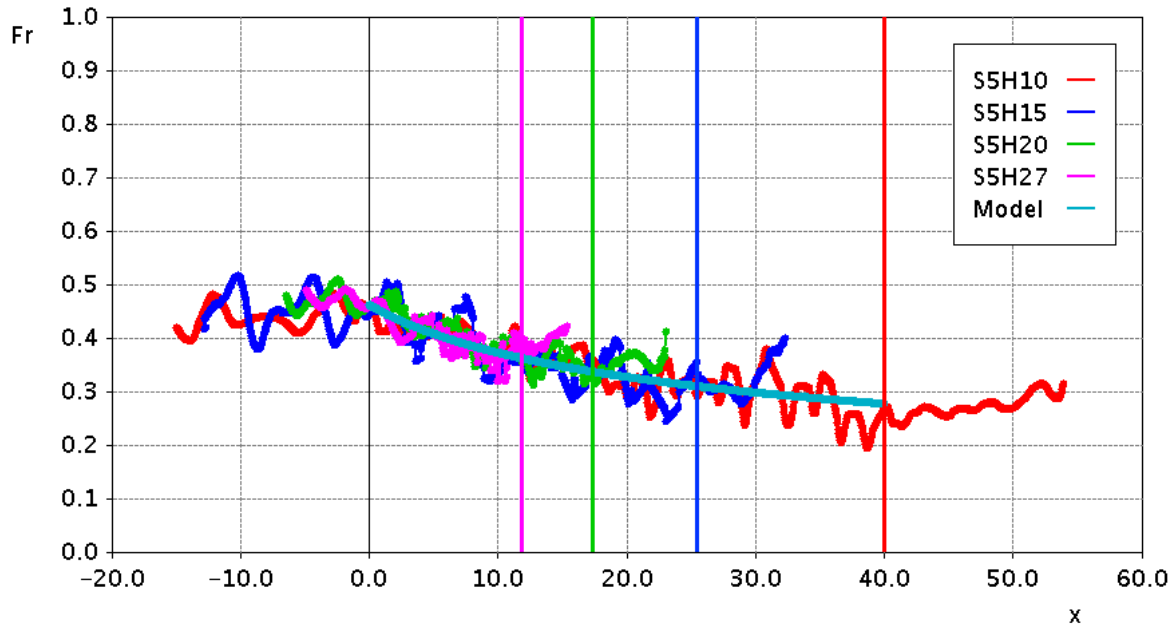

Fig. 5.23 Froude Number with time for the sparse experiments - S5H10, S5H15, S5H20 and S5H27 as well as an analytical model for the Froude number with time. The currents entered the roughness at a time of 0 and the vertical lines show the times when the currents exited the roughness.

properties of the roughness. The constant C is found empirically from the data, using an ordinary least squares fit on an average of all of the data, to be approximately 3.8. Figure 5.23 plots Equation 5.7 together with the data from Figure 5.4. The model fits the data well.

Certainly, this model ignores some fundamental physics. Particularly of concern is that it neglects the frontal region, which has been argued to govern the speed of smooth bed currents (Nokes et al., 2008). Even more problematic is the assumption that these currents travelled as linear wedges with their gradients being determined entirely by the front location. A wedge shape at the front is counter to the findings in Section 5.2 showing that the head region did not always take on wedge-like characteristics. However, if the pressure gradient in the tail is responsible for driving the front the velocity in the tail must be related to the front velocity. Furthermore, the assumption that all cylinders would equally contribute to the drag force may be unreasonable as it has been shown that in arrays of cylinders sheltering effects can occur (Raupach, 1992). However, after the initial rows of cylinders the sheltering effects could be reasonably assumed to be roughly equal on all of the cylinders. In addition, it was assumed that the drag coefficient is independent of current speed and it has been shown that for low cylinder Reynolds numbers ($Re_c = \frac{ud_c}{\nu}$) this is not the case (Koch and Ladd, 1997). Despite

these inadequacies the model is a good fit to the data and supports the notion that a current interacting with sparsely distributed roughness is predominantly driven by a balance between a pressure gradient and drag.

5.4 Velocity Measurements

5.4.1 Introduction

While the density measurements shed light on a number of important aspects of these currents there are a number of questions left unanswered. Primarily this section attempts to confirm that the currents were through-flowing and to determine whether the roughness impacts the amount of ambient fluid entrained into the currents.

5.4.2 Horizontal velocity profiles

The PTV measurements for the sparse experiments were conducted along the centreline of the channel as shown in the top down schematic in Figure 5.24. This figure shows that measurements obtained between different gaps in the cylinders could not be compared directly. At location A the fluid within the measured area would be directly behind a cylinder and hence a wake would likely be seen at this location. Wakes could cause velocities in the opposite direction to the flow. Alternatively, fluid at location B would have come from a gap between cylinders and would be directly in front of a cylinder. As such the wakes would not be as prominent at this location and the fluid would be moving in the direction of the current. To test this idea Figure 5.25 shows the velocity field in the tail for the S5H20 experiment with labels corresponding to A and B from Figure 5.24. This figure shows strong velocities in the direction of the current at B locations and velocities close to zero including negative velocities at A locations. Thus wakes were present behind cylinders at location A and not at location B.

As the velocity behaviour was different in alternating gaps between cylinders an averaging process was undertaken before generating velocity profiles. It could be argued that, provided changes to the velocity field occurred slowly, the measurement of a current travelling past location A would be equivalent to a measurement of a current travelling past the location A' and similarly a measurement of a current travelling past location B would be equivalent to a measurement of a current travelling past location B' (refer to Figure 5.24). Therefore, the

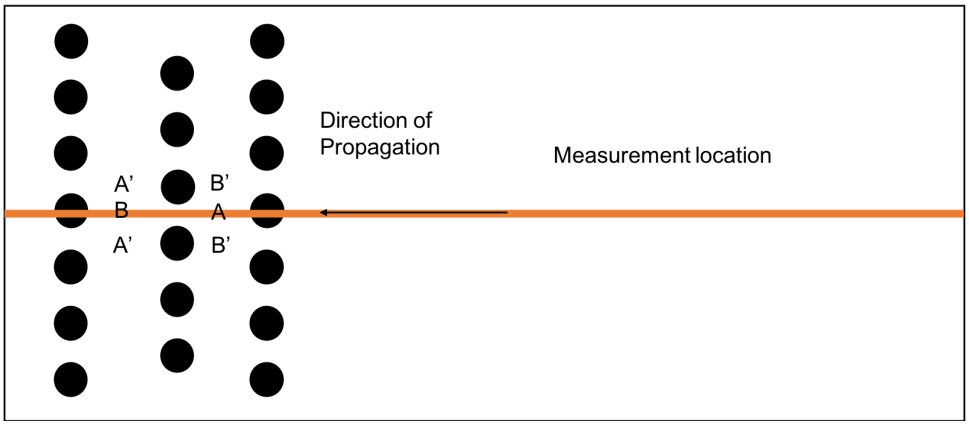

Fig. 5.24 Schematic showing the location of PTV measurements relative to the roughness elements.

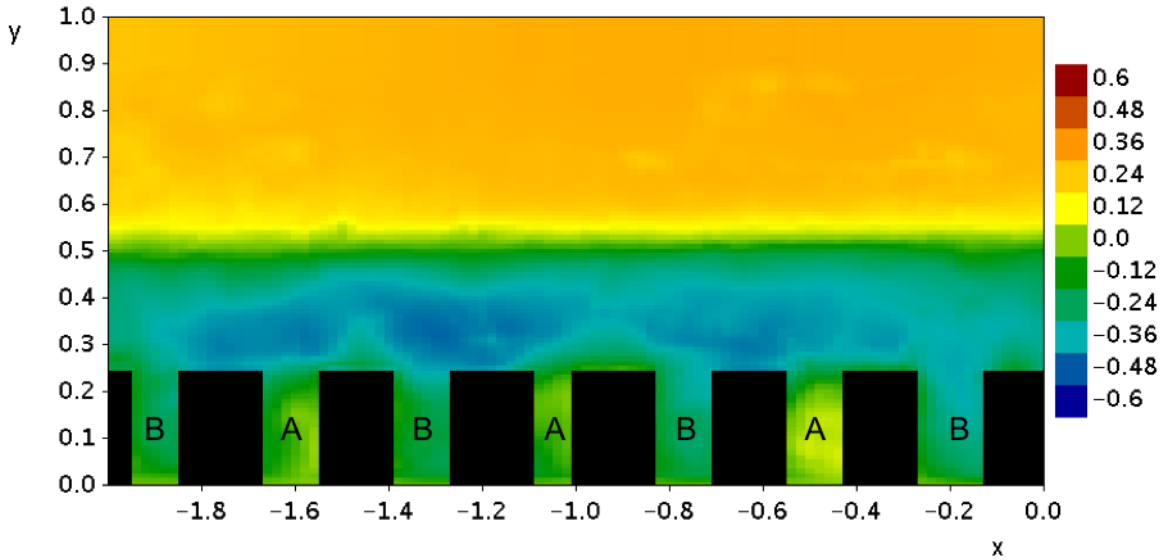

Fig. 5.25 Instantaneous horizontal velocity field for S5H20 experiment shown in false colour over the entire depth from x=-2 to x=0 at a time of 15.

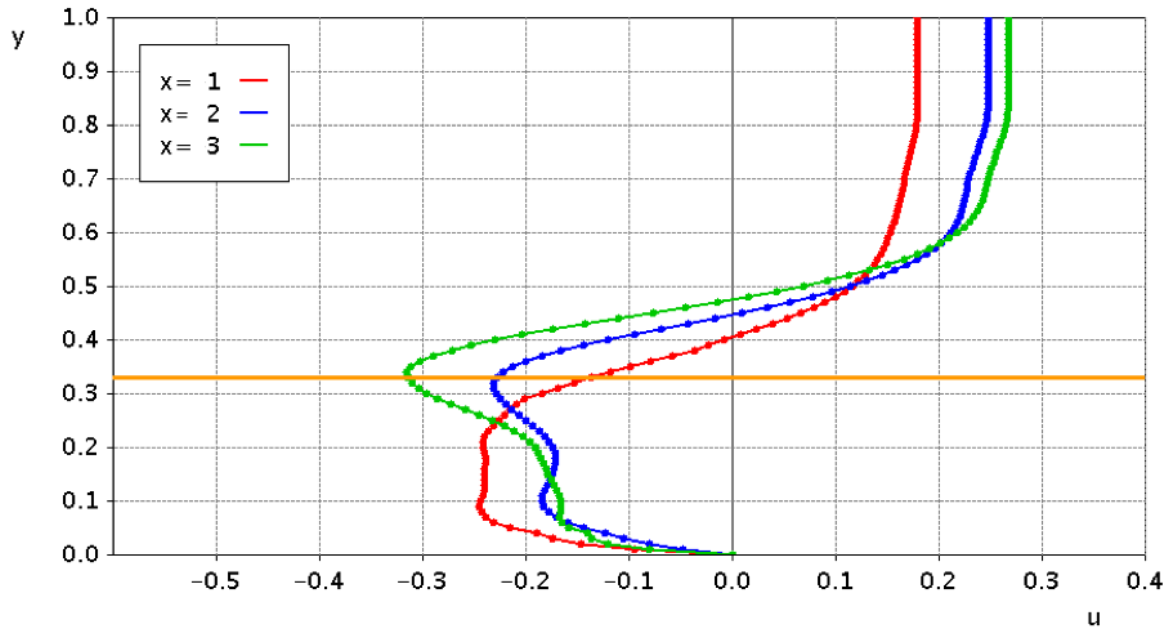

Fig. 5.26 Velocity profiles for the S5H15 experiment at a time of 10 after the current encountered the roughness and x locations of 1,2 and 3 behind the front. The orange line shows the roughness height.

average of measurements as currents passed through two gaps in cylinders would be roughly equivalent to width averaging a measurement within a single gap. To carry out this average the data was transferred into a moving frame of reference where the nose of the current was considered to be stationary and the cylinders were considered to be moving. Then the data was time averaged over short periods that covered the time taken for currents to travel past two cylinder gaps. This averaging process was applied to generate the horizontal velocity profiles presented in this section. Despite this averaging, these velocity fields could vary by as much as 5%. As such the conclusions drawn from these velocity profiles are largely qualitative.

Figure 5.26 shows horizontal velocity profiles for the S5H15 experiment at a time of 10 and three different locations relative to the front. A time of 10 was selected because at this time all of the sparse experiments could be compared. The figure shows that at the standard head location (a distance of 1 behind the front) the flow was entirely contained within the roughness. Further behind the front (distances of 2 and 3 behind the front) the peak speeds were above the roughness due to the current wedge extending beyond the top of the roughness. However, significant flow is still visible within the roughness at all locations, confirming that this current could be considered through-flowing. Additionally, the height at which the velocity became 0 increased in the upstream direction, consistent with the current having a wedge-like structure.

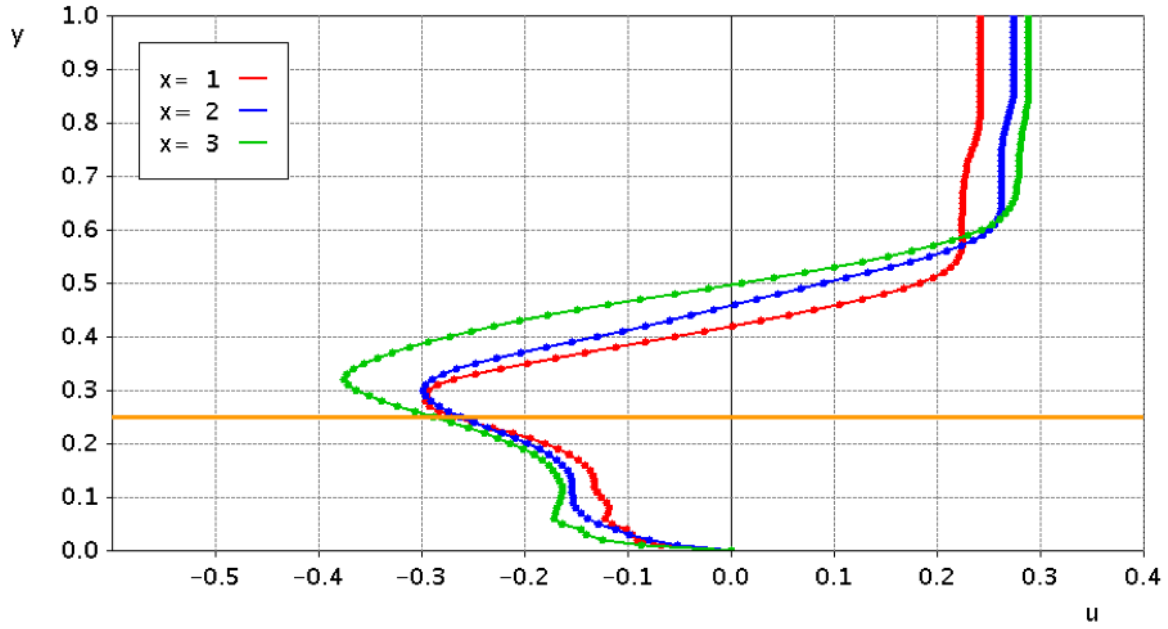

Fig. 5.27 Velocity profiles for S5H20 experiment at a time of 10 after the current encountered the roughness and x locations of 1,2 and 3 behind the front.

Figure 5.27 shows the equivalent of Figure 5.26 for the S5H20 experiment. It shows that, unlike Figure 5.26, at the standard head location there was significant flow above the roughness, indicating that the roughness was submerged within the current. Near the front the experiments with larger relative roughness heights had roughness that was emergent for a longer distance behind the front. However, as with the S5H15 experiment, there was still significant flow within the roughness. As the distance behind the current front increased the horizontal velocity of the flow at all locations in the current increased in magnitude and the current increased in height. This trend is similar to the S5H15 experiment, matching the observations in Section 5.2 that the currents were all similar behind the head.

The S5H27 experiment showed features very similar to those in Figure 5.27; however the S5H10 experiment did not. Therefore, the velocity profiles for the S5H10 experiment are shown in Figure 5.28. These profiles confirm earlier observations that the current was submerged in the roughness for most of its horizontal extent. The reason for this current being submerged within the roughness is that the relative roughness height was large enough that the vertical extent of the current with a wedge structure was naturally lower than the height of the roughness. As with the S5H15 and S5H20 experiments the height at which the velocity of this current became zero increased with x.

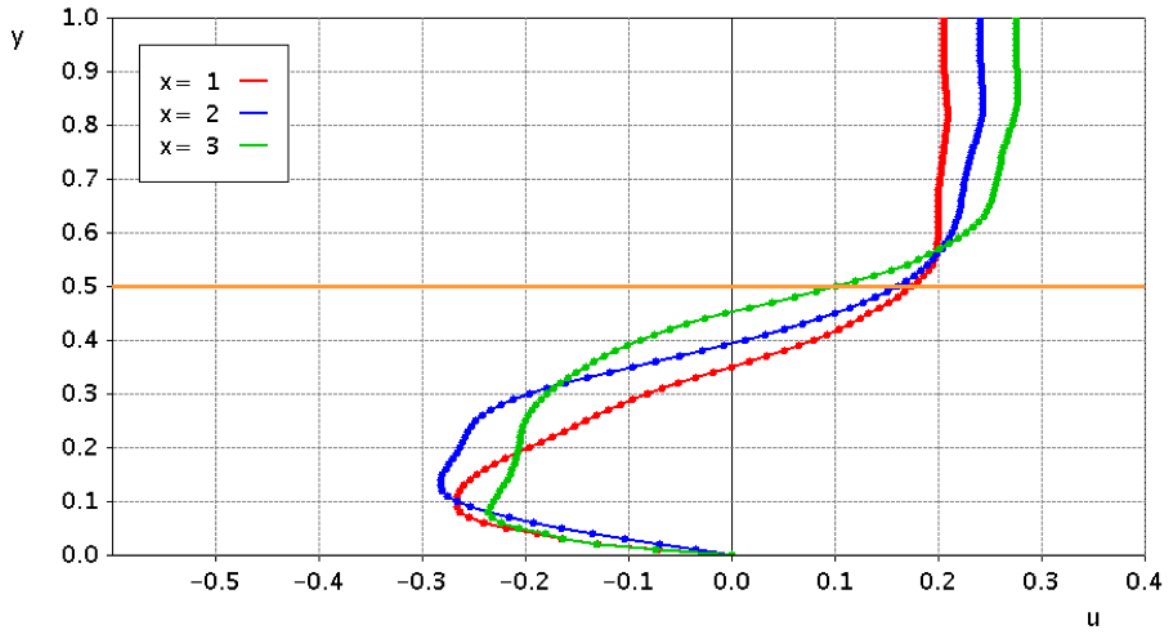

Fig. 5.28 Velocity profiles for S5H10 experiment at a time of 10 and x locations of 1,2 and 3 behind the front.

To explore the impact of time on the current velocity profiles Figure 5.29 shows the horizontal velocity of the S5H15 experiment at four different times at the standard head location. At this location the current was still primarily contained within the roughness (refer to Figure 5.26). This figure shows a large reduction in velocity and height of the current with time, consistent with the observations in Section 5.2 that the currents decreased in height and slowed as they travelled. For comparison, Figure 5.30 shows the S5H20 velocity profiles at the standard head location at 3 different times. Unlike the S5H15 experiment at this location the roughness was submerged within the current (refer to Figure 5.27). These profiles show the current decreasing in speed and size over time. However, between a time of 10 and 15, this current decreased in size and the velocity within the bed increased. Thus, as the angle of the wedge decreased a larger proportion of current fluid became through-flowing with time.

5.4.3 Volume Flux

Horizontal velocity fields can also be used to understand entrainment of ambient fluid into the current. To carry out this analysis three different two-dimensional volume fluxes are defined: the ambient flux (q_A), the current flux (q_C) and the total flux(q_T) representing, respectively, the volume flux of ambient fluid travelling past the current, the volume flux of fluid within the

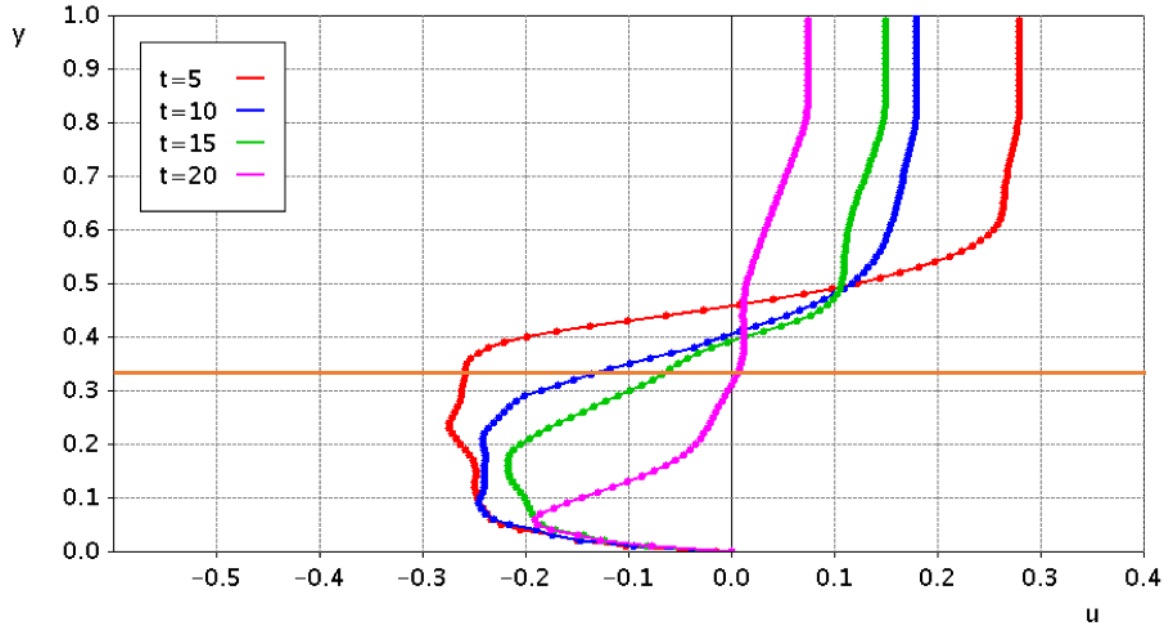

Fig. 5.29 Velocity Profile for S5H15 experiment at the standard head location at times of 5, 10, 15 and 20.

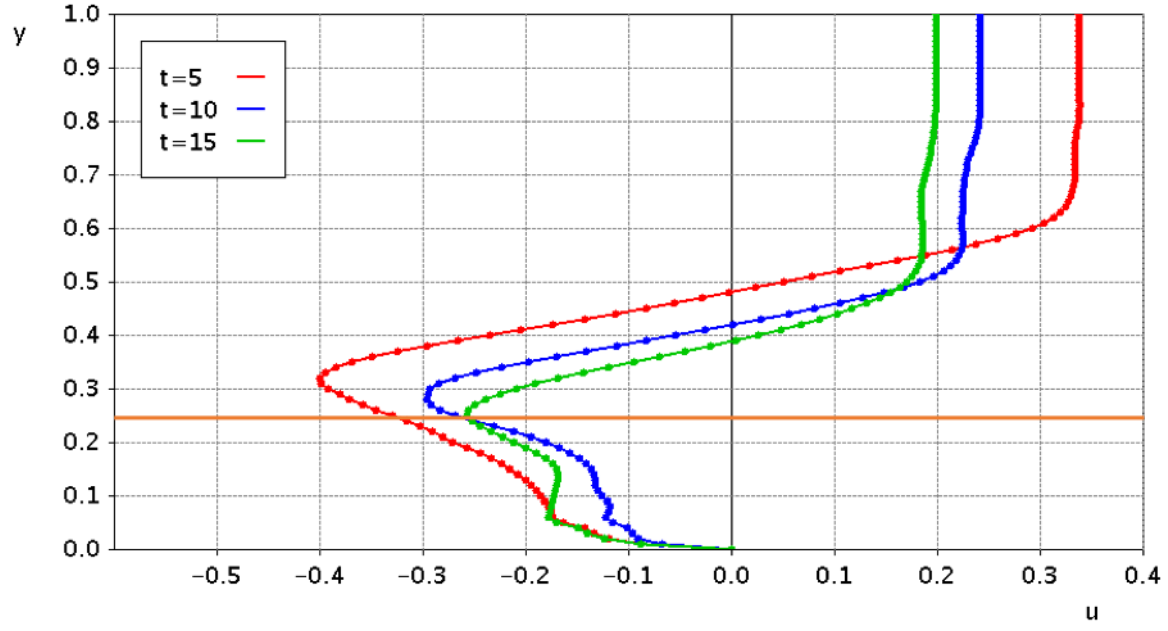

Fig. 5.30 Velocity Profile for S5H20 experiment at the standard head location at times of 5, 10 and 15.

current and the total volume flux of fluid along the centreline of the channel. These are defined as follows

$$q_A = \int_{h_c}^{1} u dy \tag{5.9}$$

$$q_C = \int_{0}^{h_c} u dy \tag{5.10}$$

$$q_T = \int_{0}^{1} u dy = q_A + q_C \tag{5.11}$$

In theory, if there is no cross-channel flow the total flux of a smooth bed current should be zero at all locations and times. However, due to the impact of the side walls and the in-homogeneity of the roughness field it is likely that some cross channel fluxes would occur. If the cross-channel flux is close to zero the ambient and current fluxes must be equal and opposite. As the ambient flux primarily includes velocities above the roughness it is largely unaffected by the roughness. Therefore, the ambient flux provides more reliable data, with cross-channel fluxes more likely to be close to zero than the current flux, meaning that the two-dimensional ambient flux could be used to approximate the three-dimensional ambient flux. On the other hand, due to wakes and locations where fluid is diverted around cylinders large cross channel fluxes are expected within a current, meaning the two-dimensional current flux is unlikely to represent the total flux per unit width. Furthermore, as the cylinders take up some of the fluid volume within the bed the two-dimensional volume flux in a gap between cylinders would not be representative of the total flux within the bed.

The two-dimensional volume fluxes were calculated for the S5H20 experiment and at a time of 11 (when the S5H27 experiment was reaching the end of the roughness) and the three fluxes are plotted together in Figure 5.31. Upstream of the roughness (x>0) the total flux is very close to zero and hence shows that without the roughness present the ambient and current fluid are equal and opposite. However, in locations where roughness is present (x<0) the current flux fluctuated between gaps in the cylinders and the total flux was not always zero. As expected, the fluctuations in the total flux appear to be determined almost entirely by the current flux as

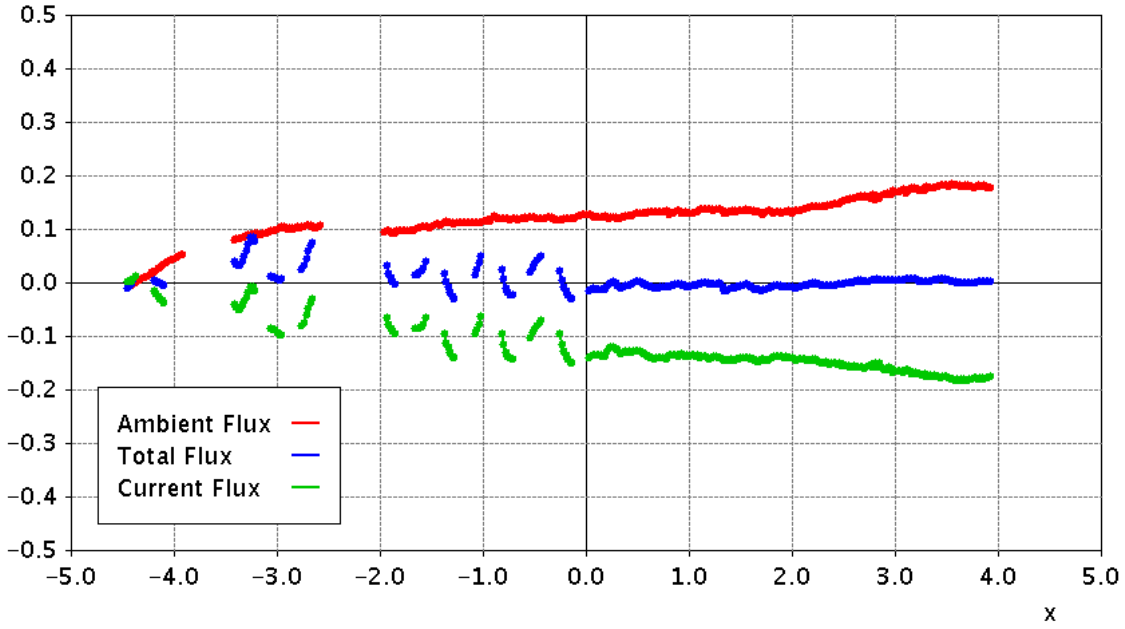

Fig. 5.31 q_A, q_C and q_T at a time of 11 for the S5H20 experiment with x. The front face of the roughness is located at x=0 and the roughness bore located at x=2.

fluctuations are not visible in the ambient flux. Therefore, the ambient fluid was essentially unaware of the cross-stream flows within the cylinders. Therefore, as it is the only quantity that accurately represents the flux per unit width, only the ambient flux is considered for the remainder of this section.

To understand the entrainment rate it was assumed that changes in the current were slow enough that at a time of 11 $\pm$ the time it took for the currents to pass two gaps between cylinders the Froude number was constant. The velocities were normalised by the front at this time before the currents were placed into a moving frame of reference where the current nose was stationary and fluid in front of the nose (which had velocities of 0 in the lab frame of reference) had a velocity of 1. The velocity field was then time averaged.

In front of the current the ambient flux calculated using this method would be 1 for all x until reaching the current. The ambient flux would remain at 1 if there was no transfer of mass between the ambient and the current. Therefore, any reduction in the flux must be caused by entrainment of ambient fluid into the current (or ambient fluid crossing the boundary defined by h_c). Figure 5.32 shows the variation of this ambient flux with x. The ambient flux of all currents reduced from 1 towards a final value of between 0.75 and 0.8 after a distance of approximately 2.5. While there is a large spread in the data there is no clear trend between experiments with

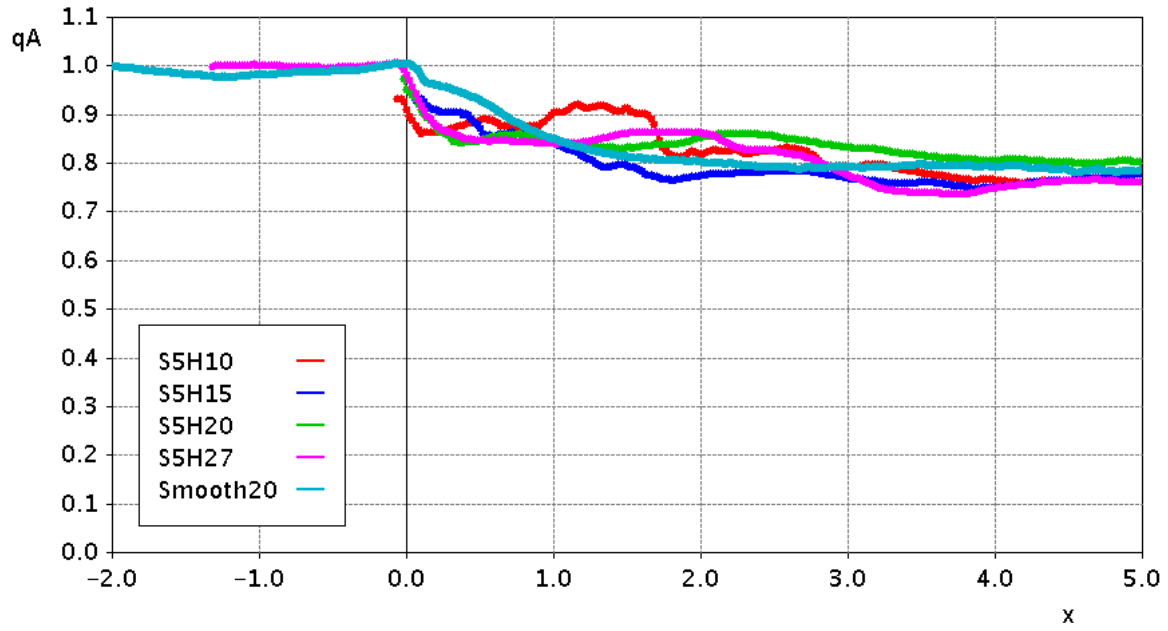

Fig. 5.32 q_A in the moving frame of reference for all of the sparse experiments S5H10, S5H15, S5H20 and S5H27 at a time of 11 as well as a time averaged smooth experiment. The front location of all experiments is redefined to be at x=0.

differing relative roughness heights or even between the smooth and rough bed experiments downstream of the front face of the roughness.

For a smooth bed current, entrainment of ambient fluid into the current is primarily due to K-H instabilities (Sher and Woods, 2015). The entrainment occurs over a distance of only 2.5 where the majority of K-H instabilities break down after which very little entrainment occurs. The similarity between the smooth bed experiment and those with roughness could be explained by one of two reasons. The first is that the K-H instabilities are also the primary cause of entrainment for a sparse configuration experiment and that the roughness elements do not significantly impact the amount of ambient fluid entrained into the current. Thus, as wakes behind the cylinders are primarily buried within the current they do not significantly increase the amount of ambient fluid entrained into the current. The other possible reason is that the effect of the K-H instabilities is lessened by the cylinders by the same magnitude that additional fluid is entrained into the current due to wakes behind the current.

Section 5.2 and Chapter 4 showed that the roughness caused the current head to dilute significantly more than that of a smooth bed current. Thus it is clear that while the roughness does not impact the rate of fluid entrained into the current it impacts what happens to the ambient fluid

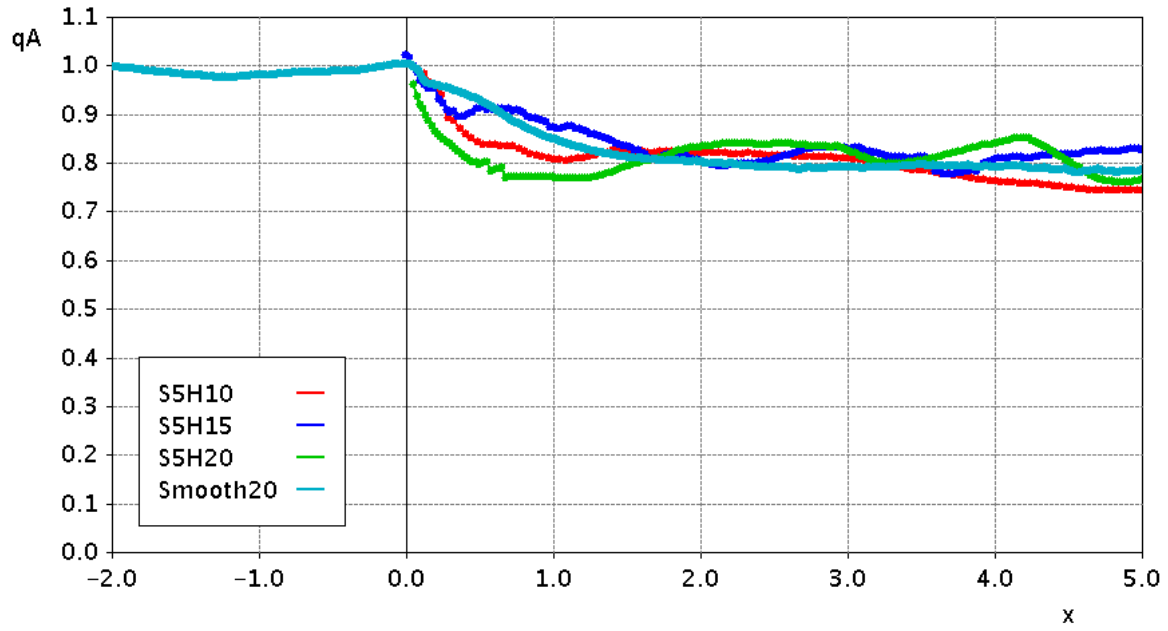

Fig. 5.33 q_A calculated using for the sparse experiments S5H10, S5H15 and S5H20 at a time of 17 as well as a time averaged smooth-bed experiment. The front location of all experiments was redefined to be at x=0. The orange line is the relative location of the front face of the roughness.

once it is entrained. For a smooth bed current as fluid is entrained into the current it is swept upstream relative to the front as the fluid near the front is replaced by fast-moving, dense tail fluid. However, with roughness present, the head dilutes more than a smooth bed current and a wedge-like structure forms as the dense fluid in the tail is unable to replenish the head.

To understand whether the entrainment is impacted by time Figure 5.33 shows the ambient flux in the moving frame of reference for the sparse experiments S5H10, S5H15 and S5H20 at a time of 17. The S5H27 experiment is not included as it had exited the roughness by this time. There is no noticeable difference between the ambient flux at a time of 11 and a time of 17. Therefore, at least after currents have travelled significant distances through the roughness, any variations in entrainment with time are small.

5.5 Summary

This chapter explored results from the sparse configuration experiments in order to understand how properties of the height, Froude number and density of a currents varies with relative roughness height and time. When a current encounters the roughness it propagates through the roughness and its structure transitions to having wedge-like characteristics. As a current

travels the angle formed by the wedge with the horizontal decreases and hence the height of the current near the front reduces with time. As a current travels it dilutes with time and its Froude number decreases. The rate at which the current decelerates is independent of the relative roughness height, while at a given time the extent to which the head has been replaced by a wedge-like structure is dependent on the relative roughness height. However, in the tail the angle and magnitude of the wedge does not depend on the relative roughness height. The existence of a wedge-like structure led to the conclusion that a current interacting with sparsely distributed roughness is driven by a balance between the pressure gradient in the tail and the drag force imposed on the current by the roughness and this balance was supported by a simple mathematical model.

It was also found that the rate of entrainment of ambient fluid into a current is not measurably impacted by the roughness. Thus, it was concluded that either the amount of fluid entrained into a current is determined entirely by the K-H instabilities and not by the cylinders or that the K-H instabilities are lessened by the same magnitude as additional entrainment due to wakes behind the cylinders. However, the cylinders do prevent dense, tail fluid from entering the current head, causing the density of the head fluid to decrease.

As a current exits the roughness and re-establishes on a smooth boundary it begins to grow and re-establishes to resemble a smooth bed current. As the current travels dense tail fluid which had been prevented from entering the current head by the roughness is able to enter the head and replace the dilute fluid. The dilute fluid is swept upstream and the average density within the head of the current grows. The increased density and height of the head causes it to increase in speed with time. Eventually the height, density and speed of the current reach a steady state but the steady values of these quantities are slightly less than that of a smooth bed current.

Chapter 6: Results From Dense Configuration Experiments

6.1 Introduction

In Chapter 4 it was found that while a current interacting with sparsely distributed roughness predominantly travels through the roughness, a current interacting with densely distributed roughness predominantly travels atop the roughness. While a sparse configuration current takes on a wedge-like structure as it travels, a current travelling over densely distributed roughness retains a structure similar to a smooth bed current while travelling over a porous boundary. It was also seen for both the dense and sparse configurations that whether the current propagates over or through the roughness a bore is reflected off the front face of the roughness to provide the necessary energy for the currents to propagate forwards. The current also re-emerges from the roughness resembling a diluted smooth bed current. As Chapter 5 explored the sparse configuration experiments in more detail, this chapter explores the dense configuration experiments. In particular several questions are addressed

- How does a current dilute with time and relative roughness height?
- How is the density structure of the current impacted by the relative roughness height and time?
- How does its Froude numbers develop with time and how is this impacted by the relative roughness height?
- Does the current reach a quasi steady state, wherein the structure of its head stops changing with time and the current propagates forward at a constant speed?
- What is the predominant driving force for the current and how is this impacted by time and relative roughness height?

- How does ambient fluid become entrained into the current and how is this impacted by the roughness?

Section 6.2 explores the results from the density fields generated using the light attenuation (LA) technique. Section 6.2.1 provides an overview of the results by examining a single experiment. The driving force and speed of this current decreased with time as it travelled through the roughness. Furthermore, this section introduces a framework to consider over-flowing currents as smooth bed currents travelling over porous boundaries. Section 6.2.2 then compares how the front speed and Froude number of all experiments varied with time. All of the currents initially propagated through the roughness with fronts propagating atop the roughness behind them. For the D5H20 and D5H27 experiments the over-flowing fronts quickly overtook the through-flowing fronts. From this time, fronts were observed to exist within the roughness field but it was apparent that these fronts did not propagate independently of the overflowing current. Instead, they were induced by the vertical exchange between the current and ambient fluid between the roughness elements. The relative roughness height of the D5H10 experiment was too large for the current to effectively propagate atop the roughness so the front propagated through the roughness in a similar way to the sparse configuration experiments discussed in Chapter 5. The D5H15 experiment is seen to be a transition between the overflowing and through-flowing regimes. This experiment retained a through-flowing front downstream of a separate over-flowing front. The Froude numbers of the over-flowing currents are seen to decrease as the currents travelled before eventually becoming constant.

To understand the mechanisms for the reduction in Froude number with time Section 6.2.3 compares the buoyant height and current envelopes of the different experiments with time. The D5H10 current lost its head and tail structure and took on a wedge-like structure as it travelled. The angle that this wedge formed with the horizontal decreased with time. This current appeared to behave similarly to the sparse configuration currents seen in Chapter 5. The over-flowing currents diluted as they travelled but unlike the sparse configuration experiments or the D5H10 experiment they did not lose their characteristic heads. While the over-flowing heads diluted their vertical extents were constant with time and resembled the shape and extent of smooth bed currents. Eventually, it was found that the average density of an over-flowing currents becomes constant as the reduction in density due to the convective instabilities balances with the dense fluid entering the head from the tail. It is argued that the currents were predominantly driven

by the buoyancy of their heads and evidence of this is seen in Section 6.2.4 where the Froude number based on local depth and density is seen to be constant with time.

Results from the velocity fields, generated by particle tracking velocimetry, are presented in Section 6.3. In Section 6.3.2 instantaneous velocity profiles confirm the structure of the D5H10 experiment to be similar to sparse configuration experiments while also showing evidence of wakes generated behind the cylinders. Velocity profiles confirmed that the remaining experiments predominantly propagated atop the roughness but that in front of the over-flowing front the D5H15 velocity profile resembled that of a through-flowing current. Section 6.3.3 analyses volume fluxes for an over-flowing current to understand the entrainment of ambient fluid into the current. It is found that upstream of the current ambient fluid was ejected from the bed into the current. Additionally, the fluxes indicate that ambient fluid from within the bed percolated upwards through the full depth of an over-flowing current to the ambient fluid above. While some of the ambient fluid mixed with the dense current fluid, the rest may have penetrated the full depth of the current.

6.2 Density Fields

6.2.1 Overview

This section explores results from the density fields generated from the light attenuation (LA) experiments. This analysis makes use of the buoyant heights; analysing how they varied with time, space and between experiments to understand the driving forces. To provide an overview of the main features of these currents Figure 6.1 shows the buoyant height in false colour for the D5H20 experiment as a function of x and t. This experiment is chosen because many of the main features seen in Figure 6.1 are representative of most of the experiments presented in this chapter. The thin vertical black lines represent the locations of the roughness, where the buoyant height could not be calculated. As seen in Chapter 4 there are large areas where, due to parallax issues, there was no visualisation within the roughness at all, explaining the additional large black rectangles.

In Figure 6.1 the pink line shows the path of the roughness bore. The increase in buoyant height after the bore had passed was larger than was seen for the experiments in the sparse configuration in Chapter 5. The buoyant height was larger for the dense configuration because

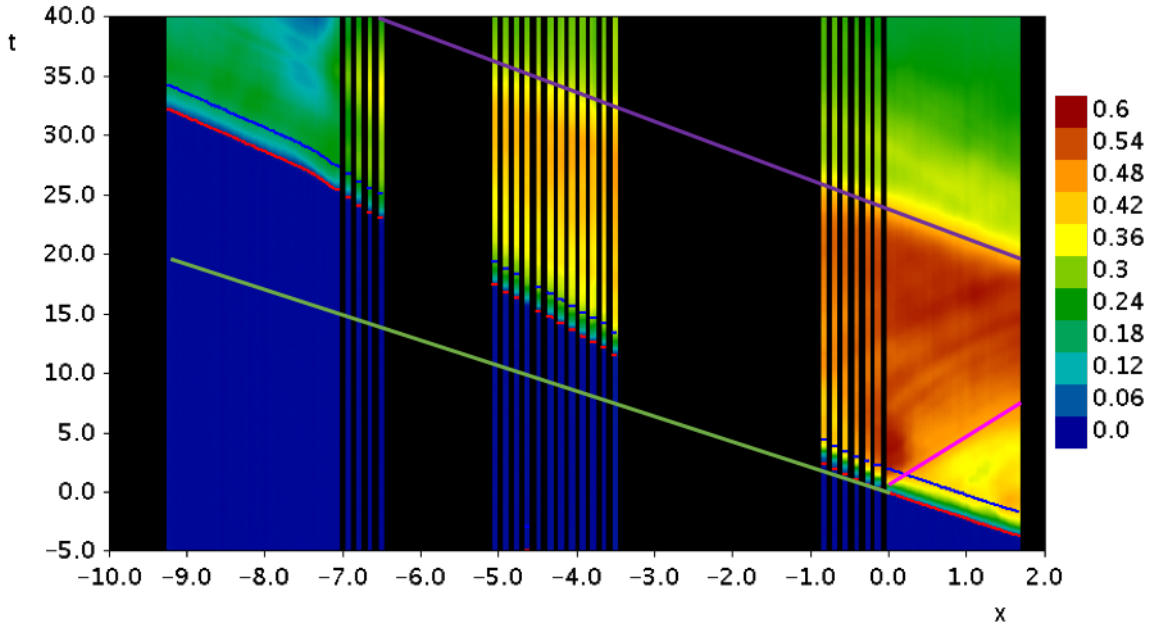

Fig. 6.1 D5H20 h_B based on the unobstructed depth displayed as false-colour with x and t. The red line shows the front location of the current, the blue line represents the standard head location, the pink line shows the path of the roughness bore and the purple line shows the path of the lock bore. The green line is an extrapolation of the path of a smooth bed current. The black regions represent locations where visualisation was insufficient to calculate the buoyant height.

its frontal area was larger than for its sparse counterpart (S5H20). A larger frontal area caused a larger proportion of the fluid to be deflected upwards as the current encountered the roughness. Otherwise the main features of Figure 6.1 are similar to those in the sparse experiments. The path of the lock bore is represented by the purple line. Additionally, the buoyant height at the standard head location decreased as the current travelled through the roughness (along the blue line). These features are explored further in Section 6.2.3.

The red line in Figure 6.1 represents the frontal location of the current with time. The frontal location is calculated as the minimum location at each time where the buoyant height is less than or equal to 0.02. Comparing the path of the current to the green line – the path of a smooth bed current extrapolated beyond the start of the roughness field– shows that the current slowed as it travelled. The slowing of currents is explored further in Section 6.2.2 where the Froude numbers of different experiments are compared. When the current exited the roughness it re-established as a smooth bed current, similarly to the sparse configuration currents seen in Chapter 5. However, unlike the sparse experiments, immediately after the current exited the roughness, but before it began to re-establish on the smooth bed, the current slowed and

its buoyant height decreased. Unlike the sparse experiments, which were able to immediately transition to a smooth bed current structure, the dense currents travelling atop the roughness had to plunge downwards towards the bed. The re-establishment of the currents will be explored further in sections 6.2.2 and 6.2.3.

In Chapter 4 it was seen that, with the exception of the D5H10 experiment, when the roughness was in the dense configuration, the currents travelled over the roughness rather that through it. Therefore, the currents could be thought of as smooth bed currents travelling over porous beds. For much of this chapter the co-ordinate system is thus redefined such that the top of the cylinders corresponds to y=0. The height previously used for non-dimensionalisation, H, known as the *total fluid depth* is replaced by the *unobstructed depth*, $\tilde{H}$, defined as the distance from the top of the cylinders to the free surface. This non-dimensionalisation is only used while a current is travelling over the roughness and not upstream or downstream of the roughness.

Figure 6.2 shows the buoyant height in false-colour based on the redefined co-ordinates where the integration is only carried out from the top of the cylinders to the free surface. In this image only the region where the current was travelling above the cylinders is shown. The black lines visible in Figure 6.1, where visualisation was unavailable due to the roughness, are not present because the integration took place above them. The remaining black rectangle represents the structural element in the channel where visualisation was not available even above the roughness. In Figure 6.2 it can be seen that the current displays a clear local maxima, which roughly lines up with the standard head location shown by the blue line. Thus, like smooth bed experiments but unlike the sparse experiments, this current exhibited a significant head. The buoyant height of the head decreased as it travelled. The dynamics of the current head will be discussed further in Section 6.2.3.

6.2.2 Front location and Froude Number

In Chapter 4 it was seen that the nose of a current in the dense configuration initially propagates through the roughness. Meanwhile, an over-flowing front initially takes time to be deflected upwards and over the roughness in order to develop as an overflowing current. Furthermore, in Section 6.2.1 it was seen that as the D5H20 experiment interacted with the roughness its speed reduced. This section will further develop these findings to investigate how a current interacts with the roughness with time. In particular, attempts will be made to determine whether the

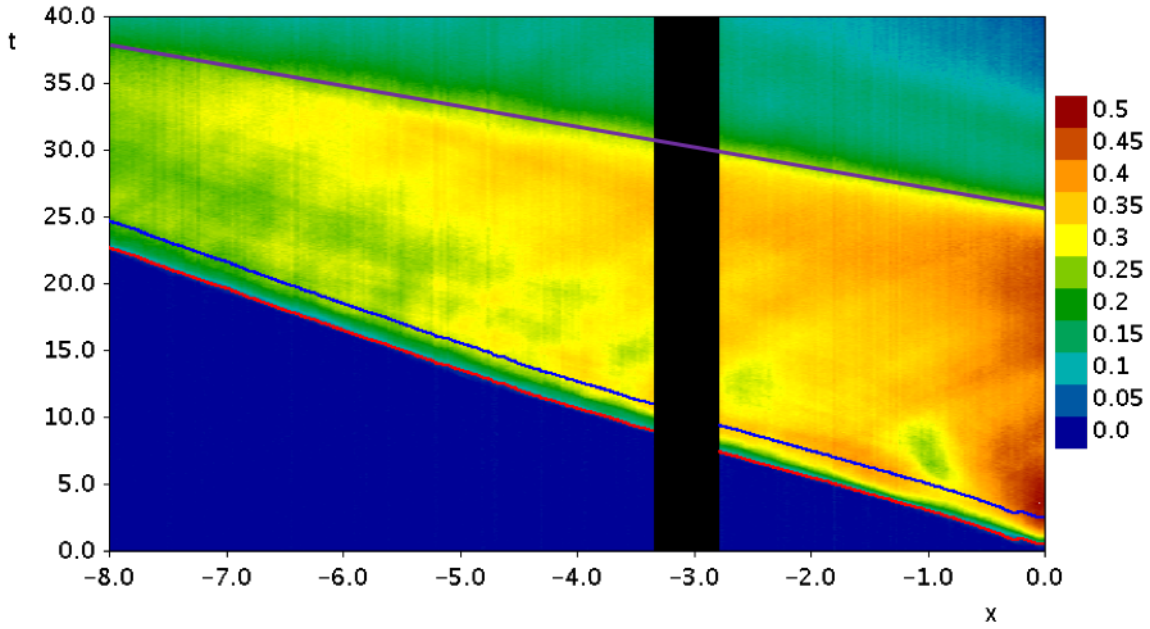

Fig. 6.2 D5H20 h_B displayed as false-colour with x and t based on $\tilde{H}$. The red line shows the front location of the current, the blue line represents the standard head location and the purple line shows the path of the lock bore. The black region represents the structural element in the channel where visualisation was insufficient to calculate the buoyant height. Only the domain of the flow field containing roughness is shown.

primary nose of a current travels above or through the roughness at different times, how its Froude number varies with time and whether the Froude number eventually asymptotes to a constant value. Furthermore, how these properties are impacted by the relative roughness height is investigated.

To determine whether the currents primarily travelled through or above the roughness the paths of each current were calculated within and above the roughness separately. For the leading edges within the roughness the density fields are integrated from 0 to half of the non-dimensional roughness height. The front location is found to be the minimum location at each time where this quantity is greater than or equal to 0.02. The integral is only calculated to half of the roughness height to exclude any over-flowing fluid that may have slightly extended into the roughness. To determine the leading edge above the roughness the density field is integrated in the vertical direction from the top of the roughness to the free surface. This leading edge is also calculated to be the minimum location at each time where this quantity is greater than or equal to 0.02. It should be stated that the presence of a leading edge within or above the roughness does not mean that there is a front moving independently at that location. For example, the presence of dense

fluid within the roughness may be due to a convective exchange of fluid between the overflowing current and the bed rather than a moving front within the bed. A front may also be observed atop the roughness due to an extension of a wedge travelling through the roughness rather than a separate front travelling atop the roughness. Before the currents reached the roughness and after they exited the roughness the paths are shown as being part of the through-flowing line because the noses of these currents are all located near the bottom boundary so can be calculated using the same method.

Figure 6.3 shows the front location within and above the roughness for all of the dense experiments from a time of 0 (when the currents entered the roughness) to a time of 20. This small time range is chosen to focus on how the currents travelled through the roughness immediately after encountering it. For the through-flowing paths there are large regions where no data was available due to the dense packing of the roughness – see the black lines on Figure 6.1. Initially, with the exception of the D5H27 experiment, the leading edges for all of the experiments within the roughness were in front of the leading edges above the roughness. The over-flowing fronts took time to be deflected upwards and establish atop the roughness while the through-flowing fronts, already having momentum from the smooth bed current, could immediately begin propagating through the roughness. As time increased the leading edges above and within the roughness became closer together for the D5H15 and D5H20 experiments because once the overflowing currents had established atop the roughness they could travel unobstructed. The leading edges of the D5H10 experiment within and above the roughness diverged as the current travelled. For this experiment, due to the large relative roughness height, the energy required for the current to travel atop the roughness appears to have been greater than the energy available to do so. In Chapter 4 it was seen that the D5H10 experiment barely had an overflowing nose and that the portion of the flow above the roughness was predominantly an extension of the wedge-like structure formed as the current travelled.

Figure 6.4 shows the leading edges within and above the roughness for all of the dense experiments over the full range of times measured. After a time of approximately 10 the leading edges of the D5H20 and D5H27 experiments were entirely above the roughness. From this time the leading edges within the roughness could be thought of not as significant moving fronts but rather due to the convective exchange of fluid between the dense fluid travelling over the roughness and the lighter fluid below. The D5H15 experiment never reached a state

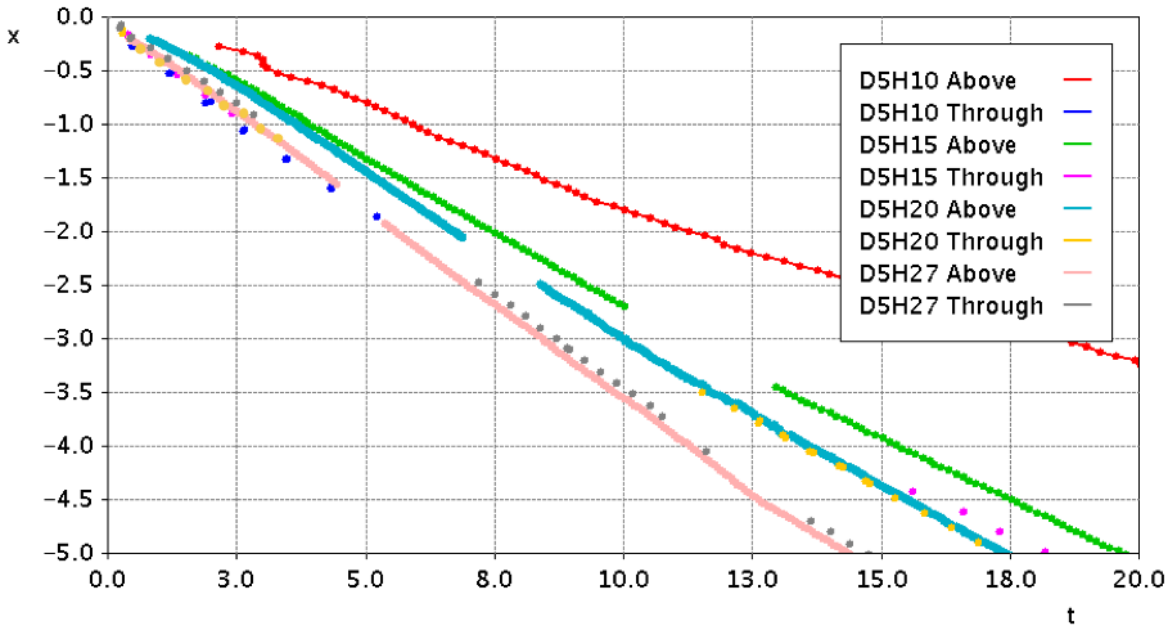

Fig. 6.3 Leading edges within and above the roughness with time for the experiments in the dense configuration from a time of 0 until a time of 20. The points on the lines represent grid point locations.

where the over-flowing current travelled ahead of the through-flowing front. However, the through-flowing and over-flowing noses quickly reached a state where they both travelled at the same speed, with the through-flowing nose slightly leading the over-flowing nose. This experiment represents a transition between the over-flowing and through-flowing regimes with the D5H10 being completely in a through-flowing regime.

The horizontal lines in Figure 6.4 show the locations where the currents exited the roughness. These lines are not shown for the D5H10 experiment because the lock bore caught up to the front before it exited the roughness. As with the sparse configuration the currents began increasing in speed after they re-established on the smooth bed.

A current in the overflowing regime could be thought of as a smooth bed current travelling over, and exchanging fluid with, a porous boundary. Therefore, the non-dimensionalisation for the over-flowing experiments is redefined using the framework introduced in Section 6.2.1. The paths of the overflowing noses are differentiated to generate plots for the Froude number with time, as shown in Figure 6.5.

In Figure 6.5 all of the overflowing dense currents initially increased in Froude number as the over-flowing currents established atop the roughness. After reaching maximum values at a time

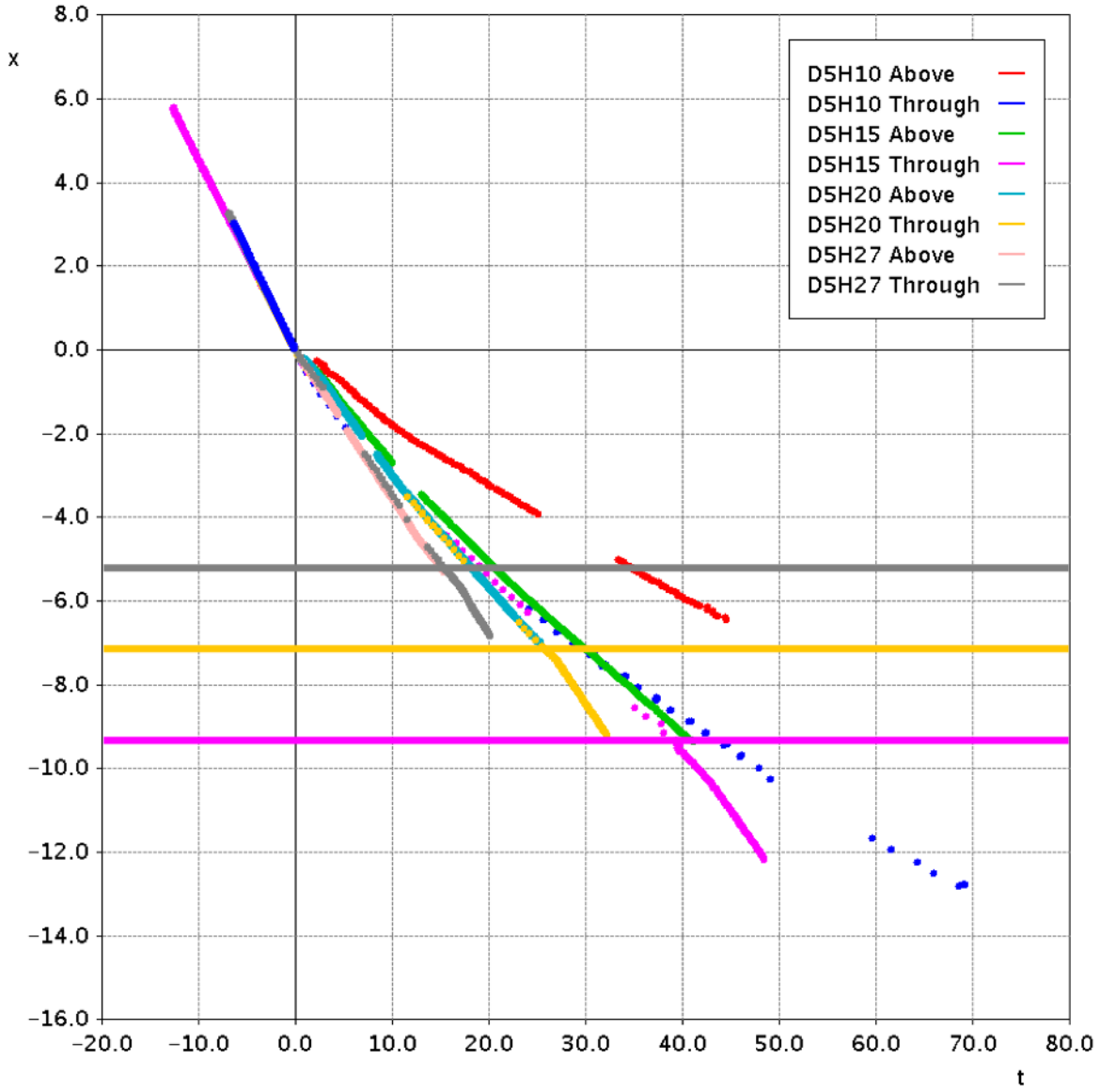

Fig. 6.4 Leading edges both above and within the current with time for the four dense experiments. The currents encountered the roughness at a location of 0 and the horizontal lines show the locations where the currents exited the roughness.

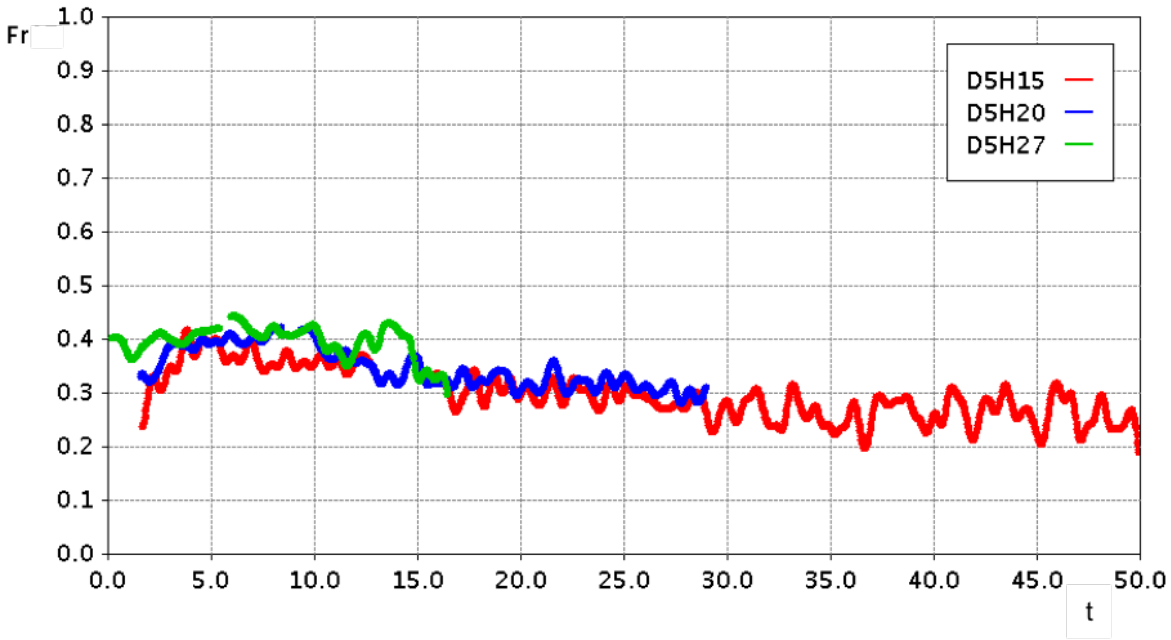

Fig. 6.5 Froude Number, based on $\tilde{H}$, with time for overflowing dense experiments. x=0 corresponds to the front face of the roughness.

of approximately 5 the Froude numbers began to decrease again. It could be argued that, unlike the currents in the sparse configuration, these did not all decrease at the same rate. However, the difference in Froude number between experiments is small and likely within the margin of error. Rather than the cylinders exerting a drag force on the currents and slowing them down the currents were impacted by a convective instability diluting the head fluid and reducing their driving force. The experiments with larger relative roughness heights had larger relative depths of fluid available within the roughness bed to dilute the currents, thus at least a small trend in the Froude number with relative roughness height is expected. Furthermore, the D5H15 experiment reached a constant Froude number of approximately 0.26 and the D5H20 experiment appears to have been approaching a steady state before reaching the end of the roughness. The D5H27 current did not travel far enough above the roughness to noticeably reach a steady state but it is believed that it would reach such a steady speed if left to travel for long enough.

The reason for the currents reaching steady speeds could involve a number of factors. For a smooth bed current as fluid in the head is diluted the more dilute fluid in the head is replaced by faster moving dense fluid from the tail. As the head of an over-flowing current loses mass, due to a convective exchange with the bed, more mass is likely to be lost to the bed than can enter the head from the tail. Thus, the driving force and Froude number decrease. However, as

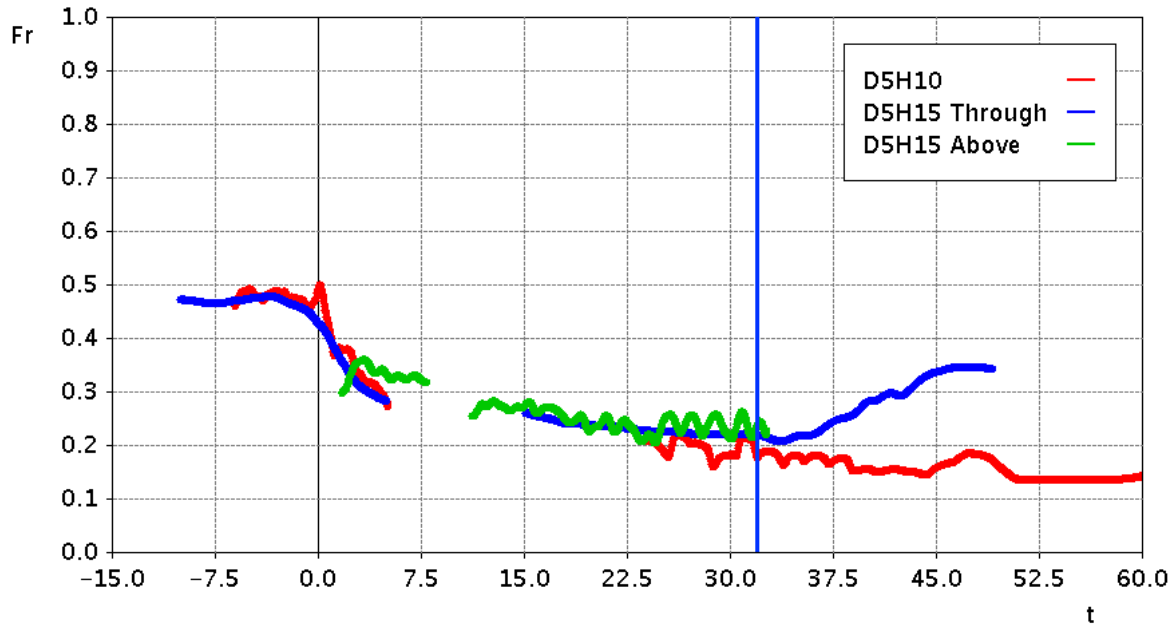

Fig. 6.6 Froude Number with time based on H for the through-flowing experiments - D5H10 and D5H15 based on the total fluid depth. For comparison the Froude number with time for the overflowing head of the D5H15 experiment is also shown with non-dimensionalisation based on H. Currents entered the roughness at a time of 0 and the vertical line represents the time when the D5H15 current exited the roughness.

the difference in density between the head and the bed decreases the mass flux into the head from the tail relative to the mass flux into the bed increases. Eventually these two fluxes, along with fluxes occurring at the shear layer between the current and the ambient fluid, are likely to become in balance causing the driving force to become constant with time.

The D5H10 experiment is not shown in Figure 6.5 because it did not have an over-flowing nose. The through-flowing nose of the D5H15 experiment, which travelled in front of the over-flowing nose, is also not shown. Figure 6.6 shows the Froude number with time for these two experiments. As a comparison it also shows the over-flowing Froude number for the D5H15 experiment but with non-dimensionalisation based on H.

This figure shows that at an early time the Froude numbers of the D5H10 and D5H15 experiments decreased with time at similar rates. At early times both of the experiments could be considered predominantly through-flowing with dynamics similar to the sparse configuration experiments. Chapter 5 showed that the sparse configuration experiments had Froude numbers independent of their relative roughness height, thus it is unsurprising that at early times the Froude numbers of the D5H10 and D5H15 experiments were similar. At early times the D5H15 over-flowing

nose had a low Froude number and this increased with time as the over-flowing current became established. When the over-flowing current reached a maximum Froude number at a time of approximately 4 the Froude number was larger than that of the D5H15 through-flowing front, causing the over-flowing front to begin catching up to the through-flowing front. At a time of between 5 and 15 the D5H15 experiment entered a separate phase where it diverged from the D5H10 experiment. The convective exchange of fluid between the over-flowing fluid and the bed provided additional buoyancy to the through-flowing nose allowing it to maintain its Froude number. However, without an over-flowing front the Froude number of the D5H10 current continued to decrease.

To understand the impact of the currents being allowed to develop before encountering the roughness Figure 6.7 compares the Froude number for the D5H15, D5H27, D5H15G and D5H27G experiments. At early times the Froude number for the experiments with the roughness beginning at the gate was slightly lower than when the currents were allowed to develop before encountering the roughness. This difference is likely due to the already developed currents having momentum as they reached the roughness, whereas when the roughness began at the gate the fluid comprising the overflowing currents was initially stationary. As time increased the currents became similar regardless of the relative location of the gate. The vertical lines show the locations of Froude number measurements by Cenedese et al. (2016) for equivalents of the D5H15 and D5H27 experiments redefined to be in terms of $\tilde{H}$. The Froude numbers measured at these locations are denoted by the X and * symbols respectively. Their measurements match the data well.

Chapter 4 indicates that as the currents emerged from the roughness the size and density of their heads increased. Figure 6.8 shows the Froude number for the dense experiments with the roughness beginning at the gate. In this figure the origin of time is redefined such that it represents the time when the currents exited the roughness. The D5H10 current is only shown until a time of 15, after which the lock bore caught up to the current.

Similar to the sparse configuration experiments in Chapter 5, when the currents exited the roughness their Froude numbers depended on the relative roughness height. This trend occurred not only because of the possible small trend between Froude number and relative roughness height in Figure 6.5 but also because the currents with larger relative roughness heights travelled larger non-dimensional distances before exiting the roughness. After re-emerging from the

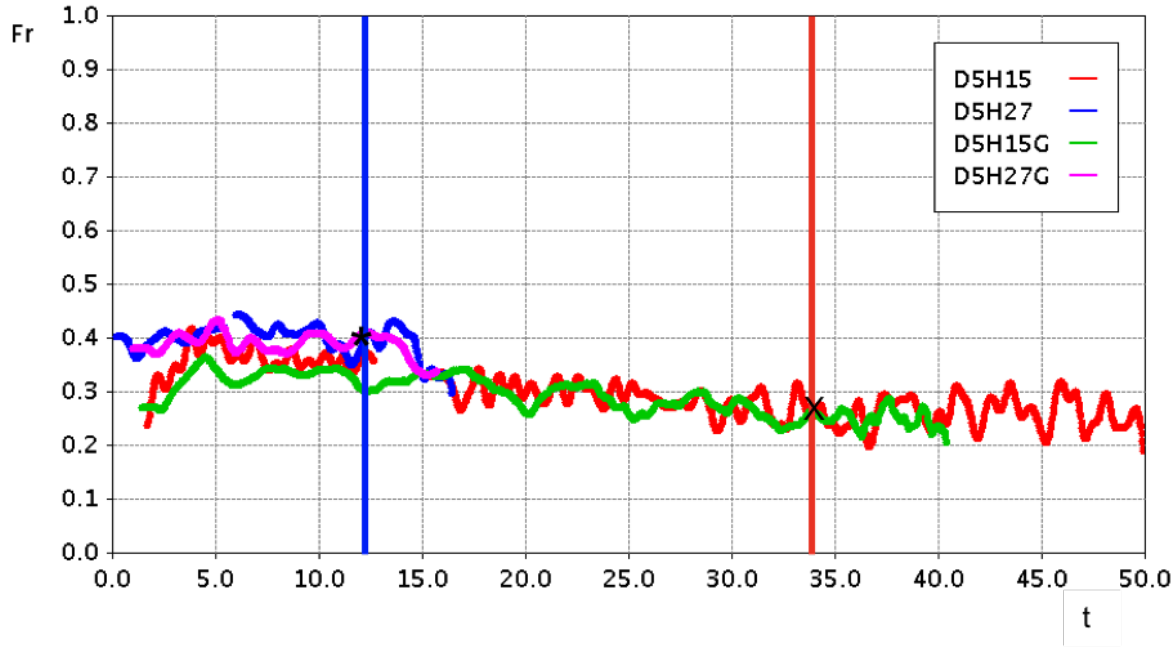

Fig. 6.7 Froude number with time for the over-flowing D5H15, S5H27, S5H15G and S5H27G fronts. Non-dimensionalisation is based on $\tilde{H}$. Vertical lines are at locations of measurements by Cenedese et al. (2016). * marks Froude number measured by Cenedese et al. (2016) for equivalent of D5H27 experiment and X marks Froude number for equivalent of D5H15 experiment.

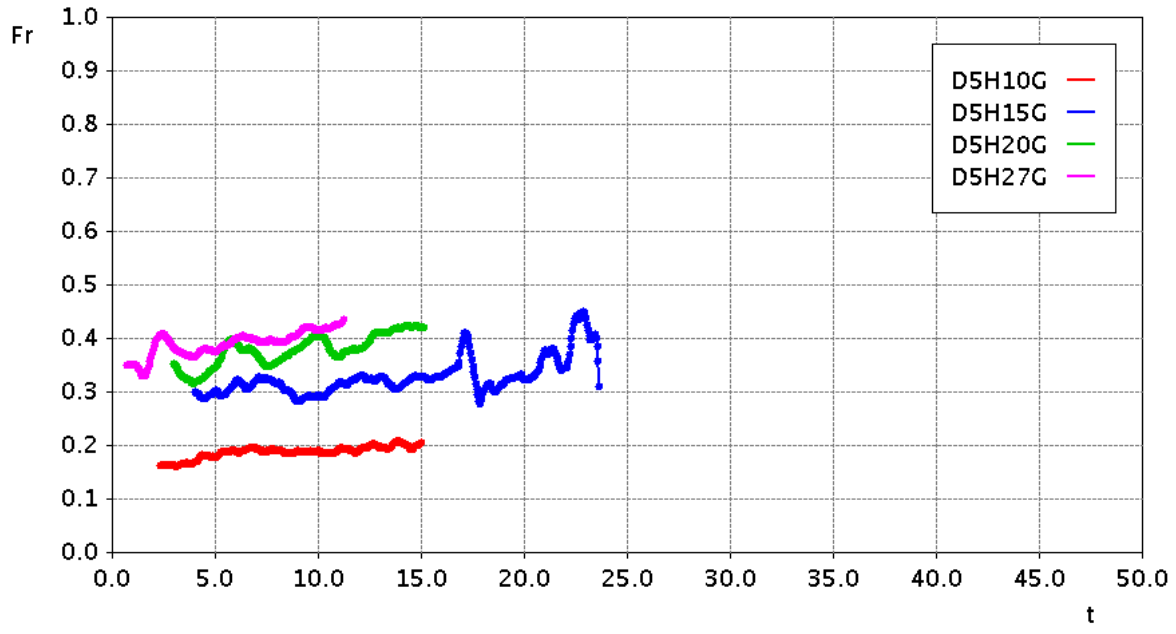

Fig. 6.8 Froude number with time for the D5H10G, D5H15G, D5H20G and D5H27G experiments after the currents re-emerged from the roughness. The origin of time is redefined such that it corresponds to the time when the currents exited the roughness. Non-dimensionalisation is based on H.

roughness the Froude number of the currents increased. The increase in Froude number as a current emerges from the roughness occurs because the salt flux into the bed from the head is removed allowing dense tail fluid to replenish the salt concentration in the current head. The density in the head of a current as it emerges from the roughness is illustrated further in Section 6.2.3. None of the currents reached constant Froude numbers. However, results from the sparse configuration experiments in Chapter 5 indicate that if left to travel for long enough these currents would likely reach steady states.

6.2.3 Current Height and Density

Overview

In Section 6.2.1 a framework was introduced wherein over-flowing currents were redefined as being smooth bed currents travelling over porous boundaries. When this framework was used the buoyant height of the D5H20 current had a local maxima at the current head, which decreased as the current travelled. In addition to this it was found in Section 6.2.2 that the fronts of the D5H20 and D5H27 experiments were entirely over-flowing, while the D5H10 experiment was entirely through-flowing. The D5H15 experiment represented a transition between the two regimes, having separate noses above and within the roughness. The Froude number of the currents in the over-flowing regime were found to approach a constant value as they travelled, whereas the D5H10 experiment did not. This section builds on these observations by attempting to understand the impact of the roughness on the density and vertical extent of the currents. In particular attempts will be made to explain the aforementioned findings.

Variation of Height and Density with x

This section aims to investigate how the structure of a current varies along the roughness field. This investigation initially considers only the D5H20 experiment as many features of this experiment are common to all of the over-flowing currents. Figure 6.9 shows the buoyant height for the D5H20 experiment with x at 5 different times. At a time of 7 a deepening at the front face of the roughness is visible while a current with a distinctive head is seen to have begun propagating forward. Over the following times the buoyant height at the head began to decrease and a wedge formed behind it. It was suggested by Nokes et al. (2008) and Anjum et al. (2013) that smooth bed currents are driven predominantly by the local conditions at their

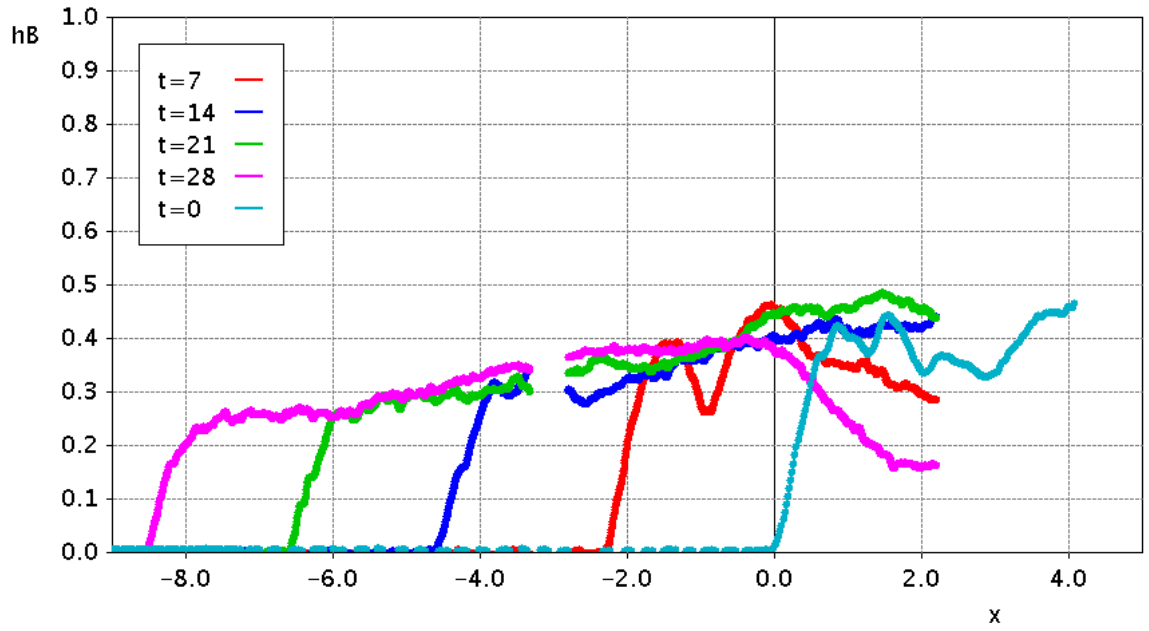

Fig. 6.9 h_B for the D5H20 experiment at times of 6,12, 18 and 20 when the current was travelling through the roughness and a time of 0 when the current was about to enter the roughness. The front face of the roughness is at a location of x=0. Co-ordinates were non-dimensionalised by $\tilde{H}$

heads. However, it was shown in Chapter 5 that this was not the case for the sparse configuration currents as they appeared to become driven predominantly by a pressure gradient formed within the tail of the currents. Unlike the sparse experiments a small but visible local maximum is visible in Figure 6.9, suggesting that the buoyancy of the head may have still been involved in driving the over-flowing currents even if the buoyant height further upstream in the tail was larger than the head. Figure 6.10 shows the D5H20 experiment at the same times as figure 6.9 with the current nose translated such that it is located at x=0 for all times. This figure clearly shows a decrease in the buoyant height at the head with time.

The reduction of the buoyant height with time was, at least in part, due to the density of fluid inside the head being lost via the convective exchange of fluid with the bed. However, it could be postulated that the vertical extent of the current may also decrease due to being drained into the bed. In order to understand how the vertical extent of the current varied with time Figure 6.11 shows the current envelope at the same times as Figure 6.10 also redefined such that the nose was at a location of x=0 for all times. As the current travelled a distinctive head formed above the cylinders and after it had formed (between a time of 7 and 14) it did not significantly change in vertical extent as it travelled. Therefore, while the density of the head reduced with time – due to the convective exchange of fluid with the bed – the total volume of fluid contained

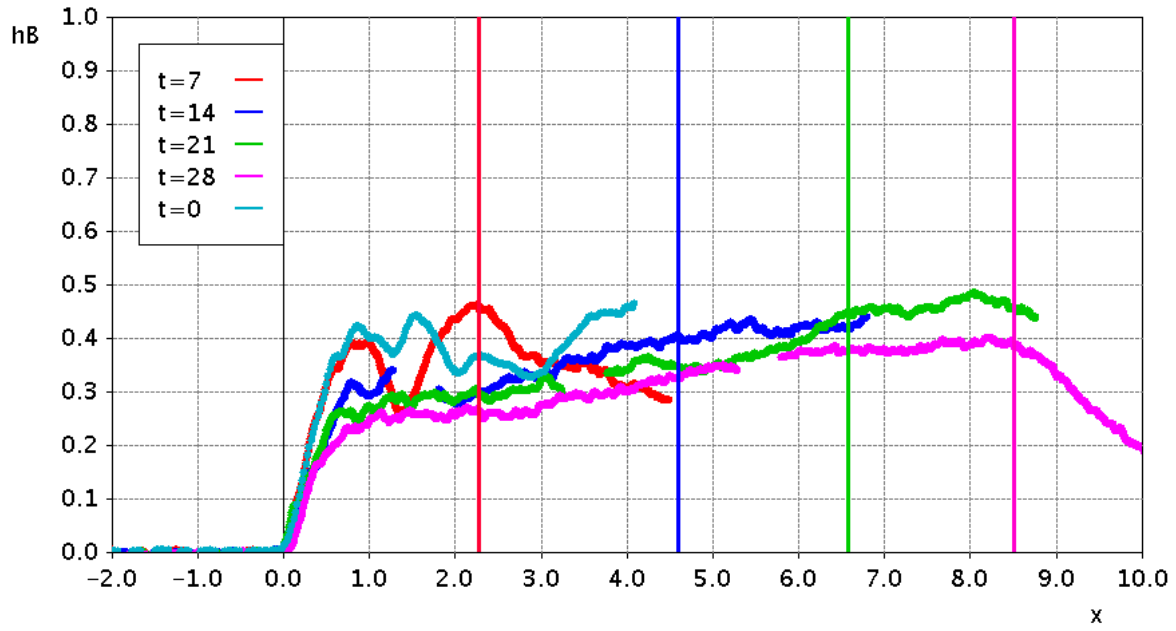

Fig. 6.10 h_B for the D5H20 experiment at times of 6,12, 18 and 20 when the current was travelling through the roughness and a time of 0 when the current was about to enter the roughness. The front of the current (defined as the minimum location where h_B=0.02) was translated such that for all times it sits at x=0. Co-ordinates were non-dimensionalised by $\tilde{H}$. Vertical lines show the the front of the roughness.

within the head was constant with time. The size of the current head also appeared to roughly match the size of a current travelling over a smooth bed (t=0, non-dimensionalised by H). This result indicates that the current head had the same vertical extent as a smooth bed current despite differing dynamics occurring at the lower boundary.

Additionally, the wedge behind the current head, as seen in the buoyant height, is not visible in the current envelope. This indicates that the wedge structure was not representative of the shape of the current but instead of the longitudinal density profile. The vertically-averaged non-dimensional density (computed as $\frac{h_B}{h_c}$) is thus illustrated in Figure 6.12 with x at different times. The average density was larger in the tail than in the head region and the average density of fluid within the head reduced with time. Furthermore, at later times the gradient of the average density with x does not significantly vary with time, indicating that the reduction in the average density is predominantly driven by a reduction in the head density.

Thus far this section has only considered how the properties of an over-flowing experiment with a fixed relative roughness height vary as it travels. While many of these features are applicable to currents with different relative roughness heights there are likely to be differences

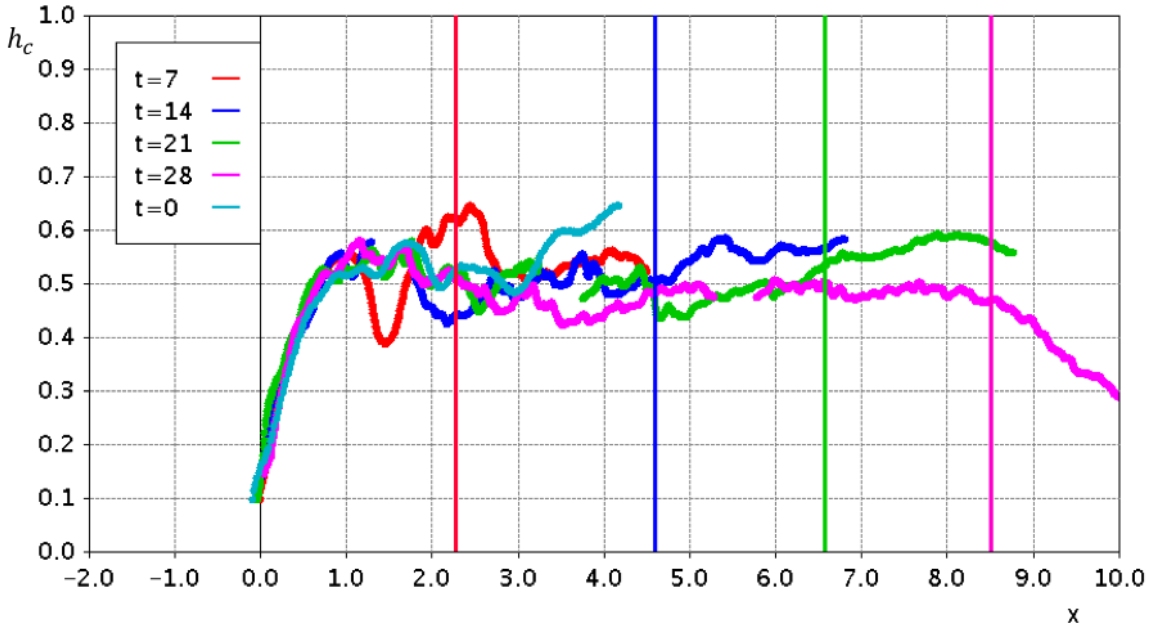

Fig. 6.11 h_c for the D5H20 experiment with x at times when the current was travelling through the roughness of 4,8,12 and 16 and a time of 0 when the current was just reaching the roughness. The front face of the roughness is at a location of x=0. Co-ordinates are non-dimensionalised by $\tilde{H}$. Vertical lines show the the front of the roughness.

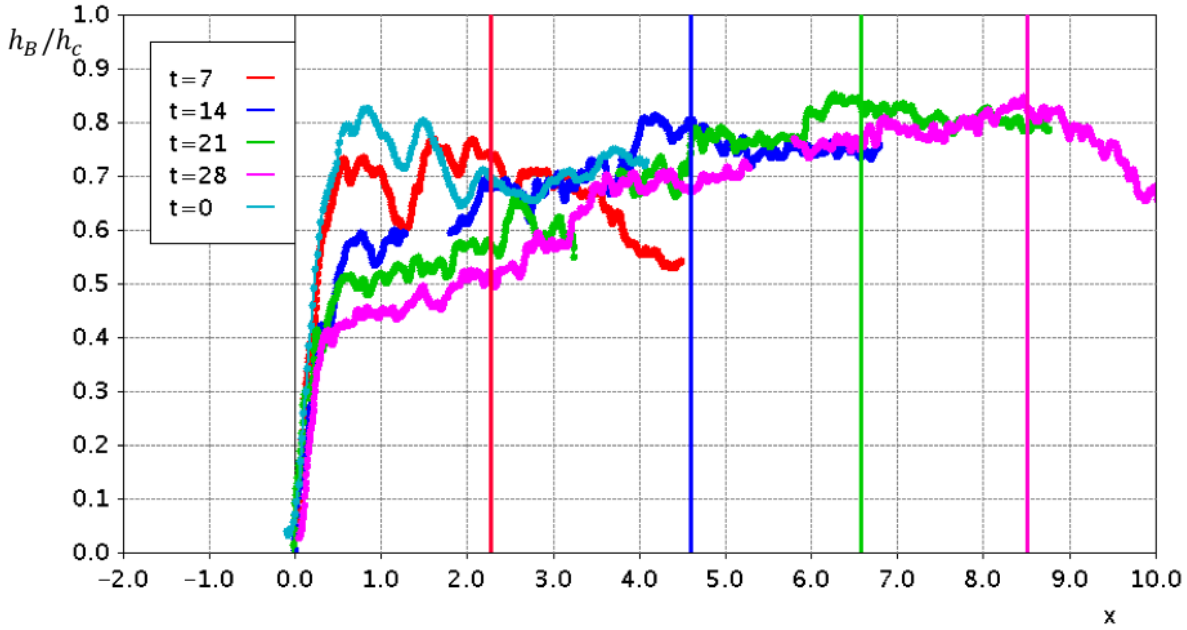

Fig. 6.12 h_B/h_c for the D5H20 experiment with x at times while the current was travelling through the roughness of 4,8,12 and 16 and a time of 0 when the current was just reaching the roughness. The front face of the roughness is at a location of x=0. Co-ordinates were non-dimensionalised by $\tilde{H}$. Vertical lines show the the front of the roughness.

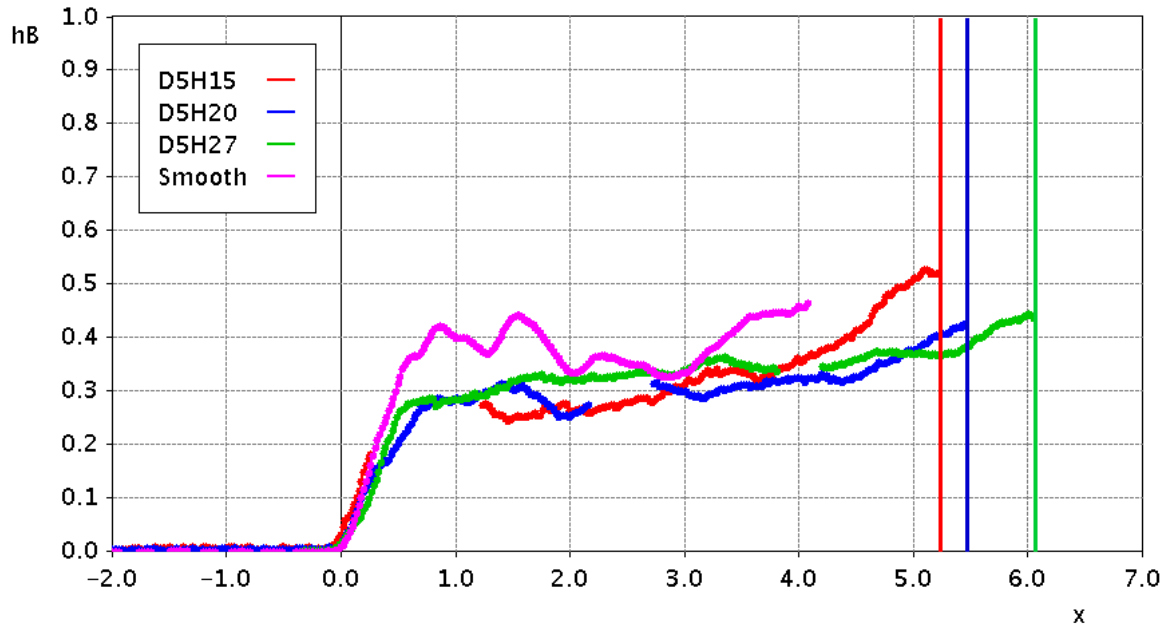

Fig. 6.13 h_B for dense experiments D5H15, D5H20 and D5H27 at a time of 16, corresponding to when the deepest current (from the D5H27 experiment) was above the final row of roughness. Co-ordinates were non-dimensionalised by $\tilde{H}$ and translated such that the noses of the currents (the minimum location where h_B=0.02) lay at x=0. Vertical lines represent the location of the front face of the roughness for different experiments. The large gap in the data is present due to the structural element in the channel, behind which data cannot be measured.

between these currents. Figure 6.13 shows the buoyant height for the three dense experiments in the overflowing regime (D5H15, D5H20 and D5H27) at a time of 16 as well as a smooth bed experiment. This is the latest time when all of the experiments could be compared (the time when the nose of the D5H27 experiment was above the final row of roughness). These currents were translated such that their noses lay at a location of x=0. As the relative roughness height decreased the buoyant height of the head may increase. However, this trend is weak and differences between experiments are within the margin of error. It is expected that the currents with larger relative roughness heights would suffer greater loss of fluid to the bed, hence a reduction in h_B, because the total volume of bed fluid available to exchange with the currents relative to the size of the currents is greater.

The conclusion that differences in buoyant height between experiments were due to decreased average density and not vertical extent is based on only the D5H20 experiment in Figure 6.11. To investigate whether all of the overflowing currents had vertical extents matching that of smooth bed currents Figure 6.14 shows the current envelope of these experiments at a time of 16.

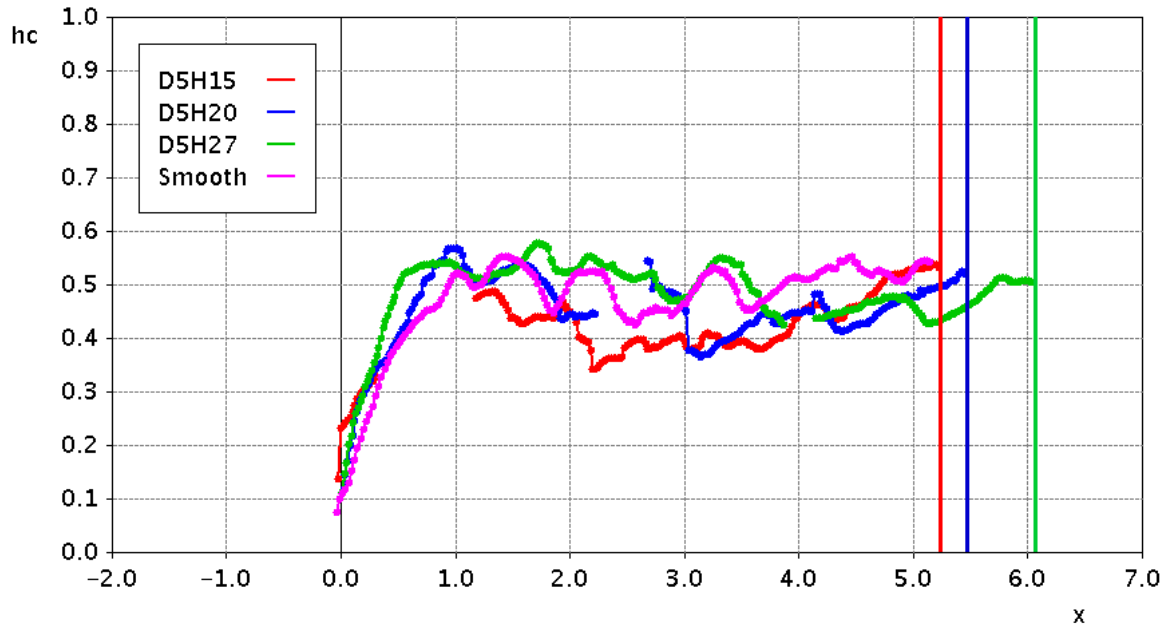

Fig. 6.14 h_c for dense experiments D5H15, D5H20 and D5H27 at a time of 16, corresponding to a time when the front of the deepest current (the D5H27 experiment) was above the final row of roughness. Co-ordinates are non-dimensionalised by $\tilde{H}$ and translated such that the front of the currents at x=0. Vertical lines represent locations of the front face of the roughness.

Figure 6.14 shows that at a time of 16 the head of the D5H20 and D5H27 currents had matching vertical extents similar to that of a smooth bed current. This similarity matches the findings in Figure 6.10, indicating that while there was a transfer of fluid between the currents and the bed causing a dilution of the current head, the total volume of fluid in the head of the currents remained constant. The D5H15 experiment did have a slightly smaller head than the D5H20 and D5H27 experiments. This difference could be explained by the leading edge of the D5H15 current propagating through the roughness causing there to be less fluid travelling atop the roughness.

It was seen in Section 6.2.2 and Chapter 4 that the D5H10 experiment did not have an over-flowing nose and instead travelled entirely as a through-flowing current similar to those with sparsely distributed roughness as seen in Chapter 5. Therefore, this experiment was non-dimensionalised based on the total water depth instead of by the unobstructed depth. To investigate how this current travelled Figure 6.15 shows the buoyant height at four different times. Between x=-7 and x=-3 data was not available because parallax errors meant visualisation was not available within the roughness at these times. Similar to the sparse configuration experiments as the D5H10 experiment travelled through the roughness the buoyant height

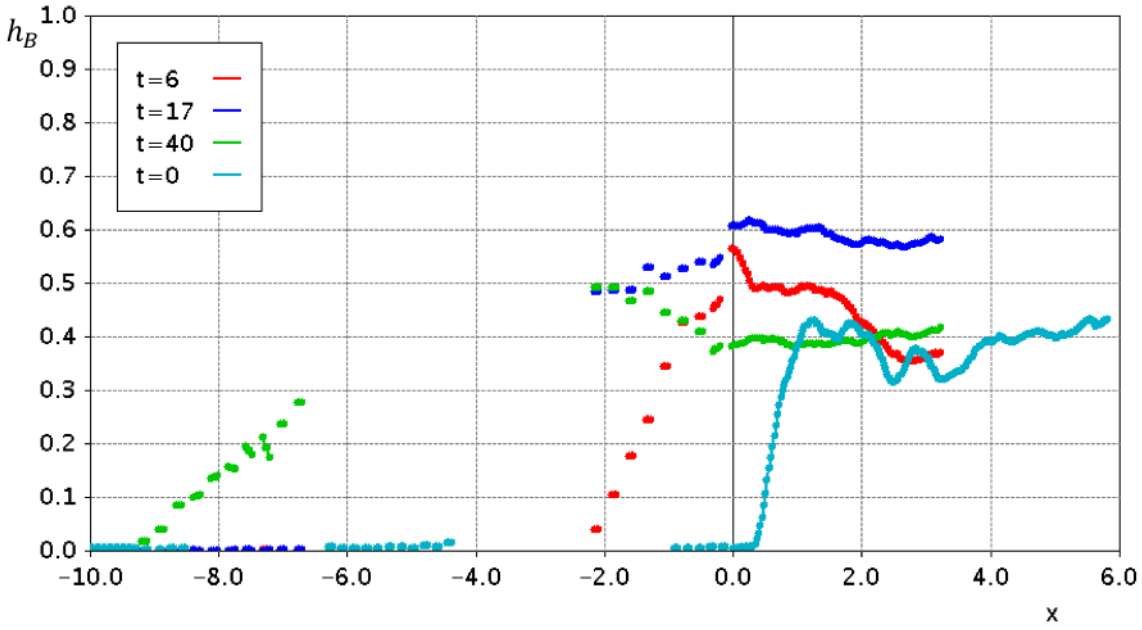

Fig. 6.15 h_B for the D5H10 experiment at times of 6,17 and 40 when the current was travelling through the roughness and a time of 0 when the current was about to enter the roughness. The front face of the roughness is at a location of x=0. Co-ordinates were non-dimensionalised by H

transitioned from having a head and tail structure to a wedge-like structure. Like the sparse configuration experiments the wedge reduced in angle as it travelled, confirming that this experiment was likely driven by the same dynamics as the sparse configuration experiments.

Variation in Height and Density with Time

The previous section provided insights into how the height and density of the dense configuration experiments varied in space. However, it did not answer the question of how they varied with time. This section will investigate this issue. To understand the dilution of the over-flowing heads with time Figure 6.16 shows the buoyant height at the standard head location with time for the three overflowing dense experiments. For all of the overflowing experiments the buoyant height initially increased with time, as the currents developed atop the roughness, before a rapid decrease. The decrease in buoyant height with time was caused by the vertical buoyancy exchange with the fluid within the bed, described earlier. At later times the buoyant height appeared to become steady with time. As the average density of the current head decreased the buoyancy flux into the bed decreased. The steady state likely occurs once the buoyancy flux from the current head into the bed decreases sufficiently that it balance the buoyancy flux from the dense tail fluid into the head and the flux of ambient fluid at the shear layer above the current.

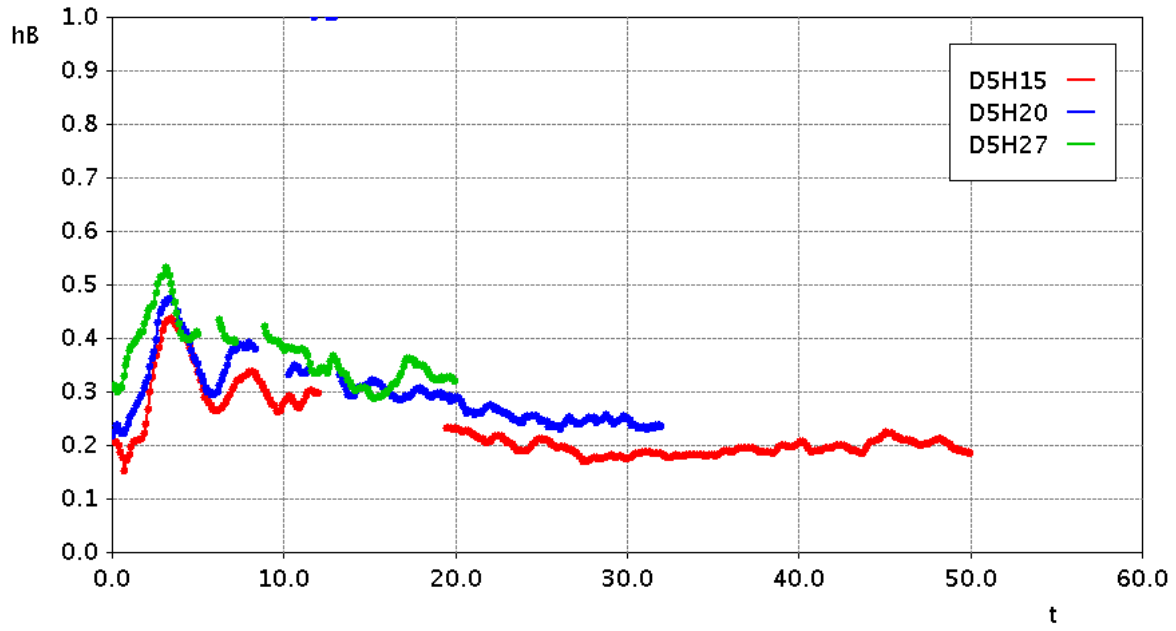

Fig. 6.16 h_B at the standard head location with t for the over-flowing experiments. A time of 0 corresponds to the time when the currents first encountered the roughness. Co-ordinates are non-dimensionalised by $\tilde{H}$.

In the previous section it was inferred that as the currents travelled the decrease in the buoyant height was caused by the loss of current fluid to the bed without a change in their vertical extent. To further investigate the variation in the current envelope with time Figure 6.17 shows the current envelope at the standard head location with time. Figure 6.17 shows an initial increase in the vertical extent, similar to that seen in Figure 6.16, due to the currents growing as they developed atop the roughness. However, once the currents had developed they did not decrease in vertical extent with time despite the significant buoyant flux into the bed and associated decrease in buoyant height. The maximum vertical extent of the D5H20 and D5H27 experiments, thought to be entirely in the over-flowing regime, was equal to that of a smooth bed experiment. The vertical extent of the over-flowing nose of the D5H15 experiment was slightly lower than the D5H20 and D5H27 experiments due to the the D5H15 experiment being in a transitional regime between over-flowing and through-flowing.

Figure 6.18 shows the vertically averaged non-dimensional density (computed as $\frac{h_B}{h_c}$) at the standard head location with time. As the currents travelled atop the roughness a similar trend to that seen in Figure 6.16 is visible. The average density initially increased as the currents became established atop the roughness. Following this increase the density decreased as the light fluid contained within the bed was exchanged with the dense current fluid. As with the buoyant height

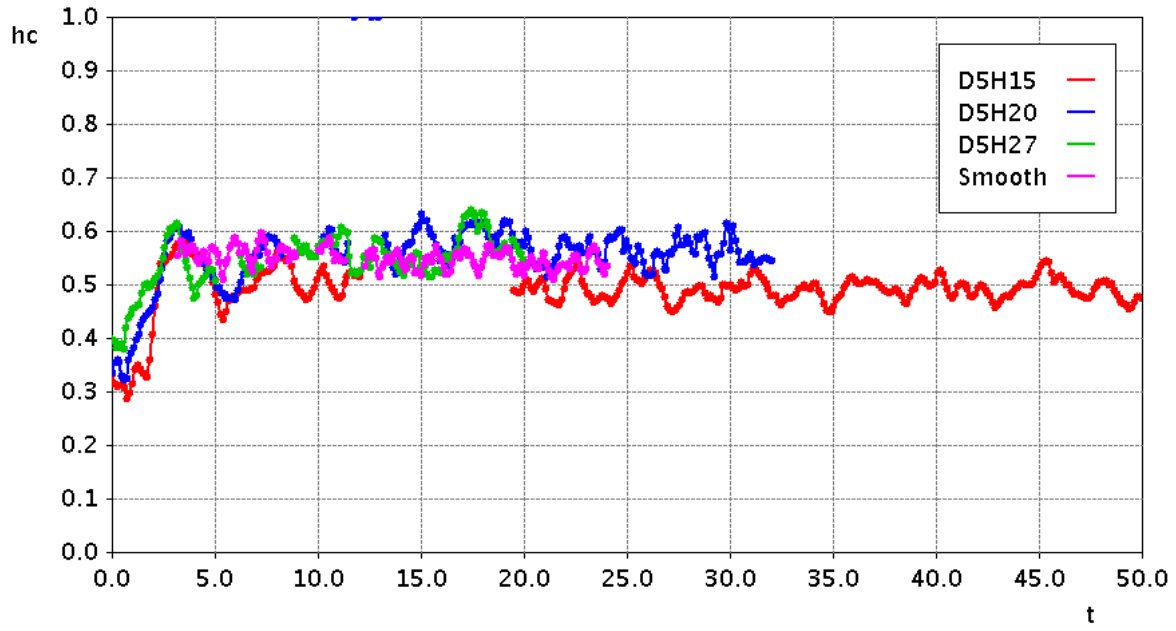

Fig. 6.17 h_c at the standard head location with time for the over-flowing experiments. A time of 0 to the time when the currents first encountered roughness. Co-ordinates were non-dimensionalised by $\tilde{H}$. For the smooth bed current a time of zero corresponds to the time when the gate was removed and co-ordinates are non-dimensionalised by H.

the average density eventually approached a steady state wherein the net buoyancy flux out of the current head became zero. As the average density in the head of the currents was seen to decrease with time, but not the vertical extent, the decrease in buoyant height, and hence driving force, within the current heads was primarily due to the loss of dense fluid to the bed.

In the previous section the D5H10 experiment was seen to have a structure similar to the sparse experiments seen in Chapter 5. To investigate whether this continued with time Figure 6.19 shows h_B, h_c and h_B/h_c for the D5H10 experiment at the standard head location with time. For the through-flowing dense experiment there was a large amount of data where visualisation was unavailable making interpretation of the data difficult. Therefore, to better understand the data linear interpolation was used wherever visualisation was unavailable – for example, between rows of roughness. This figure, again, shows similar behaviour to the sparse configuration experiments. All three of the curves in Figure 6.19 were constant with time before reaching the roughness (t<0). Upon reaching the roughness there was an increase in the current envelope as fluid was deflected upwards at the front face of the roughness. The increased vertical extent without a change in the average density caused an increased buoyant height. After the initial increase all three curves reduced with time as the current formed a wedge-like structure that

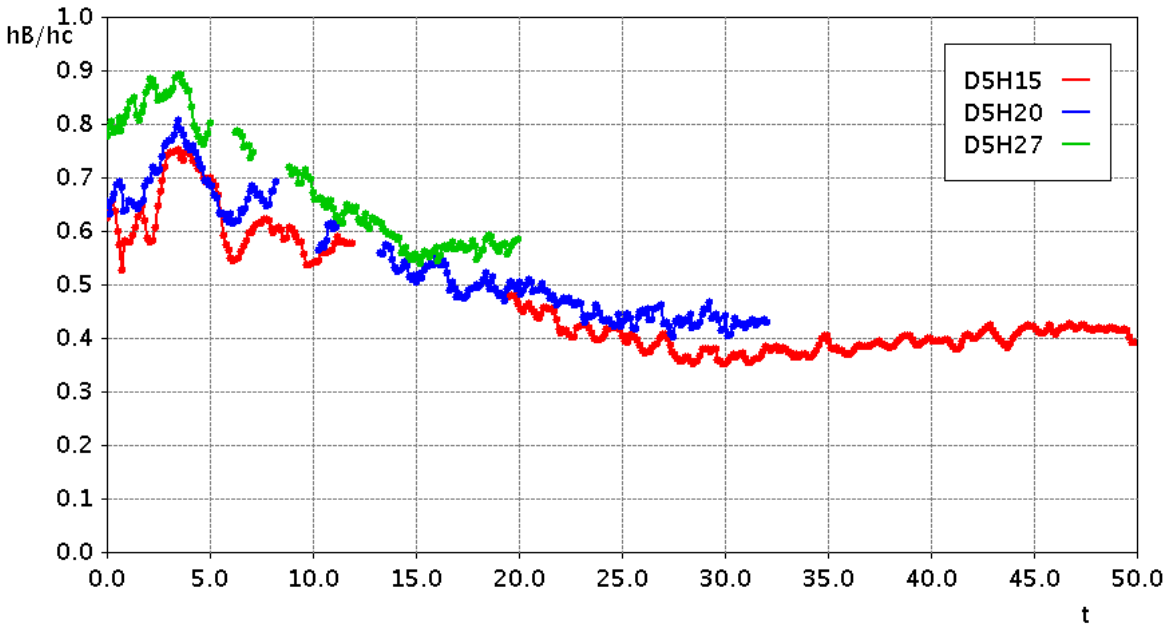

Fig. 6.18 h_B/h_c at the standard head location with time for the over-flowing experiments. Co-ordinates were non-dimensionalised by $\tilde{H}$. A time of 0 corresponds to a time when the currents first encountered the roughness.

decreased in angle and diluted with time. From a time of 35 the reductions in the curves with time became small. These results are all consistent with the current being in a through-flowing regime driven by a pressure gradient in the wedge behind the current head and slowed by a drag force exerted on the current by the cylinders.

Experiments with Roughness Beginning at the Lock Gate

Section 5.2.2 showed that at early times the experiments with roughness beginning at the gate had lower Froude numbers than the experiments with the roughness beginning downstream of the gate. However, at later times there was a negligible difference in the Froude number. Therefore, at late times it could be reasonably expected that the buoyant heights would not depend on the position of the roughness. To investigate this conclusion Figure 6.20 compares the buoyant heights of the D5H15 and D5H27 experiments with the D5H15G and D5H27G experiments. This figure shows that the impact of allowing a current to establish before interacting with roughness is minimal. However, at early times the experiments with the roughness beginning at the lock gate had slightly larger buoyant heights than the experiments where the currents were allowed to establish first. While this difference is counter to the Froude number it is not unsurprising as the head of the currents, which had been allowed to establish before reaching

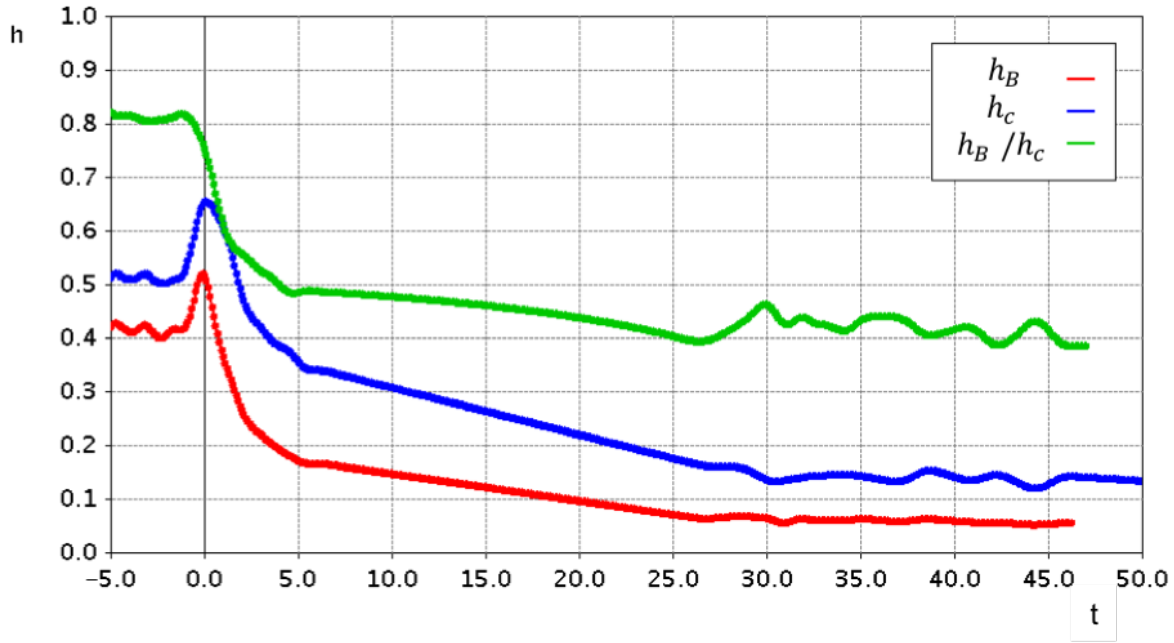

Fig. 6.19 h_B, h_c and h_B/h_c at a distance of 1 behind the current front for the D5H10 experiment with time. The current entered the roughness at t=0. Where visualisation was unavailable due to cylinders or structural elements in the channel linear interpolation is used.

the roughness, would have been slightly diluted when the currents reached the roughness. At later times the buoyant heights were very similar.

Section 6.2.2 also showed that as the currents re-established after exiting the roughness their Froude numbers increased. As these currents are thought to have been driven by the buoyancy of their heads, as the Froude number increases the buoyant height in the head should also increase. Therefore, to further investigate how the currents developed with time as they exited the roughness Figure 6.21 shows the buoyant height at the standard head location with time for the D5H10G, D5H15G, D5H20G and D5H27G experiments as the currents exited the roughness. In this figure a time of 0 corresponds to the time when the currents exited the roughness. The D5H10G current is only shown until a time of 15, after which the lock bore caught up to the current.

Similar to the Froude number discussed in Section 6.2.2 the buoyant height when the currents exited the roughness can be seen to depend on the relative roughness height. This trend is primarily due to an experiment with a larger relative roughness heights travelling a larger non-dimensional distance through the roughness before exiting. With the exception of the D5H10G current, the buoyant heights of all of the experiments increased with time. The D5H20G and

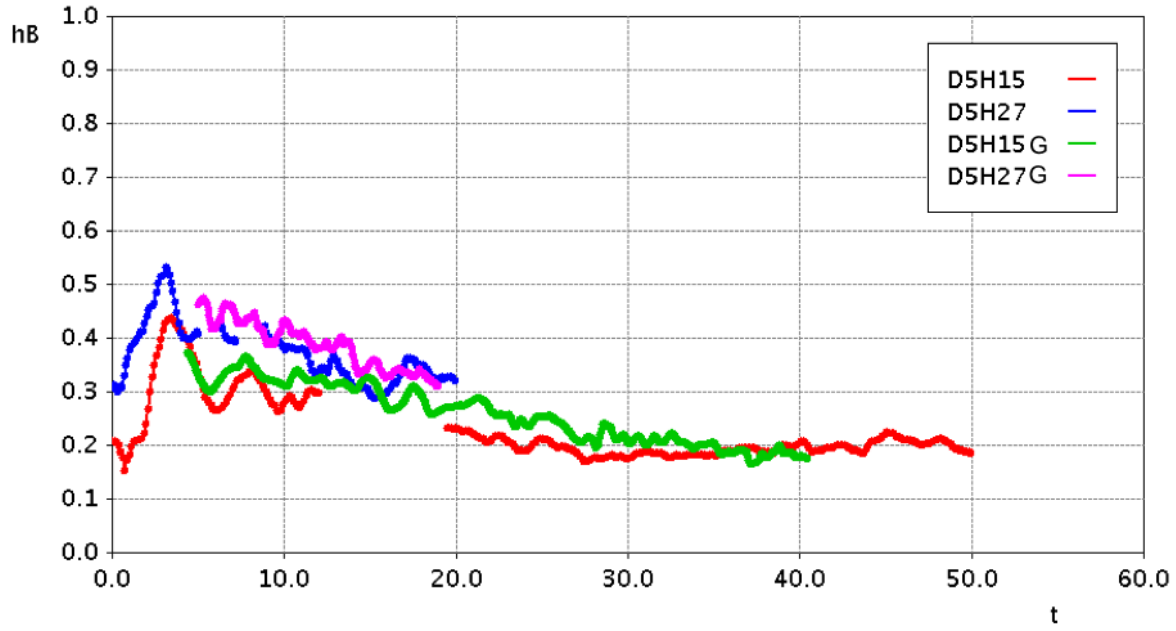

Fig. 6.20 h_B for the over-flowing D5H15, D5H27, D5H15G and D5H27G experiments. A time of 0 corresponds to the time when the currents first encountered the roughness. Non-dimensionalisation is based on $\tilde{H}$.

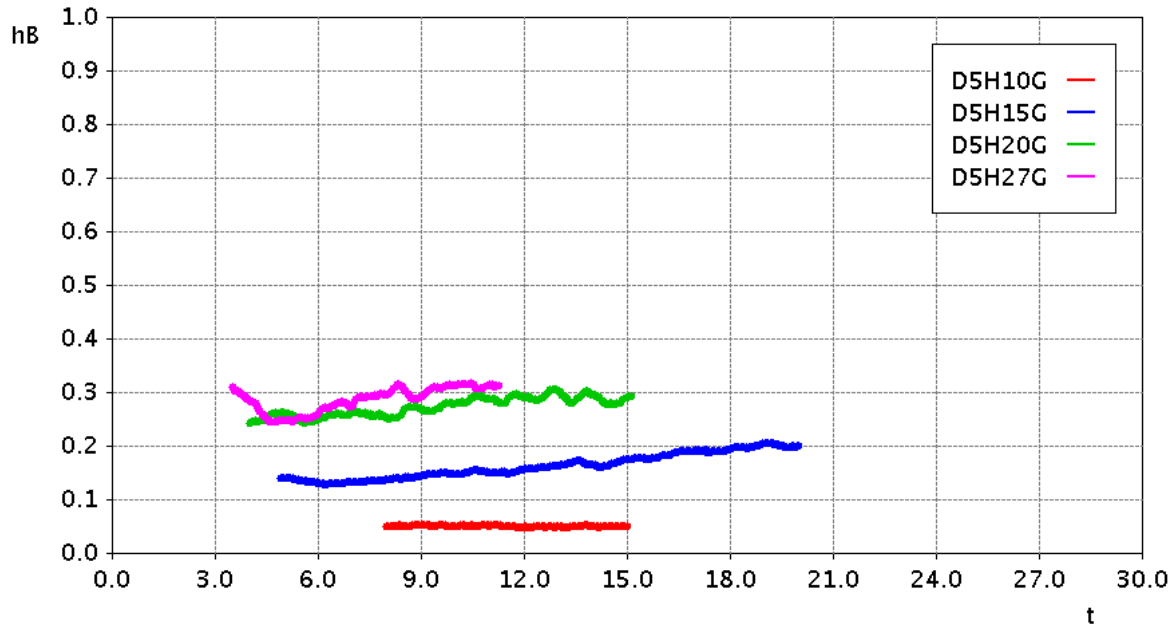

Fig. 6.21 h_B at the standard head location for the D5H10G, D5H15G, D5H20G and D5H27G experiments. A time of 0 corresponds to the time when the currents exited the roughness. Non-dimensionalisation is based on H.

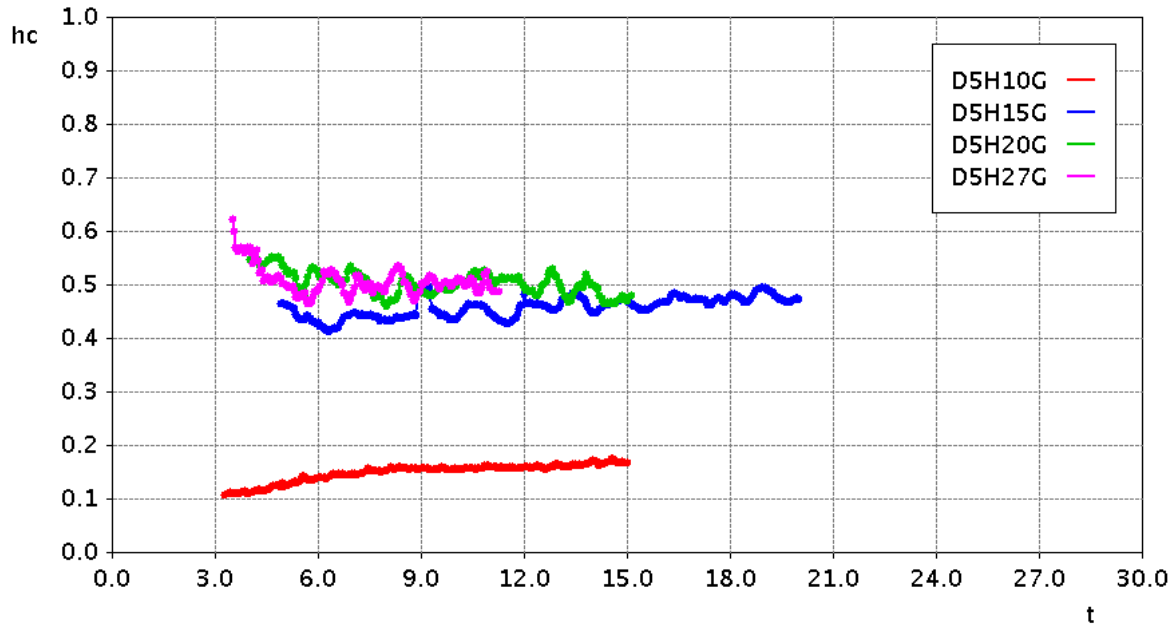

Fig. 6.22 h_c at the standard head location for the D5H10G, D5H15G, D5H20G and D5H27G experiments. A time of 0 corresponds to the time when the currents exited the roughness. Non-dimensionalisation is based on H

D5H27G experiments appeared to approach steady states at late times. However, the D5H15G experiment continued to increase. The D5H10G experiment did not significantly increase in buoyant height with time, possibly because dense fluid remained trapped within the roughness unable to re-enter the current head.

Figure 6.22 shows the equivalent of Figure 6.21 but for the current envelope. As the fully over-flowing experiments (D5H20G and D5H27G) travelled the currents plunged downwards from atop the roughness to re-establish along the smooth bed. Thus, as they were already of considerable vertical extent upon exiting the roughness they did not have to grow in extent with time. For a short time their extents decreased until becoming constant. The D5H15G experiment represents a transition between the over-flowing and through-flowing regimes. This current's vertical extent also decreased slightly upon re-establishment, however, it then grew with time as it travelled. The D5H10G experiment was fully through-flowing so did not plunge towards the bed upon establishment, instead its vertical extent grew with time similar to the sparse configuration experiments.

6.2.4 Driving Forces

Over-flowing Experiments

In the previous sections it was seen that the buoyant height and current envelopes of the D5H15, D5H20 and D5H27 experiments retained local maxima in the head. These local maxima are similar to those seen in a smooth bed experiment but inconsistent with that seen in the sparse configuration experiments in Chapter 5. Therefore, it is proposed that, unlike a through-flowing, sparse configuration current that is driven by a pressure gradient within its tail, an overflowing current is predominantly driven by the buoyancy of the current head. Therefore, the reduction in the Froude number can be explained by the buoyancy of its head decreasing with time.

Nokes et al. (2008) and Anjum et al. (2013) argued that, for a smooth bed or intrusive current, the propagation speed is determined by the local conditions at the head. Thus they argued that a steady state model based on the local conditions of the head can be used to predict the current front speed providing the rate of change of the conditions at the front are slow. The Froude number based on local conditions can be described as

$$Fr_B = \frac{u_F^*}{\sqrt{\int_0^H \frac{\rho^* - \rho_1}{\rho_2} g dy^*}} = \frac{Fr}{\sqrt{h_B}} \tag{6.1}$$

As mentioned in Chapter 2, Benjamin (1968) showed analytically that for an energy conserving current this quantity has a constant value of $\frac{1}{\sqrt{2}}$. Nokes et al. (2008) extended this model for a current where energy is only conserved at the head, finding agreement with Benjamin's model for a current with a depth of half of the total fluid depth. They provided an empirical formula for Fr_B with relative current height. However, both of these models assume that the current and ambient at the head are unmixed. Figure 6.23 shows this Froude number calculated for the three overflowing dense experiments at the standard head location. While a small reduction in time occurs in some of these curves, after an initial increase due to establishment of the currents, the trend is small compared to the variability in the data. However, the Froude number is lower than the predicted $\frac{1}{\sqrt{2}}$ for an energy conserving current. The fact that this Froude number is close to being constant with time provides good evidence that the current speed can be determined by its local depth and dilution, indicating that the predominant driver of the current is the buoyancy of

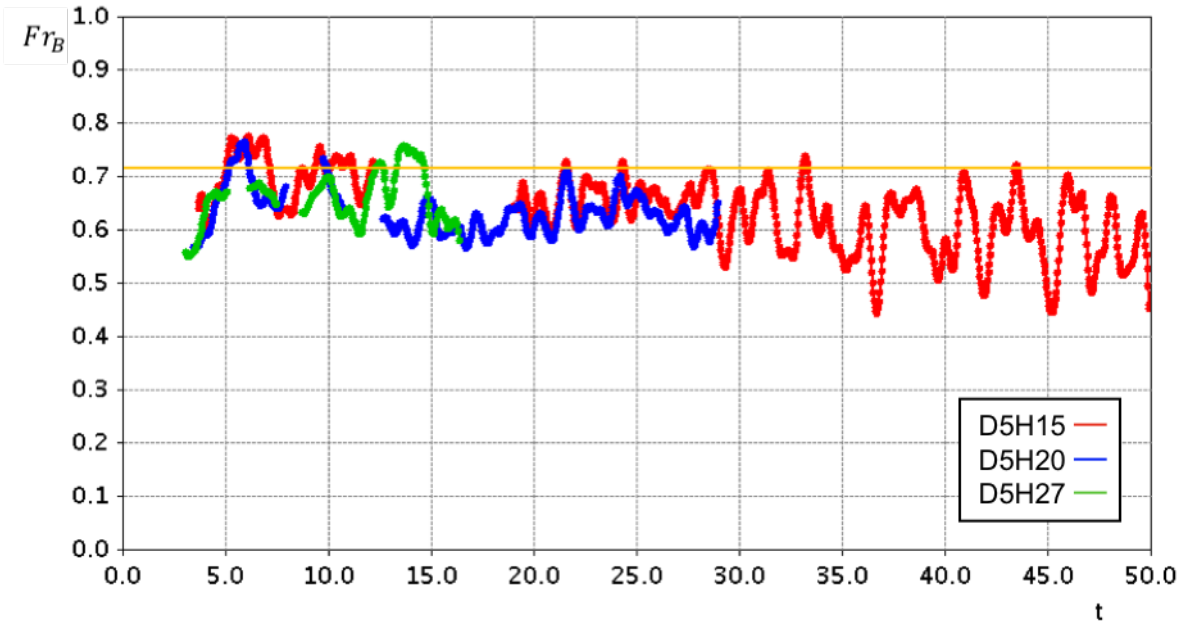

Fig. 6.23 Fr_B with time for overflowing dense experiments. The orange line corresponds to $\frac{1}{\sqrt{2}}$.

the head. It should be noted that Equation 6.1 requires knowledge of h_B and this is difficult to determine analytically due to difficulty in modelling buoyancy fluxes into and out of the head.

Through-flowing Experiment

In sections 6.2.2 and 6.2.3 it was found that, unlike the majority of the dense experiments, the D5H10 propagated through the roughness. Analysis of the buoyant height, current envelope and Froude number provided evidence that this experiment was driven by similar mechanisms to the sparse configuration experiments discussed in Chapter 5. Furthermore, it was found that the D5H15 experiment represents a transition between the over-flowing and through-flowing regimes, having a through-flowing nose travelling slightly ahead of an over-flowing nose. It was seen that at early times the through-flowing nose of the D5H15 experiment had a Froude number decreasing at the same rate as the D5H10 experiment. However, as the overflowing nose caught up to the through-flowing nose it provided additional driving force causing the Froude numbers of the two experiments to diverge.

In Chapter 5 it was argued that a sparse configuration current, which is predominantly through-flowing, is driven by a balance between the pressure gradient in a wedge behind the front of the current and the drag force exerted on the current by the roughness. A model was formulated by

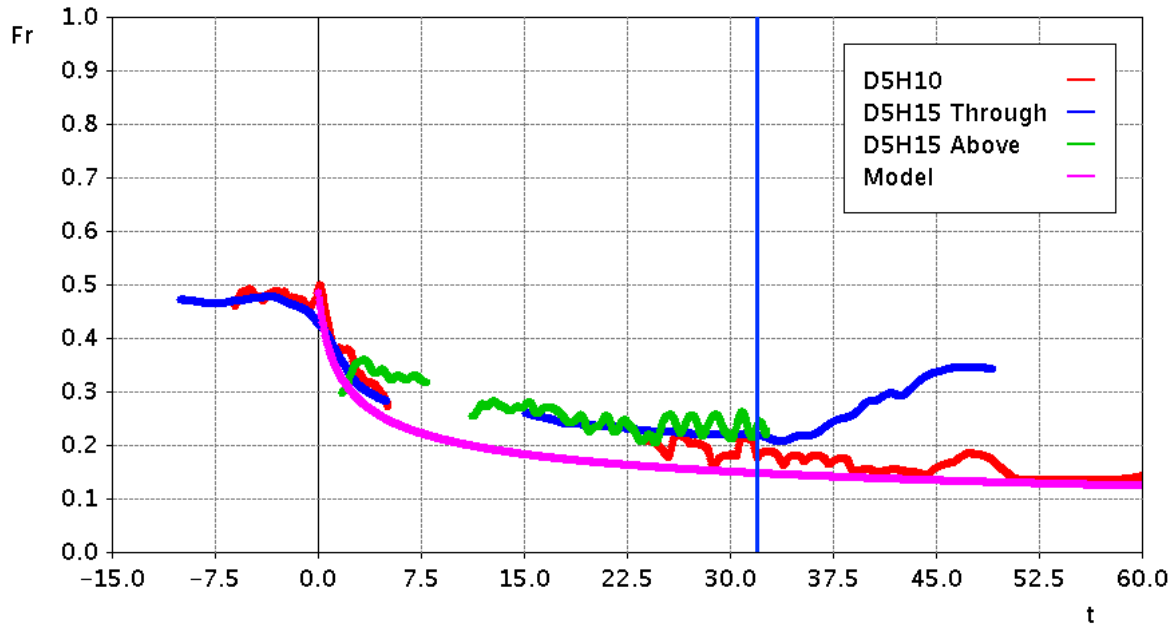

Fig. 6.24 Froude Number with time for the through-flowing dense experiments - D5H10 and D5H15 based on H as well as an analytical model for the Froude number with time. For comparison the Froude number with time for the over-flowing head of the D5H15 experiment is also shown redefined to be based on the total fluid depth. Currents entered the roughness at a time of 0 and the vertical line represents the time when the D5H15 current exited the roughness.

assuming that the pressure gradient in the current is proportional to the drag force, modelled with a quadratic drag law. This model led to the following equation

$$Fr = \left(Ct \frac{d_c \eta_c}{S_x S_z} + E \right)^{-\frac{1}{3}} \tag{6.2}$$

where C and E are constants found empirically for the sparse experiments to be 3.8 and 10.3 respectively. To test whether the through-flowing D5H10 and D5H15 fronts were driven by the same mechanisms as the sparse experiments this model is plotted with the measured Froude numbers in Figure 6.24. To show that the mechanisms were the same between these experiments and the sparse configuration experiments the empirical constants calculated for the sparse configuration experiments were used in equation 6.2. Therefore, the only differences in the model were S_x and S_z.

Figure 6.24 shows that while the model slightly under-predicts the Froude number for the D5H10 experiment it does match the trend of the experiment very well and the difference between

the measured data and the model is small. As with the D5H10 experiment the model matches the D5H15 experiment well at early times before the over-flowing front has caught up to the through-flowing front. At later times the model significantly under predicts the measured Froude number for the D5H15 experiment. These findings suggest that both of these experiments were driven by the same mechanisms as the sparse experiments at early times and that at later times the driving mechanisms of the D5H15 experiment were dominated by the overflowing nose.

6.3 Velocity Measurements

6.3.1 Introduction

While the density measurements shed light on important aspects of these currents there are a number of questions left unanswered. Primarily it was inferred, but not directly seen that, for a current deemed to be in the over-flowing regime, the flow is predominantly above the bed and that dilution is predominantly due to a vertical convective exchange of fluid. This section analyses velocity fields measured using the PTV technique to further develop these findings. Additionally, volume fluxes are calculated in order to understand the entrainment of ambient fluid into the currents.

6.3.2 Horizontal velocity Profiles

In Section 6.2 it was seen that for the D5H10 experiment, unlike the other dense configuration experiments, the relative roughness height was too large for a significant overflowing current to develop atop the roughness. Therefore, this experiment predominantly travelled through the roughness and exhibited properties similar to the sparse configuration experiments seen in Chapter 5. In Chapter 5 it was noted that when flow velocities were measured along the centreline of a through-flowing experiment a significant difference was observable between alternating gaps in roughness where visualisation was available. In every second gap the measurements took place directly behind a cylinder and a wake was observed causing significantly lower horizontal velocities and in every other gap the measurements took place directly in front of a cylinder and at this location a significant horizontal velocity was observed. However, it was argued that none of these velocities would have been representative of the speed of the current within the

bed because the velocities would have been larger slightly off centre where the current travelled around the roughness.

With the D5H10 experiment being in a through-flowing regime the wakes and differences between alternating gaps in cylinders are also expected to be present for this experiment. To investigate this Figure 6.25 shows horizontal velocity profiles for this experiment within 4 different gaps at a time of 21. This time was selected because is it large enough that the current had travelled a significant distance through the roughness but short enough that the lock bore had not yet reached the roughness. It should be noted that due to the small size of the gaps between the cylinders the accuracy of velocities measured within the data is significantly lower than those measured above the roughness. As such errors may be as large as 10 % and only qualitative findings will be considered. The distances of 0.8 and 3 were in gaps immediately upstream of roughness elements. At a distance of 0.8 behind the current front the current was entirely submerged within the roughness and a significant flow through the roughness is visible. At a distance of 3 behind the front the current was slightly larger than the roughness height with both significant flow within and above the roughness. These findings are consistent with the sparse configuration experiments in Chapter 5. The measurements at distances of 1.1 and 2.7 behind the front were directly downstream of roughness elements. At these locations small velocities in the direction counter to the flow are visible consistent with these locations being within wakes behind the cylinders.

Qualitatively the profiles in Figure 6.25 appear to have structures comparable to the sparse configuration experiments in Chapter 5. However, because of significant variability in the data little can be concluded from the magnitude of the velocities. Furthermore, as the roughness was densely packed the gaps between the cylinders were small and little data was available. Therefore, little more can be observed from the velocity data in this experiment and based on the findings from Section 6.2 and Figure 6.25 it can be reasonably assumed that the velocity data would show dynamics similar to those found for the sparse configuration experiments.

In Section 6.2 it was seen that the D5H20 and D5H27 experiments were entirely in an overflowing regime, whereas the D5H15 experiment was primarily governed by an overflowing current trailing a small through-flowing wedge. To confirm that the flow was predominantly overflowing in these experiments, Figures 6.26 and 6.27 show horizontal velocity profiles at distances of 1 and 3 behind the over-flowing front and a distance of 0.5 downstream of the front. As with

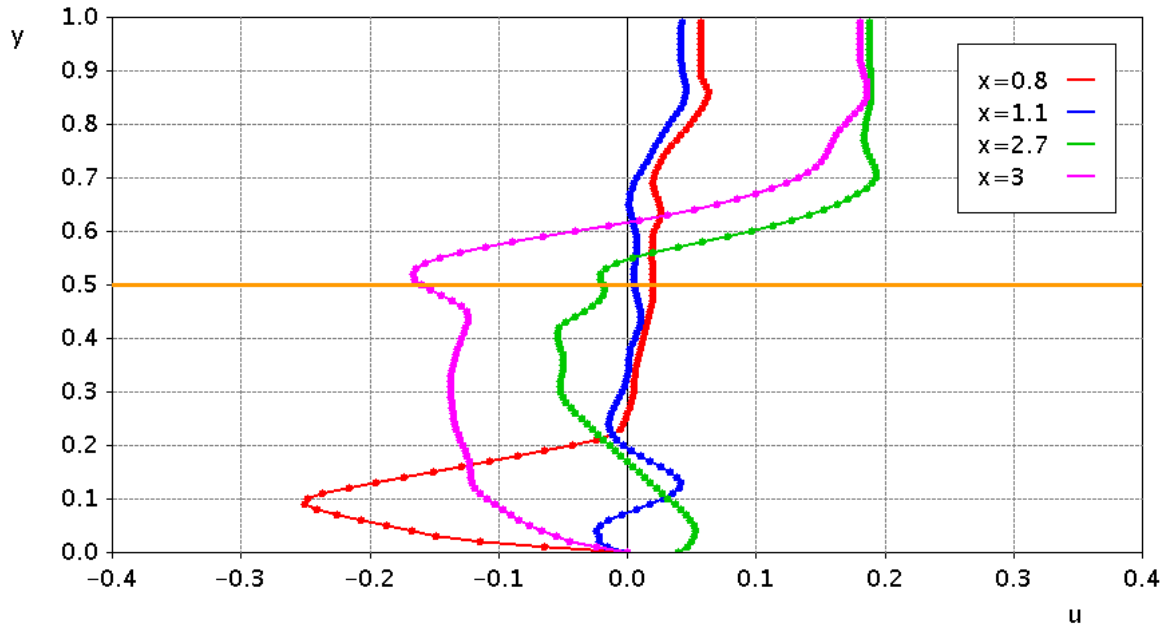

Fig. 6.25 Horizontal velocity profiles for the D5H10 experiment within gaps of roughness at distances of 0.8, 1.1, 2.7 and 3 behind the nose of the current at a time of 21. Distances of 0.8 and 3 were in gaps immediately upstream of roughness elements and distances of 1.1 and 2.7 were immediately downstream of roughness elements. The orange line shows the height of the roughness and non-dimensionalisation is based on H.

Figure 6.25 there was significant variability in the velocity data with time so while much can be learned qualitatively from the structure of these profiles, confident conclusions cannot be drawn from any trends in the magnitudes of these profiles.

At a distance of 0.5 upstream of the over-flowing nose it can be seen that the D5H15 had a significant through-flowing velocity profile similar to that at a distance of 0.8 behind the front in the D5H10 experiment. This profile suggests that the front upstream of the over-flowing nose travelled through the roughness similarly to the sparse configuration experiments. It was seen in Chapter 4 that a through-flowing profile in front of the over-flowing nose, similar to that seen in the D5H15 experiment, is not present for the D5H20 experiment at later times as this experiment was entirely over-flowing. However, in Figure 6.27 a small flow is visible within the bed in front of the current. The presence of this flow suggests that the ambient dense fluid entering the bed via convective instability may have had some horizontal momentum and forced ambient fluid within the bed forward. At locations of 1 and 2 for both the D5H15 and D5H20 experiments the velocity profiles show that these currents were predominantly over-flowing. At these locations there was still a weak flow within the roughness and this flow would likely

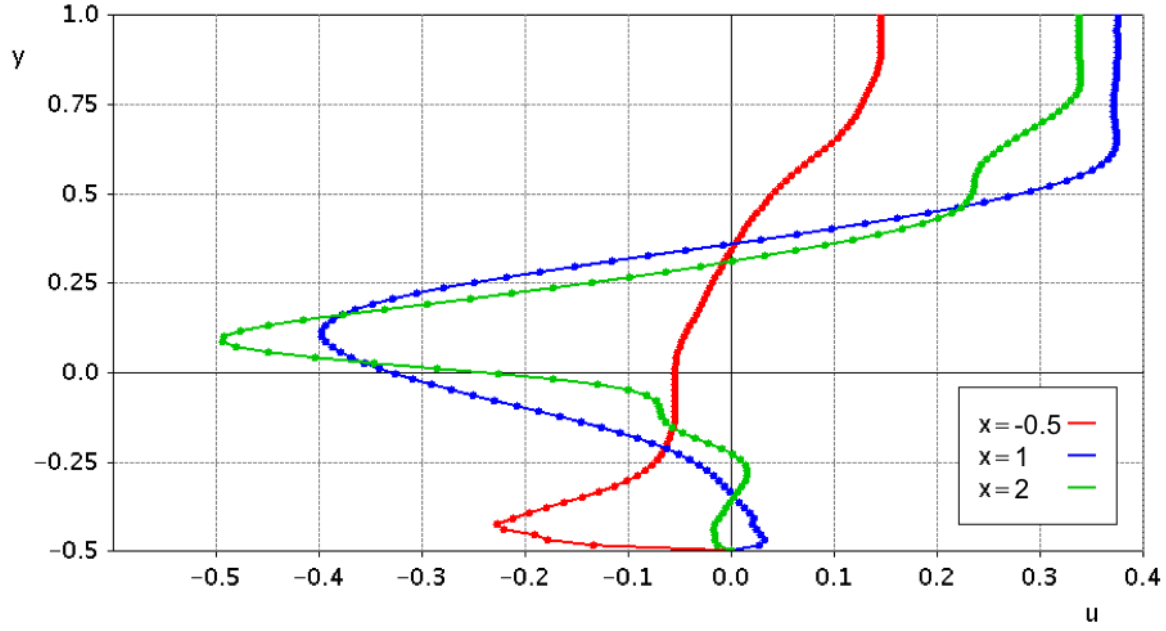

Fig. 6.26 Horizontal velocity profiles for the D5H15 experiment within gaps of roughness at a distance of 0.5 in front of the overflowing front and distances of approximately 1 and 3 behind the overflowing front behind the front of the current at a time of 21. All measurements were in the middle of gaps directly upstream of roughness. The non-dimensionalisation was based on $\tilde{H}$ and the top of the roughness was at a height of 0.

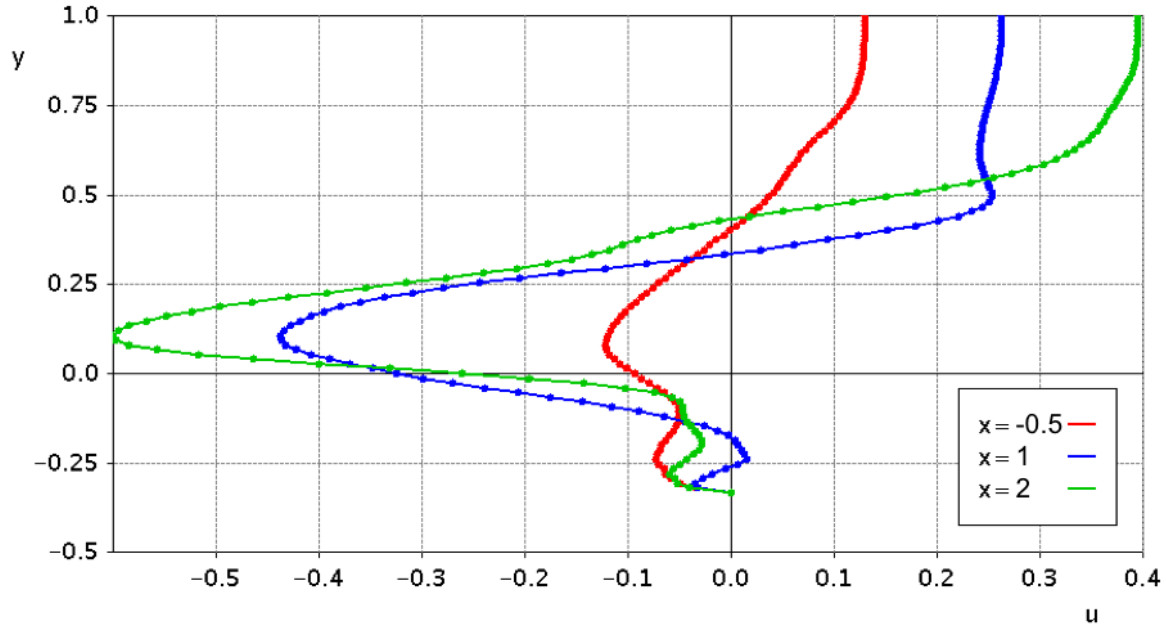

Fig. 6.27 Horizontal velocity profiles for the D5H20 experiment within gaps of roughness at a distance of 0.5 in front of the overflowing front and distances of approximately 1 and 3 behind the overflowing front behind the front of the current at a time of 21. All measurements were in the middle of gaps directly upstream of roughness. The non-dimensionalisation was based on $\tilde{H}$ and the top of the roughness was at a height of 0.

be seen to be larger if the measurements had been made off the centre of the roughness where the effects of the cylinders were minimised. Furthermore, the maximum velocity of fluid was significantly larger upstream of the head (x=2) than in the head (x=1). This is consistent with a smooth bed current where faster moving fluid in the tail enters the head to keep the current in a quasi-steady state. The profiles for the D5H27 experiment are not shown as they were similar to the D5H20 experiment.

6.3.3 Volume Flux

This section investigates the volume flux of the currents in order to understand how ambient fluid was entrained into the currents. For convenience the definitions for the ambient and total flux, as provided in Chapter 5 are repeated here

$$q_A = \int_{h_c}^{1} u dy \tag{6.3}$$

$$q_T = \int_{0}^{1} u dy \tag{6.4}$$

These fluxes were calculated for the over-flowing D5H20 experiment to understand how ambient fluid travelling over the current entrained into the current and how this was impacted by the bed. This current was selected because it was close to steady state when reaching the end of the roughness, unlike the D5H27 experiment, and was in a fully over-flowing regime, unlike the D5H15 experiment. This analysis was conducted with the co-ordinates non-dimensionalised by $\tilde{H}$ and y=0 defined to be the top of the cylinders. The domain was placed into a moving frame of reference where the current nose was stationary and the velocity field was time averaged from a time of 20 to 26 when the current was close to steady state. Finally the velocity was normalised by the front speed of the current at this time.

Using this method, locations where the velocity was 0 in the lab frame of reference had a velocity of 1. Furthermore, if no fluid were to be exchanged with the bed q_T should have a value of 1 for all x. Any increase or decrease in the total volume flux must be caused by either a cross-channel flux or by an exchange in fluid with the bed. As was discussed in Chapter 5 the ambient flux should be 1 far in front of the current, and behind the front any reduction in the

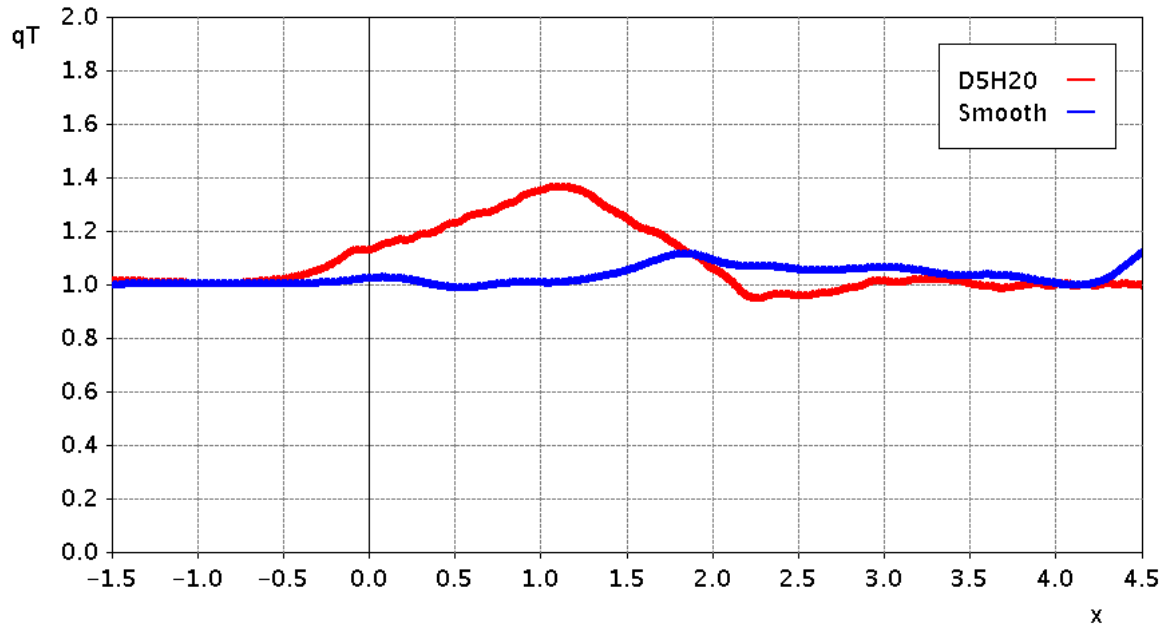

Fig. 6.28 q_T for the D5H20 experiment at a time of 23 $\pm$ 3 as well as a smooth bed current with x. Non-dimensionalisation of D5H20 is based on $\tilde{H}$ The front of the current is at x=0 and for the D5H20 experiment the top of the cylinders is defined as y=0.

ambient flux is most likely due to entrainment of ambient fluid into the current. However, for the over-flowing current changes in the ambient flux could also be related to fluid exchanged with the bed, particularly in front of the current where $q_A = q_T$. To investigate how current fluid was exchanged with the bed and the ambient, Figures 6.28 and 6.29 show the total and ambient flux respectively for the D5H20 experiment as well as for a smooth bed experiment carried out using the same method but non-dimensionalised by H.

Figures 6.28 and 6.29 show that significantly downstream of the front (e.g. x=-1) the total flux and ambient flux are both 1. However, for a distance of approximately 0.5 in front of the current both fluxes rise, indicating the presence of a flux of fluid travelling upwards from the bed in front of the current. While the majority of dense fluid motion was above the cylinders a small amount of motion took place within the bed. This motion may have pushed ambient fluid forward within the bed and hence to conserve volume within the bed some of this fluid was forced upwards in front of the nose. The increase in flux in front of the current is not present in the smooth bed experiment as the boundary beneath the current was solid. From x=0 the total flux continues increasing for a distance of approximately 1, indicating that in the head region more fluid is transferred from the bed to the current than is lost from the current to the bed. The magnitude of this is unexpectedly large as Figure 6.28 indicates that the volume flux of fluid above the

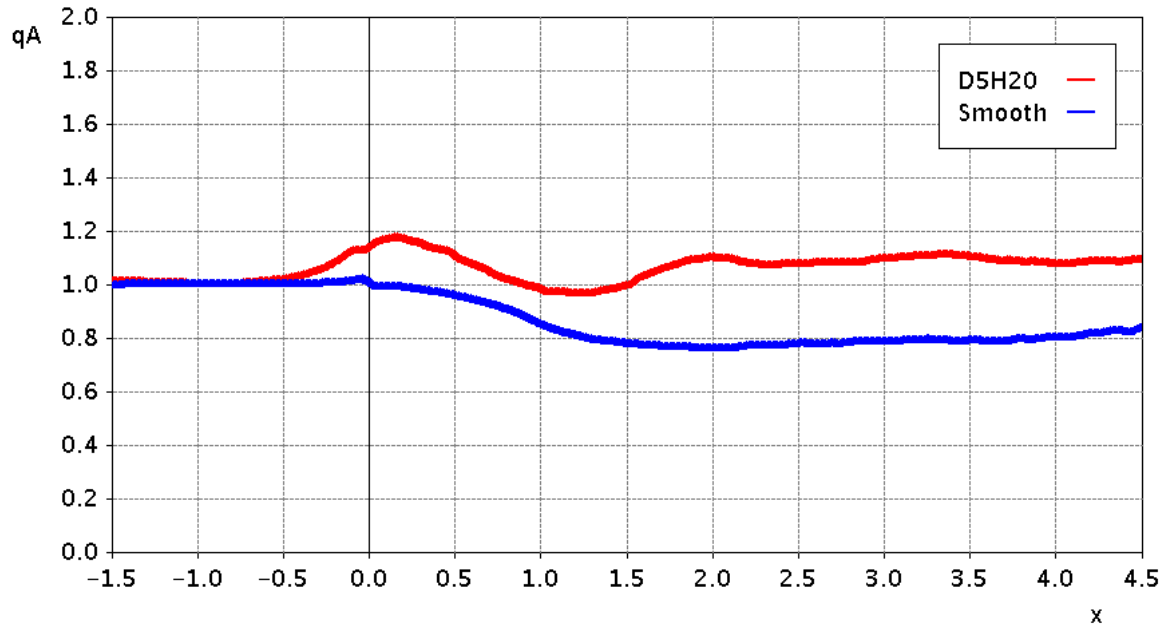

Fig. 6.29 q_A for the D5H20 experiment at a time of 23 $\pm$ 3 as well as a smooth bed current with x. Non-dimensionalisation of D5H20 is based on $\tilde{H}$ The front of the current is at x=0 and for the D5H20 experiment the top of the cylinders is defined as y=0.

cylinders increases by almost 40% between x=-1 and x=1. However, from a distance of 1 behind the front the total flux begins to decrease until a value of 1. Thus a circulation appears to have been generated wherein behind the head there is a net flux of fluid into the bed exactly matching the amount that was ejected from the bed earlier. It should be noted that behaviour is not clearly visible in the vertical velocity field due to large fluctuations.

For a smooth bed current the ambient flux reduces by 20 to 25 percent over a length of approximately 2 before becoming constant with x. This reduction is due to K-H instabilities causing ambient fluid to be entrained into the current, as discussed in Chapter 5. The ambient flux of the D5H20 experiment decreases for a length of approximately 1.2 and appears to have been trending towards a total reduction of approximately 20 percent of the ambient flux at x=0. However, between x=1 and x=1.5 the ambient flux rises. As the current fluid cannot "unmix" and cross the boundary with the ambient fluid the increase in ambient flux suggests that some light fluid initially contained within the bed may be able to percolate upwards through the current towards the ambient without mixing. This process is not dissimilar to the lobe and cleft structure formed by light fluid trapped below the nose of a smooth bed current, albeit with a significantly larger volume of trapped fluid. This fluid has been shown to percolate upwards through the full depth of the current without all of it mixing (Härtel et al., 2000a). Thus, as the quantity of light

fluid contained within the roughness is significantly larger than the fluid underneath the nose of a smooth bed current, it is not unreasonable to believe that this fluid may be able to penetrate the full depth of the current without becoming fully mixed into the current.

6.4 Summary

This chapter has explored the results from the dense configuration experiments. One question posed was how a current's speed, structure and density is impacted by roughness and how this is impacted by time and relative roughness height. When a current with a large relative roughness height encounters densely distributed roughness it begins to transition to having wedge-like characteristics and its speed begins to decrease. Over time this current dilutes, the angle formed by the wedge with the horizontal decreases and it continues to slow. The properties of this current are comparable to the sparse configuration experiments seen in Chapter 5.

When a current with a smaller relative roughness height enters the roughness it initially propagates through it but behind the through-flowing nose this current begins propagating over the roughness. When the relative roughness is small (e.g. less than 0.25) the large blockage causes the majority of the fluid to be deflected upwards and flow over top of the roughness. This over-flowing front quickly overtakes the through-flowing front, causing the fluid within the bed to be predominantly the result of the vertical exchange of fluid with the over-flowing front rather than due to a current driven within the roughness. A transitional regime exists, with a relative roughness height of approximately 0.3, where the relative roughness height is not large enough for the current to be entirely through-flowing but nor is it small enough for the current to be entirely over-flowing. This current forms a state where a through-flowing front propagates through the roughness, slightly trailed by a separate over-flowing front. Additional buoyancy is provided to the through-flowing front by the over-flowing front, allowing the two fronts to propagate forward at the same speed.

The question of how the entrainment of ambient fluid into the current and its velocity structure is impacted by roughness was also posed. As an over-flowing current travels atop the roughness it loses buoyancy and slows as fluid is exchanged with the bed. As this exchange happens the light fluid within the bed appears to not only percolate upwards and mix with the current but also penetrate the full depth of the current such that some unmixed bed fluid gets deposited

into the ambient fluid above the current. In addition to fluid percolating upwards through the current some light fluid also appears to be forced forward by dense fluid within the bed and is thus forced out of the bed in front of the current. Meanwhile, ambient fluid is entrained into the current at the upper boundary due to K-H instabilities.

An over-flowing current appears to be driven predominantly by the buoyancy of the current head. As the current loses buoyancy to the bed this driving force decreases, causing the current to slow. Evidence of this process can be seen by the Froude number based on the local depth and dilution being approximately constant with time, despite the current losing buoyancy and slowing. The speed and average density of an overflowing current approaches a constant value with time as the loss of buoyancy to the bed and entrainment of ambient fluid into the current becomes in balance with the dense fluid entering the current head from the tail.

Chapter 7: Results From Plunging Configuration Experiments

7.1 Introduction

In Chapter 4 it was found that the nose of a plunging configuration current initially travels through the roughness before fluid behind the front is deflected upwards and plunges over the top. Evidence was also seen that the current in the P5H10 experiment was too small to plunge over top of the roughness, causing fluid that was deflected upwards by each row of roughness to propagate back upstream as bores. Furthermore, as with the sparse and dense configurations, a plunging configuration current slows and dilutes as it travels. This chapter explores the plunging configuration experiments in more detail. In particular for a current encountering plunging configuration roughness several questions are addressed

- How does the current dilute with time and relative roughness height?
- How is the structure of the current impacted by the relative roughness height and time?
- How does its Froude number develop with time and how is this impacted by the relative roughness height?
- What is the predominant driving force for the current and how is this impacted by time and relative roughness height?
- How does ambient fluid become entrained into the current and how does this vary with relative roughness height?
- Can significant evidence of plunging behaviour be found and does the plunging behaviour only occur near the front of the current or does it extend into the tail?

Section 7.2 explores the results from the density fields generated using the LA technique. Section 7.2.1 provides an overview of the results by examining the buoyant height of two experiments.

It is seen that the driving force and speed of these currents decreased with time as they travelled through the roughness, similar to the sparse configuration experiments in Chapter 5. Unlike the sparse configuration currents, which were impacted by the cylinders as a field, each row of roughness impacted the plunging configuration currents with larger relative roughness height individually. Section 7.2.2 then builds on the preliminary results by comparing how the front location and Froude number of all of the experiments varied with time. Regardless of the relative roughness height the Froude numbers of all of the currents reduced at the same rate and they never approached constant speeds within the length of roughness employed. To understand why the relative roughness height did not impact the Froude number, and to address how the current density and structure varied with time, Section 7.2.3 compares the buoyant height and current envelope of all experiments with time. This section shows that the buoyant height of these currents lost their head and tail structures and took on wedge-like characteristics as the currents travelled, similar to the sparse configuration experiments seen in Chapter 5.

By comparing the currents with different relative roughness heights in Section 7.2.3 it is seen that at a given time the extent to which the heads had been replaced by wedge-like structures depended on the relative roughness height. The currents with smaller relative roughness heights had larger vertical extents and were less dilute near the front. However, behind the head region the buoyant heights of all of the experiments had wedge-like characteristics with similar angles. In the tail the driving forces were larger than those in the head. It is, therefore, concluded that the reason for the similarity in Froude numbers was due to the currents being driven by a balance between the pressure gradient in the tail and drag force due to the cylinders. A similar balance was found for the sparse configuration experiments and in Chapter 5 a model was developed based on a balance between the drag force and the pressure gradient. In Section 7.2.4 this model is applied to the plunging configuration experiments and found to be a good fit, albeit with the cylinders taking on a larger drag coefficient than the sparse configuration equivalents. Furthermore, Section 7.2.3 provides additional evidence that currents with smaller relative roughness heights experienced each row of roughness separately while currents with larger relative roughness heights experienced roughness as a distributed field.

Section 7.3 explores the results from the velocity fields generated using the PTV technique. It is found that the fronts of the currents were predominantly through-flowing with large horizontal velocities visible below the top of the roughness. However, further upstream within the tail

the velocities within the bed fell to almost 0 and the majority of flow was above the roughness. At the front any fluid which flowed over the roughness plunged downwards over top of the small through-flowing fronts, causing there to be very little flow above the roughness. However, upstream of the front the bed became saturated with dense fluid giving over-flowing fronts no reason to plunge downwards and thus leading to the currents being predominantly over-flowing at these locations.

7.2 Density Fields

7.2.1 Overview

This section explores results from the density fields generated from the light attenuation experiments. Similarly to previous chapters this analysis makes use of the buoyant height, analysing how it varied with time, space and between experiments to understand the forces driving these currents. Current envelopes are also analysed to describe the vertical extent of these currents and how these vary with space and time.

To provide an overview of the main features of these currents Figure 7.1 shows the buoyant height in false colour for the P5H20 experiment as a function of x and t. The buoyant height cannot be calculated at the roughness locations so these locations are displayed in black. As the spacing between cylinders in the stream-wise direction was larger for these experiments than those discussed in Chapters 6 and 7, these experiments allowed for visualisation over a significantly longer distance between rows of cylinders.

Figure 7.1 appears qualitatively similar to the buoyant height for the equivalent sparse regime experiment (S5H20) presented in Chapter 5. When the current reached the roughness it began to slow, as seen by the separation between the red and green lines and a bore was reflected from the front face of the roughness. The current path and Froude number are discussed further in Section 7.2.2. As the current travelled the buoyant height at the standard head location (the blue line) reduced. The reduction in the buoyant height with time is discussed further in Section 7.2.3. The lock bore is also visible with its front labelled by the purple line.

In Chapter 5 a buoyant height field was only presented for the S5H20 experiment as this experiment was believed to reasonably represent all of the experiments. In Chapter 5 the spacing

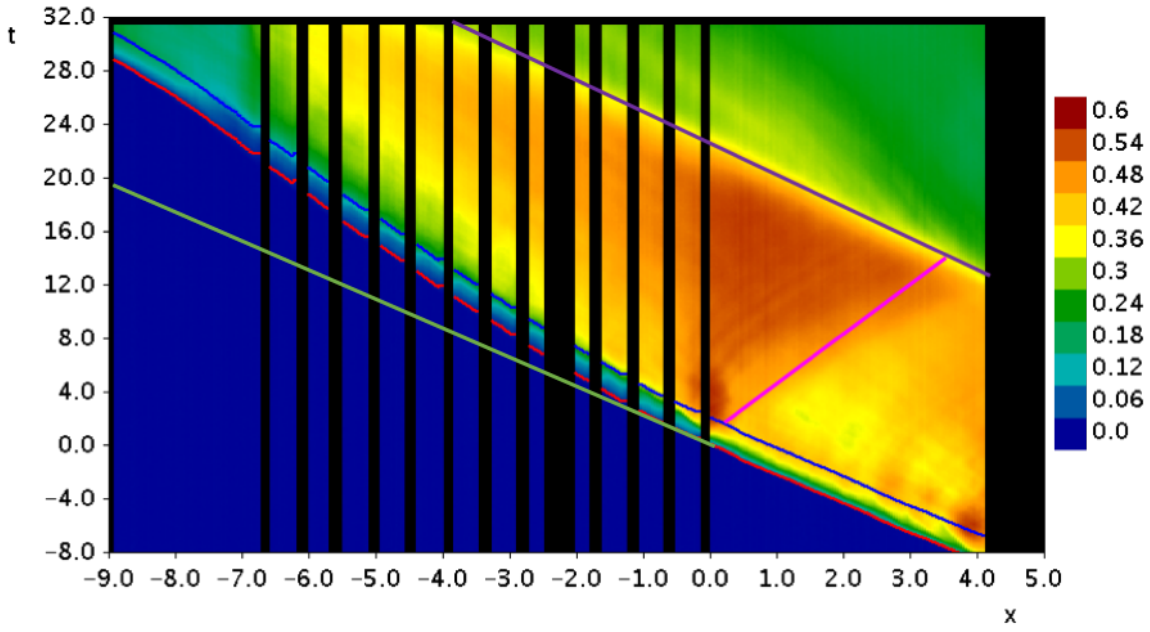

Fig. 7.1 h_B for the P5H20 experiment displayed as false-colour with x and t. The red line shows the front location of the current, the blue line represents the standard head location, the pink line shows the path of the roughness bore and the purple line shows the path of the lock bore. The green line is an extrapolation of the path of a smooth bed current. The black regions represent locations where visualisation was insufficient to calculate the buoyant height.

between rows of roughness was small enough that the currents experienced the roughness as a field rather than being impacted separately by individual rows of roughness. In the case of the plunging configuration experiments the spacing between rows of roughness was twice that of the sparse experiments. As the fluid depth relative to the spacing between rows of roughness decreased the currents became impacted individually by rows of roughness rather than experiencing them as a field. To illustrate how the roughness impacted the currents as the relative roughness height increased Figure 7.2 shows the buoyant height in false colour for the P5H15 experiment as a function of x and t.

Many of the features of Figure 7.1 are visible in Figure 7.2. However, small but prominent bores are visible being reflected from each row of roughness and these were very small if present at all in the P5H20 experiment. These bores occurred because when the front of the current reached each row some fluid propagated through the roughness and some was deflected upwards and propagated backwards as a bore. These bores were not visible for the sparse experiments because the spacing between rows of roughness was small enough that the currents experienced the roughness as a field rather than experiencing each row individually. Furthermore for an

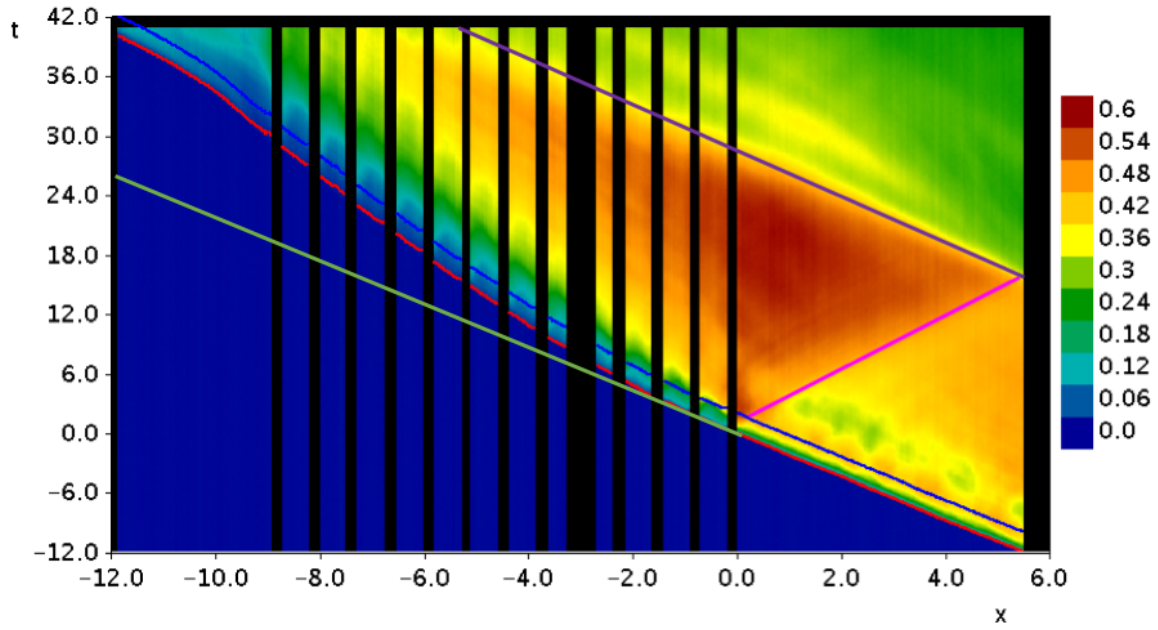

Fig. 7.2 h_B for the P5H15 experiment displayed as false-colour with x and t. The red line shows the front location of the current, the blue line represents the standard head location, the pink line shows the path of the roughness bore and the purple line shows the path of the lock bore. The green line is an extrapolation of the path of a smooth bed current. The black regions represent locations where visualisation was insufficient to calculate the buoyant height.

experiment with a small relative roughness height the bores are unlikely to be visible due to the roughness being buried within the current. The bores in Figure 7.2 are not seen reaching the preceding rows of roughness because after a small time deeper fluid from upstream overwhelmed them. This behaviour is further explored in Section 7.2.3.

7.2.2 Front Location and Speed

The previous section showed that as the currents travelled their speeds decreased. In Chapters 5 and 6 it was seen that the currents in the sparse and dense configurations also slowed with time. The rate at which their Froude numbers reduced with time did not depend on the relative roughness height when the roughness was sparsely distributed; however, there was a weak trend between relative roughness height and Froude number for the dense configuration. This section explores how the front location and Froude number of a current interacting with the plunging configuration roughness varies with time and relative roughness height in order to ascertain similarities and differences to the results found in previous chapters.

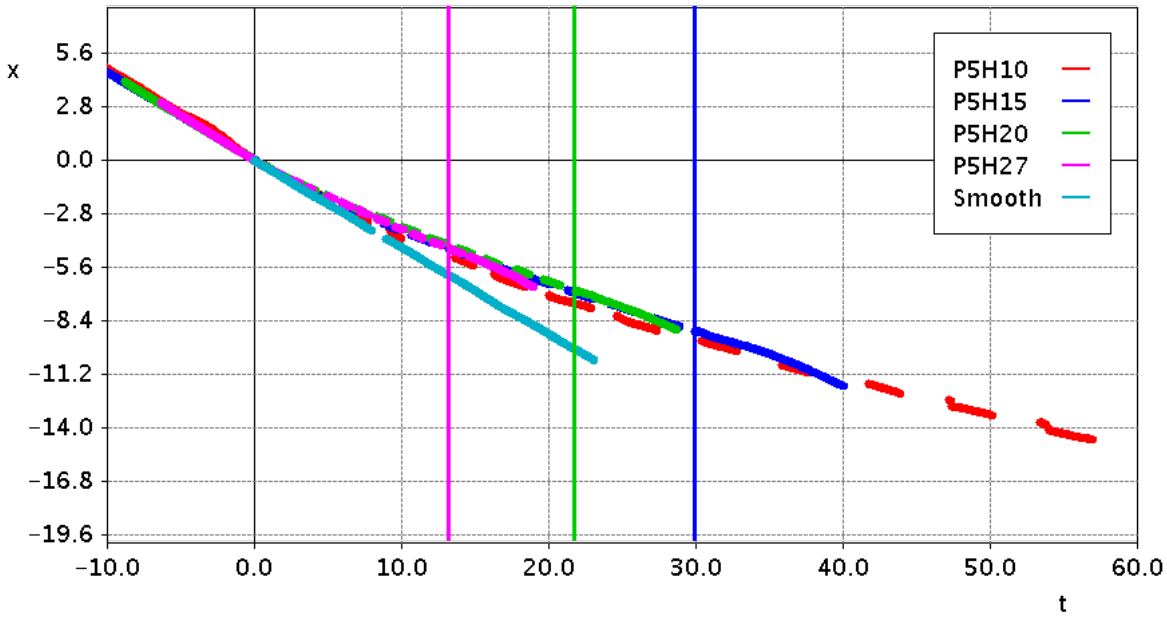

Fig. 7.3 Front location with time for the plunging experiments. The currents entered the roughness at a time and location of 0 and the horizontal lines show the locations where the currents exited the roughness. The smooth bed current is an extrapolation of behaviour prior to the roughness field.

Figure 7.3 shows the front location with time for all of the plunging experiments. Before the currents encountered the roughness (where time was less than 0) they were still smooth bed currents and the front locations of all of the currents were similar and linear with time. Once the currents encountered the roughness (from a time of 0) they all slowed with time at similar rates. The similarity between currents of different relative roughness heights is consistent with the sparse configuration experiments in Chapter 5. The vertical lines show the times when the currents exited the roughness for all of the experiments except for P5H10 because the lock bore overtook the front of the current before it could exit the roughness. Similar to the experiments in the sparse and dense configurations the currents began to increase in speed again after exiting the roughness.

While it is clear from Figure 7.3 that the currents slowed as they travelled through the roughness it is not clear how this varied with time and whether the currents approached a constant speed. Therefore, the front locations shown in Figure 7.3 were differentiated and the resulting Froude numbers are shown with time in Figure 7.4. Before the currents reached the roughness Figure 7.4 shows the Froude number to be 0.46 for all experiments. Oscillations are visible due to the presence of seiche waves generated by the opening of the gate. After the currents encountered

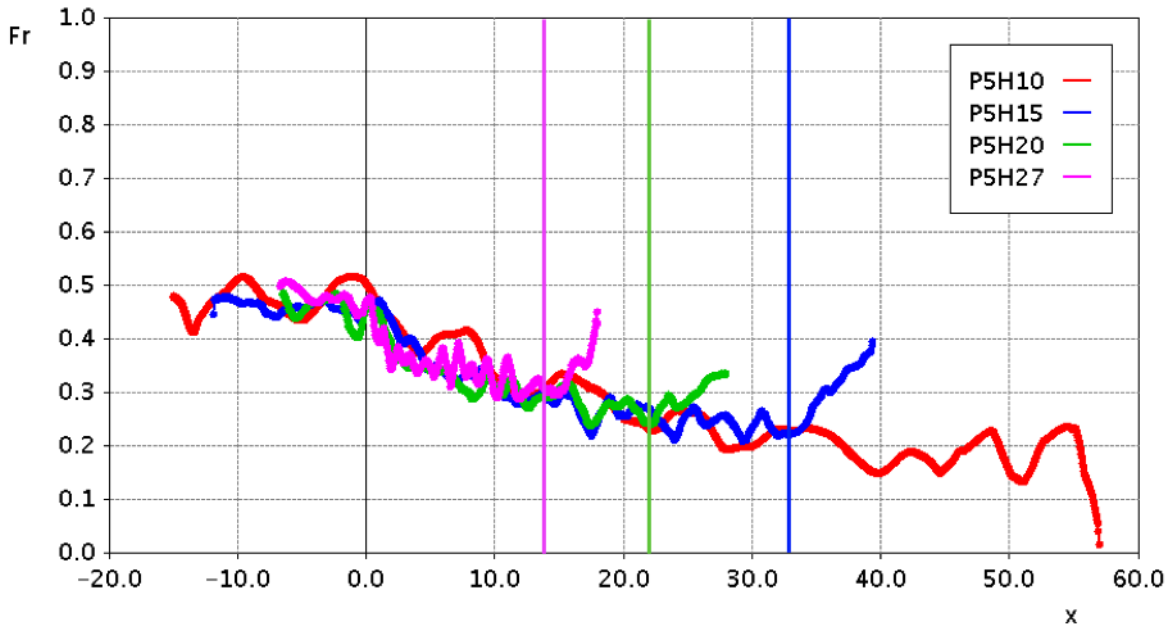

Fig. 7.4 Froude Number with time for the plunging experiments. The currents entered the roughness at a time of 0 and the vertical lines show the times when the currents exited the roughness.

the roughness a reduction in the Froude Number with time occurred and, as seen in Figure 7.3, the rate of this reduction was similar for all of the experiments. Furthermore, once the currents exited the roughness their Froude numbers began increasing, similar to the sparse and dense configuration currents in Chapters 5 and 6.

In Chapter 5 it was argued that the sparse configuration experiments were driven predominantly by a balance between the pressure gradient in the tail and the drag force imposed by the cylinders. Therefore, the similarity in the Froude numbers was due to individual rows of roughness having larger impacts on the currents with larger relative roughness heights and this being balanced by these currents passing fewer rows of roughness after travelling the same non-dimensional distance as experiments with smaller relative roughness heights. Despite the currents in this chapter exhibiting plunging characteristics over the top of the roughness it is entirely plausible that they were predominantly driven by similar dynamics to those seen in the sparse configuration. Therefore, the driving forces are explored in more detail in Section 7.2.3 and the Froude numbers are compared to the model from Chapter 5 in Section 7.2.4.

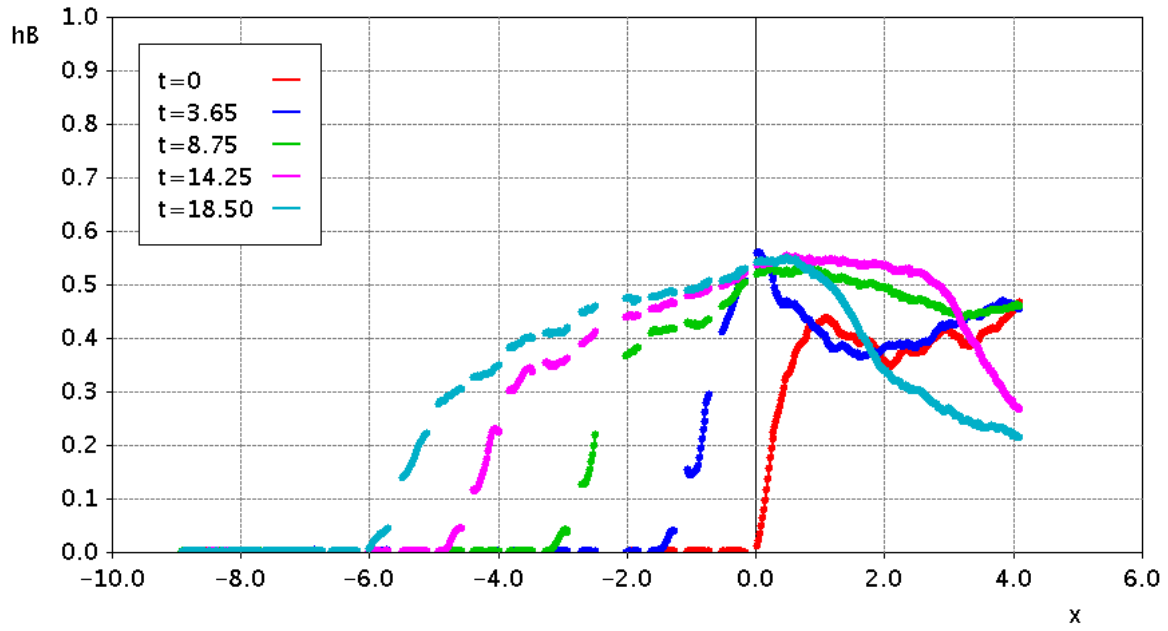

Fig. 7.5 h_B for the P5H20 experiment at times of 0, 3.65, 8.75, 14.25 and 18.5. At these times the front of the current was halfway between two rows of roughness.

7.2.3 Current Height and Density

Overview

In the previous section it was seen that the Froude number for a current interacting with plunging configuration roughness decreases with time and does not depend on the relative roughness height. Moreover, a buoyant height reduction with time was seen in Section 7.2.1 for the P5H20 experiment and it was found that as the relative roughness height increased separate rows of roughness began individually impacting the currents rather than behaving as a field of roughness. This section builds on these results while attempting to understand the impact of roughness on the height and density of the currents. In particular, the density structure is compared with experiments in previous chapters to ascertain similarities and differences in the mechanisms driving these currents.

Variation in Current Structure with x

To understand the development of these currents as they travelled the buoyant height of the P5H20 experiment is displayed in Figure 7.5 as a function of x at 5 different times. The times were selected such that the current front was situated halfway between two rows of roughness.

Figure 7.5 shows that as the current travelled its buoyant height increased at the front face of the roughness. Additionally, the buoyant height transitioned from the head and tail structure of a smooth bed current to displaying a wedge-like structure similar to the sparse experiments analysed in Chapter 5. The similarity to the sparse configuration experiments indicates that despite the fact that this current is thought to have plunged over the top of the roughness behind the front it was driven by a similar pressure gradient within the tail of the current to the sparse configuration experiments. Unlike the sparse configuration experiments, for a distance of between 0 and 0.4 behind the front the angle of this wedge was shallower than the wedge upstream. This shallow section can be explained by an initial through-flowing current, more dilute than the fluid upstream, propagating through the roughness before the current was able to plunge over the top of it. Thus, while there is a difference in the dynamics between a sparse and plunging configuration current near the nose, these dynamics are unlikely to affect the current behaviour primarily driven by the pressure gradient in the wedge.

Figure 7.6 shows the same experiment but with the front location redefined such that it was always at a location of 0. The vertical lines show the front face of the roughness. Similar to the sparse experiments the angle of the wedge reduced with time. Therefore, the driving force imposed on the current reduced with time, consistent with the reduction in the Froude number with time seen in Section 7.2.2.

To understand whether changes in the buoyant height were predominantly due to dilution of the current or a decrease in its vertical extent Figure 7.7 shows the current envelope at the same times as Figure 7.5.

Through-flowing currents propagating through the roughness before the fluid upstream could plunge over top of them can be seen by observing the separate local maxima with heights of approximately 0.4 and locations of approximately 0.5 behind the current front. As the current travelled the maximum height of the through-flowing portion appears to have grown in size, likely due to the driving force decreasing with time, causing more fluid to propagate through the roughness before the deeper fluid could be deflected over top of the roughness.

Upstream of the initial front this current did not appear to take on a wedge-like structure as seen in Figure 7.5 but instead the vertical extent from a location of approximately 1 behind the front was roughly constant with x. Therefore, the wedge-like structure seen in Figure 7.5

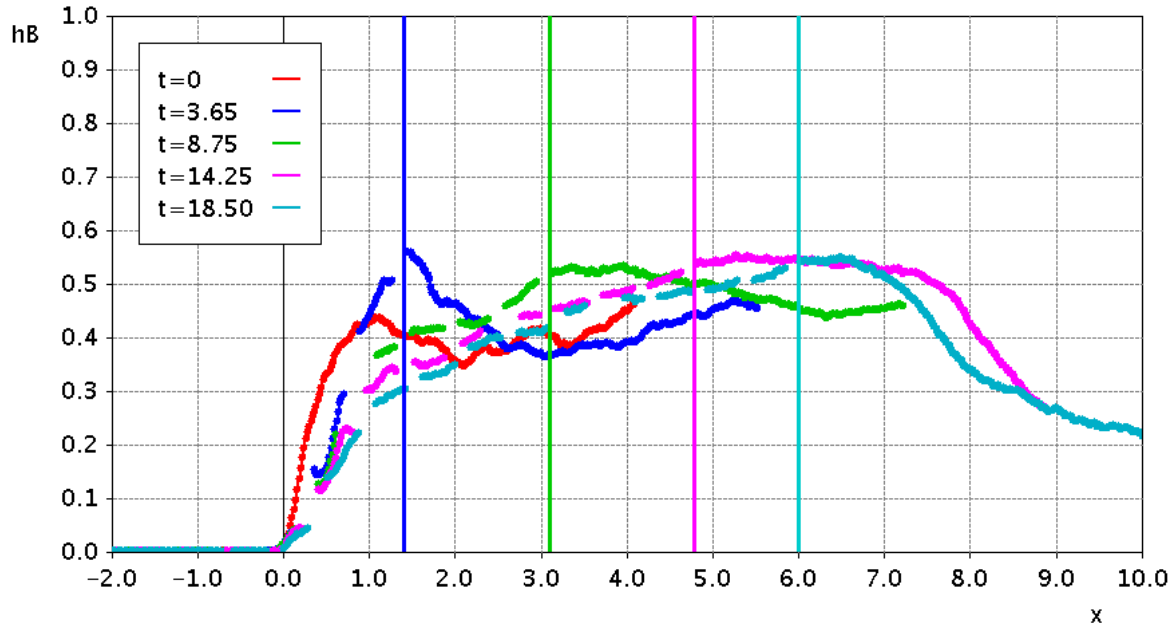

Fig. 7.6 h_B for the P5H20 experiment at times of 0, 3.65, 8.75, 14.25 and 18.5 with the current front redefined such that for all times it lies at a location of x=0. At these times the front of the current was halfway between two rows of roughness.Vertical lines show the location of the front face of the roughness.

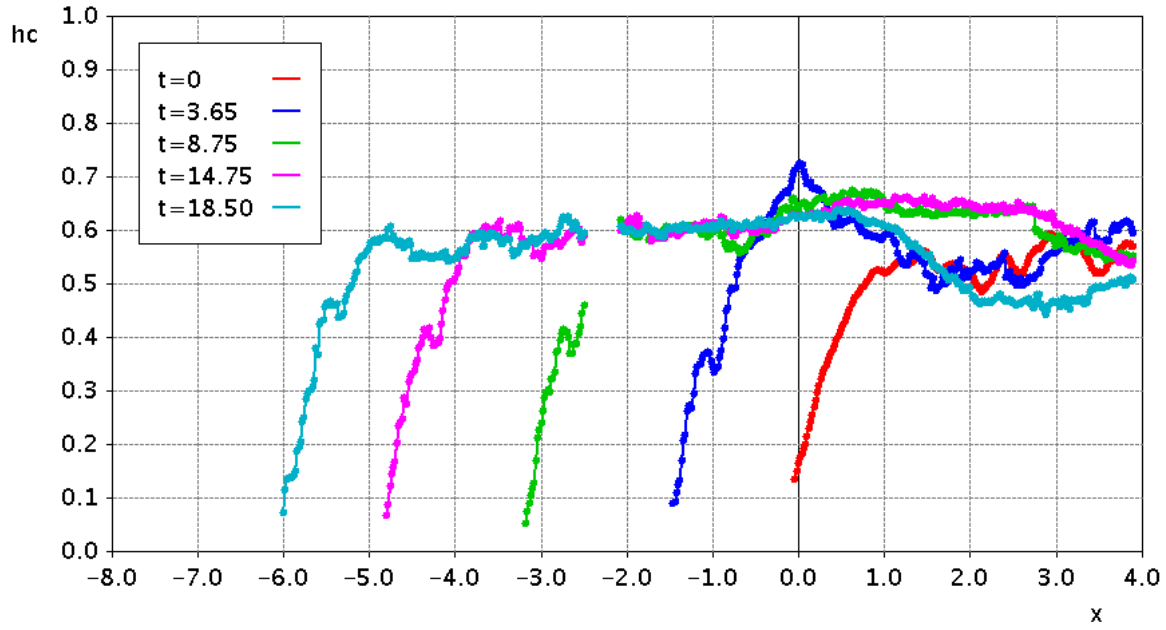

Fig. 7.7 h_c for the P5H20 experiment at times of 0, 3.65, 8.75, 14.25 and 18.5. At these times the front of the current was halfway between two rows of roughness.

indicates that the current head diluted with time and that and the density increased towards the tail. This structure implies that while the current was being driven by a pressure gradient in the tail, and shared behaviour with the sparse configuration currents near the front, behind the front it behaved more like the over-flowing, dense configuration experiments. The behaviour upstream of the front is not unsurprising as despite there being large gaps between rows of roughness the spacing was the same as the dense configuration across the channel. Thus, it may have been more energy efficient for the current to predominantly travel atop the roughness upstream of the front where the roughness was saturated with dense fluid. The possibility of over-flowing behaviour in the tail is explored further by observing velocity fields in Section 7.3.

Thus far this section has only considered how the properties of an experiment with a fixed relative roughness height varied as it travelled. While many of the features of this experiment are applicable to currents with different relative roughness heights it was seen in Section 7.2.1 that as the relative roughness height changes, the way that the currents interact with the roughness also changes. To explore how the impact of the roughness varies with the relative roughness height, Figure 7.8 shows the buoyant height for the four plunging experiments at the closest time to 14 when their fronts were all located halfway between two rows of roughness. At this time the P5H27 experiment was between the final two rows of roughness but the P5H10 experiment had only passed the fifth row of roughness. However, all of the currents had travelled the same non-dimensional distance at this time so the orange line shows the relative location of the front face of the roughness for all of the experiments.

Many features of Figure 7.8 are similar to the sparse configuration experiments. Between x=0 and x=2 (approximately in the head region of a traditional smooth bed current) there is a clear trend of increasing buoyant height with decreasing relative roughness height. However, there is a similarity in the wedge behind the head region for all of the experiments apart from P5H10. In Section 7.2.2 it was seen that the Froude numbers of all of the plunging currents, regardless of the relative roughness height, decreased at similar rates as the currents travelled through the roughness. Therefore, the fact that the buoyant height wedge in the tail had a similar gradient for all of the currents (with P5H10 as an exception) indicates that, similarly to the sparse configuration experiments, the currents were predominantly driven by a pressure gradient in their tails. It is unsurprising that the P5H10 experiment did not posses a similar structure as it is the only experiment where the current was entirely submerged within the roughness

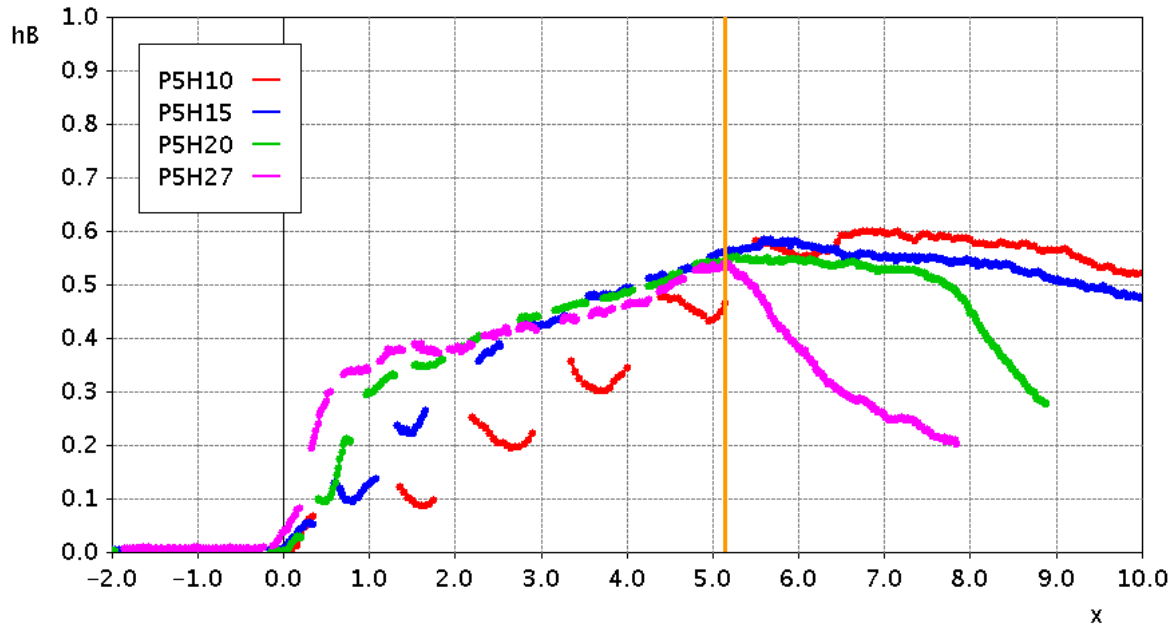

Fig. 7.8 h_B with x for the plunging experiments at the closest time to 14 when the fronts lie halfway between the two rows of roughness. Experiments are translated such that the noses of the currents lie at x=0. The orange line represents the average location of the front face of the roughness.

and thus was not large enough to plunge over the roughness. Given the fact that it appears to have had a different pressure gradient it is would be expected that this experiment would have a different Froude number than the others. One possible explanation for this current having the same Froude number of the other currents is that being submerged within the roughness meant that the drag force exerted on the current was larger and that this was balanced by the steeper pressure gradient seen in Figure 7.8.

Figure 7.8 also shows the currents being affected individually by rows of roughness as the relative roughness height decreased. The P5H20 and P5H27 experiments had buoyant heights at this time that were very similar to the sparse experiments from Chapter 5. However, the P5H15 experiment had small local maxima where fluid was deflected upwards and formed individual bores, for example at x=1.2. The locations of these maxima correspond to the front face of rows of roughness close to the current front. This behaviour is even more prominent in the P5H10 experiment where increased buoyant heights are visible in front of each row of roughness (in front of each location where there is a gap in the data). The behaviour is particularly prominent in the P5H10 experiment because the current was completely submerged within the roughness meaning no fluid was able to plunge over top of the roughness until a large distance upstream.

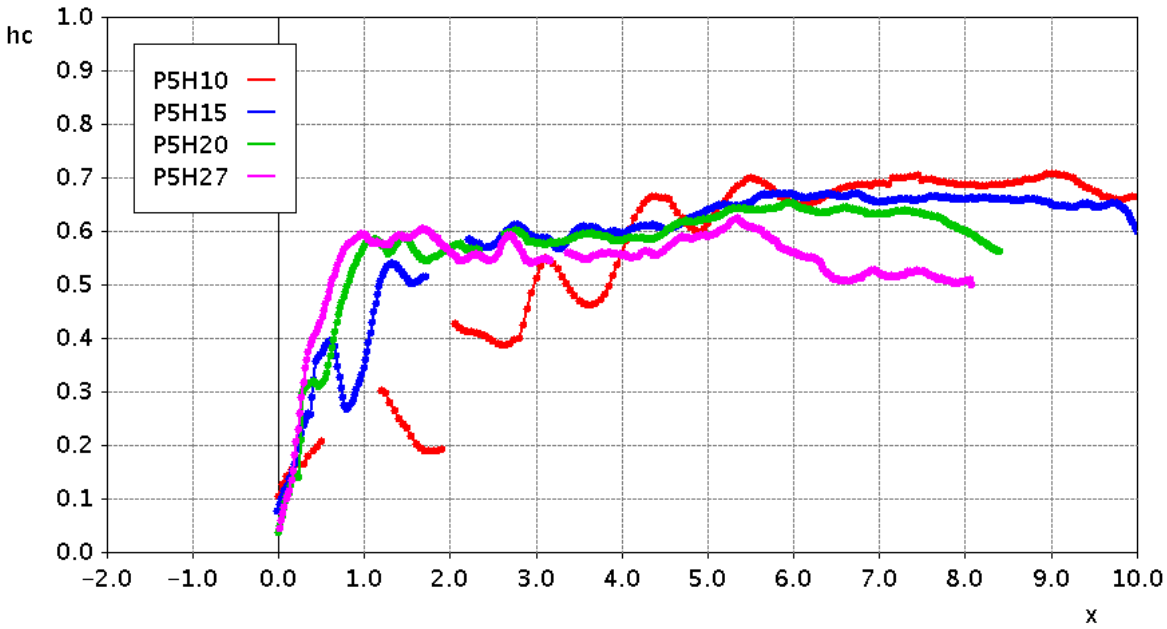

Fig. 7.9 h_c with x for the plunging experiments at the closest time to 14 when the fronts lie halfway between the two rows of roughness. Experiments are translated such that the fronts of the currents lie at x=0.

Figure 7.9 shows the current envelope for all of the plunging experiments at the same times as Figure 7.8. This figure shows, similarly to Figure 7.8, that all of the experiments, except for P5H10, were similar upstream of the head region. Upstream of the head region these currents appeared qualitatively similar to the over-flowing currents discussed in Chapter 6. In the head region the individual interactions with each row of roughness are also visible. The effect of individual rows of roughness is not clear for the P5H27 experiment and only a small local maximum is visible behind the first row of roughness for the P5H20 experiment. However, for the currents with larger relative roughness heights the impact of individual rows of roughness is seen in the form of local maxima in front of individual rows of roughness, for example at locations of 0.6 and 1.2 for the P5H15 experiment.

Whether or not a bore is visible behind a given row of cylinders appears to be related to the current envelope upstream of the row relative to the roughness height, referred to henceforth as the *relative current depth*. Observing Figure 7.9 the P5H10 experiment experiences bores behind cylinders in the tail until the current envelope is approximately 0.7. However, the P5H15 current only experiences bores until h_c is 0.5 and the P5H20 current only experiences a bore until h_c is 0.32. These 3 heights correspond to relative current depths of 1.4, 1.5 and 1.3. Thus it

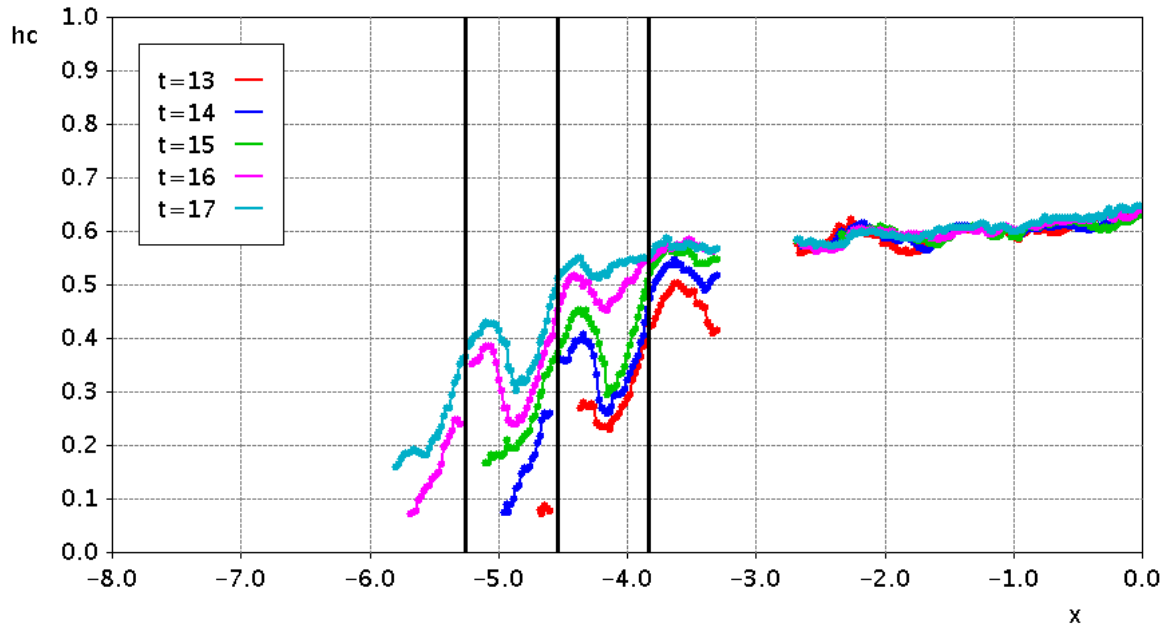

Fig. 7.10 h_c for the P5H15 experiment at times of 13, 14, 15, 16 and 17. Black lines show locations of three rows of roughness near the current front.

appears that when the relative current depth is above approximately 1.5 a bore will not form as the bore will be overwhelmed by current fluid coming from the previous row of cylinders.

To this point all of the figures in this section have considered the currents when their noses were located between two rows of cylinders. However, Figure 7.8 indicates that currents with large relative roughness heights develop as they travel between rows of roughness. To investigate the dynamics as currents with large relative roughness heights travelled between rows of roughness Figure 7.10 shows the current envelope for the P5H15 experiment at 5 different times. The vertical black lines highlight the locations of three rows of roughness. At a time of 13 the front of the current has just passed a row of roughness (the middle of the black lines). At this time only a small nose has emerged from this row and fluid is beginning to build up behind it. Over the following two times the current travels as a wedge through the gap between the two rows of roughness and fluid is seen continually building up in front of the middle row of roughness. As the current continues travelling the current passes the next row of roughness and fluid begins to build up in front of that row. At the same time, eventually deep fluid from upstream of the middle row arrives at the middle row of roughness causing the current to take on a clear tail again. At the final two times the behaviour can be seen repeating as the current begins propagating through the gap between the next two rows of roughness.

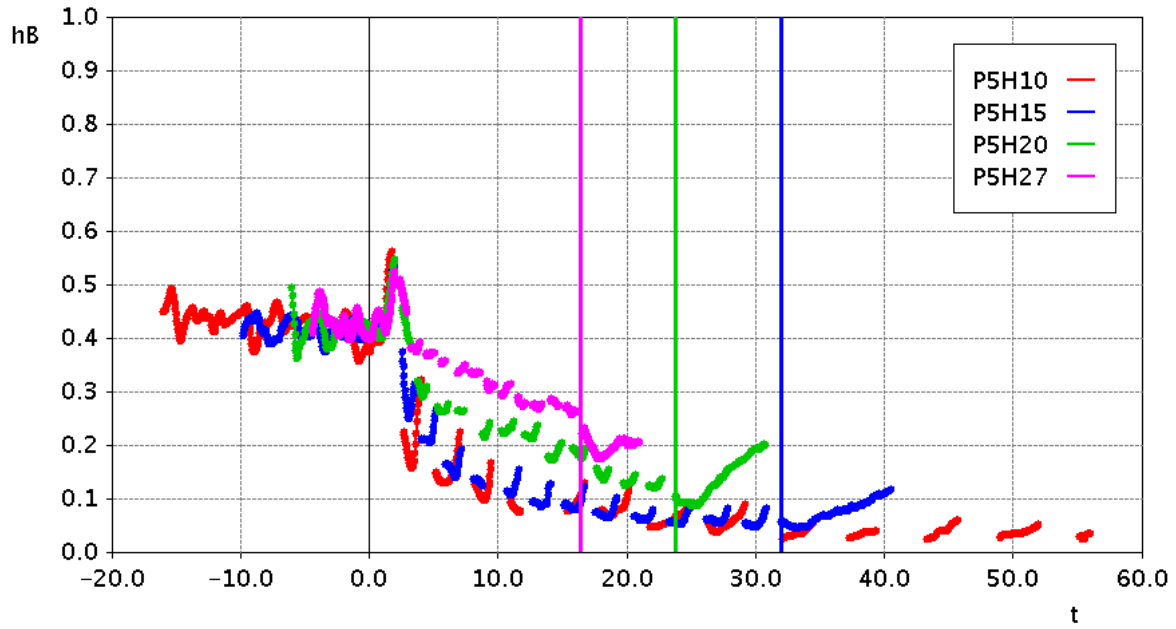

Fig. 7.11 h_B at the standard head location with time for all of the plunging configuration experiments. Vertical lines correspond to times when the currents exited the roughness. A time of 0 corresponds to the time when the currents encountered the front face of the roughness.

Variation in Height and Density with Time

The previous section provided insights into how the height and density of the plunging configuration experiments varied with space at individual times. However, it did not significantly answer the question of how they varied with time. This section will investigate this issue.

To understand how the currents varied in the head region as they travelled Figure 7.11 shows the buoyant height with time at the standard head location. Before the currents reached the roughness (when time was less than 0) all of these currents had similar buoyant heights and these were constant with time. Once the currents entered the roughness their buoyant heights began to decrease. A clear trend is visible where the currents with smaller relative roughness heights have larger buoyant heights because these currents have more pronounced heads as seen in Figure 7.8. Gaps correspond to the presence of rows of roughness at the standard head location. For the P5H10 and P5H15 experiments between rows of roughness the buoyant height would decrease slightly before increasing again until the current reached the following row. This behaviour, again, indicates that these currents experienced rows of roughness individually rather than as a field.

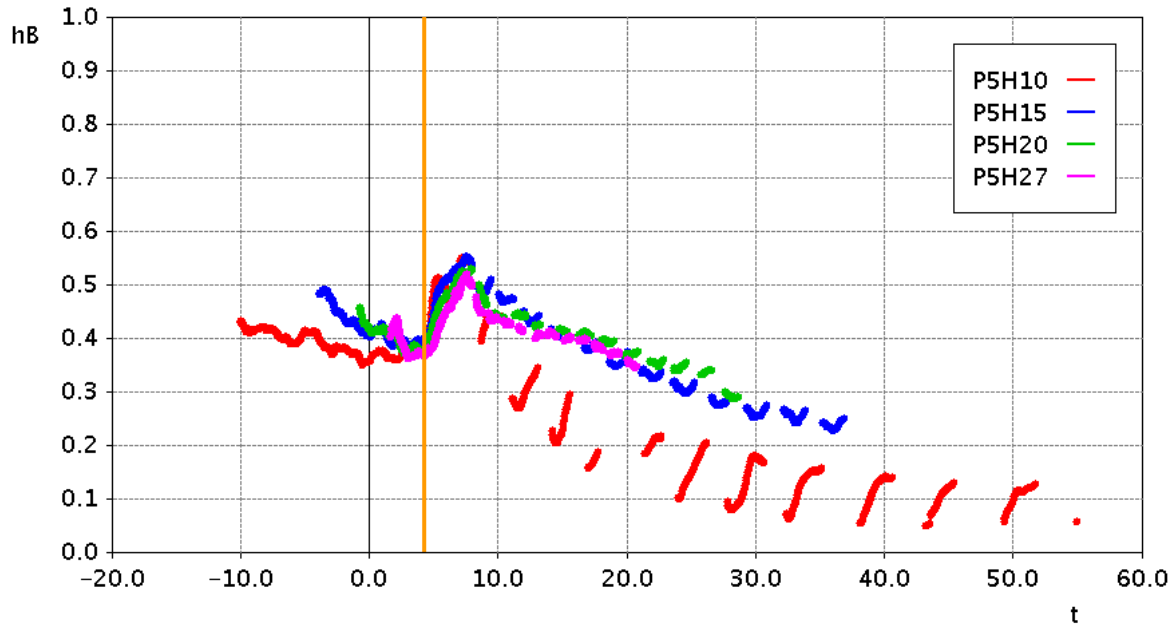

Fig. 7.12 h_B a distance of 4 behind the current front location with time for all of the plunging configuration experiments. The orange line shows the time when the currents had travelled a distance of 4 into the roughness. A time of 0 corresponds to the time when the currents encountered the front face of the roughness.

Figure 7.8 showed that while there was a trend in the buoyant height in the head region with relative roughness height, all of the experiments (apart from P5H10) exhibited a similar wedge-like structure in the tail region. A similar trend was found for the sparse configuration experiments. As the Froude numbers were similar with time for all of the sparse configuration experiments the similarity in the tail led to the conclusion that the currents were driven by a pressure gradient in the tail. To test if the plunging configuration currents were similar in the tail at all times Figure 7.12 shows the buoyant height of these currents at a distance of 4 behind the current front with time. This figure shows that with the exception of the P5H10 experiment all of the currents were similar for the full time that they were interacting with the roughness. The P5H10 experiment is likely different because it was fully submerged within the roughness, whereas the other currents extended above the roughness.

Figure 7.13 shows the current envelope for the same four experiments as Figure 7.11 at the standard head location with time. This figure shows that the vertical extent of all of the currents was constant until a time of 0, when all of the currents initially increased in height, before all but the P5H27 experiment began reducing in height with time. After initially increasing in height the P5H27 experiment became constant with time. The behaviour of the P5H27 experiment is in

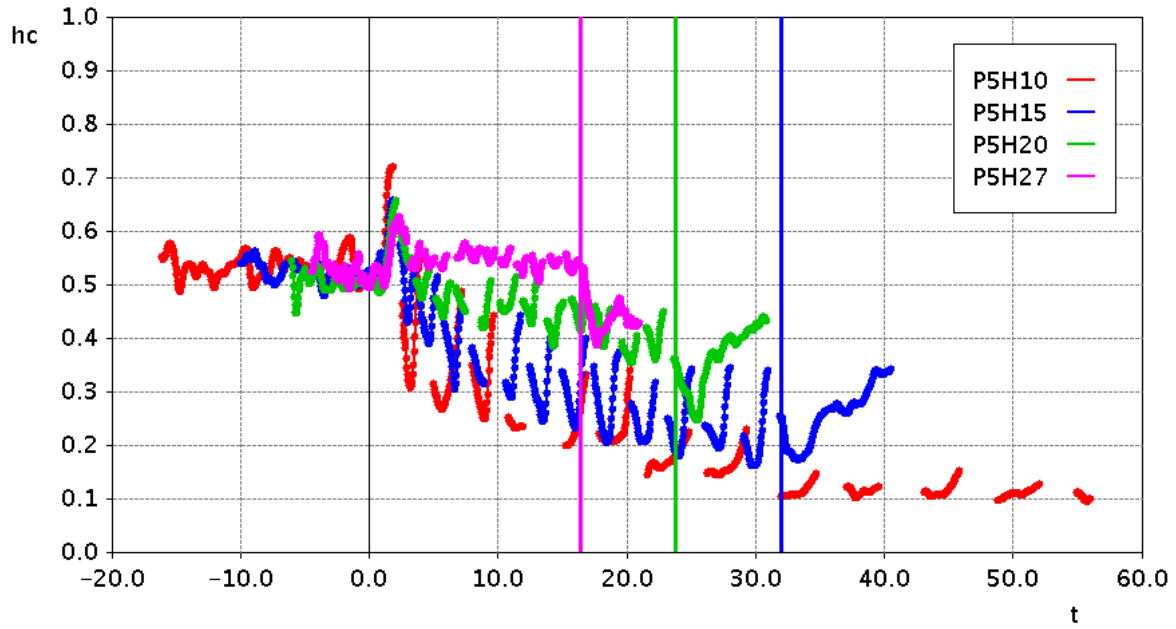

Fig. 7.13 h_c at the standard head location with time for all of the plunging configuration experiments. Vertical lines correspond to locations where the currents exited the roughness. A time of 0 corresponds to the time when the currents encountered the front face of the roughness.

line with the findings from the dense configuration experiments, indicating that as the relative roughness height decreased the currents began to behave less like through-flowing currents and more like over-flowing currents. A clear trend showing a sharper reduction in the current envelope with increased relative roughness height is also visible matching observations from Figure 7.9 and the sparse configuration experiments in Chapter 5.

The behaviour seen between rows of cylinders for currents with large relative roughness heights in Figure 7.11 is more strongly visible in Figure 7.13. When the standard head location corresponds to the front face of a row of cylinders, h_c is larger because fluid is deflected upwards. However, when the standard head location corresponds to a location slightly after the back of a row of roughness there is a local minimum because at this location the roughness has prevented some fluid from propagating through the roughness and the fluid deflected upwards has not yet plunged over the roughness.

7.2.4 Comparison with Sparse Configuration Force Balance Model

In Section 7.2.2 it was found that the Froude number of all of the plunging configuration currents reduced at the same rate. Additionally, in Section 7.2.3 it was seen that the buoyant heights of all

of the currents (apart from P5H10) had similar wedge-like structures behind the head region. In Chapter 5 similar Froude numbers and wedge-like buoyant heights were also seen for the sparse configuration experiments. Therefore, in Chapter 5 an analytical model was developed arguing that the currents were driven by a balance between a pressure gradient in the tail of the currents and the drag force imposed on the currents by the roughness. It would not be unreasonable to conclude that, given the findings in the previous sections, the same dynamics may apply to the plunging configuration experiments. Therefore, this section applies the model developed in Chapter 5 to the plunging configuration experiments. This model led to the following equation

$$Fr = \left(Ct \frac{d_c \eta_c}{S_x S_z} + E \right)^{-\frac{1}{3}} \tag{7.1}$$

The constant E in Equation 7.1 is related to the Froude number before the current reaches the roughness. Therefore, providing the preceding smooth-bed current has a Froude number of 0.46, this constant is always approximately 10.3 regardless of the properties of the roughness (as $0.46^{-3} = 10.3$). The constant C is related to the drag coefficient and for the sparse configuration this was found empirically to be 3.8. This constant is unlikely to be the same for the plunging configuration experiments because the manner in which the currents interact with the roughness is different. The constant C is therefore found empirically from the data, using an ordinary least squares fit on an average of all of the data, to be approximately 9.4.

The Froude numbers for the plunging configuration experiments with time are shown in Figure 7.14 together with the model from Equation 7.1 using both $C = 3.8$ and $C = 9.4$. The model using $C = 9.4$ fits the data well while using the original constant found empirically from the sparse configuration data over-estimates the Froude number. The over-estimation of the model using the originally determined constant indicates that the manner in which a current interacts with the cylinders does cause the Froude number to decrease more rapidly than a sparse configuration current.

The plunging regime currents decelerating more quickly than the through-flowing currents, despite the density of the roughness being equal, is in line with findings by Zhou et al. (2017). They assumed that the currents were in steady state but found the plunging regime currents to have significantly lower Froude numbers than the sparse regime experiments. It is not

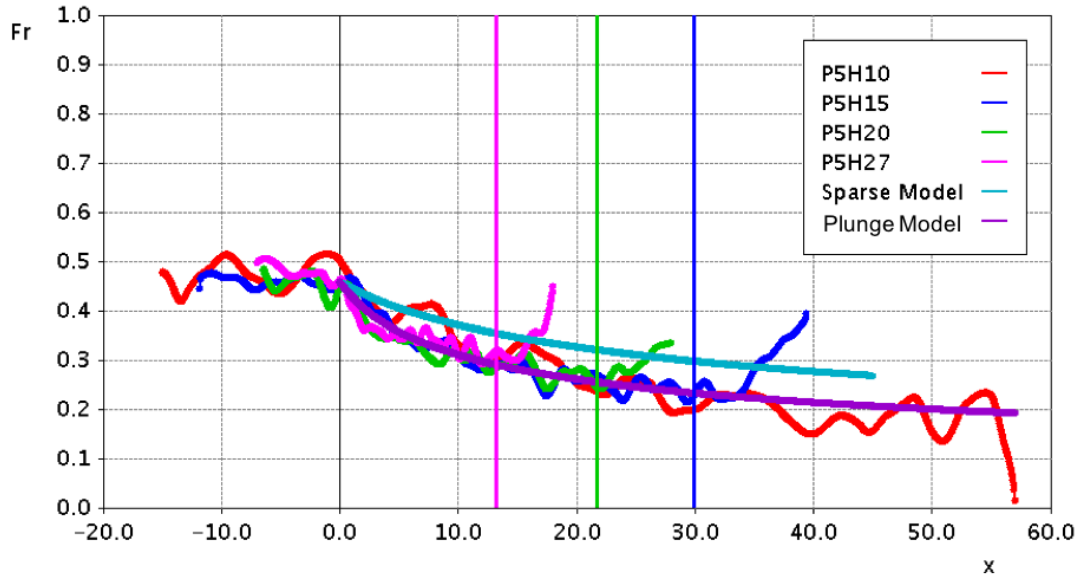

Fig. 7.14 Froude Number with time for the plunging configuration experiments as well as an analytical model for the Froude number with time. This model is shown using the coefficient C (from equation 7.1) as both 3.8 (Sparse Model) and 9.4 (Plunge Model). The currents entered the roughness at a time of 0 and the vertical lines show the times when the currents exited the roughness.

unexpected that the upwards deflection and plunging motion would cause a re-organisation of momentum and energy dissipation leading to larger reductions in the Froude number with time than through-flowing currents.

7.3 Velocity Measurements

7.3.1 Introduction

Evaluation of the current envelope in Section 7.2.3 indicated that while the currents primarily travelled through the roughness near the front, further backwards in the tail the shapes of the currents seemed to resemble the over-flowing currents from Chapter 6. This section analyses velocity fields measured using the particle tracking velocimetry (PTV) technique, thus allowing the flow above and through the roughness to be investigated. Furthermore, plunging behaviour and entrainment of ambient fluid into the currents is analysed by investigating vertical velocity fields and two-dimensional volume fluxes.

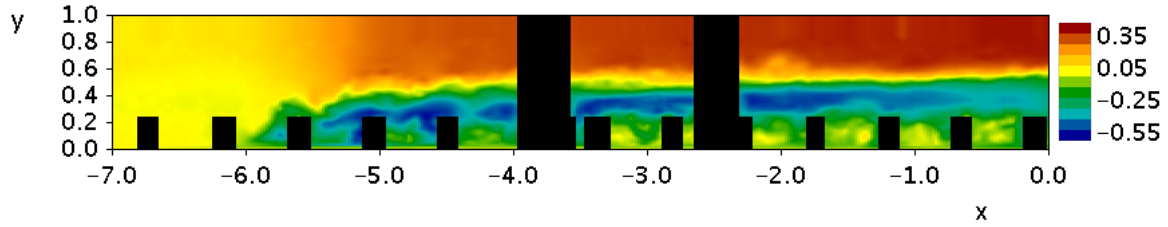

Fig. 7.15 Instantaneous horizontal velocity field for the P5H20 experiment at a time of 17.5

7.3.2 Horizontal Velocity Fields

In order to investigate whether the currents were primarily over-flowing in the tail of the currents Figure 7.15 shows the instantaneous horizontal velocity field for the P5H20 experiment at a time of 17.5. This figure supports the idea that near the front the current was entirely through-flowing before it was large enough to plunge over the top of the roughness. However, further back into the tail the current became more overflowing until from a distance of -4 (2 behind the front) the current was almost entirely over-flowing. From a distance of 1-2 behind the front most of the through-flowing fluid was directly behind the rows of roughness, for example at x=-4.5, because at these locations fluid had plunged downwards or propagated through the gaps in roughness but had not yet been impacted by the following row of roughness.

While the over-flowing and through-flowing behaviour can be seen in Figure 7.15, the pattern of behaviour within the roughness, likely caused by wakes behind cylinders and fluid being deflected upwards by cylinders, make analysing the magnitude of flow within the bed difficult. Furthermore, the errors associated with instantaneous velocity measurements are reasonably large. Therefore, this current is put into a moving frame of reference where the current nose is stationary and is time averaged from a time of 15.5 to 19.5. The period time averaged over is short enough to ensure that changes in the Froude number and current properties are minimal over this period but large enough to provide an averaged view of the current. The current is re-defined such that its nose is located at x=0. The resulting horizontal velocity field is shown in Figure 7.16. At this time the current had a Froude number of 0.28 so when transferred to a moving frame of reference the ambient fluid downstream of the current front, that was stationary in the lab frame of reference, had a velocity of 0.28.

Figure 7.16 shows that for a distance of 1 behind the current front the current was almost entirely through-flowing. For a further distance of approximately 1.5 the flow was mostly localised

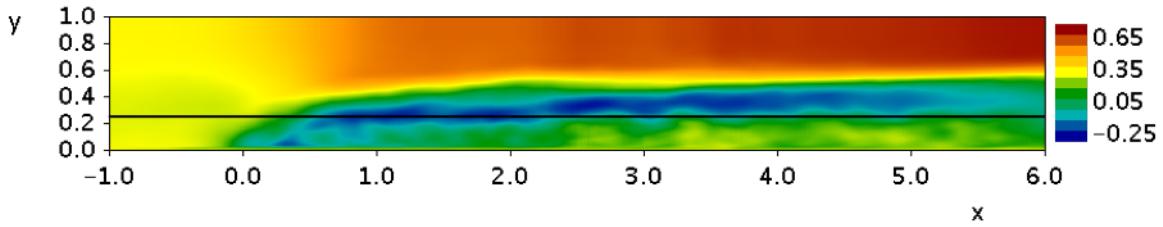

Fig. 7.16 Horizontal velocity field for the P5H20 experiment transferred to a moving frame of reference where the current front is stationary and time averaged from a time of 15.5 to 19.5. The horizontal black line shows the location of the top surface of the roughness.

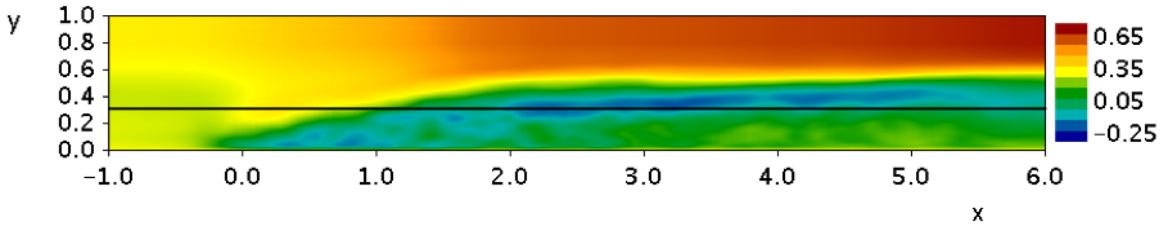

Fig. 7.17 Horizontal velocity field for the P5H15 experiment transferred to a moving frame of reference where the current front is stationary and time averaged from a time of 15.5 to 19.5. The horizontal black line shows the location of the top surface of the roughness.

towards the top of the roughness, but with significant velocity still present within the bed. Finally from a distance of 4 behind the front the current was almost entirely over-flowing. While the current was over-flowing in the tail there was no vertical buoyant exchange because the roughness was fully saturated with dense fluid and hence stably stratified.

In Section 7.2.3 the buoyant heights and current envelopes indicated that currents with larger relative roughness heights were more significantly through-flowing than the experiments with smaller relative roughness heights. To investigate this trend Figure 7.17 shows the horizontal velocity field for P5H15 put into a moving frame of reference and time averaged over the same time period as Figure 7.16. This figure shows similar behaviour to Figure 7.16; however, the current was through-flowing for a larger distance behind the front of the current. The longer through-flowing distance behind the front is expected as the volume of fluid within the roughness relative to the volume of current fluid increases with increased relative roughness height.

7.3.3 Volume Flux

Horizontal velocity fields can also be used to understand entrainment of ambient fluid into the current. In order to carry out this analysis, the experiments are transferred to a moving frame

of reference, similar to Figures 7.16 and 7.17, and time averaged from a time of 10 to 15. The time was selected such that at the end of this time window the P5H27 current was at the end of the roughness field. The velocity fields were normalised by the front speed at this time, such that the ambient fluid in front of the current, which in the lab frame of reference would have had velocities of 0, would have velocities of 1. Following the same procedures as that in Chapters 5 and 6 the volume flux in the ambient fluid travelling towards and above the current was calculated as

$$q_A = \int_{h_c}^{1} \rho dy \tag{7.2}$$

Figure 7.18 shows the ambient volume flux with x for the plunging experiments calculated using this method. If no ambient fluid was entrained into the current the ambient flux would be 1 for all x. This figure shows the ambient flux being 1 upstream of the current before reducing to between 0.7 and 0.8 over a distance of approximately 2 for most of the experiments before becoming constant. Thus, the majority of entrainment was within 2 distance units of the front. The location and magnitude of entrainment is similar to that experienced by a smooth bed current. As discussed in Chapter 5, the entrainment of fluid into the current could be due to one of two reasons. The first being that the cylinders have a negligible impact on entrainment and that the majority of entrainment into the current is caused by K-H instabilities. The other reason is that the cylinders lessen the effect of the K-H instabilities by the same magnitude that wakes cause fluid to be entrained into the current. Regardless, as the current heads were seen in previous sections to dilute more than smooth bed currents, the roughness must impact how much of the entrained fluid remains in the current head, or, how quickly dense fluid is able to replenish the head. The effect of the relative roughness height on the entrainment appears to be minor.

7.3.4 Vertical Velocities

In Chapter 4 it was observed that after a small nose propagated through the roughness the remainder of the current fluid would be deflected over the roughness and plunge downwards onto the small through-flowing nose. The plunging behaviour could not be significantly analysed in Section 7.2 because the density fields only gave information about the density distribution and not the velocity field. In order to investigate the plunging behaviour vertical velocities are

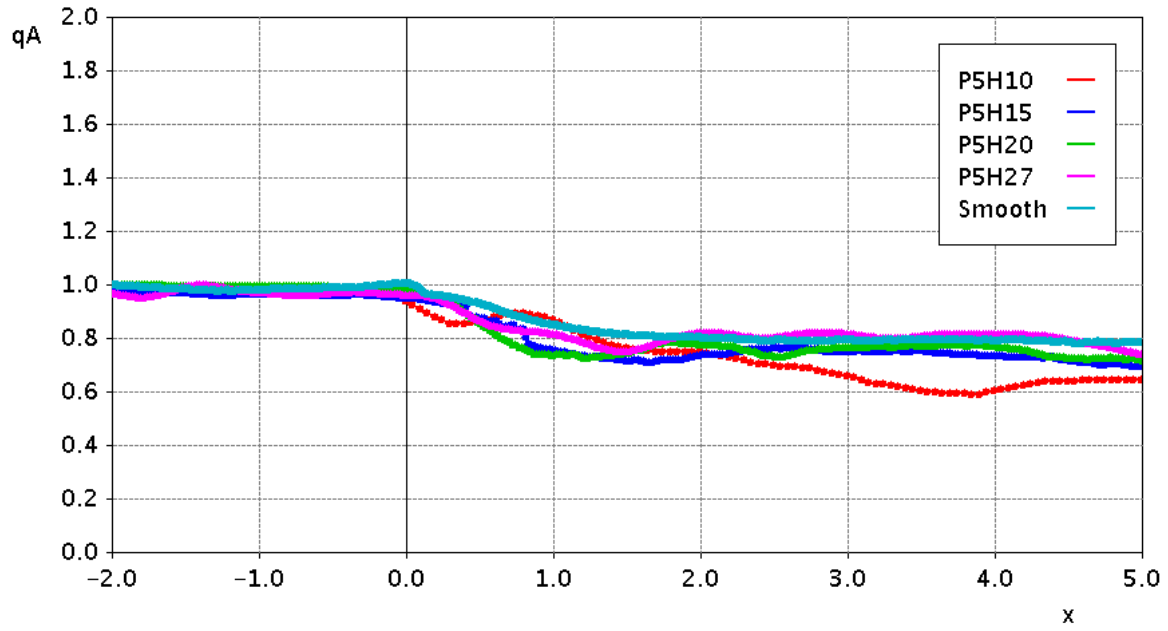

Fig. 7.18 Ambient flux with x for the plunging experiments time averaged from a time of 10 until 15. A time averaged smooth bed experiment is also shown.

explored. Firstly, to investigate how the current fluid was deflected upwards in front of the roughness the vertical velocities at a height of 0.25 (the height of the roughness) and a distance of 0.05 in front of the first, fourth, eighth and final row of roughness are plotted with time for the P5H20 experiment in Figure 7.19. The velocities are normalised by the front speed. As large vertical velocities in front of the roughness could simply be the result of ambient fluid being deflected by the arrival of the current, the vertical velocity at a distance of 2 upstream of the roughness and a height of 0.25 above the smooth bed is also plotted with time.

Figure 7.19 shows that in front of all of the rows of roughness investigated the initial maximum vertical velocity was larger than the maximum vertical velocity above a smooth bed. The larger velocity supports the notion that as fluid encountered the roughness it was deflected upwards. The magnitude of this upward velocity did not significantly increase or decrease with subsequent rows of roughness. After the fluid was deflected upwards by the first row of roughness, a significant vertical velocity remained until the lock bore arrived at a time of approximately 18. However, in front of subsequent rows of roughness the velocity fell to 0 a small time after the initial maximum velocity. The difference between the first and subsequent rows of roughness provides further evidence that the current became almost entirely overflowing upstream of the current front. At all times there was fluid travelling along the bed upstream of the roughness

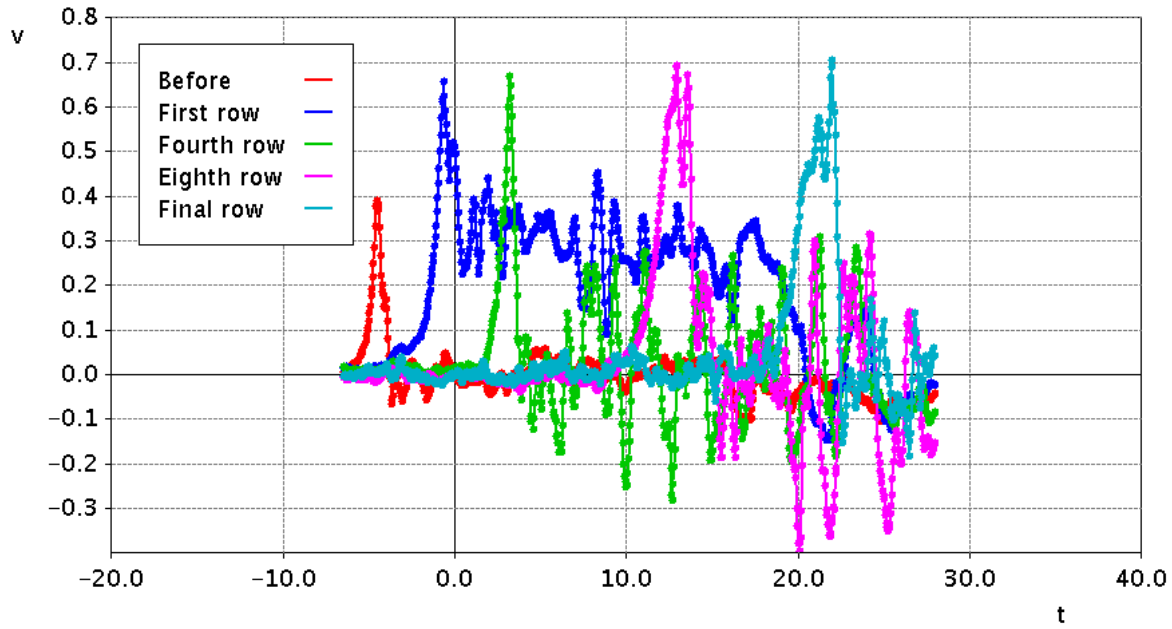

Fig. 7.19 Vertical velocity for the P5H20 experiment with time at a height of 0.25 and an x distance of 0.05 upstream of the first, fourth, eighth and final rows of roughness. Velocities are normalised by the Froude number with time. For comparison the vertical velocity with time at a height of 0.25 above a smooth bed a distance of 2 upstream of the roughness is also shown with time.

that had to be deflected upwards by the front of the roughness. However, once the current had travelled a significant distance past subsequent rows of roughness there was little flow within the roughness to be deflected upwards leading to very little vertical velocity after the initial maximum. Furthermore, Figure 7.19 shows there to be significant variability in the velocities after the fluid was initially deflected upwards. This variability indicates that the velocities were measured at a location where significant turbulent fluctuations, generated by the roughness, are present.

To investigate how the currents plunged downwards after the currents were deflected upwards and over the roughness, Figure 7.20 shows the vertical velocities for the P5H20 experiment at a height of 0.25 and at x locations of 0.05 downstream of the first, fourth, eighth and final row of roughness. Similar to Figure 7.19 these vertical velocities are normalised by the front speed with time. Initially at these locations there was a positive velocity due to ambient fluid being deflected over the current. At most locations the initial peak had a similar magnitude to the initial peak at the same height above a smooth bed as shown in Figure 7.19, indicating that the peak was not influenced by the roughness. After the final row of roughness this peak was

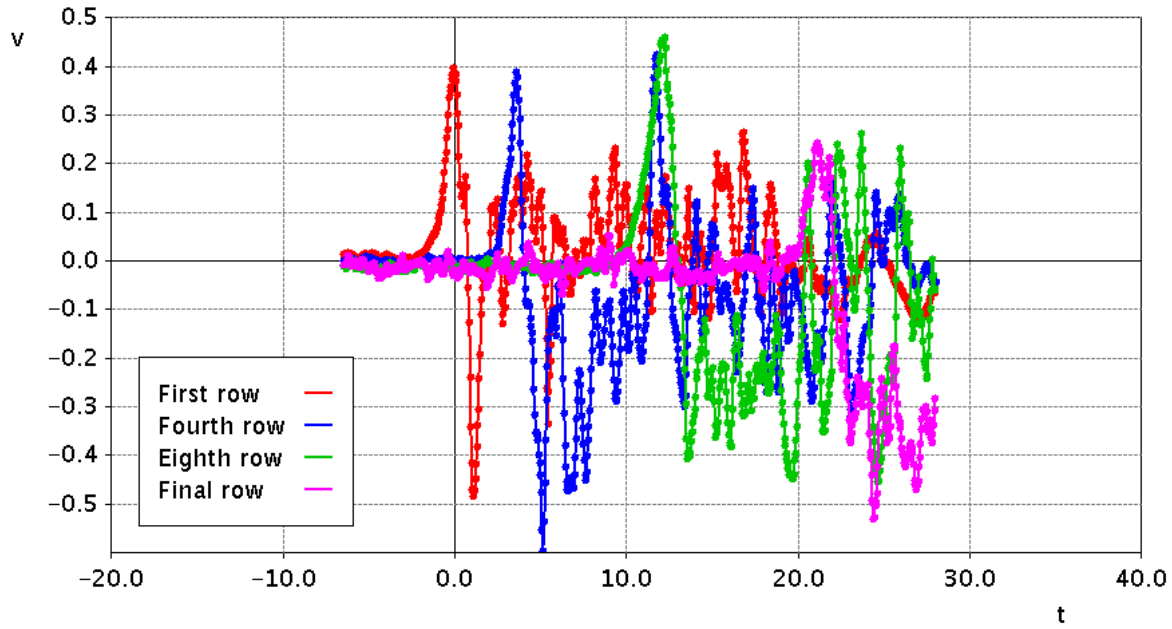

Fig. 7.20 Vertical velocity for the P5H20 experiment with time at a height of 0.25 and an x distance of 0.05 downstream of the first, fourth, eighth and final rows of roughness. Velocities are normalised by the Froude number with time.

significantly smaller, likely because at this location the current was beginning to transition to being a smooth bed current.

After an initial peak the vertical velocity directly downstream of each row of roughness became negative, providing evidence of plunging behaviour. From the times when the vertical velocities became negative there was significant variability because of significant turbulent fluctuations. As these velocities were directly downstream of the roughness the turbulent structures were felt more strongly than those in Figure 7.19, leading to more variability. This variability makes trends hard to ascertain. Nevertheless, the average velocities appear to be negative for a short time before trending towards 0 with the time taken before reaching 0 increasing with subsequent rows of roughness. Upstream of the front, Section 7.3.2 showed that the currents became almost entirely over-flowing with the bed likely saturated with dense fluid. This is consistent with the vertical velocities returning to zero in this region. After the final row of roughness the negative velocity was constant for a time of 5 before measurements ended. It is likely that the velocity remained negative for later times, unlike behind previous rows of roughness, because at this location over-flowing fluid would always have to plunge downwards to flow over the smooth bed.

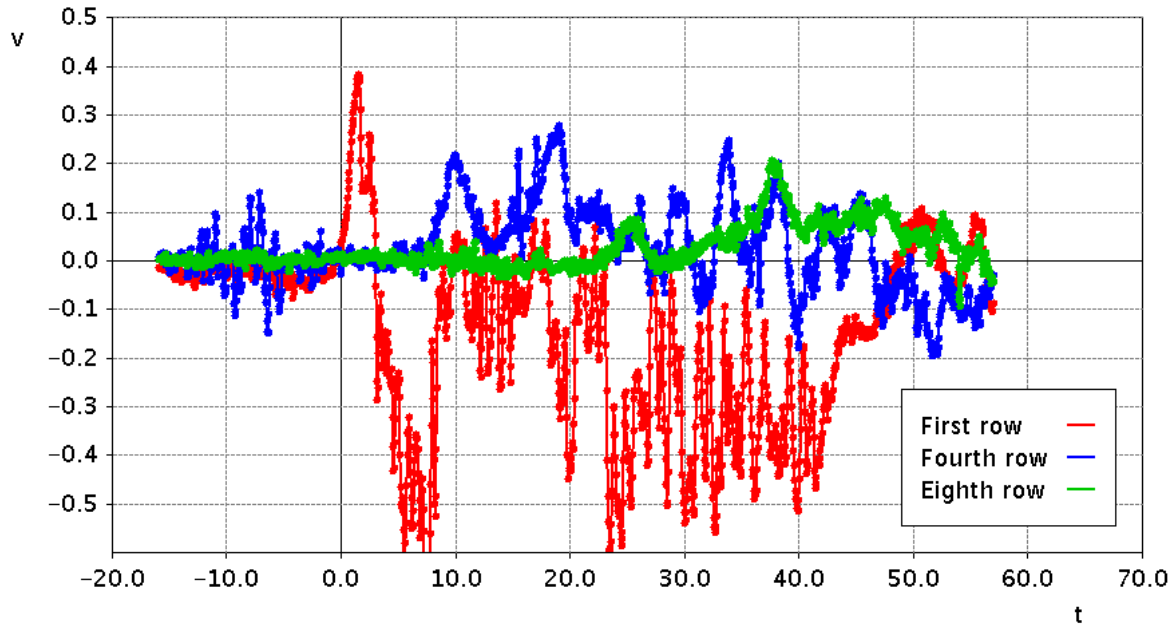

Fig. 7.21 Vertical velocity for the P5H10 experiment with time at a height of 0.5 and an x distance of 0.05 downstream of the first, fourth, eighth rows of roughness. Velocities are normalised by the Froude number with time.

Similar behaviour is seen for experiments with differing relative roughness heights. Upwards velocities stronger than those present at equivalent heights above the bed of smooth bed currents are seen in all experiments as fluid encounters each row of cylinders and is deflected upwards. Due to the strong variability in the velocity with time the impact of relative roughness height cannot be discerned and thus the P5H20 experiment is believed to be indicative of most of the other experiments. However, the P5H10 experiment did vary significantly from the other experiments. To illustrate this, the vertical velocities directly after the first, fourth and eighth row of cylinders for this experiment are shown in Figure 7.21. This figure shows that significant plunging occurred after the first row of roughness but not after subsequent rows. When the current encountered the first row of roughness it still took on the shape of a smooth bed current and was large enough for some fluid to plunge over the roughness. However, as the current travelled it formed a wedge-like structure that was not large enough to flow over the roughness so all of the fluid deflected upwards in front of each row of roughness propagated backwards in bores.

7.4 Summary

This chapter explored the results from the plunging configuration experiments. Questions of how a current's speed, density and structure are impacted by time and relative roughness height were posed. Similar to the experiments in Chapters 5 and 6, when a current initially encounters the roughness, a bore is reflected back upstream while the current travels through and over the roughness. While the current travels its head dilutes and loses fluid upstream, similar to the sparse configuration experiments seen in Chapter 5. The current also slows with the Froude numbers reducing with time. The rate of decay of the Froude number is found to be independent of the relative roughness height. Additionally, the buoyant height takes on a wedge-like structure in the tail with an angle independent of the relative roughness height. Thus, the current is believed to be driven by a balance between the pressure gradient in the tail and the drag force imposed on the current by the roughness.

Unlike the sparse configuration experiments it was found that a current with a large relative roughness height experiences each row of roughness individually with a visible bore being reflected from each row. On the other hand, a current with a smaller relative roughness height experiences the roughness as a field, similar to the sparse configuration experiments.

The front of the current is always through-flowing. As the current encounters each row the nose propagates through the gaps between the cylinders before some fluid is deflected upwards and over the roughness. The fluid being deflected over the roughness then plunges downwards onto the through-flowing front. Further upstream once the region within the roughness field is fully saturated with dense fluid the fluid travelling atop the roughness has no reason to plunge downwards, causing the current to become predominantly over-flowing.

Chapter 8: Gravity currents over fixed beds of monodisperse spheres

Preamble

This chapter consists of a published scientific journal article (Köllner et al., 2020). Several minor editorial comments have been made and the format of this paper has been edited to align with this thesis. The thesis author was the second author on this paper. The thesis author was responsible for carrying out the experiments described in Section 8.2.1 and the results from these experiments presented in Section 8.3 as well as developing the Darcy model presented at the end of Section 8.4 and co-writing the paper. The notation in this chapter is self-contained but in places conflicts with notation used in the remainder of this thesis.

Abstract

Laboratory experiments and direct numerical simulations are employed to investigate lock-exchange gravity currents propagating over close-packed, fixed porous beds of monodisperse spherical particles, and to quantify the mass and momentum transfer between the currents and the bed. The simulations show that the mass exchange of the current with the bed involves two separate steps that operate on different time scales. In a first step, the dense current front rapidly sweeps away the resident fluid in the exposed pore spaces between the top layer of spheres, while in a second step, a buoyancy-driven vertical exchange flow between the current and the deeper pores is set up that takes significantly longer to develop. This process depends on the permeability of the bed, which in turn is a function of the particle diameter. The momentum exchange between the current and the bed strongly depends on the ratio of the particle size to the viscous sublayer of the current. The bottom friction is moderate when the particle size is smaller than or comparable to the thickness of the viscous sublayer, but it jumps for particles that strongly protrude from the sublayer, leading to a more rapid deceleration of the flow.

8.1 Introduction

Density differences associated with lateral temperature, salinity or sediment concentration gradients frequently trigger the formation of gravity currents, a class of predominantly horizontal flows that are ubiquitous in the natural environment. Examples concern such phenomena as thunderstorm outflows, haboobs, sea-breeze fronts, flows over sills, turbidity currents, and plumes from desalination plants (Meiburg and Kneller, 2010; Simpson, 1997; Ungarish, 2009).

The central role that gravity currents play in a wide range of environmental settings and technical applications has motivated an extensive body of theoretical, computational and laboratory studies, along with detailed field measurements. A majority of these have focused on flows propagating over smooth, horizontal boundaries, such as the lock-exchange experiments by Huppert and Simpson (1980), Shin et al. (2004), Marino et al. (2005), and Adduce et al. (2011), as well as corresponding large-scale simulations by Härtel et al. (2000b), Cantero et al. (2007), Oezgoekmen et al. (2009), Ooi et al. (2009), and Rocca et al. (2012), among others. These studies demonstrate the existence of different stages in the life of a gravity current. Following the initial collapse, the current undergoes a slumping phase characterized by a constant front velocity. Once there is insufficient fluid left in the lock to maintain this front speed, the current decelerates, until eventually viscous effects become dominant and slow the current down further.

Motivated by applications in which gravity currents propagate over complex bottom topography, several recent studies have addressed the effects of rough boundaries in such flows. The experiments by Peters and Venart (2000), in which dense fluid is injected through an inlet entry box, show a slower slumping phase velocity as compared to a smooth bed, along with an earlier onset of the viscous phase. The authors furthermore observe enhanced fluid mixing close to the bottom boundary. These findings are consistent with the large-eddy simulations (LES) of Tokyay et al. (2011), who find that the current speed decays more quickly when the bottom roughness exerts an increased drag force on the current. Nasr-Azadani and Meiburg (2014) employ direct numerical simulations (DNS) to investigate the three-dimensional vortical flow structures generated when a turbidity current propagates over topographical features such as a Gaussian bump, along with their effects on mixing and entrainment. The recent LES simulations by Bhaganagar and Pillalamarri (2017) address lock-exchange currents over square and triangular roughness elements, with a special emphasis on the role of the friction Reynolds

number. Ozan et al. (2015) highlight the role of dilution in gravity currents propagating over arrays with horizontal axes. Wilson et al. (2017) find that a rectangular obstacle initially increases the entrainment of ambient fluid into the current, whereas during the subsequent re-establishment phase this entrainment rate decreases below that of a smooth bed current.

Qualitatively different behavior is observed for high Reynolds number flows propagating over terrain that is both rough and porous. Several investigations address stratified and homogeneous flows through emergent canopies (Belcher et al., 2012; Huq et al., 2007; Nepf, 2012). These exert increased drag on the current and significantly modify its turbulence properties. Cenedese et al. (2016) explore the role of arrays of vertical circular cylinders on gravity currents. For large periodic spacings between the cylinders they find that the currents travel through the cylinder arrays, while for dense arrays they propagate over the top. Ottolenghi et al. (2017) find that similar regimes exist when the rough boundary is sloping and with the presence of rotation. They additionally note that both the roughness and the slope of the bed increase entrainment of ambient fluid into the current. Zhou et al. (2017) identify additional flow regimes when the cylinders are non-equidistant. Zhang and Nepf (2011) and Yuksel-Ozan et al. (2016) find similar behavior in the context of buoyant gravity currents interacting with floating cylinders.

The present investigation focuses on lock-exchange gravity currents propagating over fixed porous granular beds with rough surfaces and regular matrix structures that impede vertical fluid motion. We are particularly interested in exploring the mechanisms that govern the fluid exchange and momentum transfer between the gravity current and the underlying porous bed, and in how this current/bed interaction will modify the height and velocity of the front, as well as the bottom friction it experiences. These flow properties, along with the mixing of current and ambient fluid, will be analyzed as a function of the bed structure. Some preliminary guidance is provided by previous numerical (Fang et al., 2018; Leonardi et al., 2018) and experimental (Manes et al., 2009; Pokrajac and Manes, 2009) studies of constant-density flows over beds of fixed spherical particles. These demonstrate that the bed structure can significantly affect the flow resistance, consistent with findings by Nogueira et al. (2013) and Jiang and Liu (2018) for gravity currents over gravel beds of different sizes. These authors observe a reduction in the slumping phase velocity for all cases except the largest gravel size. Further, Nogueira et al. (2014) observe repeated stretching and breaking cycles in the head of the current with the breaking period increasing with roughness of this type. Kyrousi et al. (2018) extend this line

of inquiry to gravity currents propagating over erodible beds, and find that particle erosion is strongest near the head of the current. This is also observed by Zordan et al. (2018) and Zordan et al. (2019) who show the significance of initial conditions and bed material size. They observe a feedback loop where the bed shear stress and the bed material mutually affect one another.

We employ model porous sediment beds consisting of layers of close-packed, fixed, monodisperse spherical particles, whose diameter are unaltered at 10 mm. The depth of the bed will be modified by considering one, two or three layers of spheres. By combining laboratory experiments with direct numerical simulations, we are able to obtain insight into the governing mechanisms over a wide range of spatial and temporal scales, with a particular focus on the detailed flow properties at the current/bed interface. The experimental set-up and the simulation framework are described in depth in Section 8.2. Section 8.3 presents the primary experimental and numerical findings with regard to front height and speed, as well as the structure of the concentration and velocity profiles within the current. Experimental measurements and simulation results are compared in detail and, where applicable, reasons for discrepancies are discussed. Section 8.4 aims to provide explanations for the observations of Section 8.3, by analyzing the mass and momentum transfer between the current and the bed in detail. The key findings and main conclusions are presented in Section 8.5.

8.2 Methods

8.2.1 Experiments

Experiments were conducted in a clear perspex channel as shown in Fig. 8.1, with streamwise and spanwise dimensions $\tilde{L}_x \times \tilde{L}_z = 6.2\text{m} \times 0.25\text{m}$. The left end consisted of a 1m long lock containing dense fluid, sealed off from the lighter, ambient fluid to the right by an approximately 1 mm thick stainless steel gate in plastic foam. The lock was followed by a 3m long porous bed of $\tilde{d_p} = 10\text{mm}$ glass spheres arranged in a hexagonal close-packed structure. The number of sphere layers N_l was varied between one and three, and total free surface fluid depths $\tilde{L}_y$ of 100, 150, 200 and 270mm were employed, with the depth of the fluid in the lock being equal to the depth of the ambient fluid. The above depths represent the target values, which differed somewhat from the actual measured values as listed in Tab.8.1.

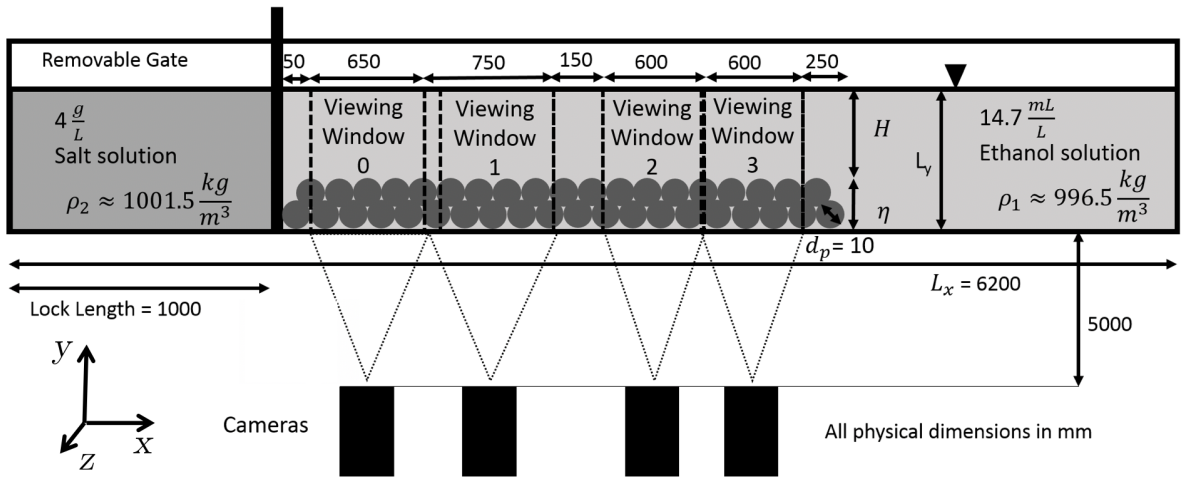

Fig. 8.1 Sketch of the experimental apparatus. Initially, the dense fluid in the lock on the left is separated from the lighter, ambient fluid on the right by a gate. These have identical depths from the base of the channel to a free surface. Upon removal of the gate, a dense gravity current forms that propagates over a fixed porous bed consisting of layers of close-packed, monodisperse spherical particles.

A relative density difference $\Delta\rho = \rho_2 - \rho_1$ of approximately 0.5% between the lock and ambient fluids was generated by mixing salt into the lock with a concentration of 4g/L, giving a density $\rho_2 \approx 1001.5\text{kg/m}^3$, and by adding 14.7mL/L of denatured alcohol to the ambient fluid, which resulted in a density $\rho_1 \approx 996.5\text{kg/m}^3$. At these concentrations the two fluids had matching refractive indices of $n = 1.3336$. The exact fluid densities, as measured with an Anton Parr density meter, are given in Tab. 8.1. The Anton Parr density meter measured density with an accuracy of ± 0.004g/L. The table furthermore provides the experimental bed height $\tilde{\eta}$, which is defined by the top of the uppermost layer of spheres, and the unobstructed water depth $\tilde{H} = \tilde{L}_y - \tilde{\eta}$ (*free depth*). Symbols that occur both in dimensional and non-dimensional form include a tilde when dimensional. We obtain characteristic scales in the form of a buoyancy velocity $\mathscr{U}_H$ and convective time $\mathscr{T}_H$ as

$$\mathscr{U}_H = \sqrt{\frac{\Delta\rho g\tilde{H}}{\rho_0}} \quad , \quad \mathscr{T}_H = \tilde{H}/\mathscr{U}_H \; , \tag{8.1}$$

where $g = 9.81\text{m/s}^2$ indicates the gravitational acceleration. For simplicity, we take as the reference density $\rho_0 = 1000$ kg/m^3. The above scales will be referred to as *free depth scales*. A Reynolds number based on $\tilde{H}$ is calculated accordingly as

$$Re_H = \mathscr{U}_H\tilde{H}/\nu \; , \tag{8.2}$$

where the kinematic viscosity is taken as $\nu = 10^{-6}\text{m}^2/\text{s}$. By interpolating values from Khattab et al. (2012) it was calculated that the denatured alcohol mixture at room temperature had a kinematic viscosity of $1.05\times10^{-6}\text{m}^2/\text{s}$, which was negligibly different to that of fresh water.

At 25°C the diffusivities of ethanol in water, $\kappa = 1.24\times10^{-9}\text{m/s}$, and of salt in water, $\kappa \approx 1.6\times10^{-9}\text{m/s}$ are approximately equal (Haynes, 2014), so that we can combine them into one effective concentration field c on which the density depends in a linear fashion

$$\rho = \rho_1 + \frac{\Delta\rho}{\rho_1}c\ . \tag{8.3}$$

For simplicity, we will refer to c as salinity from here on.

Flow data were captured by four JAI GO-5101C-PGE cameras with zoom lenses and frame rates of 22.701Hz. The locations of these cameras are shown in Figure 8.1. The cameras captured images with resolutions of 2,464 x 2,056 pixels, which were transferred directly to a fast hard drive on a PC during image capture. The regions within the bed were excluded from the experimental analysis because of the difference between the refractive indices of the fluid and the spheres, and the resulting optical distortion. The distance from the removable gate to the end of the last viewing window was 2.85m. Some of the early experiments used only three cameras, as viewing window 0 was added later to the setup. We remark that while information about the flow inside the bed could not be obtained from the experiments, such information was obtained from the simulations, highlighting the value of the combined study. Repeats of some of these experiments were carried out using single camera windows in order to identify errors associated with the measured variables.

Velocity fields were measured using the Particle Tracking Velocimetry (PTV) technique, implemented in our in-house software *Streams* (Nokes, 2017). Towards this end the flow was seeded with particles of pliolite resin ($d = 180-250\mu$m) that remained suspended in, and moved with, the flow. The particles were illuminated from above by a 10mm wide light sheet generated by an array of LED lights shining through a slot along the center line (at $z = 125$mm) of the channel. A width of 10mm was slightly larger than the width of lasers commonly used for measuring velocities through PIV experiments, for example by Zhang and Nepf (2011). The larger light sheet meant that the resulting velocity fields were slightly more averaged in the z direction than other experimental studies. The wider light sheet is also preferable for PTV

Name	N_C	$\tilde{L}_y$(cm)	η(cm)	$\tilde{H}$(cm)	$\Delta\rho$(g/L)	$\mathscr{U}_H$(cm/s)	Re_H	$Fr\|_{t/T_H=20}$
E1L10	3	10.5	1.00	9.50	5.52	7.19	6,827	0.424
E1L15	4	15.2	1.00	14.2	5.6	8.85	12,567	0.428
E1L20	3	20.0	1.00	19.00	5.58	10.2	19,411	0.441
E1L27	3	27.6	1.00	26.60	5.14	11.60	30,863	0.447
E2L10	3	11.4	1.82	9.58	5.20	7.06	6,764	0.4
E2L15	3	15.8	1.82	13.98	5.87	8.99	12,574	0.415
E2L20	3	20.2	1.82	18.38	5.45	9.93	18,255	0.418
E2L27	3	27.5	1.82	25.68	5.36	11.64	29,907	0.439
E3L10	4	10.2	2.63	7.57	5.42	6.35	4,808	0.375
E3L15	4	15.2	2.63	12.57	5.66	8.37	10,520	0.413
E3L20	4	20.4	2.63	17.77	5.46	9.77	17,367	0.429
E3L27	4	27.2	2.63	24.57	5.20	11.21	27,547	0.444
E0L20	4	20.0	0	20.0	5.51	10.42	20,840	0.463

Table 8.1 Parameters of the experiments that measure the width-averaged density field via the Light Attenuation technique. The naming convention "EaLb", where a, b are numbers, is as follows: E indicates an experimental run, a represents the number of particle layers, and b is the targeted total water depth in cm.

experiments as it ensures particles being tracked between frames are retained within the light sheet for longer. Two-dimensional velocity fields were obtained by tracking the paths of the particles through time and interpolating particle-based velocities onto a rectangular Eulerian grid of $N_x \times N_y = 4\text{mm} \times 2\text{mm}$.

Two dimensional, width-averaged density fields were generated using a Light Attenuation (LA) technique, using *Streams*. These experiments were carried out separately from the PTV experiments because for LA, illumination was provided from the rear side of the flume by a bank of LED lights, placed behind a diffuser sheet. The system was calibrated by filling the flume with seven different red dye/salt solutions and recording the ratio of red to green light at each pixel in the measurement region. Pixel-by-pixel calibration enabled conversion from the measured red-to-green light ratios to density in the actual experiments. These were finally interpolated onto a rectangular Eulerian grid of $N_x \times N_y = 4\text{mm} \times 2\text{mm}$. The experiments listed in Tab. 8.1 and Tab. 8.2 were carried out employing the LA and PTV techniques, respectively. Because some of the LA experiments involved an additional camera, an extra column showing number of cameras, N_c, is included in the table to note whether or not the camera with viewing window 0 was employed.

Name	$\tilde{L}_y$(cm)	η(cm)	$\tilde{H}$(cm)	$\Delta\rho$(g/L)	$\mathscr{U}_H$(cm/s)	Re_H	Re_L
E1L10	10.5	1.00	9.5	5.62	7.25	6,900	8,006
E1L15	14.8	1.00	13.8	5.32	8.50	11,729	13,027
E1L20	19.3	1.00	18.3	5.58	10.02	18,344	19,868
E1L27	27.2	1.00	26.2	5.54	11.95	31,314	33,124
E2L10	10.6	1.82	8.78	5.53	6.91	6,073	8,050
E2L15	15.3	1.82	13.48	6.00	8.93	12,038	14,550
E2L20	20.4	1.82	15.58	5.55	10.08	18,724	21,535
E2L27	27.3	1.82	25.48	5.54	11.79	30,056	33,325
E3L10	10.4	2.63	7.77	5.58	6.54	5,078	7867
E3L15	15.2	2.63	12.57	6.24	8.79	11,053	14,701
E3L20	20.5	2.63	17.87	5.76	10.07	17,984	22,101
E3L27	25.2	2.63	22.57	6.13	11.6	26,360	31,103

Table 8.2 Experiments carried out with Particle Tracking Velocimetry.

8.2.2 Mathematical model

Since the simulations consider the flow both above and inside the bed, i.e., across the entire flume height, they employ the total water depth in the flume $\tilde{L}_y$ as the characteristic length scale. The time $\mathscr{T}_L$, velocity $\mathscr{U}_L$, and pressure $\mathscr{P}_L$ scales are chosen accordingly as

$$\mathscr{U}_L = \sqrt{g\tilde{L}_y\Delta\rho/\rho_0}\ ,\ \mathscr{T}_L = \tilde{L}_y/\mathscr{U}_L\ ,\ \mathscr{P}_L = \mathscr{U}_L^2\rho_0\ . \tag{8.4}$$

We will refer to these as *flume scales*, as they are based on $\tilde{L}_y$. Since the non-dimensional free depth is given as $H = \tilde{H}/\tilde{L}_y$, the flume scale velocity and the free depth velocity are related to each other as

$$U_H = \mathscr{U}_H/\mathscr{U}_L = H^{1/2}\ , \tag{8.5}$$

while for the corresponding time scales we have

$$T_H = \mathscr{T}_H/\mathscr{T}_L = H^{1/2}\ . \tag{8.6}$$

The initial lock-release configuration is sketched in Fig. 8.2, using the non-dimensional notation. On the left, dense fluid of salinity $c = 1$ is located in a lock of length x_0. The fluid is at rest initially. To facilitate the evolution of three-dimensional flow structures, we perturb the initial

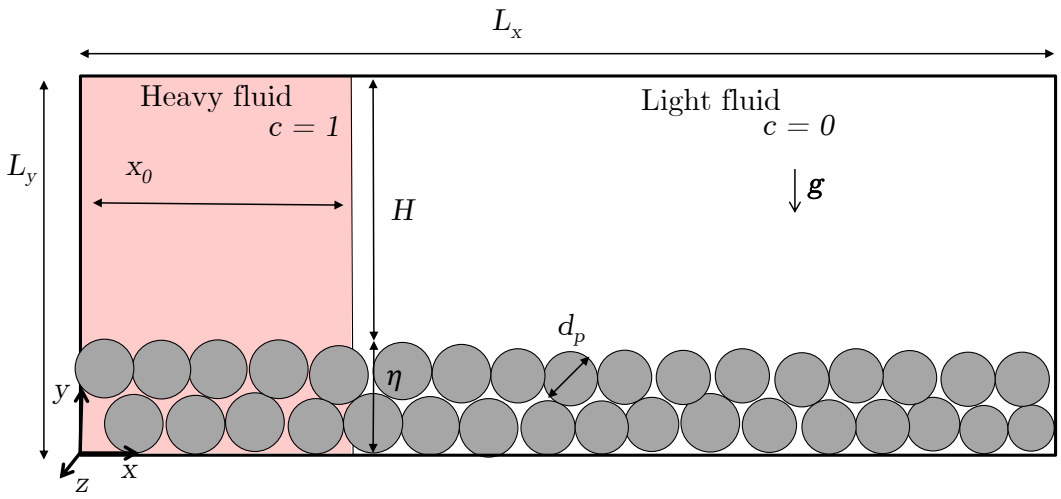

Fig. 8.2 Sketch of the numerical set-up for simulating lock-exchange gravity currents over fixed porous beds of monodisperse spherical particles arranged in periodic, close-packed configurations.

density field slightly with random numbers distributed evenly in the interval between -5×10^{-3} and 5×10^{-3}.

The bottom of the computational domain is covered with N_l layers of fixed spheres (dark gray) of diameter d_p arranged in closest hexagonal packing, giving rise to a bed height of $\eta = d_p + (N_l - 1)\sqrt{6}/3 d_p$. In contrast to the experiments, the particle layers in the simulations also cover the bottom of the lock, in order to avoid the presence of an effective forward-facing step at the gate location.

We employ the Navier-Stokes equation in the Boussinesq approximation

$$\nabla \cdot \mathbf{u} = 0 \,, \tag{8.7}$$

$$\partial_t \mathbf{u} + \mathbf{u} \cdot \nabla \mathbf{u} = -\nabla p + Re_L^{-1} \Delta \mathbf{u} + \mathbf{e}_g \xi_f c + \mathbf{f} \,, \tag{8.8}$$

where the Reynolds number Re_L is defined as

$$Re_L = \mathscr{U}_L \tilde{L}_y / \nu \,. \tag{8.9}$$

The non-dimensional velocity and dynamic pressure are denoted by $\mathbf{u}$ and p. Furthermore, (8.8) employs the indicator function of the fluid phase $\xi_f(\mathbf{x})$, i.e.

$$\xi_f(\mathbf{x}) = \begin{cases} 1 \text{ if } \mathbf{x} \in \Omega_f \\ 0 \text{ if } \mathbf{x} \in \Omega_p \end{cases} \tag{8.10}$$

where $\Omega_f \subset \mathbb{R}^3$ and $\Omega_p \subset \mathbb{R}^3$ denote the volumes occupied by the fluid and particle phases, respectively. We solve equations (8.7) and (8.8) throughout the whole numerical domain $\Omega = \Omega_f \bigcup \Omega_p = [0, L_x] \times [0, L_y] \times [0, L_z]$ and represent the fixed spherical particles by an Immersed Boundary Method (IBM). The IBM method enforces the no-slip condition at the particle surfaces

$$\mathbf{u}(\mathbf{x}) = 0 \text{ for } \mathbf{x} \in \partial\Omega_p \tag{8.11}$$

via the force density term $\mathbf{f}$ in Eq. (8.8) (Biegert et al., 2017).

The salinity field c is governed by the transport equation

$$\partial_t c + \mathbf{u} \cdot \nabla c = Pe_L^{-1} \nabla \cdot \xi_f \nabla c \ , \tag{8.12}$$

where the Peclet number

$$Pe_L = \mathscr{U}_L \tilde{L}_y / \kappa \tag{8.13}$$

measures the ratio of salinity advection to diffusion, with κ denoting the diffusivity. The Schmidt number

$$Sc = Pe_L / Re_L = \nu / \kappa \tag{8.14}$$

takes a value of 700 for salt in water as in the experiments. In order to save computational resources, most simulations employ $Sc = 7$, so that the effective diffusivity of salt in the simulations is larger than in the experiments. However, several previous investigations found that for large Re-values the effects of Sc are minimal, as long as it is greater than one (Bonometti and Balachandar, 2008; Necker et al., 2005)

The particle phase Ω_p is impermeable to salt, so that

$$\mathbf{n} \cdot \nabla c = 0 \text{ for } \mathbf{x} \in \partial\Omega_p \ , \tag{8.15}$$

where **n** denotes the outward normal to the particle boundary.

The left and bottom walls of the flume are treated as no-slip boundaries while the spanwise direction is periodic, except simulation S0L15A, where no-slip boundary conditions are employed in the spanwise direction.

The water surface is assumed to be rigid and stress-free

$$\partial_y u_x(\mathbf{x},t) = \partial_y u_z(\mathbf{x},t) = u_y(\mathbf{x},t) = 0 \text{ for } y = L_y \ . \tag{8.16}$$

Since the channel length in the simulations is shorter than in the experiments, we treat the end wall at $x = L_x$ as a stress-free boundary

$$\partial_x u_y(\mathbf{x},t) = \partial_x u_z(\mathbf{x},t) = u_x(\mathbf{x},t) = 0 \text{ for } x = L_x \ , \tag{8.17}$$

which mimics a longer channel more closely than a no-slip condition. Table 8.3 provides the parameter values for the various simulations.

Three of the simulations provide close matches for the experimental Reynolds number values and bed geometries: E3L15 $\leftrightarrow$ S3L15B, E1L15 $\leftrightarrow$ S1L15A, and E3L10 $\leftrightarrow$ S3L10A. We also compare the experiments with water depth of 20cm against simulations with lower Reynolds numbers: E0L20 $\leftrightarrow$ S0L15A as well as E3L20 $\leftrightarrow$ S3L20A, respectively. All of these have sufficiently large Reynolds numbers so that the flow properties do not depend strongly on this parameter. Simulations S0L15C and S3L20B explore the effect of a lowered Schmidt number value $Sc = 1$. For the experimental configuration with the shallowest water depth and three layers of spheres we simulate two additional cases with increased Reynolds number, *viz.* S3L10B and S3L10C, cf. Tab.8.3.

8.2.3 Numerical method

The simulation domain is discretized by a Cartesian grid of $N_x \times N_y \times N_z$ equidistant cells, with the variables arranged according to the Marker-and-Cell approach (Ferziger and Peric, 2012). All derivatives are obtained with second-order central finite differences, except for the advection term in the salinity transport equation (8.12), which is discretized by the third-order accurate QUICK scheme (Leonard, 1979). Thus the overall spatial accuracy of the numerical approach is

of second order. Time integration is performed with a third-order Runge-Kutta method. The surface of the particles is represented by discrete Lagrangian markers, at which the no-slip condition is enforced by the Immersed Boundary Method (IBM), as described in detail by Biegert et al. (2017).

In the transport equation for the salinity field, the diffusive flux vanishes inside the particles. This is implemented via the fluid phase indicator function ξ_f, by employing a Volume of Fluid approach (Prosperetti and Tryggvason, 2009) along the lines of Ardekani et al. (2018). We validated our implementation by comparing with test problems such as the heat transfer problem of Ardekani et al. (2018), settling of a sphere in a stratified environment (Doostmohammadi et al., 2014), and the effective diffusivity of a random suspension of fixed spheres (Jeffrey, 1973).

Name	d_p	$L_x \times L_y \times L_z$	η	$N_x \times N_y \times N_z$	Re_L	Pe_L	Re_H	$\frac{\langle v_F \rangle_\tau}{U_H}$	$[\tau_0, \tau_1]$	$Fr\|_{t=20T_H}$
S0L15A	–	$21 \times 1 \times 1.2$	0	$11{,}000\times 500 \times 600$	10,000	70,000	10,000	0.429	[12.5,24]	0.429
S0L15B	–	$16 \times 1 \times 1.2$	0	$8{,}000 \times 500 \times 600$	10,000	70,000	10,000	0.434	[12.5,24]	0.434
S0L15C	–	$16 \times 1 \times 1.2$	0	$8{,}000 \times 500 \times 600$	10,000	10,000	10,000	0.426	[12.5,24]	0.426
S1L15A	0.066	$16 \times 1 \times 1.2$	0.066	$9{,}600 \times 600 \times 720$	11,893	83,251	10,724	0.423	[13,25]	0.422
S3L10A	0.1	$12.5 \times 1 \times 1.25$	0.2633	$4{,}500 \times 360 \times 450$	7,004	70,000	4,429	0.400	[13.5,18.5]	0.400
S3L10B	0.1	$16 \times 1 \times 1.2$	0.2633	$8{,}000 \times 500 \times 600$	12,652	88,563	8,000	0.381	[13.5,25]	0.384
S3L10C	0.1	$16 \times 1 \times 1.2$	0.2633	$9{,}600 \times 600 \times 720$	17,397	121,774	11,000	0.376	[13.5,25]	0.380
S3L15A	0.066	$12.5 \times 1 \times 1.2$	0.1755	$6{,}250 \times 500 \times 600$	10,000	70,000	7,486	0.424	[13,17]	0.440
S3L15B	0.066	$16 \times 1 \times 1.2$	0.1755	$9{,}600 \times 600 \times 720$	13,832	96,824	10,355	0.420	[13,25]	0.423
S3L15C	0.066	$16 \times 1 \times 1.2$	0.1755	$9{,}600 \times 600 \times 720$	13,832	13,832	10,355	0.418	[13,25]	0.419
S3L20A	0.05	$16 \times 1 \times 1.2$	0.1316	$8{,}000 \times 500 \times 600$	10,000	70,000	8,092	0.428	[13,25]	0.427

Table 8.3 Physical and numerical simulation parameters. Similar to the experiments, the naming convention "SaLb", where a, b are numbers, is as follows: S indicates a simulation run, a represents the number of particle layers, and b is the target value of total water depth $\tilde{L}_y$ in cm, which includes the height of the particles. All simulations employ periodic spanwise boundary conditions with the exception of simulation S0L15A, which uses no-slip conditions. Simulation S0L15C is initialized with the data of simulation S0L15B at $t = 10$.The last three columns show quantities related to the linear fit, Eq. (8.24), applied to the time interval $[\tau_0, \tau_1]$. These are the averaged front velocity $\langle v_F \rangle_\tau$, and the densimetric Froude number evaluated at $t = 20T_H$.

.

8.3 Experimental and numerical results

8.3.1 Definitions and metrics

We will employ the notation of Sec. 8.2.2, as sketched in Fig. 8.2, with dimensionless quantities based on the flume scales (8.4). Here the bottom wall of the flume is located at $y = 0$, and $y = \eta$ denotes the top of the bed. However, at times it will be more meaningful to compare dimensionless quantities based on the free depth scales, which can be obtained by normalizing the dimensionless quantities based on the flume scales with T_H and U_H, as defined in Eqs. (8.6) and (8.5), respectively. The origin is defined in space as the position of the lock gate in and in time as the original lock lift time. The experiments are only analysed while they are in the slumping phase, i.e., before the lock runs out of fluid to constantly drive the currents.

We define the buoyant height h by the integral over the concentration above the bed (Shin et al., 2004)

$$h(x,t) = \int_{\eta}^{1} \langle c \rangle_z \mathrm{dy} \ , \tag{8.18}$$

where the angled brackets denote the average in the direction of the subscript, i.e. $\langle c \rangle_z$ is the concentration averaged in the spanwise z-direction. This height is indicative of the buoyant driving force within the current, depending on both the salinity within the current and the vertical extent of the current. The front location $x_F(t)$ of the gravity current is then determined as the rightmost location at which $h(x,t) = 0.1$, so that we subsequently obtain the front speed $v_F(t)$ as

$$v_F(t) = \frac{\mathrm{dx_F(t)}}{\mathrm{dt}} \ . \tag{8.19}$$

We furthermore define the current envelope $h_c(x,t)$ via the maximum y-locations where the spanwise averaged density has the value 0.02. We observed repeat experiments utilising single camera windows to identify the errors associated with these parameters. It was found for trends in these parameters the range of these repeats did not exceed 3 %.

8.3.2 Overview of the gravity current development

The $c = 0.1$ salinity contours shown in figure 8.3 demonstrate the spatio-temporal development of the flow for the representative simulation S3L15B, with $d_p = 0.066$ and $Re_H = 10,355$.

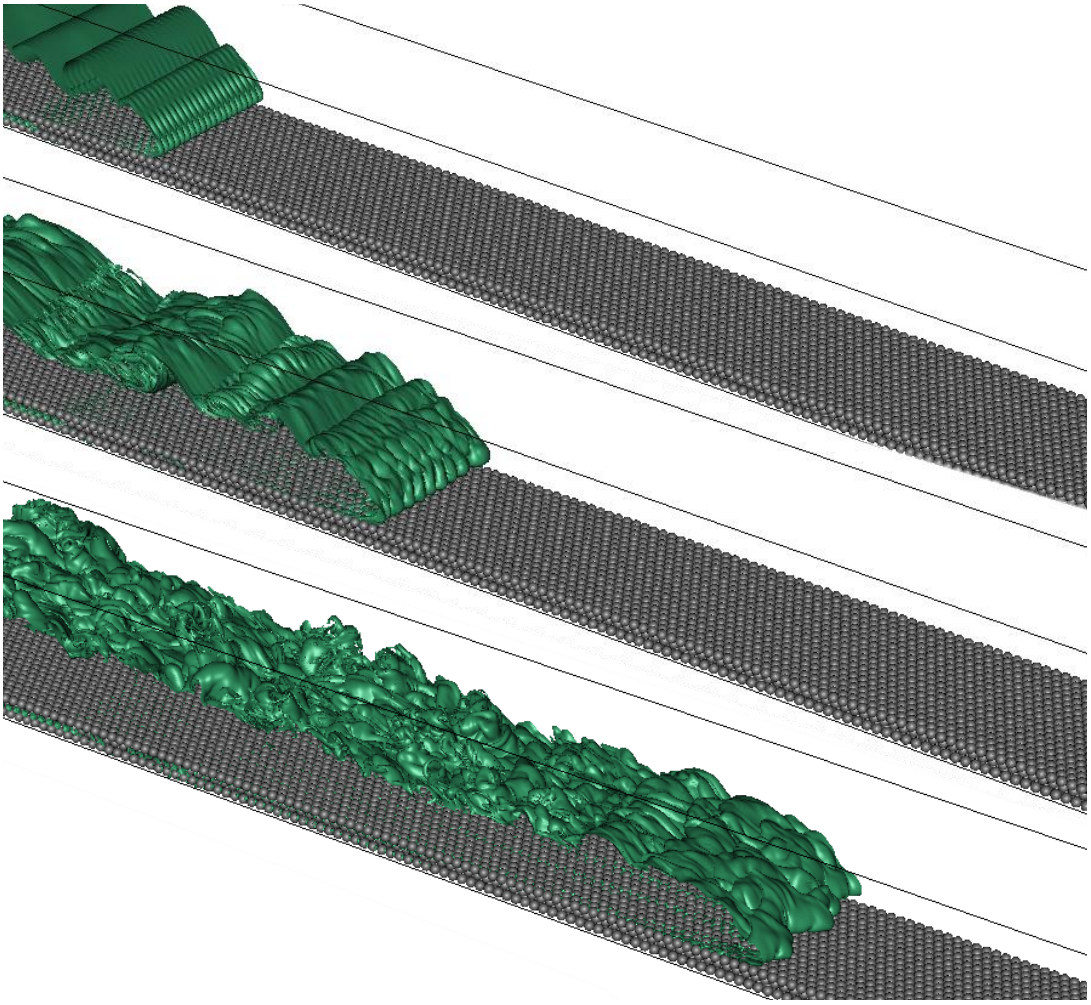

Fig. 8.3 The $c = 0.1$ salinity isosurface for simulation S3L15B at times $t/T_H = 3.3$, 7.7 and 16.5. While the early stage of the current is dominated by coherent spanwise vortices, the flow transitions to a fully turbulent state later on.

At $t/T_H = 3.3$, the current displays coherent spanwise Kelvin-Helmholtz vortices, along with regular, small frontal lobes that move along the grooves between the top layer of spheres and hence reflect the periodicity of the bed arrangement. At $t/T_H = 7.7$ these lobes remain nearly periodic, although their wavelength has doubled, while the tail is already fully three-dimensional. By $t/T_H = 16.5$ the entire current has transitioned to a turbulent state.

Figure 8.4 (a) displays the instantaneous salinity field in the plane $z = 0.4825$ for $t/T_H = 17.6$, along with the projected velocity vectors. The current is seen to mix vigorously with the ambient fluid along the upper interface. The close-ups in frames (b) and (c) focus on the detailed flow features near the top of the particle bed, and indicate the numerical resolution of 40 grid cells per particle diameter, by showing the velocity vectors and salinity values at every grid point. The close-ups furthermore visualize the fluid exchange between the current and the bed, as dense

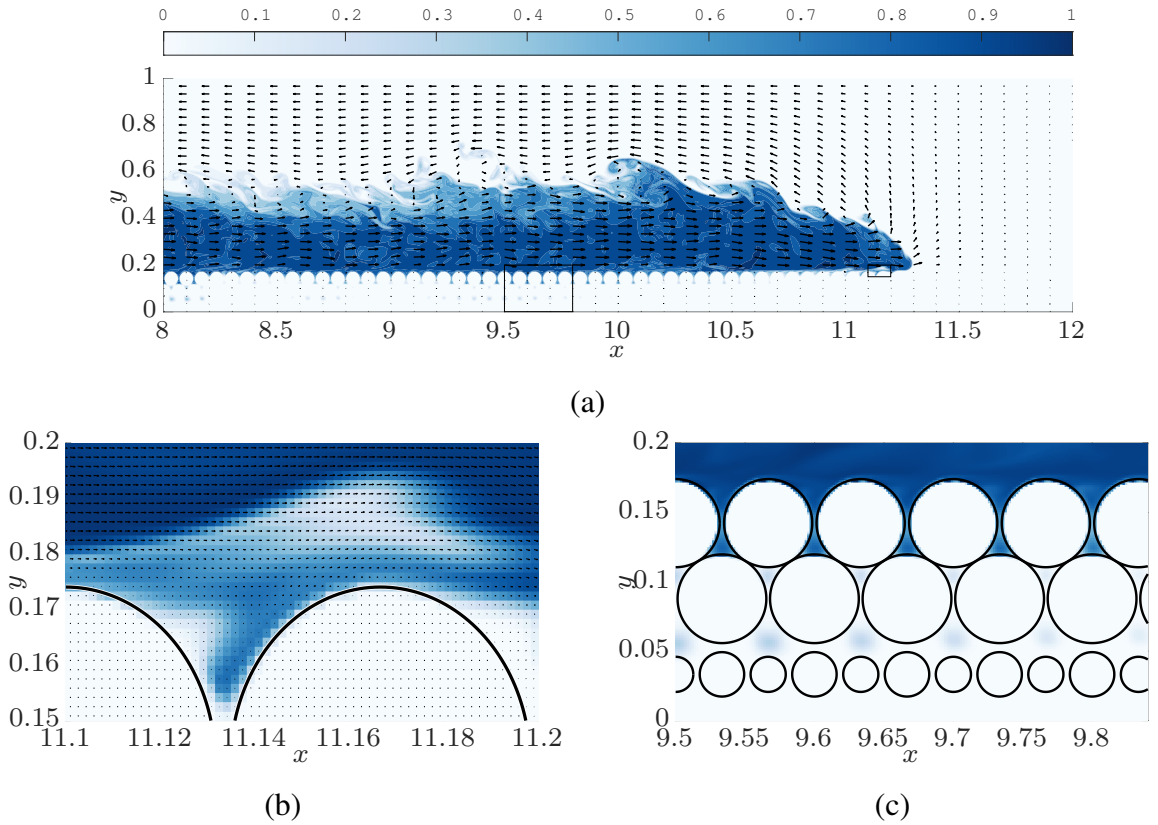

Fig. 8.4 Concentration c (in blue) and velocity vectors in the plane $z = 0.4825$, for simulation S3L15B at $t/T_H = 17.6$. Frame (a) demonstrates that the current mixes vigorously with the ambient fluid along the upper interface, while it also exchanges fluid with the porous bed. The close-ups in (b) and (c), indicated by black rectangles in (a), highlight details of this current-bed interaction. Frame (b) shows every grid cell, so that it provides a measure of the spatial resolution.

current fluid leaks through the gaps between the spheres into the pore spaces. In addition, they show that the flow separates from the top of the spheres, which results in the strong deformation and folding of the fluid interface and thereby promotes mixing.

Fig. 8.5 displays the salinity concentration field averaged in the spanwise z-direction over the fluid region only, $\langle c \rangle_z / \langle \xi_f \rangle_z$, for simulation S3L15B at times $t/T_H = 7.7$, 12.1, and 26.4. The current front propagating above the particle bed is qualitatively similar to that advancing over a flat bottom (Härtel et al., 2000b). In addition, we observe a second front inside the porous bed that moves much more slowly, which is consistent with earlier experimental observations by Cenedese et al. (2016). This second, slower front is driven by the dense fluid that leaks into the bed along the entire length of the current. The small difference between the salinity concentration values above and inside the bed in the lock region is due to numerical errors

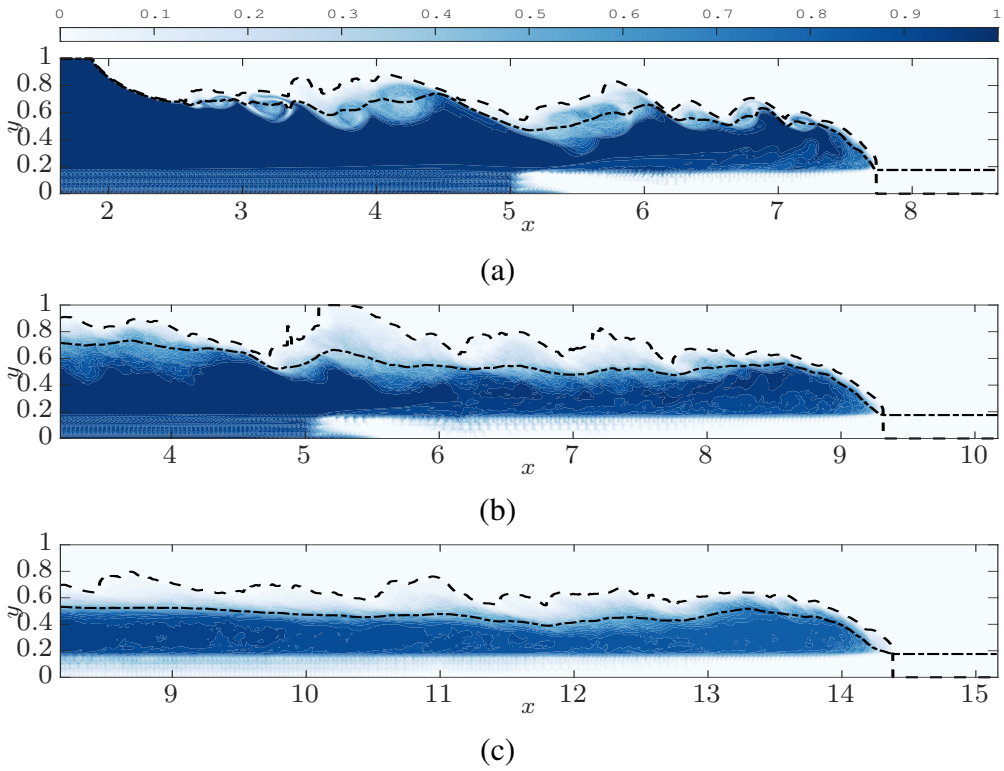

Fig. 8.5 Spanwise averaged salinity $\langle c \rangle_z / \langle \xi_f \rangle_z$ in the head region of simulation S3L15B, at times t/T_H= 7.7 (a), 12.1 (b), and 26.4 (c). A conventional gravity current front propagates above the bed, while a second front advances more slowly inside the bed. With time, both the buoyant height h (long-short dashed line) and the envelope h_c (dashed line) of the current become more uniform along the length of the current.

associated with the Volume-of-Fluid method, which cause a slight diffusive salinity flux into the particles.

During the early stages of the flow, the spanwise coherent Kelvin-Helmholtz vortices mentioned earlier mix the two fluids across nearly the entire free depth of the flow, cf. Fig. 8.5a. Later on, after the flow has become fully three-dimensional and turbulent, the most intense mixing is restricted to a narrower region around the interface. Visual inspection of the $c = 0.1$ concentration isosurfaces at various intermediate times (not shown) indicates that the simulation with $Re_H = 10,355$ (case S3L15C) transitions to turbulence somewhat earlier than the one for $Re_H = 7,486.2$ (case S1L15A), in line with our expectation that higher Reynolds numbers should promote more vigorous turbulence. We note that the dense current fluid quickly enters the spaces between the upper half of the top layer of spheres, as the resident light fluid in these exposed pores is easily carried away by the current. The infiltration of the current fluid into the lower layers of the sediment bed takes much longer, however, as the dense current fluid has to displace the lighter,

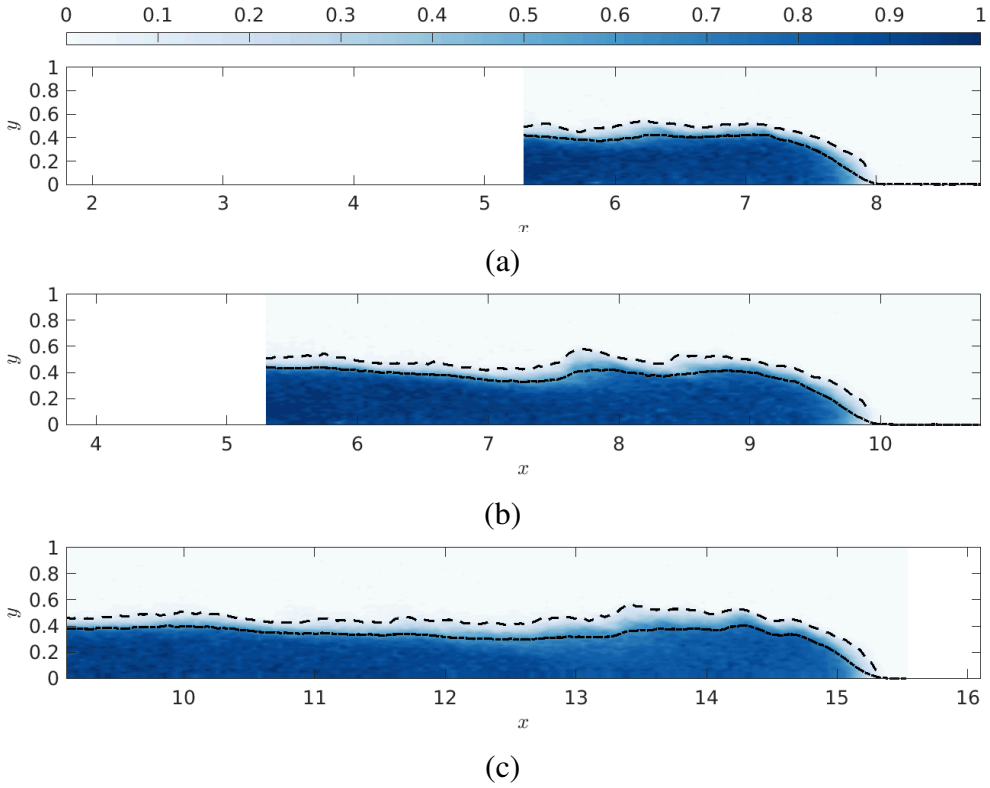

Fig. 8.6 Spanwise averaged salinity $\langle c^+ \rangle_z$ in the head region for experiment E3L15, at times t/T_H= 7.7 (a), 12.1 (b), and 26.4 (c). Current propagates above bed similarly to the simulation counterparts in 8.5; however with a more uniform buoyant height h (long-short dashed line) and the envelope h_c (dashed line).

resident fluid via a Rayleigh-Taylor-like instability in an effective porous medium. With time, both the buoyant height h (long-short dashed line) and the current envelope h_c (dashed line) tend to become more uniform along the length of the current, see Fig. 8.5(c) for $t/T_H = 26.4$.

Fig. 8.6 displays the salinity concentration field averaged in the spanwise z-direction over the fluid region only, $\langle c \rangle_z / \langle \xi_f \rangle_z$, for the experiment E3L15 at times $t/T_H = 7.7$, 12.1, and 26.4. The current front propagating above the particle bed is qualitatively similar to the simulations shown in Fig. 8.5. The simulations show a less uniform buoyant height and current envelope at earlier times because the experiments transitioned to a fully turbulent state at earlier times.

Occasionally, it is preferable to analyze the flow in the reference frame moving with the front (MRF), with the front location at the origin of the coordinate system

$$c^+(\mathbf{x} - \mathbf{e}_x x_F(t), t) = c(\mathbf{x}, t) \ , \tag{8.20}$$

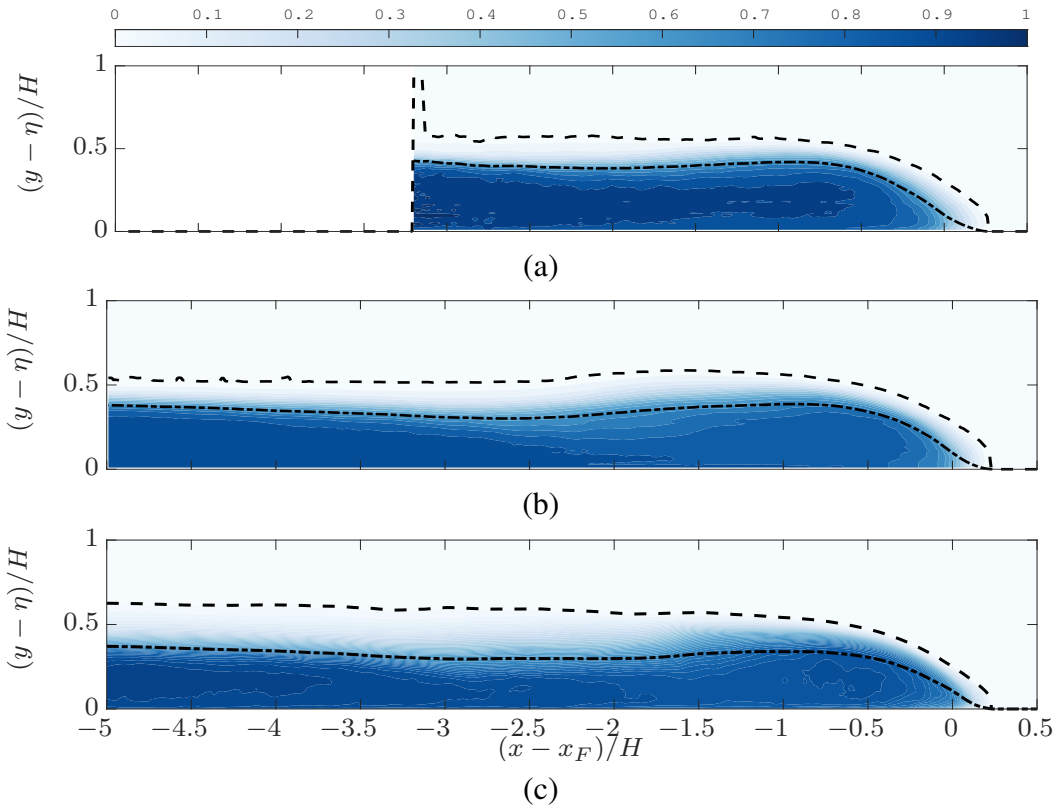

Fig. 8.7 Spanwise averaged salinity $\langle c \rangle_z$ in the head region for experiment E3L15, at times $t/T_H = 5.3$ (a) and 22 (b). The frames also include the buoyant height h (long-short dashed line) and the current envelope h_c (dashed line). Corresponding simulation results for $t/T_H = 22$, shown in frame (c), are seen to agree closely with the experimental values. All distributions are averaged around the given time for $\pm 1 T_H$.

$$\mathbf{u}^+(\mathbf{x} - \mathbf{e}_x x_F(t), t) = \mathbf{u}(\mathbf{x}, t) - v_F(t)\mathbf{e}_x \,. \tag{8.21}$$

We denote variables in this reference frame by a $^+$-superscript. Figure 8.7 shows the spanwise-averaged concentration $\langle c^+ \rangle_z$ for experiment 3L15 at two different times. In addition to averaging in the spanwise direction, which is inherent to the Light Attenuation method, we average the distribution around the given times by $\pm 1 T_H$ in order to smooth out fluctuations. For comparison, we display the corresponding simulation results for $t/T_H = 22$ in frame (c).

We note that the early experimental salinity field at $t/T_H = 5.3$ does not indicate the presence of the strong, spanwise coherent Kelvin-Helmholtz vortices that we had observed during the initial simulation stages of the simulation, cf. Fig. 8.5(a). This is likely a result of the much stronger initial perturbation introduced in the experiment by the removal of the gate, which causes the flow to transition to a fully three-dimensional turbulent state more rapidly than in the simulation. Nevertheless, by $t/T_H = 22$ the experimental and computational concentration

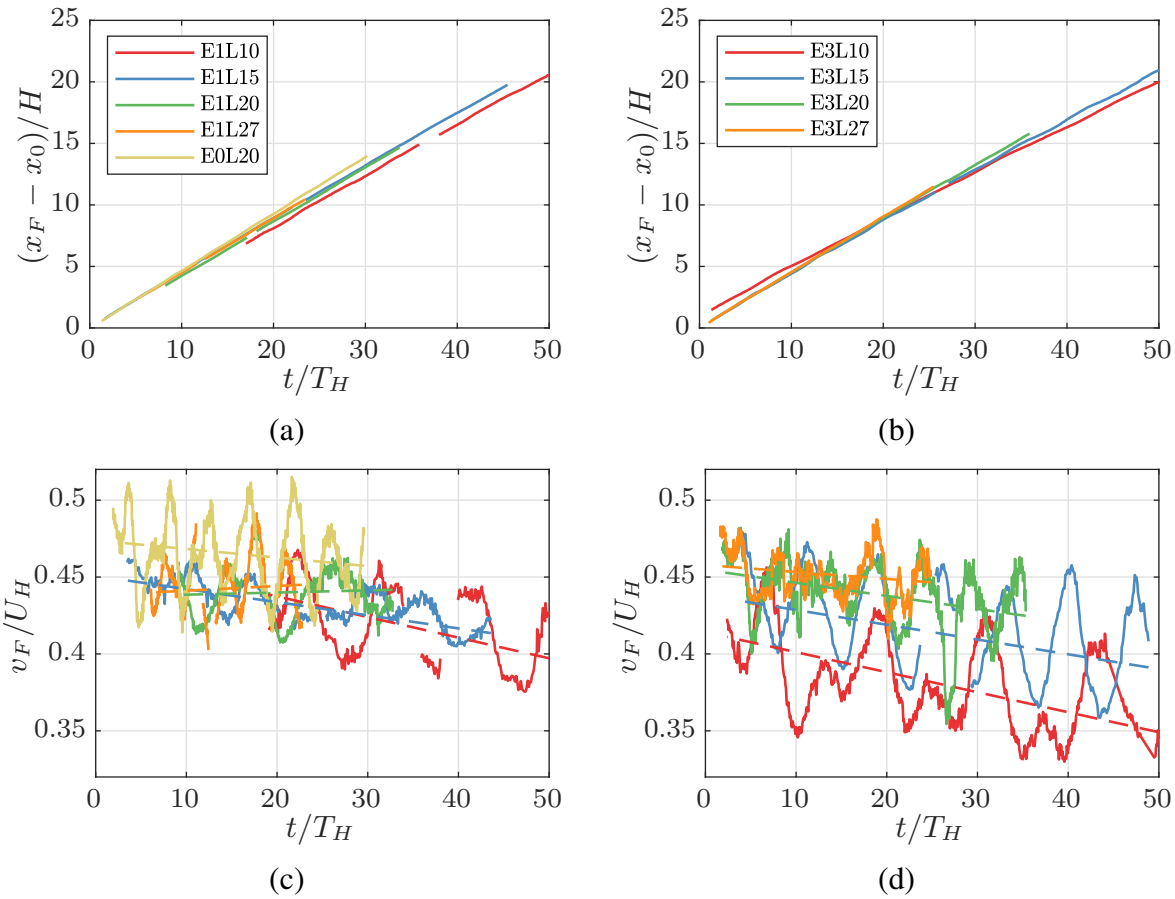

Fig. 8.8 Front location and velocity as functions of time, for the experiments listed in Tab. 8.1. The left (right) column shows results for a single layer (three layers) of spheres. The upper (lower) row presents the front locations (front velocities) in free depth scales. Dashed lines show linear best fits.

fields agree closely, especially with regard to the buoyant height as a function of the streamwise coordinate.

8.3.3 Front position and velocity

A key question concerns the influence of the porous bed on the front velocity of the current. Fig. 8.8 presents experimental results for the non-dimensional front location $(x_F - x_0)/H$ as function of time, where the value of zero corresponds to the front being at the position of the lock. While frame (a) shows values for the single-layer flows and the flat bottom, frame (b) provides corresponding data for the three-layer flows. The two-layer case behaves qualitatively similar, so that it is not shown. Within each panel the water depth $\tilde{L}_y$ is varied in order to assess its influence. Table 8.1 lists all experimental parameters.

The experimental time $\tilde{t}$ was normalized with the free depth time $\mathscr{T}_H$, and the front position with the free depth $\tilde{H}$. The time $\tilde{t} = 0$ corresponds to the moment when the lock is opened. For a constant number of layers, this scaling causes the curves for the front locations to collapse approximately, although the shallower cases still propagate somewhat more slowly even when scaled with these free depth units, reflecting their effectively lower Reynolds numbers. In particular, we note that the current advancing over a smooth bottom travels only a few percentage points faster than the one propagating over a single layer of spheres. This indicates that during the early stages of the flow, the bottom roughness and the loss of current fluid into the porous bed of a single layer of spheres do not significantly retard the current.

Differentiation of the location values in frames (a) and (b) yields the front velocities, shown in frames (c) and (d), normalized with $\mathscr{U}_H$, as a function of time. For all water depths the front velocity $\tilde{v}_F/\mathscr{U}_H$ decreases with time, although this trend is most pronounced for the shallow water depths, which indicates that over time the bed roughness and porosity have a relatively larger influence on shallower currents.

A very prominent feature of the front velocity data are their strong oscillations in time, which to the best of our knowledge had not been reported in earlier laboratory experiments. We hypothesize that these front velocity oscillations are caused by the presence of seiche waves generated by the removal of the lock gate. In order to test this hypothesis, let us consider the first seiche mode in a channel, which has a wavelength λ of twice the channel length. For our experiments this wavelength is large compared to the water depth, so that we can consider the seiche a shallow, linear wave with a phase speed $\tilde{c}_w = \sqrt{g\tilde{H}}$. The period $\tilde{T}_w$ of the wave, and the maximum speed $\tilde{u}_w$ of a fluid particle beneath the surface are given by

$$\tilde{T}_w = \frac{\tilde{\lambda}}{\tilde{c}_w} = \frac{2\tilde{L}_x}{\sqrt{g\tilde{H}}}\,, \tag{8.22}$$

$$\tilde{u}_w = \frac{g\tilde{\chi}_w}{\tilde{c}_w} = \frac{g\tilde{\chi}_w}{\sqrt{g\tilde{H}}}\,, \tag{8.23}$$

where $\tilde{\chi}_w$ denotes the maximum free surface deflection of the wave, which is small enough to be hardly visible in the experiment. For experiment E3L15 ($\tilde{H} = 0.126$m and $L_x = 6.2$m) equation (8.22) gives a period of $\tilde{T} = 11.2$s, or $\tilde{T}/\mathscr{T}_H = 7.4$. This value closely matches the oscillation

period observed for E3L15 in Fig. 8.8. For the other experiments we found a similar level of agreement. For E3L15 the maximum velocity was 0.5cm/s greater than the mean. We employ this value as an estimate for the maximum velocity of a fluid particle beneath the surface in the absence of the current. Equation (8.23) then yields a maximum free surface deflection of 0.6mm, which is small enough not to be noticed in most laboratory setups. In the following discussion, we assume that the seiche waves did not impact the mean current behaviour, beyond causing the current velocity to oscillate. We furthermore remark that the simulations do not generate seiche modes, as they assume a rigid upper surface.

Figs. 8.8(c,d) include linear fits to the front velocity data over the entire time $\tilde{T}_{exp}$ of the experiments in order to better visualise the trends in the data. We fit (by means of minimizing the squared error ε^2) the slope α to the experimental data, which formally reads as

$$\tilde{v}_F/\mathscr{U}_H = \langle \tilde{v}_F \rangle_t/\mathscr{U}_H + \alpha(\tilde{t} - \tilde{T}_{exp}/2 - \tilde{t}_0)/\mathscr{T}_H + \varepsilon. \tag{8.24}$$

In Eq. (8.24), the average front velocity is obtained as $\langle \tilde{v}_F \rangle_t = (\tilde{x}_F(\tilde{T}_{exp}) - \tilde{x}_F(\tilde{t}_0))/\tilde{T}_{exp}$, where $\tilde{t}_0$ is the time when the front gets detected initially. Moreover, we define the densimetric Froude number

$$Fr(t) = \tilde{v}_F(t)/\mathscr{U}_H. \tag{8.25}$$

Column 9 of Tab. 8.1 provide the average dimensionless front speeds. For most experiments the front velocity decreases with time, although for the deeper cases with only one particle layer, we observe a small increase during the analyzed time interval. In general, the currents slow down more rapidly for larger relative bed heights $\tilde{\eta}/\tilde{H}$.

We perform a corresponding fit for the simulations, although there we exclude the initial laminar phase of the flow. The time interval $t \in \tau = [\tau_0, \tau_1]$ over which we evaluate the linear fit is given in Tab. 8.3. In order to conduct meaningful comparisons, we evaluate the linear fit (8.24) at identical times $t/T_H = 20$ for all experiments and simulations, to obtain $Fr|_{t/T_H=20}$. When plotting $Fr|_{t/T_H=20}$ against d_p/H, see Fig. 8.9, with error bars included based on the range of repeat experiments, we find that the Froude number is primarily a function of the relative particle size d_p/H, whereas the number of layers generally plays only a secondary role. An obvious exception to this rule is the single-layer case (square symbol) for large d_p/H, which

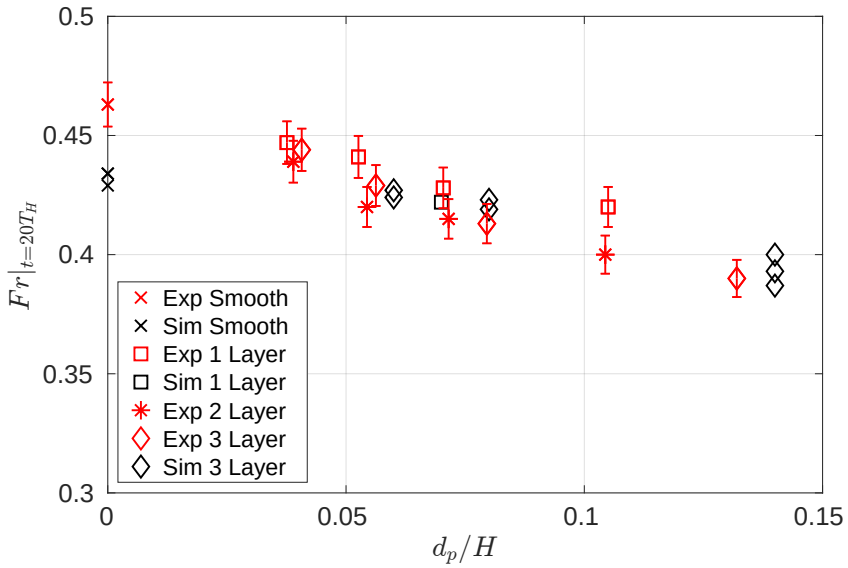

Fig. 8.9 Experimental and numerical results showing the correlation between sphere diameter d_p/H and Froude number evaluated at $t/T_H = 20$, $Fr|_{t/T_H=20}$. Different symbol shapes represent different numbers of layers, with red (black) symbols representing experiments (simulations). Error bars for experiments are based on the range of repeat experiments. Simulations for constant d_p/H but changing Reynolds and Schmidt numbers are included. The precise parameter values can be found in Tab. 8.3 (simulations) and Tab. 8.1 (experiments). As a general trend, the front velocity decreases with increasing particle size, whereas the number of layers plays a secondary role.

differs substantially from the two and three layer cases with a similar d_p/H (star and diamond symbol), in line with the observations reported in Sec. 8.3.4.

Cenedese et al. (2016) carried out lock exchange experiments with similar depths to those in the experiments reported here. They found Froude numbers similar to ours for currents propagating over smooth beds. These are also similar to other experimental studies of gravity currents over smooth beds (Cantero et al., 2007; Shin et al., 2004; Simpson, 1997). Cenedese et al. (2016) also carried out experiments with staggered beds of vertically arranged circular cylinders and when these were densely distributed the currents propagated atop the roughness. With cylinder heights of 10 mm, the same roughness height as our experiments with 1 layer of particles, they observed Froude numbers consistently lower than ours. We explain this by their experiments having a larger and more unobstructed volume of fluid within the bed such that the vertical exchange of fluid between the bed and the current head was larger than in our experiments.

Fig. 8.10(a) displays the front velocities of experiment E3L15 and the corresponding simulation S3L15C as functions of time.

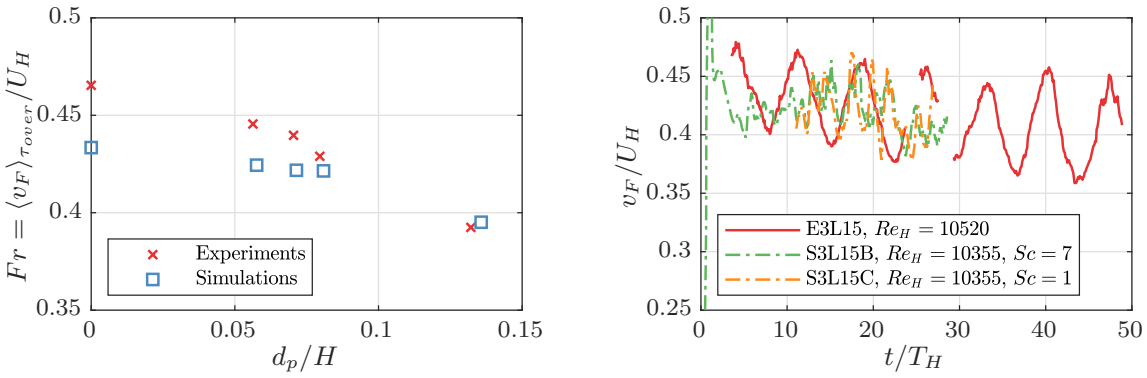

(a) (b)

Fig. 8.10 Comparison of experimental and numerical results for the front velocities/ densimetric Froude numbers. In frame (a) the evolution for experiment E3L15 is compared to different simulations showing a close fit between the experiment and simulations. Frame (b) compares experiments E0L20, E3L20, E1L15, E3L15, and E3L10 with simulations S0L15B, S3L20A, S3L15B, and S3L10A in terms of time averaged densimetric Froude numbers $\langle v_F/U_H \rangle_{\tau_{over}}$, where cases are categorized by the non-dimensional particle diameters d_p/H. For the exact values, see Tab. 8.4. These show experiments to generally have a larger front speed than the simulations with this difference being more prominent when d_p/H is small.

The experimental data again show the pronounced seiche oscillations, while the simulation results exhibit somewhat smaller, more random-like variations. Nevertheless, experimental and numerical front velocities are seen to fluctuate around comparable mean values, and they show similar rates of decline. For a quantitative comparison, we average the experimental and computational front velocities over the time interval τ_{over} from $2 < t/T_H < 28$, in order to obtain $\langle v_F/U_H \rangle_{\tau_{over}}$ shown in Fig. 8.10(b). The experimental front velocities are generally slightly higher than the computational values. This difference tends to increase as d_p/H decreases, such that the difference is largest for the smooth case. We need to keep in mind, however, that for the smooth case the experimental Reynolds number was about twice that of the corresponding simulation, which may account for much of this difference.

In order to assess the influence of *Re* and *Sc* on the front velocity, we carried out two additional simulations for the smooth case. While S0L15B uses the standard set-up, S0L15A employs no-slip side walls, and S0L15C has a reduced Schmidt number value of $Sc = 1$. We found that the lower *Sc*-value slightly reduced the front velocity, while the no-slip sidewall affected the front velocity by much less than one per cent.

Name	Re_H	η/H	d_p/H	$\langle v_f \rangle_{\tau_{over}}/U_H$	$\langle h_M \rangle_{\tau_{over}}/H$
E0L20	20,840	0	0	0.465	0.364
S0L15A*	10,000	0	0	0.434	0.397
S0L15B	10,000	0	0	0.434	0.403
S0L15C$^\diamond$	10,000	0	0	0.428	0.362
E1L15	12,567	0.07	0.07	0.4397	0.348
S1L15A	10,724	0.07	0.07	0.422	0.363
E3L15	10,520	0.21	0.08	0.429	0.341
S3L15B	10,355	0.21	0.08	0.423	0.358
S3L15C	10,355	0.21	0.08	0.419	0.357
E3L10	4,808	0.35	0.13	0.393	0.356
S3L10A	4,429	0.36	0.14	0.403	0.395
S3L10B	8,000	0.36	0.14	0.393	0.351
S3L10C	11,000	0.36	0.14	0.387	0.355

Table 8.4 Experimental and simulation values of front velocities and averaged buoyant heights. The averages are taken over τ_{over}, which is the time interval for which we have both experimental and simulation data in Fig. 8.10 and Fig. 8.12, respectively. * Simulation S0L15A was carried out with no-slip boundaries at $z = 0, L_z$. $^\diamond$ Simulations S0L15C and S3L15C were performed with Sc=1, as compared to the standard value of $Sc = 7$.

8.3.4 Current height

The velocity of a gravity current, along with its destructive potential, are largely functions of the buoyant height. This height, in turn, depends on the net exchange of fluid between the frontal region and the tail section of the current, as well as on the leakage of current fluid into the porous bed. In this section, we will present results for the buoyant height of the current front as a function of time, and subsequently analyze the respective fluid exchange of the front with the tail section and the bed.

Let us consider the average height h_M of a current within a distance $4H$ behind the front. Fig. 8.11 presents experimental results for h_M/H as a function of time for different parameter combinations. While all experiments show a decline of h_M/H with time, the rate of this decline depends on the specific experimental conditions. Frame (a) demonstrates that, when the number of sphere layers is held constant at three, the buoyant height decreases more slowly in deeper water, i.e., for a larger ratio of buoyant height to bed height, h_M/η. In frame (b), we recognize that in deep water one, two and three layers of spheres result in approximately identical buoyant

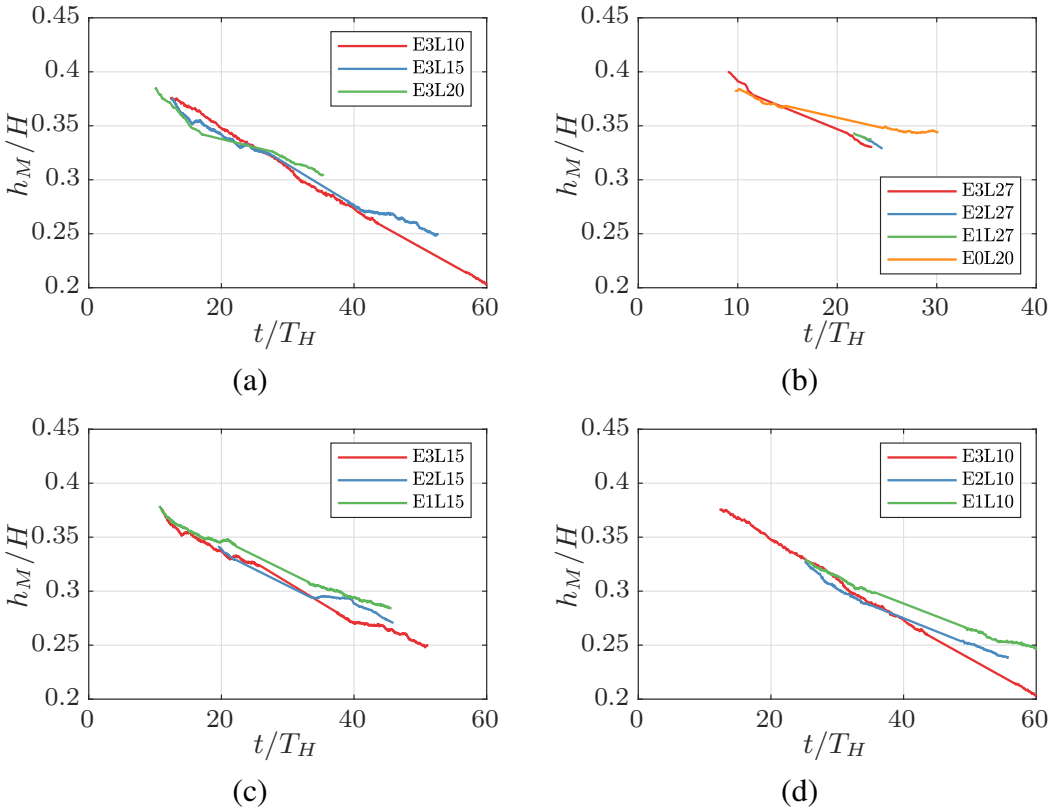

Fig. 8.11 The spatially averaged current height h_M as a function of time for four groups of experiments: (a) constant number of particle layers, but varying water depth; (b) constant water depth, but different numbers of layers; (c) water depth of 15cm, varying number of layers; and (d) water depth of 10cm, varying number of layers.

heights with similar rates of decline. However, this rate of decline is significantly larger than for a current over a flat bottom (E0L20 - orange line).

Frames (c) and (d) suggest that for shallower total water depth, the difference between currents propagating over one, two or three layers increases. Taken together, these observations indicate that currents over porous beds behave in a fundamentally different way from those over flat beds, and that the exact depth of the porous bed becomes influential only in relatively shallow water. This suggests that a thick current traveling in deep water moves so fast that only fluid from the uppermost pores gets mixed into the current front. Shallower currents that travel more slowly, on the other hand, are more likely to allow fluid from the lower pores to rise and become mixed into the current front. The fluid exchange between the current and the bed will be analyzed in more detail below.

Fig. 8.12 compares the buoyant front height h_M for the simulations to the corresponding experimental values. The time-averaged values $\langle h_M \rangle_{\tau_{over}}$ are provided in Tab. 8.4. We note that early on, the simulations tend to have larger buoyant front heights than the corresponding experiments, whereas the agreement improves at later times. This may at least partially be due to the perturbations introduced in the experiments by the removal of the gate and by the step in the sediment bed height, which are likely to promote an earlier transition to a fully turbulent state. Furthermore, the current height is seen to decrease for larger Reynolds number in the shallow simulations, which may again reflect the earlier transition to turbulence, cf. simulations S3L10A and S3L10B in Fig.8.12(c). Finally, frame (d) shows that for smooth currents a lower Schmidt number is associated with a decrease in h_M/H, while for rough beds frame (b) shows no significant difference between the simulations for Sc=7 and Sc=1.

The decrease in h_M indicates that the current head loses salinity either into the bed or into the tail section of the current. This issue will be discussed in more detail below. In order to further analyze the dilution of the current front, we calculate the height h_r as the maximum y-value where $\langle c \rangle_z = 0.1$, at the fixed streamwise location $x = -2H$ relative to the front location of the current. Fig. 8.13(a) shows that for the three-layer experiments and the smooth bottom case, respectively, h_r decreases with time. Fig. 8.13(b) indicates that h_M decreases even more rapidly than h_r, so that the currents not only see a reduced height, but also become more dilute.

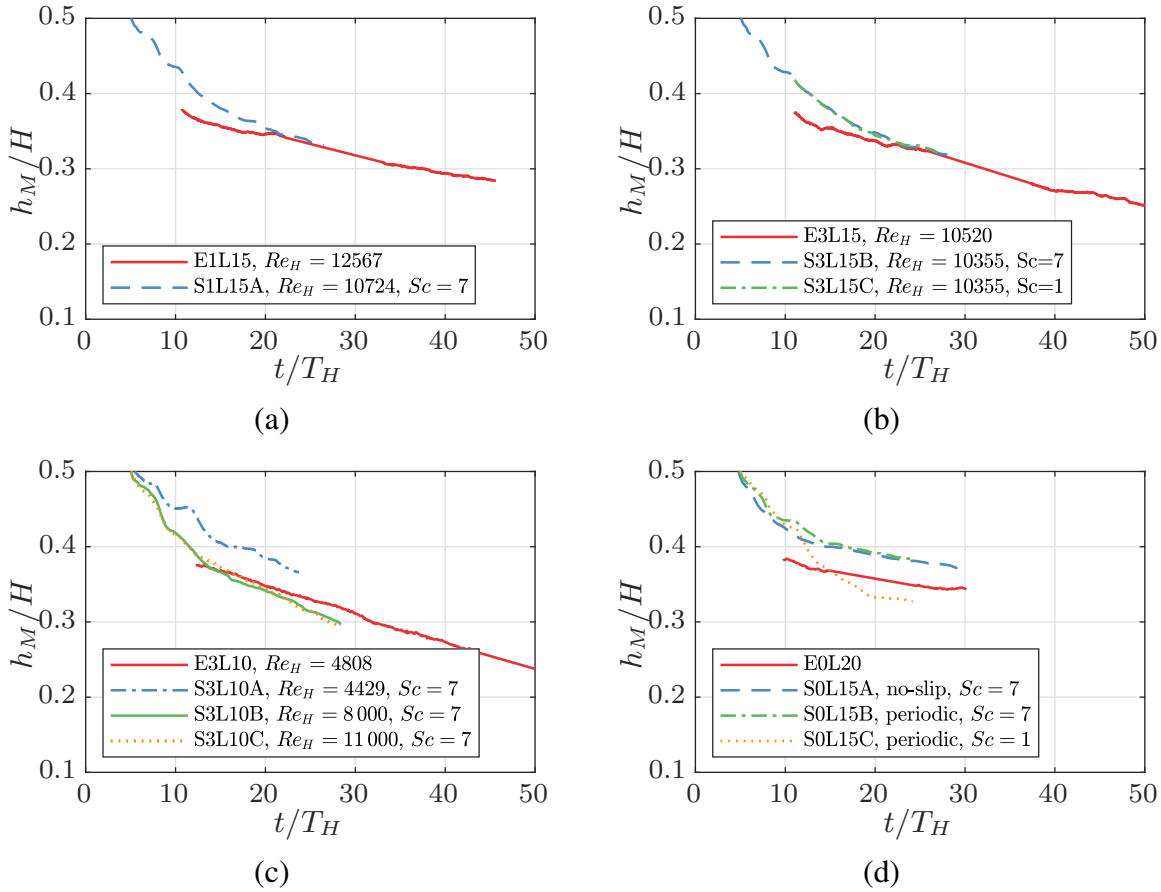

Fig. 8.12 Comparison of experimental and numerical results for the front height h_M. The agreement generally improves with time, which suggests that the discrepancy is mainly due to differences in the initialization of the currents.

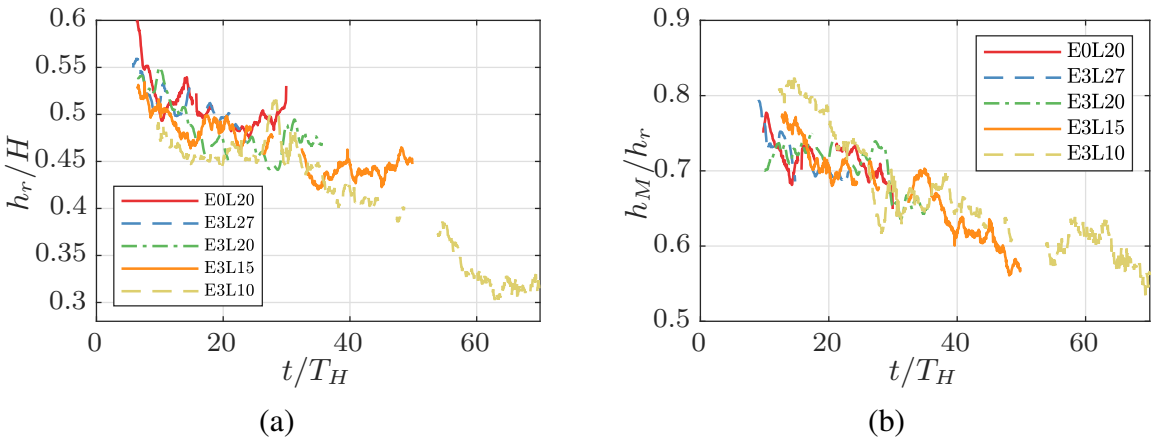

Fig. 8.13 Experimental measurements for h_r/H (a), and h_M/h_r (b) indicate that as their height decreases, the currents also become more dilute.

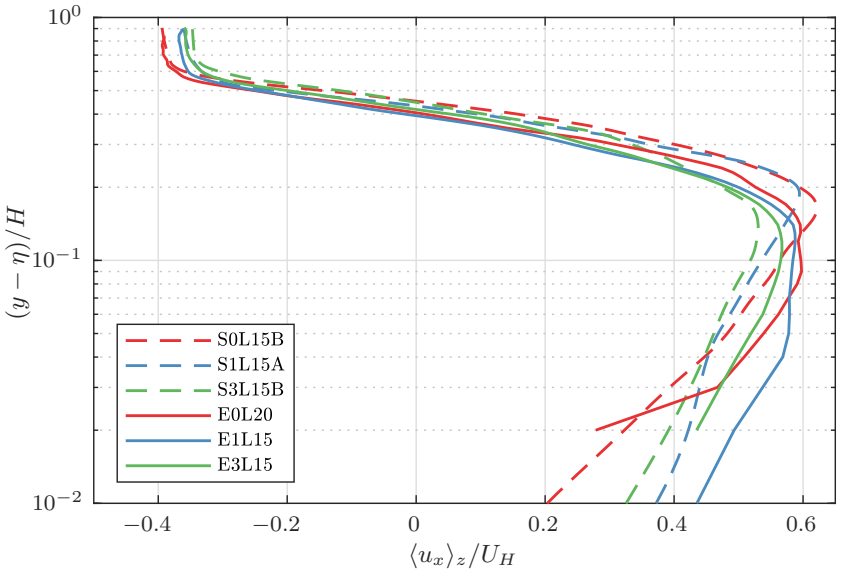

Fig. 8.14 Streamwise velocity profiles, averaged in the spanwise direction, for zero, one and three layers of spheres. The profiles are evaluated at location $x = x_F - 2H$, and they are averaged over the time interval $13 \leq t/T_H \leq 15$. When employing the PTV technique, the velocity values within roughly $3mm$ of the bottom and the top of the flume are affected by reflections, so that we do not show any experimental data in those regions.

8.3.5 Streamwise velocity profiles

Figure 8.14 compares the streamwise velocity profiles for experiments and simulations of gravity currents over a smooth wall, as well as over one or three layers of spherical particles. The velocity profiles are evaluated at a distance $2H$ behind the front, and they are averaged both in the spanwise direction and over the time interval $13 \leq t/T_H \leq 15$. The peak velocities in both simulations and experiments are somewhat larger for the smooth wall, suggesting that rough sediment beds enhance the vertical mixing of streamwise momentum. Near the smooth wall, the velocity is smaller than near the surface of the sediment beds, which indicates that gravity currents propagating over rough beds see a small effective slip velocity at the bed surface. The above velocity profiles are similar to those observed by Zhou et al. (2017) in what the authors refer to as the overflowing regime.

8.4 Analysis of mass and momentum transfer

8.4.1 Mass transfer

The experimental and simulation results presented in the preceding section show several interesting findings regarding the influence of the porous particle bed on the overall gravity current properties. Among them are the exchange of fluid between the current and the bed, a somewhat reduced front velocity that depends mostly on the particle size, a more rapid decrease of the current height and front velocity with time, and a modified velocity profile within the current due to enhanced vertical mixing of streamwise momentum. In order to obtain more detailed insight into the mechanisms by which the particle bed effects these changes, we now proceed to analyze the mass and momentum transfer between the current and the bed in depth.

We begin by analyzing the transport of salinity into and out of the current head, in the reference frame moving with the front. Towards this end, we focus on the control volume $M(t) = [x_F(t) - x_{ML}, x_F(t) + x_{MR}] \times [\eta, L_y] \times [0, L_z]$, with $x_{ML} = 4H$ and $x_{MR} = 0.5H$. Integrating transport equation (8.12) over this volume and dividing by its size $V_M = M_x H L_z$, where $M_x = x_{ML} + x_{MR} = 4.5H$, yields

$$\partial_t \frac{1}{V_M} \int_M c \, \mathrm{dV} = \frac{1}{V_M} \int_{\partial M} \left[v_F c \mathbf{e}_x - \mathbf{u} c + Pe_L^{-1} \nabla c \right] \cdot \mathbf{n} \, \mathrm{dA} \, , \tag{8.26}$$

with $\mathbf{n}$ representing the outward normal to the boundary ∂M of control volume M. By introducing the streamwise velocity in the moving reference frame $u_x^+ = u_x - v_F$ and neglecting the small contributions due to diffusion, we obtain

$$\partial_t \langle c \rangle_M = \langle u_x^+ c^+ \rangle_{\partial M, W} \frac{1}{M_x} + \langle u_y^+ c^+ \rangle_{\partial M, S} \frac{1}{H} \, . \tag{8.27}$$

Here the volume average over M is denoted by $\langle \rangle_M$, while $\langle \rangle_{\partial M, W}$ and $\langle \rangle_{\partial M, S}$ indicate the surface averages of the fluxes across the western and southern boundaries, used to define the boundaries at $x^+ = -4H$ and $y = \eta$, respectively.

Figure 8.15 presents the temporal variation of the terms in the mass balance equation (8.27), for one flow over a smooth wall and three flows over three particle layers of different size. We observe that over time all current heads lose salinity, although the loss rate tends to decrease

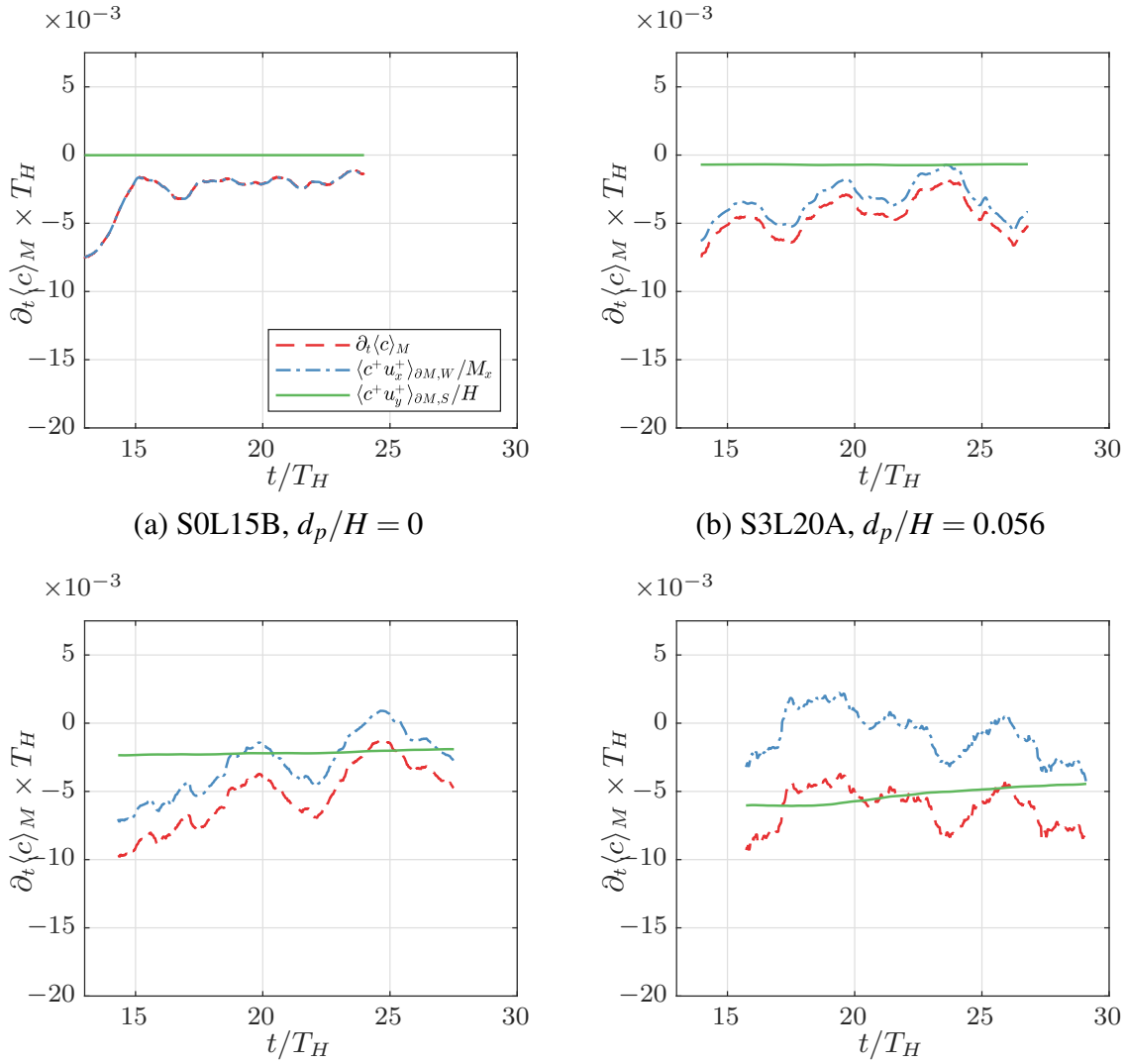

(a) S0L15B, $d_p/H = 0$

(b) S3L20A, $d_p/H = 0.056$

(c) S3L15B, $d_p/H = 0.081$

(d) S3L10B, $d_p/H = 0.14$

Fig. 8.15 Mass balance terms according to Eq. (8.27), averaged over a moving window of two time units. The loss of current fluid into the bed (green line) increases with particle size, while the loss of head fluid to the tail (blue dash-dotted line) decreases for larger particles.

with time for all flows except the one with the largest particles. The relatively large temporal fluctuations in the rate of loss to the current tail may be related to vortical structures as well as variations in the interface height. Interestingly, the loss of current fluid into the bed increases with particle size d_p/H, whereas the loss of salinity to the tail (blue dashed-dotted line) decreases. The reasons behind this influence of the particle size will be discussed below.

Fig. 8.16 presents simulation results in the moving reference frame for the averaged salinity flux $\langle c^+ u_x^+ \rangle_{z,\tau}$ across the western boundary at $x^+ = -4H$. The profiles shown are averaged over a time interval $\tau = [\tau_0, \tau_1]$ that excludes the initial laminar evolution, with the specific time values

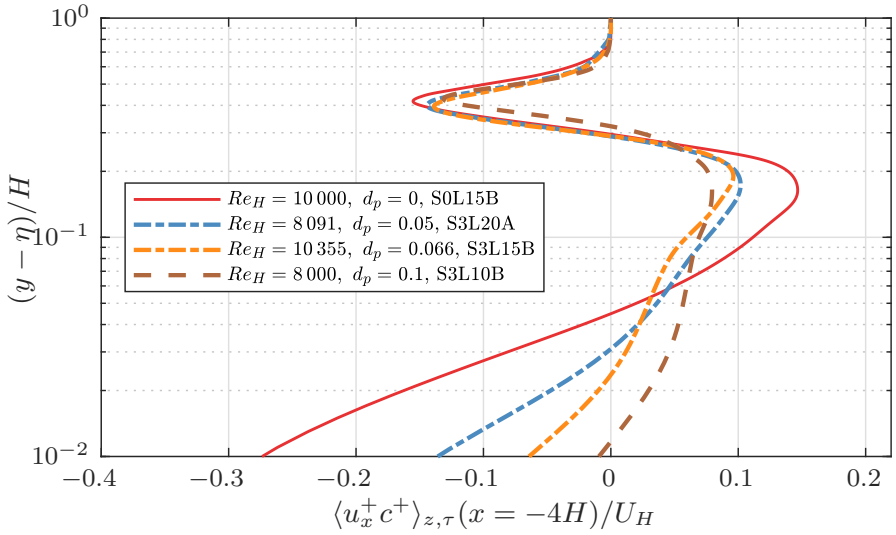

Fig. 8.16 Streamwise salinity flux in the moving reference frame $\langle u_x^+ c^+ \rangle_{z,\tau}$ across the western boundary at $x^+ = -4H$ as a function of the vertical coordinate, shown on a log scale. Compared to a flow over a smooth wall, the flows with particle beds exhibit reduced salinity fluxes from the head into the tail near the lower boundary, and from the tail into the head further away from the boundary.

provided in Tab. 8.3. Compared to the flow over a smooth wall, the flows with particle layers exhibit lower salinity fluxes from the head into the tail just above $y = \eta$, and from the tail into the head further away from the lower boundary. This observation is consistent with the velocity profiles shown in Fig. 8.14, and it reflects the influence of the effective slip velocity at $y = \eta$ mentioned earlier for the flows over particle beds, along with increased vertical mixing in those flows. We will further explore the vertical mixing of momentum in Sec. 8.4.2.

Fig. 8.17 analyzes the time-averaged salinity flux from the current head into the bed, again in the moving reference frame. At the level of the bed surface, $y = \eta$, frame (a) shows that this flux has a pronounced maximum over the interval $0 > x^+/H > -1$, while it levels off thereafter. This indicates that the current front is very effective at sweeping the ambient fluid out of the primary pore spaces and replacing it with current fluid. Here we define the primary pore spaces as the exposed pore spaces between the upper halves of the topmost layer of spheres. Larger particle sizes are associated with a larger primary pore space volume, and thus result in an increased vertical flux. The high-frequency oscillations reflect the periodicity of the bed arrangement.

The subsequent transport of current fluid into the deeper pore layers occurs more slowly. This is demonstrated by Fig. 8.17(b), which shows that the vertical flux at the center of the first particle layer, $y = \eta - d_p/2$, ramps up only gradually behind the current front. A comparison

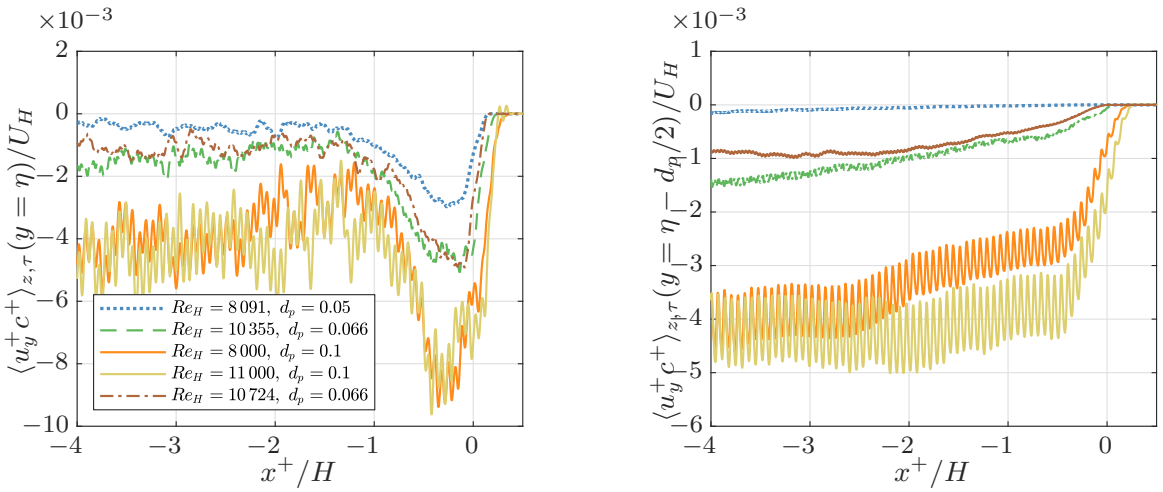

Fig. 8.17 Time-averaged vertical salinity flux from the current head into the bed. (a) Flux at the top of the bed, $y = \eta$, and (b) flux at the center of the first particle layer, $y = \eta - d_p/2$. The different lines correspond to simulations S3L20A, S3L15B, S3L10B, S3L10C, and S1L15A (top to bottom of the legend). The brown short-long-dashed line corresponds to a single layer of particles, whereas all other simulations have three layers. The small salinity flux into the bed for $x > 0$ results from our definition of the front as the location where the current height $h = 0.1$, so that the current extends slightly beyond $x = 0$.

of frames (a) and (b) indicates that for $x/H < -1$ this flux into the deeper pore spaces roughly equals the flux at the bed surface, which suggests that by then the ambient fluid has largely been removed from the primary pore volume. The effective permeability of the bed increases with the particle size, which explains the enhanced salinity flux into the deeper layers of the bed for larger particles, as seen in frame (b). Interestingly, the $Re_H = 11{,}000$ simulation (beige solid line) transports more salinity into the bed than the $Re_H = 8{,}000$ one, which may reflect the mobility increase due to the lower viscosity resistance. The single-layer simulation (brown line) shows a reduced flux due to a lower volume of bed fluid that can be exchanged, as compared to an equivalent three-layer simulation (green line).

From geometric considerations, it follows that the primary pore space volume V_{inter} per x,z-base area A is

$$V_{inter}/A = K_{inter} d_p, \text{ where } K_{inter} = \frac{\sqrt{3} - \pi/3}{2\sqrt{3}} = 0.1977\ , \tag{8.28}$$

so that the current front overruns primary pore space volume per unit width at the rate $\langle v_F \rangle_\tau K_{inter} d_p$. Within the distance H behind the front, current fluid enters the bed at the

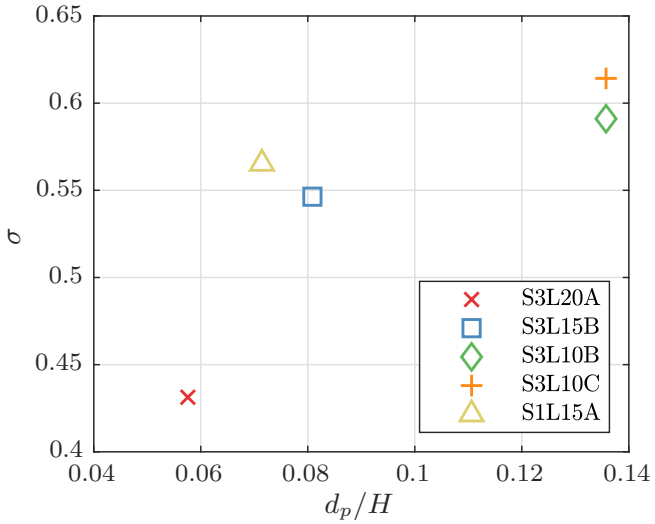

Fig. 8.18 Fraction σ of the primary pore space fluid that is flushed out by the current within a distance H behind the front.

rate $\int_{-H}^{0}\langle u_y^+ c^+\rangle_{z,\tau}\mathrm{d}x$. Hence

$$\sigma = \frac{\int_{-H}^{0}\langle u_y^+ c^+\rangle_{z,\tau}\mathrm{d}x}{-\langle v_F\rangle_\tau K_{inter} d_p} \tag{8.29}$$

denotes the fraction of primary pore space fluid that is swept out within the distance H behind the front. Fig. 8.18 indicates that σ increases with the particle diameter, and typically lies in the range of 0.5 ± 0.1. This confirms our earlier hypothesis that a significant fraction of the primary pore fluid gets flushed out within a distance H behind the front.

8.4.2 Momentum transfer

To analyze the momentum budget, we integrate the momentum balance

$$\partial_t \mathbf{u} + \nabla\cdot(\mathbf{uu}) = -\nabla p + Re^{-1}\nabla\cdot\left(\nabla\mathbf{u} + (\nabla\mathbf{u})^T\right) - \mathbf{e}_y c \tag{8.30}$$

over the moving control volume $\hat{M} = [x_F - 4H, x_F + 0.5H]\times[\eta, \eta+\zeta]\times[0, L_z]$ and divide by the spanwise domain width L_z. Note that $\hat{M}$ does not cover the entire vertical extent of the domain, but only the region from the bed surface at $y=\eta$ to the distance ζ above the bed where the streamwise velocity in the moving reference frame vanishes. Hence $y=\eta+\zeta$ can be viewed as the boundary between the current and the ambient counterflow. Fig. 8.19 displays the spanwise averaged value of ζ at different times, relative to the front position. It shows that both

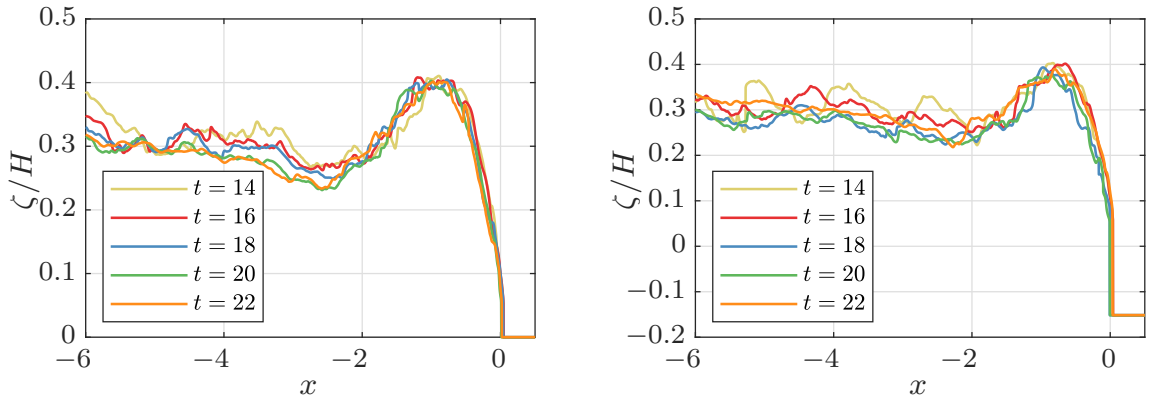

Fig. 8.19 Boundary between the current and the counterflow for evaluating the momentum balance, as defined in the text. (a) Flow simulation S0L15B over a smooth wall, and (b) flow simulation S3L20A over a bed of three particle layers.

for a smooth wall and a rough bed ζ/H fluctuates around the value of 0.3 in the tail, so that we pick $\zeta/H = 0.3$ as the upper boundary of the control volume for the momentum balance.

In compact notation, we can write the x-component of the integrated Eq. (8.30) as

$$\zeta M_x \partial_t \langle u_x \rangle_{\hat{M}} = \zeta \omega_f + \zeta \tau_p + M_x \tau_h + M_x \tau_b \,, \tag{8.31}$$

where the individual terms on the right hand side are defined as

$$\begin{aligned}
\omega_f(t) &= \langle u_x u_x - \nu_F u_x \rangle_{\hat{M},W} - \langle u_x u_x - \nu_F u_x \rangle_{\hat{M},E} \,, \\
\tau_p(t) &= \langle p \rangle_{\hat{M},W} - \langle p \rangle_{\hat{M},E} \,, \\
\tau_h(t) &= -\langle u_y u_x \rangle_{\hat{M},N} + \frac{1}{Re_L} \langle \partial_y u_x \rangle_{\hat{M},N} \,, \\
\tau_b(t) &= +\langle u_y u_x \rangle_{\hat{M},S} - \frac{1}{Re_L} \langle \partial_y u_x \rangle_{\hat{M},S} \,.
\end{aligned} \tag{8.32}$$

The terms in (8.31) represent, from left to right, the time-rate of change of x-momentum within the control volume, the net convective momentum flux across the east and west boundaries (ω_f), the net pressure stress (τ_p), the momentum flux through the top boundary of the current at a distance ζ above the bed (τ_h), and the bed stress (τ_b) due to viscous stress and the convection of momentum. Note that we neglect the viscous stresses at the west and east boundaries, along with the x-derivative of the vertical velocity at the south and north boundaries, as these terms are small.

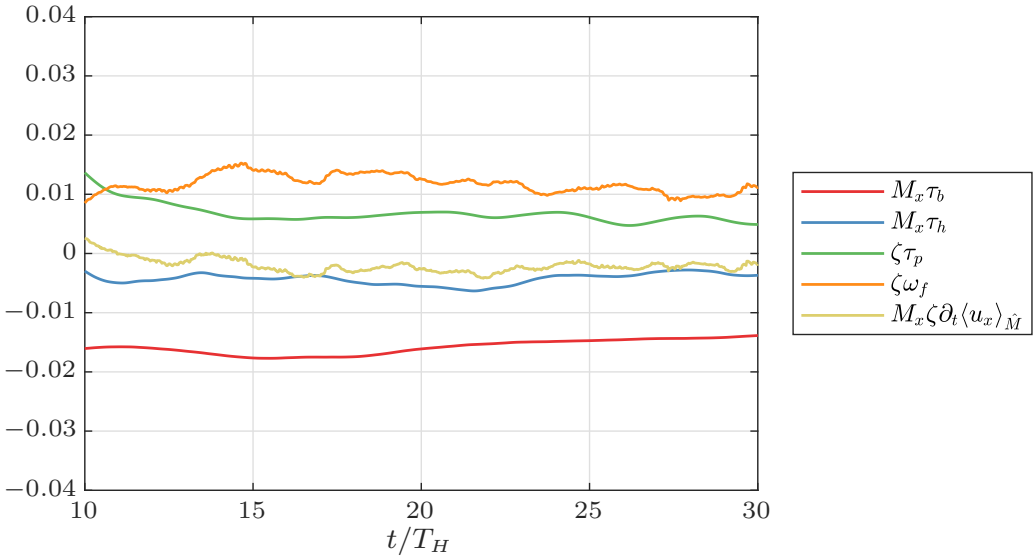

Fig. 8.20 Contributions to the streamwise momentum balance in the control volume for simulation S3L10B, according to Eq. (8.31). The data have been smoothed by employing a moving average extending over two time units. The retarding influence of the bottom and top friction is largely balanced by the convective inflow of momentum and the streamwise pressure drop.

Figure 8.20 displays the terms of Eq. 8.31 for the representative simulation S3L10B. We observe that the bottom friction τ_b represents the main stress retarding the current, with a smaller contribution coming from the top friction τ_h. These retarding forces are largely balanced by the convective momentum inflow ω_f and the streamwise pressure drop τ_p, although the current still experiences a slight overall net deceleration. A detailed comparison with results from other simulations (not shown) indicates that the relative magnitude of the terms is similar for all simulations, although the absolute values can vary significantly, as will now be discussed for the bottom friction term.

Bottom friction

In order to explore the dependence of the bottom friction on the particle size, we define the friction coefficient C_f as

$$C_f(x,z,t) = -\frac{u_y u_x - Re_L^{-1}\partial_y u_x}{v_F^2/2} \quad \text{for } y = \eta \ . \tag{8.33}$$

Here, we included the convective transport of momentum as well, because a potential simplified model of the bed might assume an impermeable surface at $y = \eta$ and then C_f could be used to represent the full momentum transport.

Time-averaged friction coefficient data (the averaging interval is given in Tab. 8.3) are provided in Fig. 8.21. These demonstrate that the friction coefficient increases with the particle size. Even for the smallest particles, the bottom friction is substantially larger than for the smooth wall. Closer inspection of the results shows that most of this increase stems from the convective term $\langle u_y u_x \rangle_{z,\tau}$, which increases significantly for the largest particles with $d_p = 0.1$.

Fig. 8.22(a) displays the mean vertical velocity at the top of the bed as a function of the streamwise coordinate for selected simulations. The figure demonstrates that ahead of the front fluid is ejected out of the bed, while it is pushed into the bed below the current head. Frame (b) shows the variance of the vertical velocity at $y = \eta$ for the same set of simulations sharing the line style with frame (a). We find that its value increases with the particle size and the Reynolds number, as a result of the increased fluid mobility within the bed.

Based on Darcy's law, we can estimate the magnitude of the vertical velocity u_D into the porous bed as

$$u_D \cdot \frac{\mu}{\tilde{K}} = \nabla p, \tag{8.34}$$

where $\tilde{K}$ denotes the permeability of the bed. Carman (1997) showed empirically for flow through glass spheres with a porosity ϕ_f that the permeability can be approximated by

$$\tilde{K} = \frac{d_p^2 \phi_f^3}{180(1-\phi_f)^2} \tag{8.35}$$

For a densely packed bed with $\phi_f = 0.26$ and $d_p = 0.01$ m, this results in a permeability of $\tilde{K} = 1.8 \times 10^{-8}$ m^2. For a current height of approximately half the depth and negligible dilution, we can write Eq. (8.34) as

$$u_D = \frac{\frac{1}{2}\Delta\rho g \tilde{H}\tilde{K}}{\rho_1 \tilde{H}\nu} = \frac{1}{2}\mathscr{U}_H \frac{\tilde{K}}{\tilde{H}^2} Re_H \tag{8.36}$$

or

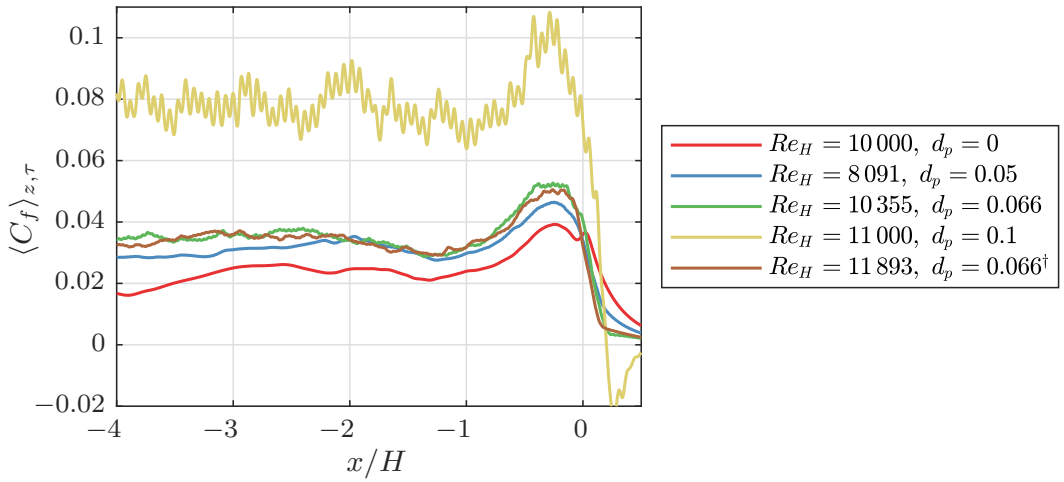

Fig. 8.21 Time-averaged bottom friction coefficient $\langle C_f \rangle_{z,\tau}$ according to definition (8.33), for simulations S0L15B, S3L20A, S3L15B, S3L10C, and S1L15A (from top to bottom in the legend).

$$u_D/\mathscr{U}_H = \frac{1}{2}\frac{\tilde{K}}{\tilde{H}^2} Re_H. \tag{8.37}$$

We find that this predicts the correct order of magnitude for the downward velocities in Fig. 8.22(a). However, it significantly underpredicts the increasing velocities into the bed with increasing d_p, and overpredicts the increase in velocity with Reynolds number. The imperfections in applying the Darcy model to the flow into the bed are not unexpected because of the shallow depth of the rough bed, the relatively large size of the grains, and the side walls adding complexity to the flow. Due to the large pore size a Darcy-Brinkman formulation may be more applicable to the problem. The empirical constants in such a model are less accurately predictable and the model would still experience imperfections due to the side walls and the shallow depth of the bed.

Based on classical investigations of turbulent flows over rough walls (Nikuradse, 1931; Pope, 2000; Schlichting, 1936), we expect the bottom friction to depend on the ratio of the particle radius to the thickness of the viscous sublayer. In order to be able to estimate the latter, we introduce the friction velocity

$$u_\tau = \frac{\sqrt{\nu \partial_{\tilde{y}} \tilde{u}_x}}{\mathscr{U}_L} = \sqrt{\partial_y u_x / Re_L}\,, \tag{8.38}$$

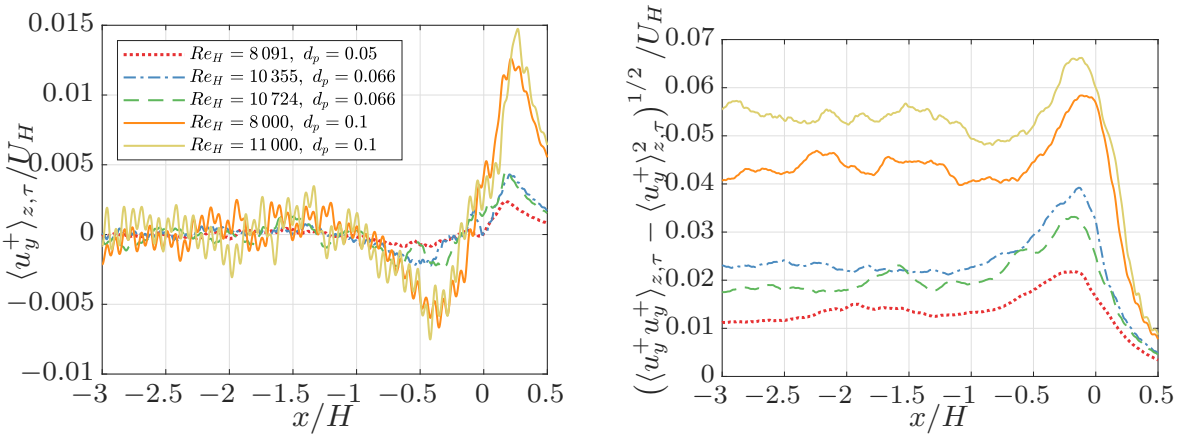

(a) (b)

Fig. 8.22 (a) Mean vertical velocity component at the top of the bed for five simulations of flows over particle beds (S3L20A, S3L15B, S1L15A, S3L10B, S3L10C) (from top to bottom in the legend). Fluid is ejected out of the bed ahead of the front, and into the bed below the gravity current head. (b) Variance of the vertical velocity. This quantity increases with the particle size and the Reynolds number, reflecting the increased mobility of the fluid within the bed.

and a length scale L_W for the near-wall region

$$L_W = \frac{\nu}{\tilde{u}_\tau \tilde{L}_y} = (\partial_y u_x Re_L)^{-1/2} = u_\tau^{-1} Re_L^{-1} \tag{8.39}$$

Fig. 8.23(a) displays streamwise velocity profiles in wall units (solid line) at $x - x_F = -2H$, for three different simulations. A comparison with the linear profiles $u_\tau y/L_W + u_x(y = \eta)/u_\tau$ (dashed line) demonstrates that the viscous sublayer extends to the typical value of five wall units, i.e., $y - \eta \approx 5L_w$. Frame (b) shows the mean friction coefficient as a function of the particle radius normalized by the wall unit L_W. All of the cases with particle layers are seen to fall into the transitional roughness regime $10 < d_p/(2L_W) < 30$, indicating that the particle radius is slightly to substantially larger than the viscous sublayer thickness. Interestingly, the friction coefficient strongly increases once the particle radius exceeds about twenty wall units, as a result of the increased advective momentum mixing seen earlier in Fig. 8.22. This observation is consistent with the work of Fang et al. (2018) and Manes et al. (2009), who investigated open channel pressure-driven flows over fixed beds of spheres, finding enhanced momentum mixing for larger bed permeabilities.

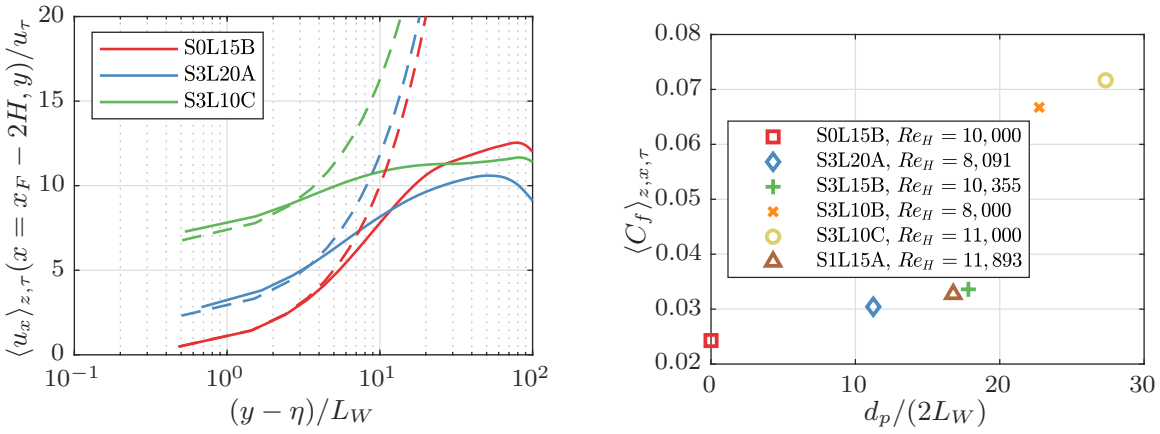

(a) (b)

Fig. 8.23 (a) Spanwise and time-averaged streamwise velocity profiles, evaluated $2H$ behind the front and scaled with wall units, cf. Eqs. (8.38) and (8.39). Frame (b) shows the averaged friction coefficient, Eq. (8.33), as function of the particle size scaled with the wall length L_W. The values of the wall lengths are $L_W = 2.2 \times 10^{-3}$, 2.2×10^{-3}, 1.9×10^{-3}, 2.2×10^{-3}, 1.8×10^{-3}, and 2.0×10^{-3}, respectively, for simulations S0L15B, S3L20A, S3L15B, S3L10B, S3L10C, S1L15A. Note that the friction coefficient increases significantly when the particle radius exceeds about twenty wall units.

8.5 Discussion and conclusion

We have presented a detailed experimental and computational study into gravity currents propagating over fixed beds of monodisperse spherical particles. The investigation provides insight into how the number of particle layers and the ratio of particle size to water depth affect the exchange of mass and momentum between the current and the bed, and hence the decay of current height and velocity with time.

We find that the mass exchange between the current and the bed involves two separate steps that operate on different time scales. In a first step, the dense current front rapidly sweeps away the resident fluid in the exposed pore spaces between the top layer of spheres. We develop a conceptually simple quantitative model for this process that compares well with experimental and simulation data. As a second step, a buoyancy-driven vertical exchange flow between the current and the deeper pores is set up that takes significantly longer to develop. This process depends on the permeability of the bed, which in turn is a function of the particle diameter, and it plays an important role mostly for shallow currents that travel relatively slowly.

The momentum exchange between the current and the bed strongly depends on the particle size as well, and especially on its relative magnitude compared to the viscous sublayer of the current. The bottom friction is moderate when the particle size is smaller than or comparable to the thickness of the viscous sublayer, but it jumps for particles that strongly protrude from the sublayer, leading to a more rapid deceleration of the flow. At the same time, the number of particle layers is seen to affect the front velocity only weakly.

We note that the present lock-exchange experiments and simulations focused primarily on the early stages of the gravity current development. While we expect that the current/bed interaction gains in importance during the later stages of the flow, when the current becomes shallower and slows down as a result of viscous effects, current experimental and simulation resources did not allow us to address these late stages.

Chapter 9: Conclusions

9.1 Summary

This thesis explored results from experiments investigating the impact of roughness on gravity currents. The experiments were motivated by the myriad of situations in the built and natural environment where gravity currents are likely to interact with rough beds.

Chapter 4 explored initial results from experiments consisting of interactions between gravity currents and roughness consisting of arrays of vertical circular cylinders. Three roughness configurations were investigated, termed sparse, dense and plunging, with the relative roughness height ($\sigma = \frac{\eta}{H}$) varied for each configuration. More detailed results for each configuration were presented in Chapters 5, 6 and 7.

Experiments were conducted with currents being allowed to develop before encountering the roughness and with the roughness present at the point of generation. It was found that allowing the currents to develop before encountering the roughness had a minimal impact on their dynamics. Once the currents entered the roughness, regardless of their roughness configuration, their Froude numbers and average density within their heads reduced with time. A number of flow regimes were identified depending on the relative roughness height and roughness configuration. Generally, each current could be considered as either through-flowing, over-flowing, plunging or in a transition between any two of these. The through-flowing regime is characterised by the current flowing between the cylinders, forming a wedge-like structure and driven by a balance between the pressure gradient in the tail and the drag force from the cylinders. The wedge-like structure is distinct from a smooth bed current that has a clear head with a relatively shallower tail. An over-flowing current is characterised by a current flowing over the top of the roughness with a structure similar to a smooth bed current flowing over a porous boundary. The plunging regime is characterised by a current flowing over each row of roughness and plunging downwards between rows of roughness. A current in the plunging regime appears to be driven by wedge-like characteristics similar to the through-flowing currents.

The experiments and simulations outlined in Chapter 8 explored the impact of beds of closely packed solid spheres on gravity currents. As the spheres were closely packed the currents were seen to predominantly travel over them in a manner similar to the over-flowing regime. When the roughness consists of vertical circular cylinders the convective exchange of fluid between the current and the bed occurs quickly due to the open matrix of the bed. However, when the bed consists of spheres the bed is made of a structured matrix such that the convective exchange of fluid is more difficult and occurs more slowly. The exchange of fluid between the bed and the current involves two separate processes that occur over different timescales. The first process is exchanging fluid in the exposed pore spaces with current fluid. This process occurs rapidly, similar to the exchange seen by a current over-flowing arrays of cylinders. The second process is the penetration of dense fluid into the bed. This process takes significantly longer to develop and is more important in currents with larger relative roughness heights that travel more slowly.

9.2 Regime Dependence on Relative Roughness Height and Spacing

As described in Chapter 2, Zhou et al. (2017) used LES to simulate gravity currents interacting with similar fields of vertical circular cylinders. They fixed the relative roughness height at 0.185 but varied the spacing between cylinders and whether cylinders were staggered (as in the sparse and dense experiments in this thesis) or in line (as in the plunging experiments in this thesis). They carried out 220 simulations to fully explore the parameter space and assumed the currents were in a quasi-steady state as they travelled. They calculated Froude numbers by assuming the Froude numbers were constant from times of 2 until 21. Figure 9.1 shows the Froude numbers from their study relative to that of a smooth bed current in $\mu_x - \mu_y$ space. As a reminder, μ_x and μ_y are the cylinder diameter normalised by the cylinder spacing defined as

$$\mu_x = \frac{d_c}{S_x} \tag{9.1}$$

$$\mu_z = \frac{d_c}{S_z} \tag{9.2}$$

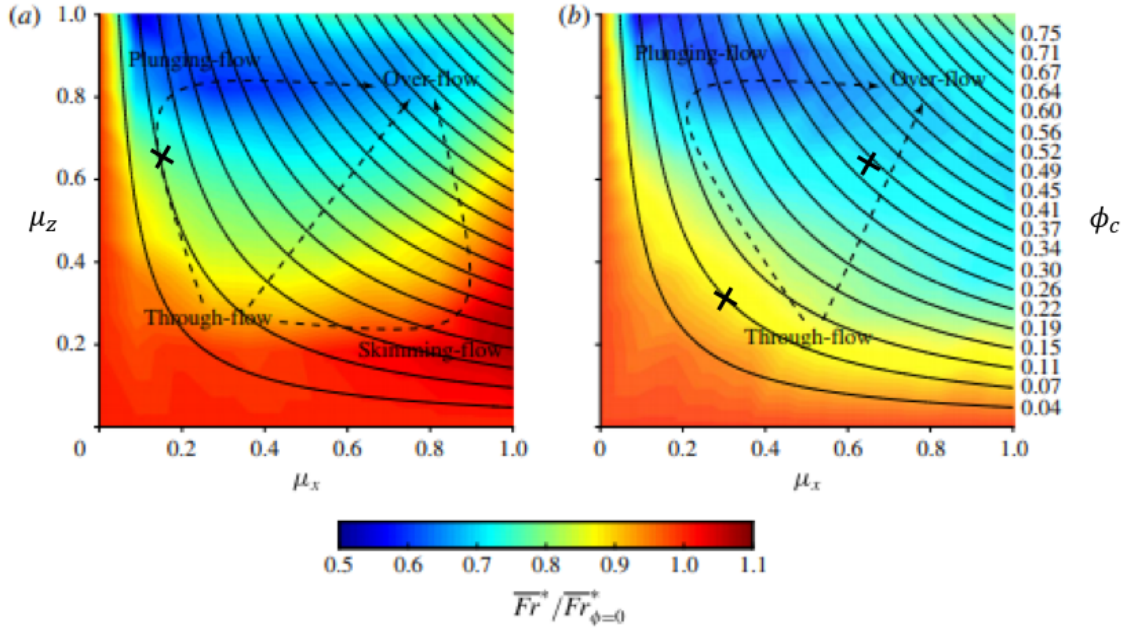

Fig. 9.1 Variation in the time averaged Froude number relative to that of a smooth bed current in the $\mu_x - \mu_z$ space. Adapted from Zhou et al. (2017). Arrows show transitions between different regimes. Points show locations of experiments from the present study.

where d_c is the cylinder diameter and S_x and S_z are the cylinder spacings in the direction of flow and across the channel respectively. In Figure 9.1 arrows show transitions between through-flowing, skimming, plunging and over-flowing regimes and solid lines are plotted to represent contours where the proportion of the bed covered in cylinders, ϕ_c, is constant. As a reminder the skimming regime occurs when sparsely distributed roughness across the channel and densely distributed roughness in the flow direction cause the current to flow in channels between lines of cylinders. Three experiments from this thesis (S5H27, D5H27 and P5H27) have the same relative roughness height as Zhou et al. (2017) and the locations of these are plotted as X's on Figure 9.1.

While Zhou et al. (2017) held the relative roughness (σ) height constant, the regime of a current depends on the relative roughness height along with μ_x and μ_z. Thus, Figure 9.1 is, in reality, a two-parameter slice through a regime diagram that must have at least three parameters - μ_x, μ_y and σ. Based on the findings from the present experiments and the findings of Zhou et al. (2017) a set of regime diagrams for staggered arrays of cylinders were created. The staggered case is selected for this diagram as the skimming flow regime, as defined by Zhou et al. (2017), was not investigated in the present study and this regime only occurs when cylinders are arranged in lines. These are shown in Figure 9.2. Each of these diagrams display μ_x on the x axis and μ_z on

the y axis and each diagram is for a different relative roughness height. Different regimes are denoted S for smooth-bed O for over-flowing, P for plunging, T for through-flowing and B for fully blocked. Crosses show locations of the experiments from this thesis. In reality, regions occur where currents are in transitions between different regimes. For example the D5H15 experiment had both a through-flowing and over-flowing front as it was in transition between the through-flowing and over-flowing regimes. As such the regime boundaries should not be considered sharp distinctions between regimes but instead locations estimated to be within transitional regions.

Zhou et al. (2017) showed that for a single relative roughness height the transition between plunging and through-flowing was similar whether the cylinders were in-line or staggered. Therefore, despite the plunging configuration experiments described in this thesis containing cylinders arranged in lines, these experiments are used to inform Figure 9.2. This figure is generated based on a very limited number of experiments, and hence the locations of transitions between regimes are speculated based on trends rather than measured directly. As such this figure should be viewed as a qualitative representation of the parameter space rather than a quantitative description of the locations of transitions between regimes. The regime at $\sigma = 0.185$ is based on the data of Zhou et al. (2017) as well as experiments from the present study. Diagrams from $\sigma = 0.25$, 0.33 and 0.5 are based on the experiments captured in this study along with known trends. The remaining diagrams are estimated based on trends seen in the present experiments. Moreover, unlike Figure 9.1, this figure does not attempt to plot averaged Froude numbers as insufficient data is available to do so and because previous chapters have shown the Froude number to significantly vary with time. Variation in time is considered in more detail in Section 9.3.

Through-flow Regime

The through-flow regime generally occurs where μ_x and μ_z are small or σ is large. However, when μ_x and μ_z approach zero a current must transition from being through-flowing to resembling a smooth-bed current.

All of the sparse configuration experiments were in the through-flowing regime and hence these experiments indicate that for $\mu_x = \mu_z = 0.31$ gravity currents will be through-flowing for most relative roughness heights. However, as the relative roughness height decreased the heads

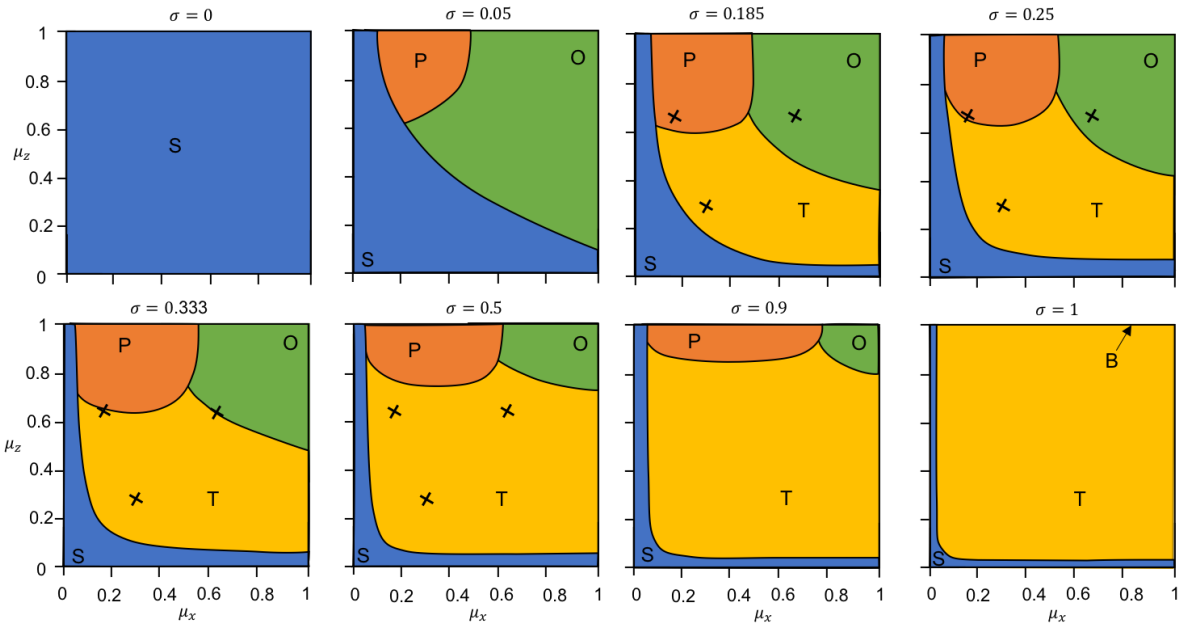

Fig. 9.2 Approximate regime diagram for gravity currents interacting with staggered arrays of cylinders with μ_x, μ_z and σ. Crosses show locations of experiments from the present study. Regimes are denoted S (blue) for smooth bed, O (green) for over-flowing, P (orange) for plunging, T (yellow) for through-flowing and B (uncoloured) for fully blocked.

of these currents transitioned from having wedge-like characteristics to resembling smooth bed currents. As the relative roughness heights decreased further the currents must eventually transition to resemble smooth bed currents and cease to be driven by wedges in their tails. As such, the values of μ_x and μ_z required to transition from the smooth to the through-flowing regime increases with decreasing relative roughness height. As the relative roughness height tends to zero, the currents must resemble smooth bed currents regardless of the spacing.

Over-flow Regime

The over-flowing regime generally occurs where μ_x and μ_z are large. For the dense configuration experiments ($\mu_x = \mu_z = 0.625$) with relative roughness heights of 0.185 or 0.25 the currents were in the over-flowing regime. However, as σ increased the currents transitioned from the over-flowing to the through-flowing regime with $\sigma = 0.333$ representing a transition between the through-flowing and over-flowing regime. Thus, as the relative roughness height increases the μ_x and μ_z required for a current to transition from the through-flowing to over-flowing regime must increase. Furthermore, as the values for μ_x and μ_z required to transition from smooth to the through-flowing regime increase with an increased σ the values required for a transition from through-flowing to over-flowing decrease with increased σ. It is hypothesised that at small but

non-zero relative roughness height (e.g. $\sigma = 0.05$) a current will not become through-flowing but that instead as the cylinder spacing decreases a current would transition directly from the smooth to the over-flowing regime.

At $\sigma = 1$ the current becomes unable to enter the over-flowing regime as the roughness becomes emergent. For the majority of the parameter space with $\sigma = 1$ a current must be in the through-flowing regime. However, at $\mu_z = 1$, instead of the current over-flowing it becomes entirely blocked by the roughness. This regime is referred to as *fully blocked*.

Plunging Regime

The plunging regime occurs when μ_z is large but μ_x is small. Similar to the dense configuration experiments, the plunging configuration experiments ($\mu_x = 0.18$, $\mu_z = 0.625$) showed that as the relative roughness height increased the regimes changed from plunging to through-flowing. Therefore, at a small value for μ_x the value for μ_z required for a current to transition from through-flowing to plunging increases with increased σ.

The experiments in this thesis did not cover the transition between the plunging and over-flowing regime. However, at the limit of $\mu_z = 1$ and where μ_x is small the current must be in a plunging regime regardless of the relative roughness height, provided the relative roughness height is not so large that the roughness creates a complete blockage. Furthermore, as the relative roughness height increases the spacing required for a current to transition from a through-flow to over-flowing regime must increase. Thus, for large μ_z, the value of μ_x required for the current to transition from plunging to over-flowing must increase as the relative roughness height increases.

The final transition between regimes not covered by the experiments in this thesis, but worth discussing, is where μ_x is small but μ_z and σ are large enough that a through-flowing regime does exist for some locations in the $\mu_x - \mu_z$ space. When μ_x is 0 the current must be in the smooth regime and when μ_x is non-zero but small and μ_z is 1 the current must be in a plunging regime or transitioning to smooth bed. However, when μ_x is small and μ_z is close to, but below, 1 a transition may occur from plunging to through-flow before transitioning to being smooth. However, insufficient data is available to fully understand this transition.

9.3 Regime Dependence on Time

The Froude numbers in Figure 9.1 were formulated on the basis that the currents were in a steady state. This thesis has investigated the time varying behaviour of gravity currents and found that the majority of currents were not in steady states. As such, in addition to the relative roughness height and spacings the distance (or time) that a current has travelled through the roughness will have an impact on the properties of the current.

For all of the currents explored in this thesis, once they fully established in a regime they did not change regimes. Most of the over-flowing currents initially entered the roughness in the through-flowing regime before transitioning at an early time. It was shown in Chapter 6 that once these currents travelled a sufficient distance in the over-flowing regime they could reach a quasi-steady state as any head fluid lost to the bed and ambient fluid entrained into the current at the upper surface could be balanced by dense fluid entering the head from the tail. A similar balance exists for a smooth bed current but without the possibility of fluid exchanging with the bed. Thus, smooth bed currents and currents in the over-flowing regime do not change regimes once fully established.

Neither currents in the through-flowing or plunging regimes reached quasi-steady states as these currents are predominantly driven by wedge-like structures. As a wedge-driven current travels the angle of the wedge reduces and thus the driving force will reduce. However, it was seen in Chapters 5 and 7 that these currents do reach states where the wedge angles and speeds vary slowly. As such, once the currents reach such a state they are likely to persist in that regime for a long time. Furthermore, currents in the through-flow regime slow and decrease in size near the front as they travel and hence are less likely to transition to the plunging or overflowing regimes once they are established. However, it is possible that currents in the transitional region between the plunging and through-flowing regimes could transition to through-flowing as the angle of the wedge decreases. It is also possible that a current in transition between smooth and through-flowing could develop a wedge as it travels. However, in general, once a current has developed within the roughness, the distance travelled by the current appears to have less impact on the current regime than variations in μ_x, μ_z or σ.

9.4 Future Research

The regime diagram described in the previous section was based on a small number of experiments. In order to accurately locate the transitions in such a diagram further experimentation is necessary. In future studies, focus should be placed on regions where transitions between regimes are likely to occur. This thesis has shown that whether or not a current is allowed to develop before interacting with roughness has a minimal impact on the final current. Therefore, to maximise the length of roughness before interference with the lock bore occurs, it would be recommended that these experiments utilise roughness beginning at the lock gate. Furthermore, a longer roughness field could be employed in order to better understand and confirm how over-flowing currents reach steady states.

One approach to selecting the experimental parameters (μ_x, μ_z and σ) could be to conduct experiments close to transitions in Figure 9.2. As many experiments, or numerical simulations, would be required to fully explore the parameter space it may be of value to perform these in such a way that they may be conducted in a short amount of time. This would likely come at the expense of detailed quantitative data or analysis such as that presented in this thesis. One possible approach would be to conduct experiments with dye in the lock but without calibrating dye concentration with density. As such, experiments could be conducted very quickly but would be entirely qualitative and could be used solely to locate regions in a regime diagram. Froude numbers could still be generated by measuring the front location of the dye with time. Full LA, or similar, experiments could be conducted in regions where dynamics require further understanding. For example where the relative roughness height is significantly smaller or larger than explored in this thesis or in other regions not explored in Figure 9.2.

In Chapter 5 it was seen that the amount of ambient fluid entrained into the head of a through-flowing current at the upper boundary is similar to the amount entrained into a smooth bed current. It was argued that there were two possible reasons why this occurred. The first is that the primary driver of entrainment into the head of a through-flowing current is K-H instabilities similar to a smooth bed current and that the roughness does not affect these. The other is that the roughness diminishes the K-H instabilities and that this reduction is balanced by additional entrainment caused by wakes behind the cylinders. In order to determine which, if either, of the proposed explanations is valid, detailed simultaneous velocity and density fields would be

required in order to calculate the density flux into the current. These could be provided by DNS simulations.

Additionally, in many situations where gravity currents are found, for example in oceans, the beds are likely to be sloping. As Chapter 2 showed, sloping beds can have significant impacts on gravity current dynamics and the differences between flat and sloping beds may be even stronger when the beds are rough. Therefore, a thorough investigation into how gravity currents interact with roughness on sloping boundaries is required. Experiments could be easily generated using either a lock exchange or constant flux system fixed atop a sloping channel and could be analysed using LA and PTV techniques similar to those utilised in this thesis. Interactions between gravity currents and rough, sloping boundaries could also be studied via LES or DNS.

There are many other aspects of rough boundary gravity currents yet to be investigated. Further studies could investigate interactions between gravity currents and randomly distributed arrays of cylinders or cylinders with μ_x and μ_z that are not constant either vertically or in the direction of flow. Furthermore, studies could consider the difference between constant flux and lock exchange currents in their interaction with roughness or the impacts of ambient stratification or rotation on gravity currents interacting with rough boundaries.

References

Adduce, C., Sciortino, G., and Proietti, S. (2011). Gravity currents produced by lock exchanges: experiments and simulations with a two-layer shallow-water model with entrainment. *J. Hydraul. Eng.*, 138(2):111–121.

Allen, J. (1971). Mixing at turbidity current heads, and its geological implications. *Journal of Sedimentary Research*, 41(1).

Anjum, H. J., Mcelwaine, J. N., and Caulfield, C.-c. P. (2013). The instantaneous froude number and depth of unsteady gravity currents. *Journal of Hydraulic Research*, 51(4):432–445.

Ardekani, M. N., Abouali, O., Picano, F., and Brandt, L. (2018). Heat transfer in laminar Couette flow laden with rigid spherical particles. *J. Fluid Mech.*, 834:308–334.

Barnes, P., Orpin, A., Howarth, J., Patton, J., Lamarche, G., Woelz, S., Hopkins, J., Gerring, P., Mitchell, J., Quinn, W., et al. (2017). New sedimentary-core records and a recent co-seismic turbidite help to unravel the paleoseismicity of the hikurangi subduction zone, new zealand. In *EGU General Assembly Conference Abstracts*, volume 19.

Barr, D. (1967). Densimetric exchange flow in rectangular channels. *La Houille Blanche*, 6:619–632.

Beghin, P., Hopfinger, E. J., and Britter, R. E. (1981). Gravitational convection from instantaneous sources on inclined boundaries. *Journal of Fluid Mechanics*, 107:407–422.

Belcher, S. E., Harman, I. N., and Finnigan, J. J. (2012). The wind in the willows: flows in forest canopies in complex terrain. *Annu. Rev. Fluid Mech.*, 44:479–504.

Benjamin, T. B. (1968). Gravity currents and related phenomena. *Journal of Fluid Mechanics*, 31(02):209.

Bhaganagar, K. and Pillalamarri, N. R. (2017). Lock-exchange release density currents over three-dimensional regular roughness elements. *J. Fluid Mech.*, 832:793–824.

Biegert, E., Vowinckel, B., and Meiburg, E. (2017). A collision model for grain-resolving simulations of flows over dense, mobile, polydisperse granular sediment beds. *J. Comput. Phys.*, 340:105–127.

Birman, V. K., Martin, J. E., and Meiburg, E. (2005). The non-boussinesq lock-exchange problem. part 2. high-resolution simulations. *Journal of Fluid Mechanics*, 537:125–144.

Bonometti, T. and Balachandar, S. (2008). Effect of schmidt number on the structure and propagation of density currents. *Theor. Comp. Fluid Dyn.*, 22(5):341.

Borden, Z. and Meiburg, E. (2013). Circulation based models for boussinesq gravity currents. *Physics of Fluids*, 25(10):101301.

Brandes, E., Vivekanandan, J., Tuttle, J., and Kessinger, C. (1995). A study of thunderstorm microphysics with multiparameter radar and aircraft observations. *Monthly weather review*, 123(11):3129–3143.

Britter, R. E. and Linden, P. F. (1980). The motion of the front of a gravity current travelling down an incline. *Journal of Fluid Mechanics*, 99(03):531–543.

Britter, R. E. and Simpson, J. E. (1978). Experiments on the dynamics of a gravity current head. *Journal of Fluid Mechanics*, 88(02):223–240.

Britter, R. E. and Simpson, J. E. (1981). A note on the structure of the head of an intrusive gravity current. *Journal of Fluid Mechanics*, 112(-1):459.

Cantero, M. I., Balachandar, S., and Garcia, M. H. (2007). High-resolution simulations of cylindrical density currents. *Journal of Fluid Mechanics*, 590:437–469.

Cantero, M. I., Balachandar, S., García, M. H., and Bock, D. (2008). Turbulent structures in planar gravity currents and their influence on the flow dynamics. *Journal of Geophysical Research: Oceans*, 113(C8).

Carman, P. C. (1997). Fluid flow through granular beds. *Chem. Eng. Res. Des.*, 75:S32–S48.

Cenedese, C. and Dalziel, S. B. (1998). Concentration and depth fields determined by the light transmitted through a dyed solution. In *Proceedings of the 8th International Symposium on Flow Visualization*, volume 8, pages 1–37.

Cenedese, C., Nokes, R. I., and Hyatt, J. (2016). Lock-exchange gravity currents over rough bottoms. *Environmental Fluid Mechanics*, pages 1–15.

Cenedese, C., Whitehead, J. A., Ascarelli, T. A., and Ohiwa, M. (2004). A dense current flowing down a sloping bottom in a rotating fluid. *Journal of Physical Oceanography*, 34(1):188–203.

Charba, J. (1974). Application of gravity current model to analysis of squall-line gust front. *Monthly Weather Review*, 102(2):140–156.

Chen, G., Iwai, H., Ishii, S., Saito, K., Seko, H., Sha, W., and Iwasaki, T. (2019). Structures of the sea-breeze front in dual-doppler lidar observation and coupled mesoscale-to-les modeling. *Journal of Geophysical Research: Atmospheres*, 124(5):2397–2413.

Choi, S.-U. and García, M. H. (2002). k-ε turbulence modeling of density currents developing two dimensionally on a slope. *Journal of Hydraulic Engineering*, 128(1):55–63.

Constantinescu, G. (2014). Les of lock-exchange compositional gravity currents: a brief review of some recent results. *Environmental Fluid Mechanics*, 14(2):295–317.

Crouvi, O., Dayan, U., Amit, R., and Enzel, Y. (2017). An israeli haboob: Sea breeze activating local anthropogenic dust sources in the negev loess. *Aeolian Research*, 24:39–52.

Doostmohammadi, A., Dabiri, S., and Ardekani, A. M. (2014). A numerical study of the dynamics of a particle settling at moderate Reynolds numbers in a linearly stratified fluid. *J. Fluid Mech.*, 750:5–32.

Emmanuel, R. and Johansson, E. (2006). Influence of urban morphology and sea breeze on hot humid microclimate: the case of colombo, sri lanka. *Climate research*, 30(3):189–200.

Fang, H., Han, X., He, G., and Dey, S. (2018). Influence of permeable beds on hydraulically macro-rough flow. *J. Fluid Mech.*, 847:552–590.

Feistl, T., Bebi, P., Christen, M., Margreth, S., Diefenbach, L., and Bartelt, P. (2015). Forest damage and snow avalanche flow regime. *Natural Hazards and Earth System Science*, 15(6):1275–1288.

Ferziger, J. H. and Peric, M. (2012). *Computational Methods for Fluid Dynamics*. Springer Science & Business Media.

Geyer, W. and Cannon, G. (1982). Sill processes related to deep water renewal in a fjord. *Journal of Geophysical Research: Oceans*, 87(C10):7985–7996.

Gonzalez-Juez, E., Meiburg, E., and Constantinescu, G. (2009). Gravity currents impinging on bottom-mounted square cylinders: flow fields and associated forces. *Journal of Fluid Mechanics*, 631:65–102.

Gunter, W. S. and Schroeder, J. L. (2015). High-resolution full-scale measurements of thunderstorm outflow winds. *Journal of Wind Engineering and Industrial Aerodynamics*, 138:13–26.

Härtel, C., Carlsson, F., and Thunblom, M. (2000a). Analysis and direct numerical simulation of the flow at a gravity-current head. part 2. the lobe-and-cleft instability. *Journal of fluid mechanics*, 418:213–229.

Härtel, C., Meiburg, E., and Necker, F. (2000b). Analysis and direct numerical simulation of the flow at a gravity-current head. *Journal of Fluid Mechanics*, 418:189–212.

Haynes, W. M. (2014). *CRC handbook of chemistry and physics*. CRC press.

Hogg, A. J., Hallworth, M. A., and Huppert, H. E. (2005). On gravity currents driven by constant fluxes of saline and particle-laden fluid in the presence of a uniform flow. *Journal of Fluid Mechanics*, 539:349–385.

Hopfinger, E. (1983). Snow avalanche motion and related phenomena. *Annual review of fluid mechanics*, 15(1):47–76.

Huppert, H. E. and Simpson, J. E. (1980). The slumping of gravity currents. *Journal of Fluid Mechanics*, 99(04):785–799.

Huq, P., White, L. A., Carrillo, A., Redondo, J., Dharmavaram, S., and Hanna, S. R. (2007). The shear layer above and in urban canopies. *J. Appl. Meteorol. Climatol.*, 46(3):368–376.

Idso, S. B., Ingram, R. S., and Pritchard, J. M. (1972). An american haboob. *Bulletin of the American Meteorological Society*, 53(10):930–935.

Jacobson, A. (2007). Sphere packing lattice generation.

Jeffrey, D. J. (1973). Conduction through a random suspension of spheres. *Proc. Royal Soc. Lond.*, 335(1602):355–367.

Jiang, Y. and Liu, X. (2018). Experimental and numerical investigation of density current over macro-roughness. *Environ. Fluid Mech.*, 18(1):97–116.

Karami, S., Ranjbar, A., Mohebalhojeh, A., and Moradi, M. (2017). A rare case of haboob in tehran: observational and numerical study. *Atmospheric Research*, 185:169–185.

Keramaris, E. and Prinos, P. (2016). Gravity currents in a vegetated valley of trapezoidal shape. *Journal of Applied Fluid Mechanics*, 9(3).

Khattab, I. S., Bandarkar, F., Fakhree, M. A. A., and Jouyban, A. (2012). Density, viscosity, and surface tension of water+ ethanol mixtures from 293 to 323k. *Korean J. Chem. Eng.*, 29(6):812–817.

Klemp, J. B., Rotunno, R., and Skamarock, W. C. (1994). On the dynamics of gravity currents in a channel. *Journal of Fluid Mechanics*, 269:169–198.

Koch, D. L. and Ladd, A. J. (1997). Moderate reynolds number flows through periodic and random arrays of aligned cylinders. *Journal of Fluid Mechanics*, 349:31–66.

Köllner, T., Meredith, A., Nokes, R., and Meiburg, E. (2020). Gravity currents over fixed beds of monodisperse spheres. *Journal of Fluid Mechanics*, forthcoming.

Krause, D. C., White, W. C., PIPER, D. J. W., and Heezen, B. C. (1970). Turbidity currents and cable breaks in the western new britain trench. *Geological Society of America Bulletin*, 81(7):2153–2160.

Kumar, G. (2014). Performance of snow fence at banihal top in himalayan region. *Journal of Cold Regions Engineering*, 29(4):05014001.

Kyrousi, F., Leonardi, A., Roman, F., Armenio, V., Zanello, F., Zordan, J., Juez, C., and Falcomer, L. (2018). Large eddy simulations of sediment entrainment induced by a lock-exchange gravity current. *Adv. Water Resour.*, 114:102–118.

Lehtonen, S. (2018). Haboob near phoenix, arizona - United states universities space research association. Online; Accessed September 2 2019.

Leonard, B. P. (1979). A stable and accurate convective modelling procedure based on quadratic upstream interpolation. *Comput. Methods Appl. Mech. Eng.*, 19(1):59–98.

Leonardi, A., Pokrajac, D., Roman, F., Zanello, F., and Armenio, V. (2018). Surface and subsurface contributions to the build-up of forces on bed particles. *J. Fluid Mech.*, 851:558–572.

Lowe, R. J., Linden, P. F., and Rottman, J. W. (2002). A laboratory study of the velocity structure in an intrusive gravity current. *Journal of Fluid Mechanics*, 456:33–48.

Manes, C., Pokrajac, D., McEwan, I., and Nikora, V. (2009). Turbulence structure of open channel flows over permeable and impermeable beds: A comparative study. *Phys. Fluids.*, 21(12):125109.

Marino, B. M., Thomas, L. P., and Linden, P. F. (2005). The front condition for gravity currents. *Journal of Fluid Mechanics*, 536:49–78.

Mason, M. S., Wood, G. S., and Fletcher, D. F. (2009). Numerical simulation of downburst winds. *Journal of Wind Engineering and Industrial Aerodynamics*, 97(11-12):523–539.

Maxworthy, T. (2010). Experiments on gravity currents propagating down slopes. part 2. the evolution of a fixed volume of fluid released from closed locks into a long, open channel. *Journal of Fluid Mechanics*, 647:27–51.

Maxworthy, T. and Nokes, R. I. (2007). Experiments on gravity currents propagating down slopes. part 1. the release of a fixed volume of heavy fluid from an enclosed lock into an open channel. *Journal of Fluid Mechanics*, 584:433–453.

McBryde, J. (2008). Experimental and numerical modelling of gravity currents preceding backdrafts. Master's thesis, University of Canterbury, Christchurch, New Zealand.

Meiburg, E. and Kneller, B. (2010). Turbidity currents and their deposits. *Annu. Rev. Fluid Mech.*, 42:135–156.

Meiburg, E., Radhakrishnan, S., and Nasr-Azadani, M. (2015). Modeling gravity and turbidity currents: computational approaches and challenges. *Applied Mechanics Reviews*, 67(4):040802.

Miller, S., Keim, B., Talbot, R., and Mao, H. (2003). Sea breeze: Structure, forecasting, and impacts. *Reviews of geophysics*, 41(3).

Mitchell, K. E. and Hovermale, J. B. (1977). A numerical investigation of the severe thunderstorm gust front. *Monthly weather review*, 105(5):657–675.

Mueller, C. K. and Carbone, R. E. (1987). Dynamics of a thunderstorm outflow. *Journal of the Atmospheric sciences*, 44(15):1879–1898.

Naaim-Bouvet, F., Naaim, M., Bacher, M., and Heiligenstein, L. (2002). Physical modelling of the interaction between powder avalanches and defence structures. *Natural Hazards and Earth System Science*, 2(3/4):193–202.

Nasr-Azadani, M. M. and Meiburg, E. (2014). Turbidity currents interacting with three-dimensional seafloor topography. *J. Fluid Mech.*, 745:409–443.

Nasr-Azadani, M. M., Meiburg, E., and Kneller, B. (2016). Mixing dynamics of turbidity currents interacting with complex seafloor topography. *Environmental Fluid Mechanics*, pages 1–23.

Necker, F., Härtel, C., Kleiser, L., and Meiburg, E. (2002). High-resolution simulations of particle-driven gravity currents. *International Journal of Multiphase Flow*, 28(2):279–300.

Necker, F., Härtel, C., Kleiser, L., and Meiburg, E. (2005). Mixing and dissipation in particle-driven gravity currents. *J. Fluid Mech.*, 545:339–372.

Negretti, M. E., Zhu, D. Z., and Jirka, G. H. (2008). The effect of bottom roughness in two-layer flows down a slope. *Dynamics of atmospheres and oceans*, 45(1):46–68.

Nepf, H. M. (2012). Flow and transport in regions with aquatic vegetation. *Annual Review of Fluid Mechanics*, 44:123–142.

Nikuradse, J. (1931). Strömungswiderstand in rauhen Rohren. *J. Appl. Math. Mech.*, 11(6):409–411.

Nogueira, H., Adduce, C., Alves, E., and Franca, M. (2014). Dynamics of the head of gravity currents. *Environ. Fluid Mech.*, 14(2):519–540.

Nogueira, H., Adduce, C., Alves, E., and Franca, M. J. (2013). Analysis of lock-exchange gravity currents over smooth and rough beds. *Journal of hydraulic Research*, 51(4):417–431.

Nokes, R. I. (2017). Streams 3.0. *University of Canterbury*.

Nokes, R. I., Davidson, M. J., Stepien, C. A., Veale, W. B., and Oliver, R. L. (2008). The front condition for intrusive gravity currents. *Journal of Hydraulic Research*, 46(6):788–801.

Oezgoekmen, T. M., Iliescu, T., and Fischer, P. F. (2009). Large eddy simulation of stratified mixing in a three-dimensional lock-exchange system. *Ocean Model.*, 26(3-4):134–155.

Ooi, S. K., Constantinescu, G., and Weber, L. (2007a). A numerical study of intrusive compositional gravity currents. *Physics of Fluids*, 19(7):076602.

Ooi, S. K., Constantinescu, G., and Weber, L. (2009). Numerical simulations of lock-exchange compositional gravity current. *Journal of Fluid Mechanics*, 635:361–388.

Ooi, S. K., Constantinescu, G., and Weber, L. J. (2007b). 2d large-eddy simulation of lock-exchange gravity current flows at high grashof numbers. *Journal of Hydraulic Engineering*, 133(9):1037–1047.

Ottolenghi, L., Cenedese, C., and Adduce, C. (2017). Entrainment in a dense current flowing down a rough sloping bottom in a rotating fluid. *J. Phys. Oceanogr.*, 47(3):485–498.

Ouillon, R., Meiburg, E., Ouellette, N. T., and Koseff, J. R. (2019). Interaction of a downslope gravity current with an internal wave. *Journal of Fluid Mechanics*, 873:889–913.

Ozan, A. Y., Constantinescu, G., and Hogg, A. J. (2015). Lock-exchange gravity currents propagating in a channel containing an array of obstacles. *J. Fluid Mech.*, 765:544–575.

Özgökmen, T. M., Fischer, P. F., Duan, J., and Iliescu, T. (2004). Entrainment in bottom gravity currents over complex topography from three-dimensional nonhydrostatic simulations. *Geophysical Research Letters*, 31(13).

Pantillon, F., Knippertz, P., Marsham, J. H., Panitz, H.-J., and Bischoff-Gauss, I. (2016). Modeling haboob dust storms in large-scale weather and climate models. *Journal of Geophysical Research: Atmospheres*, 121(5):2090–2109.

Peters, W. D. and Venart, J. E. S. (2000). Visualization of rough-surface gravity current flows using laser-induced fluorescence. In *9th (Millennium) International Symposium on Flow Visualization*.

Pokrajac, D. and Manes, C. (2009). Velocity measurements of a free-surface turbulent flow penetrating a porous medium composed of uniform-size spheres. *Transport Porous Med.*, 78(3):367.

Pope, S. B. (2000). *Turbulent Flows*. Cambridge University Press.

Prosperetti, A. and Tryggvason, G. (2009). *Computational Methods for Multiphase Flow*. Cambridge University Press.

Raffel, M., Willert, C., and Kompenhans, J. (1998). *Particle Image Velocimetry: A Practical Guide*.

Raupach, M. (1992). Drag and drag partition on rough surfaces. *Boundary-Layer Meteorology*, 60(4):375–395.

Reible, D., Simpson, J., and Linden, P. (1993). The sea breeze and gravity-current frontogenesis. *Quarterly Journal of the Royal Meteorological Society*, 119(509):1–16.

Rocca, M. L., Adduce, C., Lombardi, V., Sciortino, G., and Hinkelmann, R. (2012). Development of a lattice Boltzmann method for two-layered shallow-water flow. *Int. J. Numer. Meth. Fl.*, 70(8):1048–1072.

Roget, E. and Colomer, J. (1996). Flow characteristics of a gravity current induced by differential cooling in a small lake. *Aquatic sciences*, 58(4):367–377.

Rottman, J. W. and Simpson, J. E. (1983). Gravity currents produced by instantaneous releases of a heavy fluid in a rectangular channel. *Journal of Fluid Mechanics*, 135:95–110.

Rottman, J. W., Simpson, J. E., Hunt, J., and Britter, R. E. (1985). Unsteady gravity current flows over obstacles: Some observations and analysis related to the phase ii trials. *Journal of Hazardous Materials*, 11:325–340.

Schlichting, H. (1936). Experimentelle Untersuchungen zum Rauhigkeitsproblem. *Arch. Appl. Mech.*, 7(1):1–34.

Schmidt, W. (1911). Zur mechanik der boen. *Z. Meteorol*, 28:355–362.

Sequeiros, O. E., Cantelli, A., Viparelli, E., White, J. D., García, M. H., and Parker, G. (2009). Modeling turbidity currents with nonuniform sediment and reverse buoyancy. *Water Resources Research*, 45(6).

Sha, W., Kawamura, T., and Ueda, H. (1991). A numerical study on sea/land breezes as a gravity current: Kelvin–helmholtz billows and inland penetration of the sea-breeze front. *Journal of the atmospheric sciences*, 48(14):1649–1665.

Sher, D. and Woods, A. W. (2015). Gravity currents: entrainment, stratification and self-similarity. *Journal of Fluid Mechanics*, 784:130–162.

Sher, D. and Woods, A. W. (2017). Mixing in continuous gravity currents. *Journal of Fluid Mechanics*, 818.

Shin, J. O., Dalziel, S. B., and Linden, P. F. (2004). Gravity currents produced by lock exchange. *Journal of Fluid Mechanics*, 521:1–34.

Simpson, J. E. (1997). *Gravity currents: In the environment and the laboratory*. Cambridge university press.

Simpson, J. E. and Britter, R. E. (1979). The dynamics of the head of a gravity current advancing over a horizontal surface. *Journal of Fluid Mechanics*, 94(3):477–495.

Singh, M. P. and Ghosh, S. (1987). Bhopal gas tragedy: model simulation of the dispersion scenario. *Journal of Hazardous materials*, 17(1):1–22.

Smyth, W. D. and Moum, J. N. (2012). Ocean mixing by kelvin-helmholtz instability. *Oceanography*, 25(2):140–149.

Tanino, Y., Nepf, H. M., and Kulis, P. S. (2005). Gravity currents in aquatic canopies. *Water Resources Research*, 41(12).

Thomas, L. P., Dalziel, S. B., and Marino, B. M. (2003). The structure of the head of an inertial gravity current determined by particle-tracking velocimetry. *Experiments in Fluids*, 34(6):708–716.

Thomas, L. P., Marino, B. M., and Linden, P. F. (1998). Gravity currents over porous substrates. *Journal of Fluid Mechanics*, 366:239–258.

Thompson, W. T., Holt, T., and Pullen, J. (2007). Investigation of a sea breeze front in an urban environment. *Quarterly Journal of the Royal Meteorological Society: A journal of the atmospheric sciences, applied meteorology and physical oceanography*, 133(624):579–594.

Tokyay, T., Constantinescu, G., and Meiburg, E. (2011). Lock-exchange gravity currents with a high volume of release propagating over a periodic array of obstacles. *J. Fluid Mech.*, 672:570–605.

Tokyay, T., Constantinescu, G., and Meiburg, E. (2012). Tail structure and bed friction velocity distribution of gravity currents propagating over an array of obstacles. *Journal of Fluid Mechanics*, 694:252–291.

Tokyay, T., Constantinescu, G., and Meiburg, E. (2014). Lock-exchange gravity currents with a low volume of release propagating over an array of obstacles. *Journal of Geophysical Research: Oceans*, 119(5):2752–2768.

Twisdale, L. A. and Vickery, P. J. (1992). Research on thunderstorm wind design parameters. *Journal of Wind Engineering and Industrial Aerodynamics*, 41(1-3):545–556.

Ungarish, M. (2009). *An Introduction to Gravity Currents and Intrusions*. Chapman and Hall/CRC.

Ungarish, M. and Huppert, H. E. (2000). High-reynolds-number gravity currents over a porous boundary: shallow-water solutions and box-model approximations. *Journal of Fluid Mechanics*, 418:1–23.

von Karman, T. (1940). The engineer grapples with nonlinear problems. *Bulletin of the American Mathematical Society*, 46(8):615–683.

Wilson, R. I., Friedrich, H., and Stevens, C. (2017). Turbulent entrainment in sediment-laden flows interacting with an obstacle. *Phys. Fluids.*, 29(3):036603.

Wilson, R. I., Friedrich, H., and Stevens, C. (2018). Flow structure of unconfined turbidity currents interacting with an obstacle. *Environmental Fluid Mechanics*, 18(6):1571–1594.

Wood, R., Stromberg, I., and Jonas, P. (1999). Aircraft observations of sea-breeze frontal structure. *Quarterly Journal of the Royal Meteorological Society*, 125(558):1959–1995.

Yuksel-Ozan, A., Constantinescu, G., and Nepf, H. (2016). Free-surface gravity currents propagating in an open channel containing a porous layer at the free surface. *J. Fluid Mech.*, 809:601–627.

Zhang, X. and Nepf, H. M. (2011). Exchange flow between open water and floating vegetation. *Environmental fluid mechanics*, 11(5):531–546.

Zhou, J., Cenedese, C., Williams, T., Ball, M., Venayagamoorthy, S. K., and Nokes, R. I. (2017). On the propagation of gravity currents over and through a submerged array of circular cylinders. *Journal of Fluid Mechanics*, 831:394–417.

Zordan, J., Juez, C., Schleiss, A. J., and Franca, M. J. (2018). Entrainment, transport and deposition of sediment by saline gravity currents. *Adv. Water Resour.*, 115:17–32.

Zordan, J., Schleiss, A., and Franca, M. (2019). Potential erosion capacity of gravity currents created by changing initial conditions. *Earth Surf. Dynam.*, 7:377–391.

Appendix A: Details on PTV analysis

To undertake particle tracking, three different costing strategies were used in series. What follows is the costing strategies used and the Streams inputs used. For all strategies, search windows 4 mm in the y direction and 7 mm in the x direction centred on the particles were employed. For information on these strategies and their parameters, see Nokes (2017).

- First a global optimisation, distance-based costing was used. One iteration was carried out with a maximum matching cost of 1. A velocity field formula was not input.
- Following this a global optimisation, local velocity costing was used. Three iterations were carried out alternating forward and backward iterations with a maximum matching cost of 0.5. The velocity window had a width of 30 mm and a height of 8 mm.
- Following the local velocity costing a residual optimisation was carried out using the recent velocity costing. Three iterations were carried out alternating forward and backward iterations with a maximum matching cost of 0.5.

Appendix B: Full Derivation for Mathematical Model Developed in Chapter 5

Assuming the current takes the shape of a wedge the current height at a location x from the start of the roughness is

$$h = \frac{x_F^* - x}{x_F^*} aH \tag{B.1}$$

Assuming the pressure is hydrostatic throughout the current, the pressure at the base of the channel at a given time (constant x_F) is given by

$$\begin{aligned} P(x) &= \rho_1 g(H-h) + \rho_2 gh \\ &= \rho_1 g(H - \frac{x_F^* - x}{x_F^*} aH) + \rho_2 g \frac{x_F^* - x}{x_F^*} aH \\ &= \rho_1 gH + (\rho_2 - \rho_1) gaH(1 - \frac{x}{x_F^*}) \end{aligned} \tag{B.2}$$

$$\frac{dP}{dx} = \frac{(\rho_2 - \rho_1) gaH}{x_F^*} \tag{B.3}$$

Following a quadratic drag law, the drag force per unit volume is

$$\frac{F_D}{V} = \frac{c_D \rho_2 (\alpha u_F^*)^2 N d_c \eta_c}{2Bx_1 H} \tag{B.4}$$

Balancing the pressure gradient with the drag force per unit volume gives

$$\begin{aligned}
\frac{\rho_2 {u_F^*}^2 N d_c \eta_c}{ABx_1 H} &= \frac{(\rho_2 - \rho_1) g H}{x_F^*} \\
{u_F^*}^2 &= \frac{(\rho_2 - \rho_1)}{\rho_1} g \frac{ABx_1 H^2}{x_F^* N d_c \eta_c} \\
&= \frac{Ag' S_x S_z H^2}{d_c \eta_c x_F^*} \\
u_F^* &= \sqrt{\frac{Ag' S_x S_z H^2}{d_c \eta_c x_F^*}} \qquad \text{(B.5)} \\
Fr &= \frac{u_F^*}{\sqrt{g'H}} \\
&= \sqrt{\frac{AS_x S_z H}{d_c \eta_c x_F^*}} \\
&= \sqrt{\frac{AS_x S_z}{d_c \eta_c x_F}} \qquad \text{(B.6)}
\end{aligned}$$

To transfer this dependence from x_F to t, differentiating Equation B.6 with respect to time gives

$$\frac{dFr}{dt} = -\frac{1}{2}\sqrt{\frac{AS_x S_z}{d_c \eta_c}} x_F^{-3/2} \frac{dx_F}{dt} \qquad \text{(B.7)}$$

From Equation B.6

$$x_F = \frac{AS_x S_z}{d_c \eta_c} \frac{1}{Fr^2} \qquad \text{(B.8)}$$

Hence

$$\begin{aligned}
\frac{dFr}{dt} &= -\frac{1}{2}\sqrt{\frac{AS_x S_z}{d_c \eta_c}} \left(\frac{AS_x S_z}{d_c \eta_c} \frac{1}{Fr^2} \right)^{-3/2} Fr \\
&= -\frac{1}{2} \frac{d_c \eta_c}{AS_x S_z} Fr^4 \qquad \text{(B.9)}
\end{aligned}$$

Integrating this equation with respect to time gives

$$
\begin{aligned}
-\frac{1}{3}Fr^{-3} &= -\frac{1}{2}\frac{d_c\eta_c}{AS_xS_z}t + E \\
Fr &= \left(\frac{3}{2}\frac{d_c\eta_c}{AS_xS_z}t + E\right)^{-\frac{1}{3}} \\
&= \left(C\frac{d_c\eta_c}{S_xS_z}t + E\right)^{-\frac{1}{3}}
\end{aligned}
\tag{B.10}
$$